AD-A110 488 NAVAL RESEARCH LAB. WASHINGTON DC F/G 4/2
REPORT AND ANALYSIS OF THE MAY 1979 MARINE SURFACE LAYER MICROM--ETC(U)
DEC 81 T V BLANC
UNCLASSIFIED NRL-8363 NL

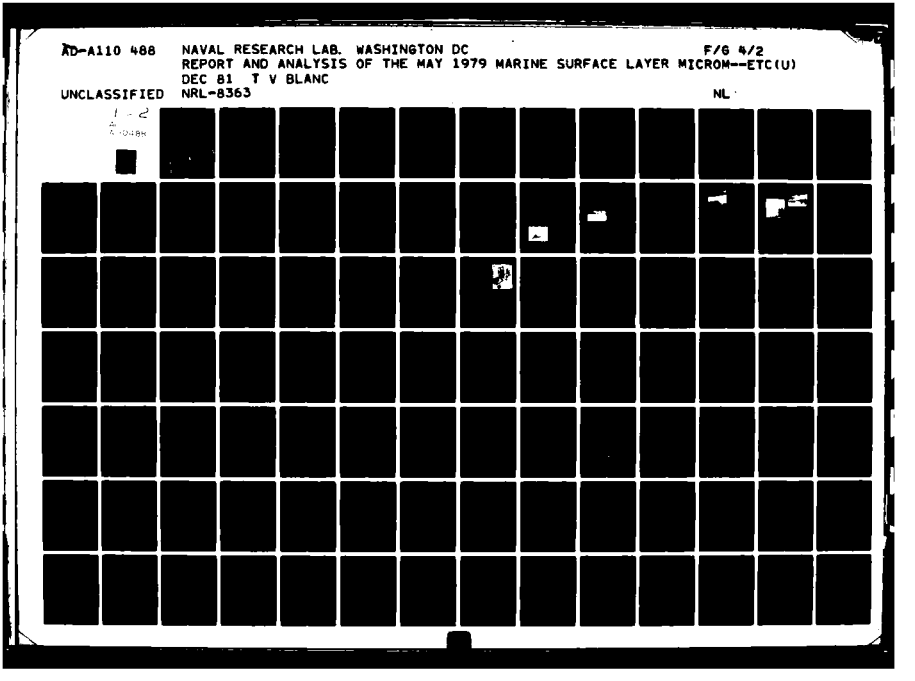

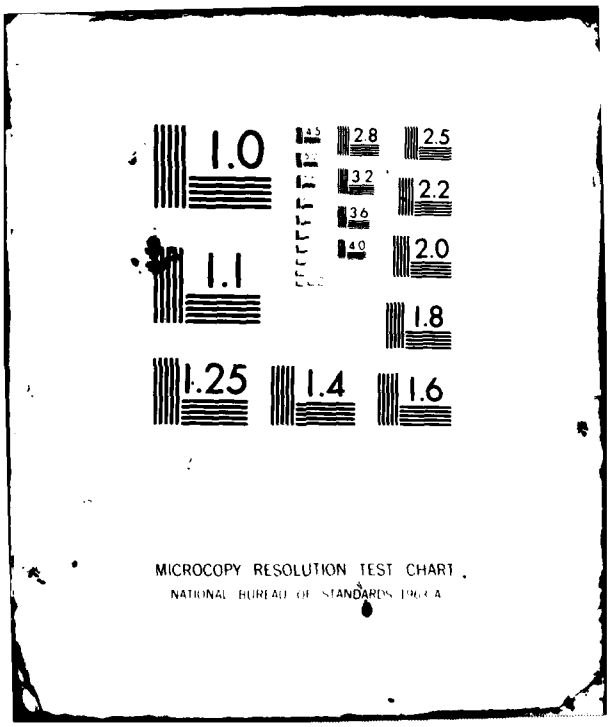
1.0
1.1
1.25
1.4
1.6
1.8
2.0
2.2
2.5
2.8
3.2
3.6
4.0
MICROCOPY RESOLUTION TEST CHART
NATIONAL BUREAU OF STANDARDS 1963-A

LEVEL II

NRL Report 8563

Report and Analysis of the May 1979 Marine Surface Layer Micrometeorological Experiment at San Nicolas Island, California

THEODORE V. BLANC

Atmospheric Physics Branch
Environmental Sciences Division

150p.

December 31, 1981

NAVAL RESEARCH LABORATORY
Washington, D.C.

SECURITY CLASSIFICATION OF THIS PAGE (When Data Entered)

REPORT DOCUMENTATION PAGE		READ INSTRUCTIONS BEFORE COMPLETING FORM
1. REPORT NUMBER NRL Report 8363	2. GOVT ACCESSION NO. AD-A110488	3. RECIPIENT'S CATALOG NUMBER
4. TITLE (and Subtitle) REPORT AND ANALYSIS OF THE MAY 1979 MARINE SURFACE LAYER MICROMETEOROLOGICAL EXPERIMENT AT SAN NICOLAS ISLAND, CALIFORNIA		5. TYPE OF REPORT & PERIOD COVERED Final report on one phase of an NRL problem 6. PERFORMING ORG. REPORT NUMBER
7. AUTHOR(s) Theodore V. Blanc		8. CONTRACT OR GRANT NUMBER(s)
9. PERFORMING ORGANIZATION NAME AND ADDRESS Atmospheric Physics Branch Naval Research Laboratory Washington, DC 20375		10. PROGRAM ELEMENT, PROJECT, TASK AREA & WORK UNIT NUMBERS Program Element: 62759N Task Area: ZF59551002 Work Unit: 43-1134-0-1
11. CONTROLLING OFFICE NAME AND ADDRESS Naval Ocean Systems Center San Diego, CA 92152		12. REPORT DATE December 31, 1981 13. NUMBER OF PAGES 149
14. MONITORING AGENCY NAME & ADDRESS(if different from Controlling Office)		15. SECURITY CLASS. (of this report) Unclassified 15a. DECLASSIFICATION/DOWNGRADING SCHEDULE

16. DISTRIBUTION STATEMENT (of this Report)

Approved for public release; distribution unlimited.

17. DISTRIBUTION STATEMENT (of the abstract entered in Block 20, if different from Report)

18. SUPPLEMENTARY NOTES

19. KEY WORDS (Continue on reverse side if necessary and identify by block number)

Marine atmospheric surface layer	Air-sea interaction
Marine micrometeorology	Gradient & bulk flux comparison
Coastal meteorology	Downward marine humidity flux
Wind profile beach escarpment effect	Simple two-level bulk method
Flux & stability error analysis	Electro-optical meteorology

20. ABSTRACT (Continue on reverse side if necessary and identify by block number)

One hundred thirty-six hours of profile and bulk measurements of momentum, moisture, and sensible heat flux, accompanied by determinations of stability, were made in the marine atmospheric surface layer over the Pacific Ocean from an upwind, low-profile promontory of San Nicolas Island, California, at 33° North latitude and 120° West longitude. A search of the literature revealed that only 15% of the previous marine profile data had been taken outside the equatorial region of the Atlantic Ocean and that only 1% had been acquired under stable atmospheric

(Continued)

DD FORM 1 JAN 73 1473 EDITION OF 1 NOV 65 IS OBSOLETE
S/N 0102-014-6601

SECURITY CLASSIFICATION OF THIS PAGE (When Data Entered)

20. ABSTRACT (Continued)

conditions; no reliable marine profile data could be found for wind speeds in excess of 12 m sec^{-1}. Over a 10-day period a wide variety of meteorological conditions were observed in which the average wind speed ranged from 2 to 17 m sec^{-1}, air-water temperature differences from −2.1 to +0.6°C, and dew point-water temperature differences from −7.5 to −2.0°C. Subsequently, 10% of the data were acquired under stable atmospheric conditions and 15% at wind speeds in excess of 12 m sec^{-1}. A review of previous marine surface layer profile measurements is presented, and the need for additional high wind speed flux measurements is demonstrated. Extensive analysis of the San Nicolas Island data revealed that the measurements were made upwind and above the internal boundary layer formed by the island. Additionally, a generalized technique was developed for correcting the wind-profile modification induced by the inherent change in elevation associated with many beaches. A comparison with previous profile measurements determined that earlier experimenters had overestimated the accuracy of their humidity measurements and that it was impractical to introduce buoyancy into the stability equation. An analysis performed to determine the relative magnitude of the flux and stability measurement errors associated with both the profile and bulk methods determined that the errors were typically in excess of 100%. The largest errors were found to be in the bulk-derived sensible heat flux and stability. The substantial size of the average bulk stability error (~300%) suggested that, unless an independent measurement technique to determine stability accompanied the bulk method, little could be gained by employing a stability-dependent bulk-coefficient scheme like that proposed by Liu et al. and by others. A review of the influence platforms have upon measurements demonstrated that the distortions introduced by the presence of a beach are simpler and better understood than those generated by a ship or a large fixed ocean tower. Hoeber estimated the errors introduced in the bulk determination of fluxes to be on the order of 100% due to the use of a ship as a measurement platform. It was concluded that the discrepancies observed between the island data and the data reported from a ship were not due to an island influence, as speculated by Fairall et al. and Noonkester et al., but were due rather to the ship-induced distortions of the shipboard measurements. A comparison made with other similar overwater experiments demonstrated that the island results were typically as good as those profile experiments conducted from buoys or offshore towers. An analysis revealed that, because the bulk temperature was employed to compute the sea surface temperature, the bulk method was consistently less likely to detect stable atmospheric conditions. It was demonstrated that the inherent difficulty with the bulk method is lack of an accurate technique for measuring the water surface temperature. Approximately 10% of the time a downward humidity flux (condensation) was detected with the profile measurement without fog or rain present. Nine instances are cited from the literature in which a similar downward humidity flux was observed. The bulk method was found to be less likely to detect such relatively infrequent phenomena, because the technique tends to average out the influence of such events. The Friehe-Schmitt bulk scheme, in conjunction with the Smith-Banke bulk drag coefficient scheme, was found to work as well as other bulk schemes for computing fluxes at wind speeds below 12 m sec^{-1}. For wind speeds above 12 m sec^{-1}, the bulk drag coefficient scheme of Kuznetsov was found to be more appropriate. As an alternative to the Smith & Banke scheme, one combining the Mitsuta-Tsukamoto results with the results of Kuznetsov is proposed for wind speeds ranging from 1 to 18 m sec^{-1}. The bulk method was found to differ from the profile method in two principle aspects. Where the profile method is appropriate for local mesoscale determinations, the bulk method is appropriate only for synoptic macroscale determinations. Where the profile method estimated the actual flux value, the bulk method determined only the most probable flux value from among a large number that could be valid under exactly the same synoptic conditions. Recommendations for future bulk method measurements are presented and a simple two level bulk method is proposed. An extensive bibliography is given, and the topic of horizontal homogeneity of the marine boundary layer is discussed. The experiment data base is to be made available on magnetic floppy disk and in hard-copy form.

CONTENTS

	Abstract	1
1.	Introduction	2
2.	Experiment Location	2
3.	Selection of a Flux Measurement Technique	3
4.	Survey of Marine Surface Layer Profile Data	7
5.	Measurement Platforms and Their Influence on Data	9
	Determination of the Minimum Measurement Height Above a Beach	10
7.	Determination of the Minimum Vertical Separation Between Profile Measurement Levels	13
8.	Profile Measurement Accuracy as a Function of the Number of Measurement Levels	16
9.	The Measurement Site	17
10.	Special Micrometeorological Tower Design and Location of Sensors	20
11.	Correction of Beach-Escarpment-Induced Accelerations	21
12.	Instrumentation and Measurement Accuracies	25
13.	Data Acquisition, Measurement Averaging Period, and Availability of Experiment Database	29
14.	Outline of Micrometeorological Calculations	31
15.	Error Analysis and a Comparison with Previous Experiments	33
16.	Statistical Distribution of Observations and the Presentation Format	39
17.	Meteorological, Oceanographic, and Aerosol Observations	42
18.	Flux and Stability Observations	56
19.	Drag Coefficient and Roughness Length Observations	63
20.	Friction Velocity and Other Scaling Parameter Observations	65
21.	Tests for Island Influence in the Flux and Stability Data	68
22.	Comparison of Profile and Bulk Observations	69
23.	Comparison of Drag Coefficient Results With Other Experiments	77
24.	Merits of the Bulk Technique	81
25.	Recommendations for the Bulk Technique	83
26.	Downward Humidity Fluxes Over the Ocean	84
27.	Horizontal Homogeneity and the Optical Measurements	85
28.	Summary and Conclusions	86
29.	Acknowledgments	90
30.	Bibliography	90
APPENDIX A —	Escarpment and Wind Speed Correction Tables	99
APPENDIX B —	Dew Point Field Calibration Device	102
APPENDIX C —	Beach Observations and Tests for Island Influence	103
APPENDIX D —	Example of Combined Two Level Profile—Bulk Flux Method	111
APPENDIX E —	Calculations	112

REPORT AND ANALYSIS OF THE MAY 1979 MARINE SURFACE LAYER MICROMETEOROLOGICAL EXPERIMENT AT SAN NICOLAS ISLAND, CALIFORNIA

THEODORE V. BLANC

Atmospheric Physics Branch
Environmental Sciences Division
Naval Research Laboratory
Washington, D.C.

Abstract—One hundred thirty-six hours of profile and bulk measurements of momentum, moisture, and sensible heat flux, accompanied by determinations of stability, were made in the marine atmospheric surface layer over the Pacific Ocean from an upwind, low-profile promontory of San Nicolas Island, California, at 33° North latitude and 120° West longitude. A search of the literature revealed that only 15% of the previous marine profile data had been taken outside the equatorial region of the Atlantic Ocean and that only 1% had been acquired under stable atmospheric conditions; no reliable marine profile data could be found for wind speeds in excess of 12 m sec^{-1}. Over a 10-day period a wide variety of meteorological conditions were observed in which the average wind speed ranged from 2 to 17 m sec^{-1}, air-water temperature differences from −2.1 to +0.6°C, and dew point-water temperature differences from −7.5 to −2.0°C. Subsequently, 10% of the data were acquired under stable atmospheric conditions and 15% at wind speeds in excess of 12 m sec^{-1}. A review of previous marine surface layer profile measurements is presented, and the need for additional high wind speed flux measurements is demonstrated. Extensive analysis of the San Nicolas Island data revealed that the measurements were made upwind and above the internal boundary layer formed by the island. Additionally, a generalized technique was developed for correcting the wind-profile modification induced by the inherent change in elevation associated with many beaches. A comparison with previous profile measurements determined that earlier experimenters had overestimated the accuracy of their humidity measurements and that it was impractical to introduce buoyancy into the stability equation. An analysis performed to determine the relative magnitude of the flux and stability measurement errors associated with both the profile and bulk methods determined that the errors were typically in excess of 100%. The largest errors were found to be in the bulk-derived sensible heat flux and stability. The substantial size of the average bulk stability error (~300%) suggested that, unless an independent measurement technique to determine stability accompanied the bulk method, little could be gained by employing a stability-dependent bulk-coefficient scheme like that proposed by Liu et al. and by others. A review of the influence platforms have upon measurements demonstrated that the distortions introduced by the presence of a beach are simpler and better understood than those generated by a ship or a large fixed ocean tower. Hoeber estimated the errors introduced in the bulk determination of fluxes to be on the order of 100% due to the use of a ship as a measurement platform. It was concluded that the discrepancies observed between the island data and the data reported from a ship were not due to an island influence, as speculated by Fairall et al. and Noonkester et al., but were due rather to the ship-induced distortions of the shipboard measurements. A comparison made with other similar overwater experiments demonstrated that the island results were typically as good as those profile experiments conducted from buoys or offshore towers. An analysis revealed that, because the bulk temperature was employed to compute the sea surface temperature, the bulk method was consistently less likely to detect stable atmospheric conditions. It was demonstrated that the inherent difficulty with the bulk method is lack of an accurate technique for measuring the water surface temperature. Approximately 10% of the time a downward humidity flux (condensation) was detected with the profile measurement without fog or rain present. Nine instances are cited from the literature in which a similar downward humidity flux was observed. The bulk method was found to be less likely to detect such relatively infrequent phenomena, because the technique tends to average out the influence of such events. The Friehe-Schmitt bulk scheme, in conjunction with the Smith-Banke bulk drag coefficient scheme, was found to work as well as other bulk schemes for computing fluxes at wind speeds below 12 m sec^{-1}. For wind speeds above 12 m sec^{-1}, the bulk drag coefficient scheme of Kuznetsov was found to be more appropriate. As an alternative to the Smith & Banke scheme, one combining the Mitsuta-Tsukamoto results with the results of Kuznetsov is proposed for wind speeds ranging from 1 to 18 m sec^{-1}. The bulk method was found to differ from the profile method in two principle aspects. Where the profile method is appropriate for local mesoscale determinations, the bulk method is appropriate only for synoptic macroscale determinations. Where the profile method estimated the actual flux value, the bulk method determined only the most probable flux value from among a large number that could be valid under exactly the same synoptic conditions. Recommendations for future bulk method measurements are presented and a simple two level bulk method is proposed. An extensive bibliography is given, and the topic of horizontal homogeneity of the marine boundary layer is discussed. The experiment data base is to be made available on magnetic floppy disk and in hard-copy form.

Manuscript submitted December 21, 1981.

1. Introduction

To properly characterize the marine atmosphere in terms of those meteorological parameters which most influence optical and infrared transmission, not only must the ambient values of such quantities as humidity and temperature be measured, but their turbulent fluxes must be determined as well. The turbulent fluxes play a key role in the energy transport mechanism of the ocean-atmosphere system and are essential to an understanding of the generation and transport of such optically important properties as humidity and aerosol size distribution. A correct quantitative description of these processes requires the measurement of the turbulent fluxes of heat, moisture, and momentum in the marine atmospheric surface layer. The ability to determine these quantities in the future from standard synoptic observations requires an additional understanding of the physics involved in the interaction of the air and the sea. A principle objective of this experiment was to measure the fluxes on the local scale and attempt to relate the findings to the synoptic situation with the bulk-flux method.

Of particular importance to the study of air-sea interaction is the heating and cooling of the sea surface by turbulent heat exchange and evaporation, the generation of wind waves due to the action of turbulent wind upon the sea surface, and the formation of turbulent mixed surface layers in the ocean. The development of each of these three processes in the ocean leads in turn to specific changes in the processes which take place in the atmosphere. For example, the development of wind-generated waves can lead to a modification of the sea surface roughness, which in turn changes the turbulent characteristics of the wind. Cooling of the oceanic surface layer can lead to a decrease in the intensity of energy exchange over the ocean because of the formation of a very stable temperature stratification in the atmospheric surface layer. Turbulent mixing in the oceanic surface layer brings the atmosphere into interaction not only with the thin layer at the surface, but also with the typically cooler underlying layers.

An effort has been made to make this text as understandable as possible to non-micrometeorologists. The report deals with many of the practical aspects of the work as seen through the eyes of an experimentalist. An attempt has been made to explain not only what has been done but, more importantly, how and why it was done. If the reader is unable to obtain copies of the more obscure manuscripts or the English translations of some of the references cited, please contact the author to obtain a copy. For those readers who may be unfamiliar with some of the concepts or terminology used in this work, McIntosh & Thom (1973) and Roll (1965) are suggested references.

2. Experiment Location

The marine surface layer can be divided into two general regimes: the open-ocean regime, in which the marine atmosphere interacts only with the ocean; and the coastal regime, in which the air-sea interaction is significantly affected by the presence of a land mass. The influence of a large land mass, particularly on marine aerosols, has been shown in some cases to extend more than 100 km upwind of a continental coast line. The extent of the coastal regime can be frequently related to the local prevailing synoptic scale weather system and, particularly, to the history and trajectory of frontal systems. Generally speaking, the coastal regime can be regarded as the more complex of the two.

Since a comparison of open-ocean-regime and coastal-regime differences would be of interest, a location representative of both would be desirable. As an initial experiment site, however, one predominately representative of the less-complex, more-pervasive, and less-polluted open-ocean regime was thought to be preferable. To distinguish between the two regimes, a method described by Larson (1978) to measure the radon-222 content of the air mass under study could be employed in the field to determine its origin. Sites located off the coast of the eastern United States were eliminated, since the prevailing wind field would be from the continent. An experiment site situated as far upwind as possible from the west coast was regarded as the most desirable location.

Because the primary purpose of the micrometeorological measurements would be to characterize the marine surface layer, in which simultaneous infrared and optical transmission measurements were to be made, the experiment location would require at least two fixed ocean platforms several kilometers apart, from which double-ended optical experiments could be conducted. This would also allow a determination of the lateral homogeneity of the marine surface layer under study. Additionally, it was considered highly desirable that the experiment location be routinely subjected to a wide variety of maritime atmospheric phenomena.

After an extensive search of the western coast of the United States, the most suitable location was found to be on the upwind side of San Nicolas Island, located 105 km off the coast of southern California at 33°15′ North latitude, 119°30′ West longitude (see Fig. 2.1). The approximately 5- by 14-km island is operated by the U.S. Navy as a radar tracking station, and surface and radiosonde observations have been routinely made from it for more than 30 years. Information obtained from experienced observers suggested that the local upwind weather tended to occur in 2- or 3-day cycles, during which conditions remained relatively uniform, and that

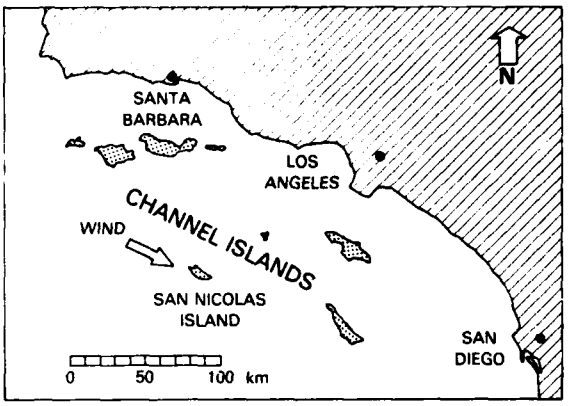

Fig. 2.1 — The location of San Nicolas Island in relation to the southern California coast and the prevailing wind direction

typically over a span of 2 or 3 weeks a diverse spectrum of such uniform periods could be expected. Table 2.1 shows the surface climatology of San Nicolas Island vicinity.

The island had several low-profile parallel promontories which afforded stable optical platforms pointing into the prevailing open-ocean wind direction. This configuration made possible three overwater optical paths, 1.5, 2.5, and 4.1 km long, which were oriented approximately perpendicular to the prevailing wind. The optical paths ranged from 0.2 to 1.0 km upwind of the island's main leading edge, assuring that they would be forward of the locally generated surf. From a logistical perspective, the island had a fully operational air field with daily air service to the mainland, food and housing facilities for visitors, hardline electrical power to the experiment sites, a microwave communication link to the mainland, and available motor-vehicle transportation. In short, from a scientific and logistical prospective the upwind vicinity of the island was considered to be a virtually ideal experiment location.

3. Selection of a Flux Measurement Technique

There are four principle observational techniques for measuring the atmospheric turbulent fluxes of momentum, heat, and humidity Dobson et al. (1980) has presented a brief overview of the use of these techniques in the marine surface layer.

The eddy-correlation technique is a direct method which measures, at a single altitude location, the covariance of vertical velocity fluctuations with those of longitudinal velocity, temperature, and humidity. The technique requires sophisticated sensor instrumentation, with an effective frequency response of up to ~10 Hz, and it typically involves measurements made over a vertical cross section ranging from 1 to 20 cm in scale. A synopsis of the direct-measurement method may be found in Kaimal (1975).

The dissipation technique is a semiempirical method which estimates the fluxes by measuring, at a single altitude location, the one-dimensional spectral density (and/or multimoment-derived derivative statistics) of wind speed, temperature, and humidity. The technique requires small, sophisticated sensor instrumentation, with an effective frequency response of up to ~2 kHz, and it typically involves measurements made over a vertical cross section ranging from 1 mm to a few centimeters in scale. A synopsis of the dissipation method may be found in Champagne et al. (1977).

The profile (or gradient) technique is a semiempirical method in which estimates of the fluxes are made from measurements, at multiple altitude locations, of the average values of wind speed, temperature, and humidity. From these measurements, various height-dependent differential values are determined in order to gauge the vertical fluxes. The technique requires well-calibrated sensors with an effective frequency response of up to ~0.1 Hz and typically involves measurements made over vertical cross sections ranging from about 1 m to 50 m in scale. An elementary description of the profile method may be found in Chapter 9 of McIntosh & Thom (1973).

The bulk (or aerodynamic) technique is a semiempirical method which estimates the flux by measuring, at a single altitude location and just below the surface of the water, the average values of velocity, temperature, and humidity. From these measurements, the various differential values are determined in order to gauge the vertical fluxes. The technique requires relatively unsophisticated sensors with an effective frequency response of up to ~0.02 Hz and typically involves measurements made over a vertical cross-section of about 10 m. An overview of the bulk method may be found in Pedersen and Bǿyum (1980) and in Chapter 4 of Kitaigorodskii (1973).

The eddy-correlation method, unlike the other three, uses a direct measurement of the fluxes and is, presumably, the most desirable in terms of measurement quality. However, from a practical perspective, the present state of the art of sensor instrumentation and data processing has yet to overcome several major impediments to its use in the marine environment for long periods of time.

The best device to date for measuring the velocity fluctuations required for the eddy-correlation technique is the rather expensive three-dimensional sonic anemometer. The device determines the wind velocity fluctuation components by measuring the transit times of rapidly switched directed acoustical pulses. A more

Table 2.1 — San Nicolas Island, California, Surface Climatology

Month	Wind Speed[a] (m sec^{-1})				Wind Direction[a] (True)		Air Temperature[a] (°C)			Mean Sea Surface Temperature[b] (°C)
	% Freq. <1.5	Mean	Av. Max.	% Freq. >10.8	Most Frequent	Max. Wind Speed	Av. Min.	Mean	Av. Max.	
January	16	6.2	26.8	4	NW	WNW	8.9	12.1	15.2	14.6
February	17	7.2	20.6	6	NW	NW	9.3	12.6	15.8	14.4
March	10	7.7	22.1	10	NW	WNW	9.0	12.4	15.8	14.4
April	11	7.7	21.6	11	NW	NW	9.8	13.3	16.9	14.4
May	11	8.2	21.6	13	NW	WNW	10.6	13.9	17.3	14.6
June	11	7.2	23.2	7	NW	WNW	11.7	15.1	18.4	15.3
July	12	6.7	23.2	4	NW	NW	13.1	16.7	20.4	17.3
August	14	6.7	21.1	3	NW	WNW	13.8	17.5	21.2	18.3
September	16	6.7	20.1	4	NW	WNW	14.3	18.0	21.7	18.8
October	19	6.2	21.1	4	NW	NW	11.5	16.0	20.4	18.2
November	20	6.2	21.1	5	NW	WNW	11.4	14.9	18.4	16.6
December	18	6.2	21.6	4	NW	NW	9.7	12.8	15.9	15.7

Table 2.1 (Continued)

Month	Relative Humidity[a] (%)			Ceiling Heights[a] (m)		Precipitation[a]	Wave Heights[b] (m)	
	Av. Min.	Mean	Av. Max	% Freq.< 320 above Sea Level	% Freq.< 930 above Sea Level	(av. no. of days)	% Freq. >0.6	% Freq. >1.8
January	59	75	86	8	21	5.7	61	16
February	60	76	88	7	25	4.6	70	25
March	59	76	88	4	22	4.3	74	25
April	58	76	87	5	28	3.4	74	25
May	64	80	90	8	39	0.8	69	25
June	66	83	93	13	47	0.7	67	20
July	65	83	94	17	42	0.3	60	12
August	63	82	94	15	39	0.1	68	11
September	59	78	89	11	36	0.9	68	16
October	57	75	86	9	27	1.2	59	17
November	58	76	86	6	19	4.4	66	17
December	58	75	85	7	19	5.4	60	19

[a]Based upon 25 years of data taken from the southeast side of the island at an altitude approximately 170 meters above sea level. Source: de Violini (1974).

[b]Based upon 21 years of data taken from ships in the vicinity of the island. Source: Naval Weather Service Environmental Detachment (1971).

detailed description of the device may be found in Kaimal & Businger (1963) and Mitsuta (1966). Recent articles by Larsen et al. (1979) and Campbell & Unsworth (1979) have suggested the possible introduction of relatively inexpensive sonic devices within the next few years.

Other experimenters have attempted, with varying degrees of success, to circumvent the use of expensive sonic devices by employing various types of mechanical propeller and hot wire (or film) devices. Examples of two such devices are reported by Pond et al. (1979) and by Shaw et al. (1973). Some of the typical problems encountered with mechanical propeller devices and their proposed solutions are reported by McBean (1972), Horst (1973), and Francey & Sahashi (1979). A three-dimensional pneumatic device designed for use in the marine environment is presently under development by W. A. *Oost at the Koninklijk Nederlands Meteorologisch* Instituut, as reported by Burt (1979). S. D. Smith (1980b) has reported the construction of a mechanical thrust anemometer which has been successfully calibrated in the field against a sonic device.

An additional difficulty encountered with an eddy-correlation velocity device, described by Kaimal & Haugen (1969), is the necessity of maintaining the device level to $\sim \pm 0.1°$. This is a difficult task on an experiment platform such as a buoy or even an ocean tower. Active and passive in situ methods for dealing with this problem have been reported by Kaimal & Haugen (1971) and by Hyson et al. (1977). Maritime sonic anemometer results taken from floating platforms have been reported by Pond et al. (1971) and by Mitsuta & Fujitani (1974), and results from fixed structures near the beach by Miyake et al. (1970b) and by Naito (1978). A description of the device and review of some of the precautions which must be taken when employing a sonic anemometer in the marine environment may be found in Kaimal (1980)

The major difficulty encountered in the marine environment with eddy-correlation temperature and humidity sensors is the problem of salt contamination. The temperature devices typically employ a fine wire (or film) resistance or microthermistor sensor. In some cases, small thermocouples have been employed. The small size of the sensors is necessitated by the relatively fast response characteristics required for use with the eddy-correlation method. Slower sensors having a larger thermal mass do not appear to be seriously affected by the problem. The contamination of fast thermal sensors due to salt in the marine environment was first suggested by LaRue et al. (1975) and later identified by Schmitt et al. (1978, 1979). These findings may, in part, explain the relatively poor agreement between the marine eddy-correlation and profile derived sensible heat fluxes reported by Paulson et al. (1972) and by Krügermeyer (1976).

The work of Fairall et al. (1979a) would suggest that fast thermal sensors when exposed to the marine environment may require cleaning or replacement at intervals shorter than one hour. Such a constraint would render the eddy-correlation method difficult or impractical for experiments of long duration. A review of fast *thermal sensors and their use in the marine environment* may be found in Larsen et al. (1980).

The most widely used device for sensing the humidity fluctuations required for the eddy-correlation method is the Lyman-α hygrometer. The device measures the absorption by water vapor of the hydrogen Lyman-α spectral line at 1216Å across a sampling path approximately 0.5 to 10 cm long. A description and design of one such device may be found in Buck (1976). Friehe et al. (1975) have argued that the major difficulty in using Lyman-α devices in the marine environment is the rapid deterioration of the device's ultra violet windows when exposed to moist air, salt contamination, or precipitation. Such limitations render the device usable for periods of only a few tens of hours under the best of conditions.

A possible alternative fast-response humidity sensor is an infrared absorption hygrometer proposed by Raupach (1978). In the future such a device may eliminate, or at least minimize, the salt contamination and moisture problems encountered with the Lyman-α device. McGavin & Vetter (1965) have suggested the use of a microwave refractometer as a humidity device and have presented on outline of the basic design philosophy. A review of fast-response humidity sensors and their use in the marine environment may be found in Hay (1980).

Notwithstanding the above mentioned difficulties of operating the sensor systems in a marine environment, because flux data for the San Nicolas Island experiments would be required continuously for periods as long as several hundreds of hours, the most serious constraint to the implementation of the eddy-correlation method would be the amount and rate at which data would need to be recorded and/or processed. To achieve a cross correlation over a bandwidth of ~ 0.001 to 10 Hz, 20 Hz data would need to be analyzed over a period as long as 1 hour. Assuming a minimum of six channels of data, the eddy-correlation method would require data being handled at the rate of $\sim 2 \times 10^6$ bytes h^{-1}. Such a data rate would require ~ 400 m h^{-1} of magnetic tape for postexperiment data reduction or the utilization of a dedicated medium-size computer (by 1977 standards) in the field for in-situ reduction. In either case, the eddy-correlation data processing is neither trival or inexpensive. Kaimal et al. (1966) have presented a description of a field computer facility used for such an experiment.

Because of the data-processing difficulty, most experimenters have had to be content with recording a few tens of hours of flux data on magnetic tape for later

analysis back in the laboratory. This procedure has often necessitated the operation of expensive and logistically complicated field experiments without benefit of reduced data in the field. An instrument malfunction or some other undetected problem in the field has often caused the irretrievable loss of unique and expensive data. An encouraging prospect for the future is a portable and relatively inexpensive microprocessor-based eddy-correlation system for real-time heat and humidity flux measurements recently described by Campbell et al. (1981).

A more esoteric consideration with the eddy-correlation method is the desire in the San Nicolas Island work to characterize the entire approximately 50-meter high marine surface layer in a general manner. Because of the necessarily small atmospheric cross section required for the high-frequency response, the eddy-correlation method typically samples less than 0.5% of the entire vertical expanse of the atmospheric surface layer. Although it is tacitly assumed that the surface layer is a region of uniformly distributed vertical flux, Dyer & Hicks (1972) have noted that theoretical considerations would allow variations in flux of the order of $\pm 20\%$. Kaimal (1969) has experimentally observed vertical variations in measured surface-layer fluxes over land of the order of $\pm 20\%$.

The dissipation method is more practical in terms of sensor expense and vertical alignment than is the eddy-correlation method, however; it requires that data to be analyzed over a wider spectral range, typically ~ 0.001 Hz to 2 kHz. Because of existing fast-Fourier-transform techniques, the dissipation-method data processing reduces to about the same level of difficulty as that of the eddy-correlation method.

Dissipation-method experiments typically measure a one-dimensional wind-speed fluctuation by observation of the cooling induced in a very small heated resistance wire (or film) sensor. An extensive bibliography of thermal anemometery techniques may be found in Freymuth (1978). An ion-deflection fast-response device for observing two-dimensional wind velocity fluctuations up to 1 kHz has been reported by Waletzko (1975). The device measures the transit times of ionized air molecules and is now being commercially manufactured.*

Air-temperature fluctuations for the dissipation technique are usually measured with a resistance sensor in much the same manner as for the eddy-correlation method, except the sensors are much smaller. At the present time, the dissipation method lacks a humidity fluctuation sensor which can directly observe fluctuations greater than ~ 10 Hz. Because of the inherently smaller size of the sensors, the dissipation method suffers even more acutely than the eddy-correlation method from the problems of salt contamination and a small representative sampling cross section. Additionally, Dobson et al. (1980) have noted that a number of the dissipation method's underlying assumptions are often not fulfilled in the real world and that a sizable experimental effort is still required to verify the technique.

Although it is anticipated that the next decade will see sweeping changes, at the present time the implementation of either the eddy-correlation or dissipation techniques for measuring all three of the simultaneous fluxes is impractical in the marine environment for periods longer than a few tens of hours.

Of the two remaining flux-measurement techniques, the most widely employed in the marine surface layer has been the profile method. This method uses a sensor array that is significantly less expensive and more durable than other arrays, that is relatively unaffected by salt contamination, and that uses a vertical sampling cross section most representative of the entire surface layer. Although the development of the profile method was based exclusively on over-land data, Badgley et al. (1972) and others have demonstrated that it is equally valid over water, provided that the measurements are taken high enough above the region of wave influence. Assuming a minimum of six channels of data, the profile method would require data to be averaged and handled at the rate of $\sim 2 \times 10^4$ bytes h^{-1}. This computational task is easily handled by existing small desk-top computers usable in the field.

Encompassed within the profile method are several semiempirically derived profile-flux relationships which have been summarized by Yaglom (1977). The two principal competing relationship schemes are those proposed by Dyer & Hicks (1970) and by Businger et al. (1971). Dyer (1974) has reviewed the differences between the two schemes. Lo & McBean (1978) found that the two schemes could yield differences as large at 40% in the estimated fluxes; they suggested that the discrepancies could be resolved by setting the von Kármán constant equal to 0.40, instead of the recommended 0.35, when using the Businger et al. scheme. This, in effect, would render the Businger et al. scheme equivalent to that of Dyer & Hicks. A justification for this approach was subsequently provided by Wieringa (1980).

To relate the profile observed fluxes to the synoptic situation, it was decided to employ the bulk method as an adjunct to the profile. A principle advantage of the bulk method is its relative simplicity. However, Hasse et al. (1978b) have argued that the simplicity of the bulk technique is achieved at a very sizable cost to its micrometeorological relevance and that it is appropriate

*TSI Inc., St. Paul, Minnesota 55164, Model 202 two-axis wind-velocity sensor.

only as a tool in terms of synoptic macroscale* climatology.

To maintain the bulk technique's principal advantage of measurement simplicity, it is necessary to assume that the surface temperature of the water can be determined by a bulk water measurement. Saunders (1967) has suggested that the typical surface-bulk water temperature difference is on the order of 0.3°C and, under extreme conditions, is as large as 1°C. James & Fox (1972) found that the differences between bucket and ship engine intake temperatures were about the same order of magnitude. This would suggest that not only is the manner in which the water-temperature measurement is made important, but the depth at which it is made is also. Hinzpeter (1967) and Simpson & Paulson (1980) have described some of the difficulties encountered in making direct temperature measurements at the ocean surface. Their work would suggest that it is extremely difficult to make direct temperature measurements much more accurately than $\sim \pm 0.5$°C.

Given the present state of measurement technique, even if the water surface temperature measurement were readily available, the measurement uncertainty would be about the same order of magnitude as the typical surface-bulk difference. The relatively large uncertainty in the surface temperature measurement is particularly critical because the bulk method is a differential measurement. It acquires catastrophic proportions when the air-sea temperature difference is small. A review of the instrumentation and techniques used in measuring sea surface temperature may be found in Katsaros (1980a).

A more esoteric difficulty with the bulk method is that the constituent components of the mediums being measured often arrive at the observation site from drastically different trajectories and at considerably different speeds. Water-current and wind-speed directions are frequently very different. It is not really the water temperature observed immediately below the air-temperature measurement which is most relevant, but rather the integrated effective surface temperature along the wind fetch trajectory. Bill et al. (1980) observed that a significant disagreement occurred between eddy-correlation and bulk-derived sensible and latent heat flux when the sea surface temperature was observed to change with time. These findings would tend to support the contention of Hasse et al. (1978b) that the bulk method is suitable only for synoptic climatology and not for local micrometeorology observations.

Encompassed within the bulk method are more than 20 different competing semiempirical bulk-flux relationship schemes. Partial summaries may be found in Pond et al. (1974), Friehe & Schmitt (1976), and Kondo (1977). The various types of proposed schemes run the complete gambit in terms of complexity and sophistication. For example, where Friehe and Schmitt use single statistical conglomerate coefficients, Krügermeyer (1976) employ stability-dependent coefficients, and Liu et al. (1979) utilize a computational iteration technique requiring five input parameters for twelve dependent variables in five equations which reduce to three simultaneous equations of three unknowns. At the present time there is no single universally excepted bulk-flux scheme. Depending upon which scheme is used, the same input data can yield estimated fluxes differing by as much as 100%.

Admittedly, the selection of a bulk-flux relationship scheme is of necessity somewhat arbitrary. The basic scheme proposed by Friehe & Schmitt (1976), as employed in Friehe & Pazan (1978), was chosen because of its simplicity and apparent statistically broad data base. The Friehe & Schmitt scheme was expanded for the San Nicolas Island experiment to incorporate the computation of the drag coefficient using the Smith & Banke (1975) formulation, as suggested by Friehe (1978), along with several minor alterations.

To summarize: After an extensive review it was determined that, given the present state of the art, the profile method was the most practical and appropriate flux-measurement technique for use in the marine environment for an experiment of extended duration such as San Nicolas Island. The Businger et al. (1971) profile-flux scheme with the von Kármán constant set equal to 0.40 was selected. It was further determined that the bulk method, although suitable only as an auxiliary technique, should be employed as an adjunct for comparative purposes. The Friehe & Schmitt (1976) bulk-flux scheme with the drag coefficient computed using the Smith & Banke (1975) formulation was selected.

4. Survey of Marine Surface Layer Profile Data

One of the earliest experiments to be found in the literature is that of Wüst (1920), which reported wind profile measurements taken from a ship in the Baltic Sea. Perhaps the earliest observations, as noted by Barenblatt et al. (1975), were those conducted by G. I. Taylor in 1913 using instruments sent aloft with a kite from the stern of a whaling ship under sail off the coast of Newfoundland. A list of marine surface layer wind profile measurements reported up to 1962 may be found in Tables X and XXIV of Roll (1965). A current survey of marine surface layer wind profile observations accompanied by temperature and/or humidity profile measurements is presented in Table 4.1.

As indicated in the table, there are two basic observational strategies for acquiring such profile data.

*Defined here to mean planetary surface scales greater than 10 km by 10 km in area.

Table 4.1 — Marine Surface Layer Wind Speed Profile Observations Accompanied by Temperature and/or Humidity Profile Measurements Reported in the Literature Over the Last 25 Years

Source	Experiment (name or location)	Type and Number of Profile Measurement Levels			Altitude Cross-Section Above mean Sea Level (meters)	Observational Strategy (M = Multiple sensors fixed at measurement levels; S = Single sensor sequentially moved to measurement levels)	Environmental Regime	Measurement Platform	Amount of Data (hours)	Approximate Range of Wind Speeds (m sec^{-1})
		Wind Speed	Temperature	Humidity						
Deacon et al (1956)	Port Phillip Bay	6	2		1.5-13	M	Coastal & Inland Water	Ship	49	1-14
Takahashi (1958)	Kagoshima Bay	5	5	5	0.3-4	M&S	Inland Water	Boat & Offshore Pole	67	1-7
Fleagle et al (1958)	East Sound	8	4	4	0.4-4	M&S	Inland Water	Raft	30	3-9
Bruce et al (1961)	Lake Erie	6	6		0.6-13	S	Coastal	Ship	20	3-6
Deacon (1962)	Port Phillip Bay	3	2		3.0-13	M	Coastal & Inland Water	Ship	93(?)	4-15
Bogorodskiy (1964)	?	2	2		1.0-10	M	?	Boat	13	2-7
Hoeber (1969)	Equatorial Atlantic	4	4	4	1.6-9	M	Open Ocean	Buoy	288	4-10
Miyake et al (1970a)	Spanish Bank	5	5	5	0.6-5	S	Coastal (?)	Offshore Mast (?)	6	4-9
Badgley et al (1972)	Indian Ocean	6	6	6	1.6-8	S	Open Ocean & Coastal	Buoy	79	2-8
Garratt (1972)	Lough Neugh	5	5	5	1.0-16	M	Inland Water	Offshore Tower	<1	7
Paulson et al (1972)	BOMEX[a]	4	4	4	2.0-11	S	Open Ocean	Stabilized Ship	113	2-8
Dunckel et al (1974)	ATEX[b]	7	4	4	1.2-8	M	Open Ocean	Buoy	124	4-11
Hasse et al (1975)	GATE[c]	9	5	5	0.5-8	M	Open Ocean	Buoy	6	2-7
Peterson (1975)	Risø	7	8		7.0-123	M	Inland Coastal	Onshore Tower	?	6-9
Hupfer et al (1976)	Baltic Sea	5	5		1.5-7	S	Coastal	Onshore Pole	4	~7
Krügermeyer (1976)	ATEX[b]	7	4	4	1.2-8	M	Open Ocean	Buoy	124	4-11
Hasse et al (1978b)	GATE[c]	7	5	5	1.1-8	M	Open Ocean	Buoy	1,419	1-12

[a]BOMEX = Barbados Oceanographic and Meteorological Experiment, 1969.
[b]ATEX = *Atlantic Trade Wind Experiment*, 1969.
[c]GATE = Global Atmospheric Research Program Atlantic Tropical Experimental, 1974.

The first is to employ a number of identical sensors permanently situated at various altitudes, which acquire data on a continuous bases. The second is to employ a single sensor, which is sequentially moved from one altitude to another, acquiring data while stationary at the desired altitude. The table summarizes the profile data found in the current literature taken over various natural bodies of water. However, the data acquired over inland bodies should be viewed as being primarily indicative of continental regime which has been modified to some degree by the presence of water. Additionally, as noted earlier, it is important to distinguish between the open-ocean and coastal regimes in the maritime environment. It can be argued that the coastal regime is more then the simple superposition of the open-ocean and continental systems, but rather a more complex and unique third regime.

The literature search revealed the existence of only about 2,100-hours of previous profile measurements in which all three of the primary fluxes had been measured; 85% of the data had been obtained in the equatorial region of the Atlantic Ocean. It was further determined that only 1% of the entire previous data base had been acquired under stable atmospheric conditions and that there existed virtually no reliable data taken at wind speeds in excess of 12 m sec $^{-1}$.

5. Measurement Platforms and Their Influence on Data

As suggested in the review of earlier experiments presented in the previous section, marine surface layer profile measurements can be made from a variety of platforms. The various types of platforms could be characterized as belonging to one of five general categories: shipborne, buoy, airborne, offshore tower, and onshore tower.

Augstein et al. (1974a), in a comparison of data taken simultaneously from the deck of a ship and from a buoy, concluded that the ship's hull and superstructure induced sizable distortions in simple measurements of wind speed, air temperature, and humidity. Hoeber (1977), in a specially designed experiment in which data were taken simultaneously from the deck and from a forward boom, found that even rudimentary shipboard measurements (including barometric pressure) were very difficult; he estimated that the errors in some of the resultant bulk derived fluxes were on the order of 100%. Goerss & Duchon (1980), with an arrangement similar to that of Hoeber, observed air-temperature difference errors during the GATE experiments of more than 2°C due to a heating influence of the ship during the day. Reed (1978) reported similar results.

Ching (1976), in a comparison of wind speed measurements made from a number of ship's masts and booms during BOMEX, found that the magnitude of the observed error was a function of the relative angle of approach of the wind to the ship. Kidwell & Seguin (1978), in a similar comparison during GATE to that of Ching, found with identical sensors on four ships that the forward-mounted boom sensors did not necessarily yield more realistic measurements than those taken from the mast. These seemingly conflicting results were resolved by Mollo-Christensen (1979) from wind-tunnel tests which demonstrated that not only must the measurements be made from a boom located upwind of the measurement platform, but that the boom must be of a length equivalent to several times the windward cross section of the structure. Bogorodskiy (1966) reported a poor agreement between wind profile measurements taken from an 8-meter boom mounted forward of a ship and those taken from a buoy.

The ramifications of the ship distortion studies are threefold. First, they clearly demonstrate that it is exceedingly difficult to take even simple bulk flux measurements, much less profile or eddy-correlation flux measurements, from a ship and that such a platform would not be practical for the San Nicolas Island experiments. Second, as suggested by Neumann (1959), it clearly brought into question the data of Deacon et al. (1956) and Deacon (1962). The Deacon results were the only marine profile data in Table 4.1 that were obtained at wind speeds in excess of 12 m sec $^{-1}$. Third, they strongly suggested that the discrepancy observed between the San Nicolas Island measurements and those obtained simultaneously from the research vessel *Acania* (without benefit of instruments mounted on a forward boom) was probably due to the influence of the ship and not due to an island influence as speculated by Fairall et al. (1979b) and Noonkester et al. (1980). A determination of the actual extent of the island's influence in the San Nicolas Island measurements is the topic of Section 21.

As attested to by the results of Hasse et al. (1978b), the best available profile data taken at wind speeds below 12 m sec $^{-1}$ were acquired from a narrow-masted buoy platform. Wucknitz (1977), in a detailed study of the wind-field distortions induced by an instrument-supporting mast, found that even a narrow, single-element, cylindrical mast could significantly influence wind profile measurements. Wucknitz concluded that, if the support structure cross section to sensor distance ratio were sufficiently large (in excess of 1:15), and if the sensors were mounted in a symmetrical pattern on opposing sides of the narrow mast, the measurement error could be kept to an acceptable level. However, Augstein & Wucknitz (1969) had earlier determined that the major limitation to the use even of a semistabilized buoy for profile flux measurements was the problem of wave-induced platform motion. This constraint would render buoy-type platforms unsuitable under the high-wind and high-sea state conditions anticipated at San Nicolas Island. It should be noted that eddy-correlation-method momentum and sensible heat-

flux measurements made from a specially designed stabilized buoy at winds up to 22 m sec^{-1} have been recently reported by S. D. Smith (1980a).

Examples of airborne marine-profile measurements have been reported by Warner (1971, 1972), Augstein et al. (1974b), Raynor et al. (1979), Nicholls & Readings (1979), and Wylie & Ropelewski (1980). Apart from the obvious difficulties of platform stability, the use of airborne platforms is typically restricted to the region of the planetary boundary layer above, or just within, the upper portion of the surface layer, because of safety or operational constraints. In addition, airborne platforms would be practical only for comparatively short measurement periods and usable only under a limited variety of weather conditions.

The two remaining types of platforms are towers and differ only in location. Until a recent paper published by Wieringa (1980), the importance and ramifications of measurement distortions produced upwind of a tower had been generally overlooked or underestimated by most experimenters. Previous papers, such as Moses & Daubek (1961), Gill et al. (1967), and Camp & Kaufman (1970), were primarily concerned with the downwind effects of towers. One of the earliest indications of a possible problem appeared in a paper by Izumi & Barad (1970), in a comparison made between sonic and cup anemometers on the upwind side of a tower. With the two sensors located at different horizontal positions approximately one tower aspect width (or lateral cross section) from the tower, Izumi & Barad observed wind-speed differences ranging from 8 to 16%. They attributed most of the difference (-10%) to an "overspeeding" of the cup anemometers and $\pm 5\%$ to the upwind influence of the tower. Since turbulence eddies over land increase in size with increased height, it would be expected that the overspeeding would be greatest at the lower measurement levels. However, they could find no strong relationship between the amount of overspeed and the anemometers' height above ground. Meshal (1977), in a similar comparison made from a tower over water, found no significant overspeeding of the cup anemometers. His two measurements were found to agree within 2%.

In one of the first papers to deal directly with the upwind influence of a tower, Angell & Bernstein (1976) observed -7% reduction in the average wind-speed measurement made at a similar distance-to-tower aspect ratio as that used by Izumi & Barad. The influence of the tower is of particular concern in regard to the profile-derived momentum flux, since a 6% error in the average measurement made at one level could yield an error in the order of 80% in the estimated momentum flux. Mollo-Christensen (1979), in a paper dealing with the upwind distortions induced by ships and offshore towers, graphically described the problem by demonstrating the existence of a wind-field vortex upwind of an obstruction at a distance-to-tower aspect ratio approximately equal to that used by Imuzi & Barad and by Angell & Bernstein. Based upon these observations, prudence suggested the necessity of mounting the sensors as far forward of a tower as possible, at a distance no less than several times the towers aspect width. A review of the importance of taking into consideration the flow distortions introduced by measurement towers may be found in Wucknitz (1980). A presentation of the precautions taken to insure a minimum upwind distortion induced by the tower employed in the San Nicolas Island experiment is the topic of Section 10.

An offshore measurement tower was initially thought to be most desirable for San Nicolas Island. However, an extensive site survey and feasibility study conducted by Chern (1977) concluded that the island vicinity was unsafe for an offshore platform of a type that could be afforded by the project and that the only viable alternative was an onshore structure. Although such a site would afford obvious logistical advantages, it would also require insuring that the measurements would be unaffected by the island's influence. Previous experiments reported by Peterson (1975), Hupfer et al. (1976), and Dyer & Garratt (1978)*, demonstrated the difficulties that could be encountered in attempting to acquire overwater data from an onshore tower. A description of the precautions taken for the San Nicolas Island beach site is presented in Sections 6 and 11.

6. Determination of the Minimum Measurement Height Above a Beach

Figure 6.1 demonstrates that when the flow distortion introduced by an island beach is compared to other measurement platforms, it is the least complex and easiest to correct. A beach platform affords an additional advantage in that the flow distortion can be adjusted to the desired configuration by altering the beach topography with earth-moving equipment.

Some of the earliest experimental observations of the influence of the land-sea interface upon the marine surface layer were conducted by the University of Texas and were reported by Echols (1970) and by Echols & Wagner (1972). Over the last decade much of the experimental impetus for the work has been spearheaded by S. A. Hsu at Lousiana State University (see, for example, Hsu (1977)).

The modification of the marine surface layer due to the influence of a beach can be separated into four general categories. First is the modification induced in the wind field by a change in surface roughness as the marine air moves overwater to the aerodynamically rougher beach. Second is the modification induced in the temperature and humidity fields by the local surface

*Also see, Mitsuta et al. (1979).

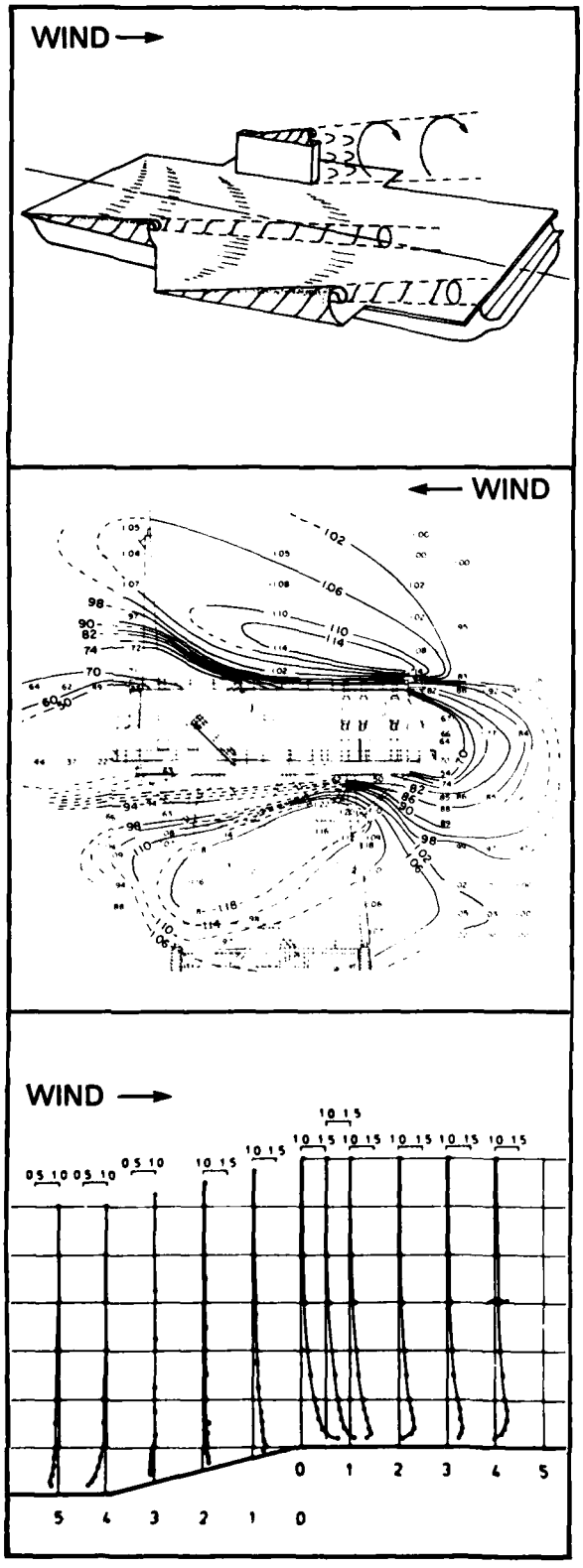

Fig. 6.1 — Three examples of the flow distortions introduced by various ocean measurement platforms. The top figure depicts the typical downwind distortion introduced by a large structure such as a ship (courtesy of the Naval Ship Research and Development Center). The middle figure, from Thornthwaite et al. (1965), depicts the upwind and downwind distortion introduced by a typical large fixed ocean platform in which the contour lines are those of equal wind speed amplification. The bottom figure, from the wind tunnel studies of Bowen & Lindley (1977), depicts the typical upwind and downwind distortion introduced by a beach with an aspect ratio of 0.25 in which the profiles are those of wind speed amplification.

heating of the dry beach, the evaporation of the wet beach, and the spray of the upwind surf zone. Third is the acceleration of the wind field induced by the change in elevation inherent in all beaches. Fourth, though not limited just to beach regions, is the influence of the wave height on the wind field.

When a marine wind field in equilibrium with the underlying sea surface passes over a beach with a different roughness, an atmospheric boundary is formed over the beach in which the air adjusts to the new surface conditions. This boundary, known as an internal boundary layer, is formed in the vicinity of the water's edge and increases in height as a function of downwind distance from the water. The phenomenon was first theoretically considered in the pioneering work of Elliot (1958), in which he determined that under neutral atmospheric stability conditions the internal boundary layer should develop with a height-to-fetch ratio of approximately 1:10. Elliot further determined that the boundary height should be independent of wind speed and that thermal stability should have only a minor influence (on the order of 10%) on the height of the boundary, raising it slightly under unstable conditions and lowering it under stable conditions (see Fig. 6.2).

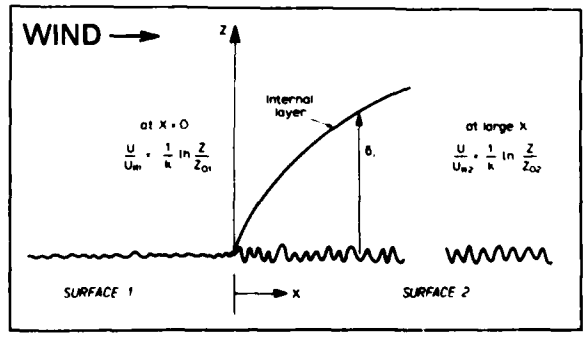

Fig. 6.2 — Figure from Wood (1978) depicting the formation of an internal boundary layer due to a change in surface roughness in which u is wind speed, u_* is friction velocity, z is altitude, z_0 is roughness length, and k is the von Kármán constant

Based upon different theoretical considerations than Elliot used, Panofsky & Townsend (1964) confirmed that the expected boundary-layer height-to-fetch ratio was about 1:10 and predicted that the boundary should be marked by a well-defined interface. Based upon yet another theoretical approach, Peterson (1969) predicted that the transition to the internal boundary layer should be marked by an inflection in the velocity profile. Defining the top of the internal boundary layer to be the height at which the downstream value has changed from the upstream value by 1%, Shir (1972) theoretically determined the height-to-fetch ratio to be about 1:10 for stress (momentum flux) and 1:20 for velocity. The ratios differ because stress is defined in terms of the velocity derivative and, therefore, is more sensitive to change. Because it had been previously decided to measure the momentum flux using the profile method, and because velocity could not be measured much more accurately then about ±1%, it was anticipated that for all practical purposes the detectable boundary formed by the underlying beach would lie somewhere between a height-to-fetch ratio of 1:20 and 1:10.

Echols & Wagner (1972) conducted an experiment over a ±1-meter undulating beach, with a mean upwind slope of about 1:14, from a tower located 90 meters from the water—conditions similar to those anticipated for San Nicolas Island. With seven levels of wind-speed sensors located between 1 and 27 meters, Echols & Wagner found the boundary layer height-to-fetch ratio to vary from about 1:15 to 1:12 (see Fig. 6.3).

Because San Nicolas Island is routinely subjected to extreme storms, safety constraints would dictate that a tower could not be located any closer then about 100 meters from the mean sea level mark. Using the worst case found by Echols & Wagner and adding 10% for stability-dependent variations, the minimum profile-sensor height unaffected by the internal boundary layer formed by the island beach would be about 9 meters for a tower located 100 meters from the water.

In a later experiment, Peterson et al. (1979) conducted measurements under nearly neutral stability conditions over a marsh which contained virtually no change (mean slope ~1:400) in elevation. They used three towers located at the water's edge, at 82 meters downwind, and at 160 meters downwind, with six levels of sensors located between 1 and 12 meters in altitude. The change in roughness was determined to be equal to about one order of magnitude. The Peterson et al. data suggested that, in the absence of large-scale beach undulations or changes in elevation, velocity profile data taken above 9 meters could be indicative of upstream values at distances up to 160 meters from the water's edge, within the limits of the wind speed measurement error of ±1%. This would suggest a height-to-fetch ratio of about 1:18 (see Fig. 6.4).

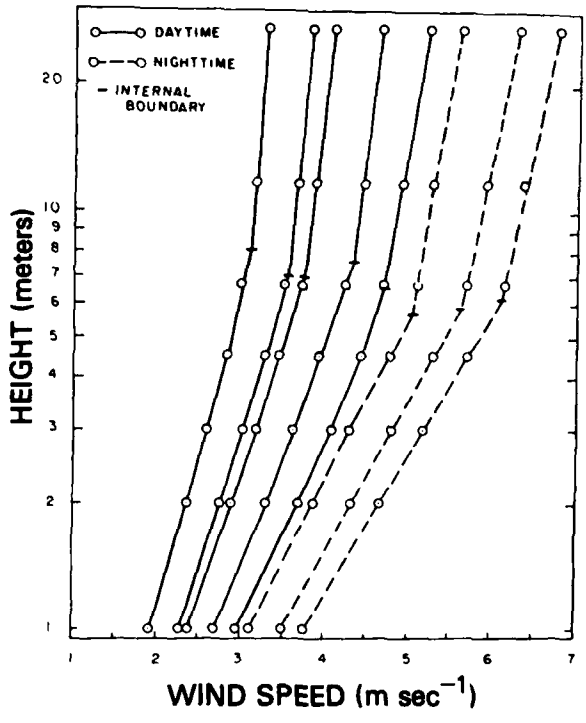

Fig. 6.3 — Figure from Echols & Wagner (1972) showing the wind profiles above a beach obtained 90 meters downwind from the waters edge. Note the kink in the profile associated with the internal boundary layer formed by the underlying beach.

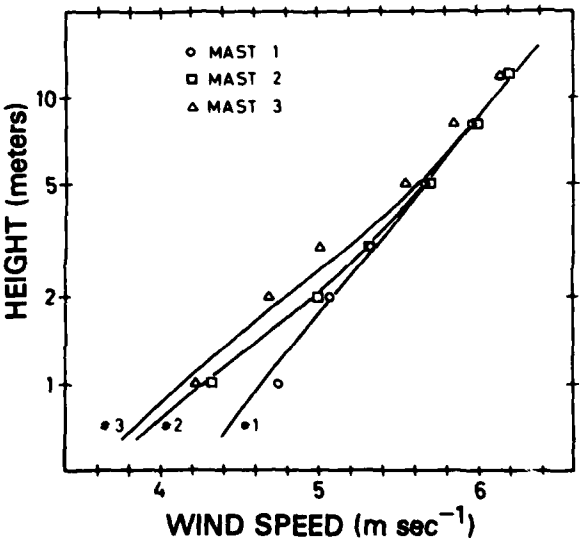

Fig. 6.4 — Figure from Peterson et al. (1979) in which masts 1 thru 3 have fetch lengths equal to 0, 82, and 160 meters, respectively, from the water's edge

The contrast between the height-to-fetch ratio determined by Echols & Wagner and that suggested by Peterson et al. could be explained in terms of the difference in the change in elevation. This would imply, in a general sense, that if the change in surface-roughness phenomena could be separated from the effects of a change in elevation, and if the elevation-induced modifications could be properly corrected, then profile measurements above 9 meters could be made at distances as great as 160 meters from the water's edge.

The second category of possible beach influence is the modification induced in the temperature and humidity fields by surface heating, evaporation, and surf spray. Temperature profile studies conducted on a beach under onshore wind conditions have been reported by Hsu (1973), by Vugts & Businger (1977), by Makita & Kikuchi (1977), and by Jehn & Jehn (1979). Unfortunately, almost all of their data was limited to the region slightly above the internal boundary layer or the region well within it. Since the only source of information found for humidity profiles was Vugts (1980), who indicated that their data were in the process of being published, it was assumed for this experiment that the humidity and temperature fields above the internal boundary layer were affected in an identical manner. The theoretical work of Taylor (1970) would suggest that the height of an internal boundary layer formed by a change in surface roughness coincides approximately with that of the thermal internal boundary layer formed by a change in surface temperature. The experimental work of Hupfer et al. (1976) found, from measurements made on a beach 75 meters from the water's edge, that the inflection in the wind-speed profile marking the internal boundary layer coincided with a corresponding inflection in the temperature profile.

The third category of consideration is the change in elevation inherent in varying degrees to all beaches. This phenomenon was first brought to the attention of this author by Friehe (1979). Because of the elevated tide which usually accompanies severe storms, it would be impractical to place a tower in a location with little change in elevation. For the San Nicolas Island vicinity, it was determined that a minimum beach elevation of 5 meters above mean sea level would be required to insure a reasonable survival probability.

Jackson & Hunt (1975) and Taylor (1977), in theoretical and wind-tunnel studies, proposed methods to model the wind flow over surface changes in elevation in which the surface roughness remained uniform. Lo (1977) proposed a method which incorporated a change in roughness with a change in surface elevation for slopes up to 1:5, utilizing a curvilinear coordinate system. In general, these studies portray the wind flow over an increase in elevation, such as would be encountered on a beach, as a height-dependent positive acceleration, affecting the flow up to an altitude approximately equivalent to five times the change in elevation. Further, the movement of the air up such an incline would occur in relatively smooth streamlines, carrying the upstream temperature and humidity-profile information along with them. Thus, if the profile measurements were made above and forward of the internal boundary layer, the only correction required would be to adjust the wind-speed profile for the height-dependent increase in wind speed. A method of correcting the wind profile due to the change in beach elevation is given in Section 11.

The fourth and final category of consideration is the influence on the wind profile of the upwind wave height. Krügermeyer et al. (1978) and Hasse et al. (1978a) have suggested that much of the scatter and disagreement among various experiments in determining the drag coefficient (or momentum flux) were due to wind-profile data being acquired at too low an altitude above the water in a region influenced by wave action. Krügermeyer et al. concluded that profile measurements should be taken at a height greater than three times the wave height. Based upon 21 years of data, the Naval Weather Service Environmental Detachment (1971) concluded that in the upwind vicinity of San Nicolas Island wave heights of more than 3 meters occured not more than 5 to 10% of the time. A lowest measurement height no lower than 9 meters above the beach would ensure that the Krügermeyer criteria could be met at least 90% of the time. Additionally, this would probably ensure that the data would be unaffected by breaking waves in the surf zone upwind of the beach.

7. Determination of the Minimum Vertical Separation Between Profile Measurement Levels

It is possible to determine the minimum vertical separation appropriate for profile measurements based upon the various sensor measurement accuracies. From a measurement perspective, the observable span of the planetary surface layer over the ocean can be said to extend from 1 to 50 meters above the surface. As can be seen from Table 4.1, measurements are usually not taken at heights below 1 meter; this is to keep waves from splashing against the sensors. Kitaigordskii (1973) has indicated that the top of the marine surface layer is typically considered to be about 50 meters.

Experience has shown that, generally, within fluid surface layers the various properties of the layers tend to change logarithmically with increasing distance from the surface. If one were to plot such observed parameters on a log-linear graph, with height represented on a vertical log axis, the observed values would tend to exhibit a linear form. Since linear relationships are generally easier to work with, most atmospheric scientists rapidly learn to think in terms of descriptions represented in a two-dimensional log-linear space. In such a representation bounded by the limits of 1 and 50 meters, the

geometric midpoint would lie at a position approximately equivalent to 7.1 meters. This position is called the geometric mean height (GMH). If z_1 and z_2 are the limiting heights, GMH = $\sqrt{z_1 \cdot z_2}$.

It can be argued that in the atmospheric surface layer the smallest magnitude of vertical temperature difference that has to be resolved is the dry adiabatic lapse rate. The adiabatic laspe rate is the mean temperature gradient of dry air in the lower atmosphere under neutral stability conditions; it is usually represented as being approximately equal to $-0.01°K\ m^{-1}$. However, this is a linear relationship and would appear as a curve on a log-linear representation. This minor difficulty can be overcome by approximating the curve as a straight line over an appropriately small increment of height. By centering the increment about the geometric mean, it can be argued that it is, on the average, representative of the overall surface layer.

As can be seen from Fig. 7.1, under adiabatic conditions, between the measurement heights of 6.6 and 7.6 meters, one would expect to observe a temperature difference of about 0.01°C. In our log-linear representation space, the vertical separation is equivalent to $\Delta \ln z = 0.14108$, where $\ln z$ is the natural logarithm of the height, z, expressed in meters. Applying this in a more general sense to the entire surface layer, a temperature differential of 0.01°C can be thought of as corresponding to a $\Delta \ln z = 0.14108$ in log space.

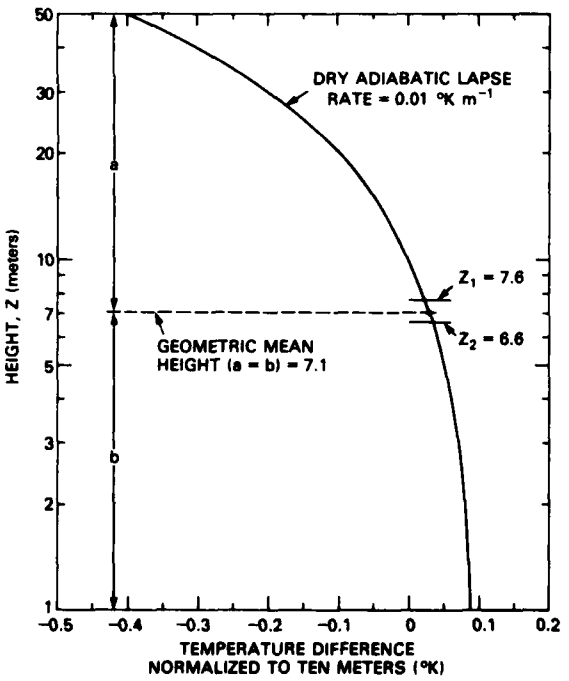

Fig. 7.1 — A log-linear representation showing the geometric mean height, the dry adiabatic lapse rate; and the incremental region of approximation, $\Delta \ln z = \ln z_1 - \ln z_2$

It could be equally well argued that such an approximation should be centered about the geometric mean height of the particular vertical sensor array being used, since measurements are not usually made up to a height of 50 meters. However, such an approach would result in a diminished general applicability of the values determined for the entire surface layer. Lowering the geometric mean height by lowering one or both of the limits would result in increasing the $\Delta \ln z$ value equivalent to the adiabatic laspe rate. The most general case in this situation also turns out to be the best suited for determining the minimum $\Delta \ln z$ separation.

If the accuracy of a given air temperature sensor were ±0.010°C, the accuracy of a differential measurement using two such sensors would be the root mean square (rms) of the two values, about ±0.014°C. However, to be able to observe a true differential between the two sensors and not just the measurement uncertainty, it would be further necessary to require that the temperature difference be twice that of the rms uncertainty, or about ±0.028°C. This is equivalent to specifying an allowable uncertainty of 50% in the smallest observable differential measurement.

Based upon this criterion, for a temperature difference equivalent to the adiabatic laspe rate, with sensors accurate to ±0.010°C, the minimum vertical separation between the two sensors would correspond to $\Delta \ln z = \frac{2 \times \text{rms}}{0.01} \times 0.14108 = 0.39903$. In the same manner, the appropriate minimum sensor spacings can be computed for other typical temperature sensor accuracies. In general,

$$\Delta \ln z \geqslant 39.903\, A_t, \tag{7.1}$$

where z is the required minimum vertical separation in meters and A_t is the measurement accuracy of the air temperature sensors in °C.

Clearly, for a given minimum detectable gradient, the less accurate the sensors, the greater the minimum vertical separation required. Conversely, for a given sensor accuracy, the smaller the vertical separation, the larger the minimum detectable gradient. The operation of temperature sensors at a vertical separation smaller than that indicated by Eq. (7.1) would result in a diminished ability to distinguish between stable and unstable situations and an increase in the relative uncertainty in determinating temperature gradients in general.

It would be desirable to establish a similar criterion for humidity sensors. The virtual temperature, T_v, is a measure of the humidity content of the atmosphere in °K and is represented by the equation

$$T_v = T + T(0.608\, q),$$

where T is the ambient air temperature in °K and q is the specific humidity in kg kg^{-1}. If T is typically about 295°K, it can be seen that

$$\frac{\partial T_v}{\partial z} \approx 179.36 \frac{\partial q}{\partial z}.$$

If we employ the same criterion for the virtual temperature that we did for air temperature, namely the adiabatic laspe rate, we see that

$$\frac{\partial q}{\partial z} \approx 5.5754 \times 10^{-5} \text{ kg kg}^{-1};$$

this would correspond to $\Delta \ln z = 0.14108$. Utilizing the same 2 × rms measurement criterion as before, the appropriate minimum sensor spacings can be computed as a function of the humidity-sensor accuracy:

$$\Delta \ln z \geqslant 7157.0 A_q, \qquad (7.2)$$

where z is the required minimum vertical separation in meters and A_q is the measurement accuracy of the humidity sensors in kg kg^{-1} specific humidity.

To complete the exercise, it would be desirable to establish a similar criterion for the vertical separation of wind-speed sensors. As can be seen from Fig. 7.2, the smallest wind-speed differentials typically occur under unstable conditions, decreasing in value with increased instability.

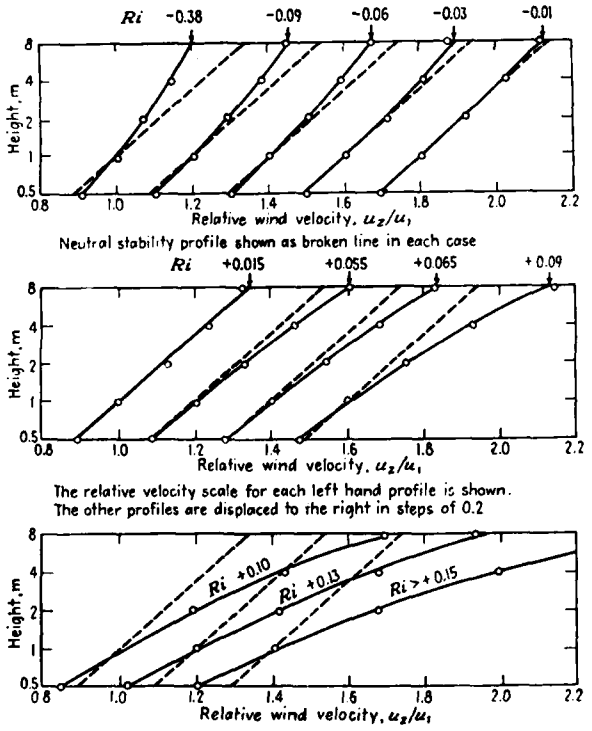

Fig. 7.2 — Figure from Sutton (1953) demonstrating the decrease in wind speed differential with increasing instability ($-Ri$)

The Richardson number, Ri, is a dimensionless ratio which is a measure of the degree of stability or instability:

$$Ri = \frac{g \dfrac{\partial \theta}{\partial z}}{\bar{T}\left(\dfrac{\partial u}{\partial z}\right)^2},$$

where

$$\frac{\partial \theta}{\partial z} = \frac{\theta_1 - \theta_2}{(z_1 z_2)^{1/2} \ln (z_1/z_2)}$$

$$\frac{\partial u}{\partial z} = \frac{u_1 - u_2}{(z_1 z_2)^{1/2} \ln (z_1/z_2)}$$

$$g = 9.8 \text{ m sec}^{-1}$$

$$\bar{T} \approx 295 \text{°K};$$

g is the acceleration due to gravity, $\bar{T}$ is the average ambient air temperature, z is the height above the surface in meters, θ is the potential temperature in °K, u is the wind speed in m sec^{-1}, and the subscripts 1 and 2 are used to denote the upper and lower measurement levels, respectively. A negative Richardson number value denotes an unstable condition.

Employing the same minimum requirements and domain of approximation as in our earlier log-linear representation, we set: $z_1 = 7.6$, $z_2 = 6.6$, and $\theta_1 - \theta_2 = \pm 0.01$. Substituting these values into the above equations and solving for Δu, we obtain for the unstable case:

$$\Delta u \approx \sqrt{\frac{-0.01 \times 0.03322}{-Ri}}.$$

To solve the equation for the smallest ΔU, it is necessary to determine an upper limit for the magnitude of $-Ri$. From Businger et al. (1971) it can be seen that the largest reliable Ri value under unstable conditions is typically about -2.

Substituting -2 for $-Ri$ in the equation for Δu, we obtain $\Delta u = 0.012888$ m sec^{-1} which would correspond, as before, to $\Delta \ln z = 0.14108$. Using the same 2 × rms measurement criterion as before, the appropriate minimum sensor spacing can be computed as a function of the wind-speed sensor measurement accuracy by

$$\Delta \ln z \geqslant 0.61922 A_u \qquad (7.3)$$

where z is the required minimum vertical separation in meters and A_u is the measurement accuracy of the wind speed sensors in average percent of reading for the entire operating range of the experiment. Where the accuracies stated in percent of reading were converted to units of m sec^{-1} for the standard wind speed of 2 m sec^{-1}, since that wind speed is the lowest reliable operating speed most anemometers have in common.

Because the wind-speed determination is typically the least accurate of the various atmospheric profile

measurements, it was anticipated that the wind speed sensors would require the greatest vertical separation. As will be seen in Section 12, the best calibrated laboratory wind speed standards are about ± 1%. If the air temperature and humidity sensors were located at the same levels as the wind speed sensor, with the lowest level no lower than 9.0 meters as determined from the previous section, Eq. (7.3) would indicate that only two additional profile measurement levels, located at heights no closer to the ground than approximately 16.7 and 31.1 meters, could be deployed and still remain within the marine surface layer.

8. Profile Measurement Accuracy as a Function of the Number of Measurement Levels

In addition to the vertical separation of the measurement levels discussed in the preceding section, the number of levels is also important. From Table 4.1 it can be seen that the number of measurement levels employed in previous marine surface layer profile measurements has ranged from two to nine. Since a two-level system is the most elementary, we will use it for comparison to determine the increased measurement accuracy to be gained by employing additional levels.

Let N be the number of measurement levels and n be the number of independent measurements of the same profile. Two measurement levels are needed for each independent measurement. Let ξ be the rms error associated with each independent profile measurement. If the measurement errors are random it can be seen from Meyer (1975) that the typical overall uncertainty, expressed in terms of the sample standard deviation σ, decreases as a function of the number of equally valid independent measurements,

$$\sigma = \frac{\xi}{\sqrt{n}}. \tag{8.1}$$

A method of visualization, which yields approximately the same results, is to compute the mean uncertainty of all usable measurement pairs scaled to the error associated with a single pair. To insure that all the measurements are equally valid, a log-linear profile is assumed in which each vertical measurement level is separated by the same logarithmic interval and each sensor is equally accurate. Consider, for example, one such case represented in Fig. 8.1 for a five-level profile sensor array, where ξ is the rms profile measurement error associated with any adjacent pair of measurement levels.

The typical combined profile measurement error, σ, of the five-level sensor array depicted in Fig. 8.1 can be approximated by computing the mean of all possible pair error combinations:

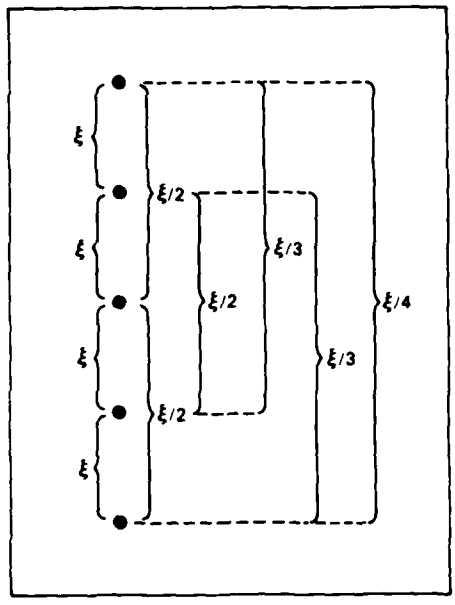

Fig. 8.1 — Profile measurement error components depicted for a five level sensor array for a log-linear profile in which the measurement levels are vertically spaced at equal logarithmic intervals; ξ is the rms profile measurement error associated with an adjacent pair of measurement levels

$$\sigma \approx \frac{\frac{\xi}{4} + 2\frac{\xi}{3} + 3\frac{\xi}{2} + 4\xi}{10} = 0.642\xi.$$

In a more general form, the approximation method can be stated as

$$\sigma \approx \frac{\sum_{x=1}^{N-1} x\frac{\xi}{N-x}}{\sum_{x=1}^{N-1} x},$$

where, as before, N is the number of equally spaced logarithmic measurement levels with sensors of equal accuracy.

As can be seen from Table 8.1, quadrupling the number of measurement levels results in only a 50% reduction in the profile measurement uncertainty. Clearly, increasing the number of measurement levels, with the resulting operational complexity, is not an efficient method for increasing the profile measurement accuracy. As detailed in the previous section, it would be more efficient to increase the vertical separation between the measurement levels. The criteria established in this and the previous section will prove to be of considerable assistance in Section 15, where the San Nicolas Island profile measurement accuracies are compared to those of other experiments.

Table 8.1 — Reduction in Profile Measurement Uncertainty as a Function of the Number of Measurement Levels Compared to a Two-Level Sensor System

No. of Measurement Levels (N)	No. of Independent Measurements (n)	Measurement Uncertainty (σ) from Eq. 8.1	Reduction in Measurement Uncertainty (%)
2	1	ξ	—
3	~1.5	0.816 ξ	18
4	2	0.707 ξ	29
5	~2.5	0.632 ξ	37
6	3	0.577 ξ	42
7	~3.5	0.535 ξ	47
8	4	0.500 ξ	50
9	~4.5	0.471 ξ	53

9. The Measurement Site

Since it would be [illegible] to place the measurement site on an island [illegible], it was important to select a location which would be least influenced by the island land mass. The choice of San Nicolas Island as the experiment location was particularly fortunate, because the major island promontory, Vizcanio Point, extended directly into the prevailing wind; de Violini (1974) reported that the prevailing wind fetch observed on the island was from the northwest (±45°) 62% of the time. The end of Vizcanio Point, located at 33° 16′ 41″ North and 119° 34′ 38″ West, was selected as the measurement site and can be seen in the lower left hand corner of Fig. 9.1.

The additional promontories utilized for the double-ended optical experiments and the bay located to the east of the point, where the tide-table data were collected, can be seen in the center left hand side of the

Fig. 9.1 — Aerial photograph from de Violini (1974) of San Nicolas Island looking east. The Vizcanio Point peninsula can be seen in the lower left hand corner.

Fig. 9.1. The launch site for the radiosondes used to determine the height of the marine inversion can be seen as the island protrusion located in the center bottom of the photo. The general topography of the Vizcanio Point promontory is present in Fig. 9.2.

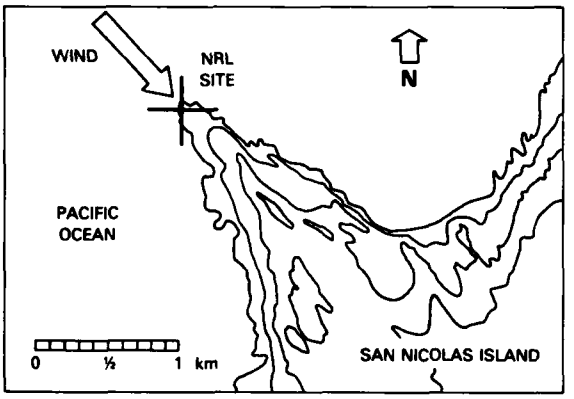

Fig. 9.2 — The topography of the Vizcanio Point peninsula of San Nicolas Island, exhibited in 15 meter contour lines, and the prevailing wind direction

Vizcanio Point is located at the end of a narrow 1.5-km-long low-profile peninsula, which has a mean net slope of approximately 1:20. The selected measurement site afforded a wind fetch from the open ocean which roughly paralleled the local continental coastline and a water depth which increased rapidly with upwind distance from the island (see Table 9.1). The National Ocean Survey (1978) indicated that the rocky bottom 0.5 km upwind of the site had a mean slope (315° True, ±45°) of ~1:50. Wave-height and wave-period information obtained during the experiment was acquired from a buoy located near Begg Rock at 33° 21′ 45″ North and 119° 41′ 40″ West, 15.6 km upwind and northwest of the island in water approximately 100 meters deep.

Table 9.1 — The Typical Water Depths for the Prevailing Wind Fetch Direction (315° True, ±45°)

Upwind Distance[a] (km)	Typical Water Depth [b] (meters)
0.1	2
0.2	6
0.5	10
1	20
2	30
5	50
10	80
20	100
50	1,000

[a]Distance from mean water mark on beach.
[b]Depth measured from mean sea level.

The tip of Vizcanio Point consisted of an escarpment, or knoll, 4.7 meters above mean sea level,* which dropped off rapidly on the seaward sides due to wave errosion. The top of the escarpment was approximately level, extending 40 meters both parallel to and perpendicular to the axis of promontory symmetry. Tide-table data employed during the experiment indicated that the normal extreme tide levels were 1.2 meters above and below mean sea level. A survey concluded that the measurement site would range from 20 to 200 meters from the water's edge, depending upon the wind direction and tide height (see Fig. 9.3).

Fig. 9.3 — Low altitude aerial view of the measurement site looking south at low tide

From a composite of aerial photographs taken at low altitude over the experiment site, it was possible to estimate the distances from the sensors, located on the tower, to the water's edge as a function of wind direction and tide. The resulting overhead view is presented in Fig. 9.4 and in Table A.3 of Appendix A.

The location chosen for the bulk water temperature sensor can be seen in Figure 9.4 as the small blight in the low-tide line approximately 60 meters west of the sensor location on top of the escarpment. The water temperature sensor was located about 0.3 meters below the surface, in a location continuously feed by breaking waves. The electrical cable running to the water temperature sensor can be seen in the lower right hand side of Fig. 10.2. Vedder & Norris (1963) described the beach material located between the high and low tide lines as a

*Elevations referenced to mean sea level are equal to elevations measured from the mean lower level water minus 0.76 meters.

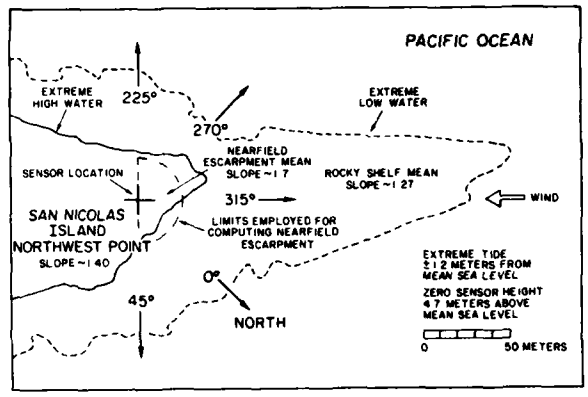

Fig. 9.4 — Diagram based upon composite overhead view of the measurement site

light-gray, very thick-bedded, concretionary, medium-grained sandstone, containing a few thin beds of intercalated sandstone and siltstone. They described the overlying escarpment material as a light-tan, unconsolidated, lime-cemented sand.

Because the local mean slopes of the escarpment top (~1:40) and the upwind rocky ledge (~1:27) were small, a survey of the escarpment conducted in January 1980 was confined to the immediate vicinity, or near field, of the upwind side of the measurement site. The position on top of the escarpment that fell immediately below the sensors, mounted on the end of the fully extended arms of the tower, was marked and used as a reference point for the survey. The results of the survey are presented in Fig. 9.5 and in Table A.1 of Appendix A, where the reference point is signified by an upwind distance and an escarpment depth equal to zero. Readings taken at 1-meter intervals radiating out upwind from the reference point were recorded as a function of 15° increments through ±90° of true northwest.† The mean slope of the near-field escarpment was found to vary from about 1:12 to 1:5.

The approximately level rocky shelf exposed upwind of the site during low tide consisted of widely scattered, approximately round rocks, ranging in size from about 0.1 to 1 meters in diameter (see Fig. 9.6). The mean surface irregularity was estimated to be about 0.3 meters in diameter. Hsu (1971), from profile measurements made close to a ±0.5 meter undulating beach with a mean slope of ~1:30, found the roughness length to be on the average $\sim 0.3 \times 10^{-2}$ meters at a distance of 25 meters from the water's edge. Assuming the mean surface irregularity upwind of the escarpment to be 0.3 meters, Huschke (1959) would predict a roughness length of $\sim 1.0 \times 10^{-2}$ meters. Scaling the same 0.3 meter mean surface irregularity size to the wind tunnel

†True direction at San Nicolas Island is equal to the magnetic direction plus 14.5°.

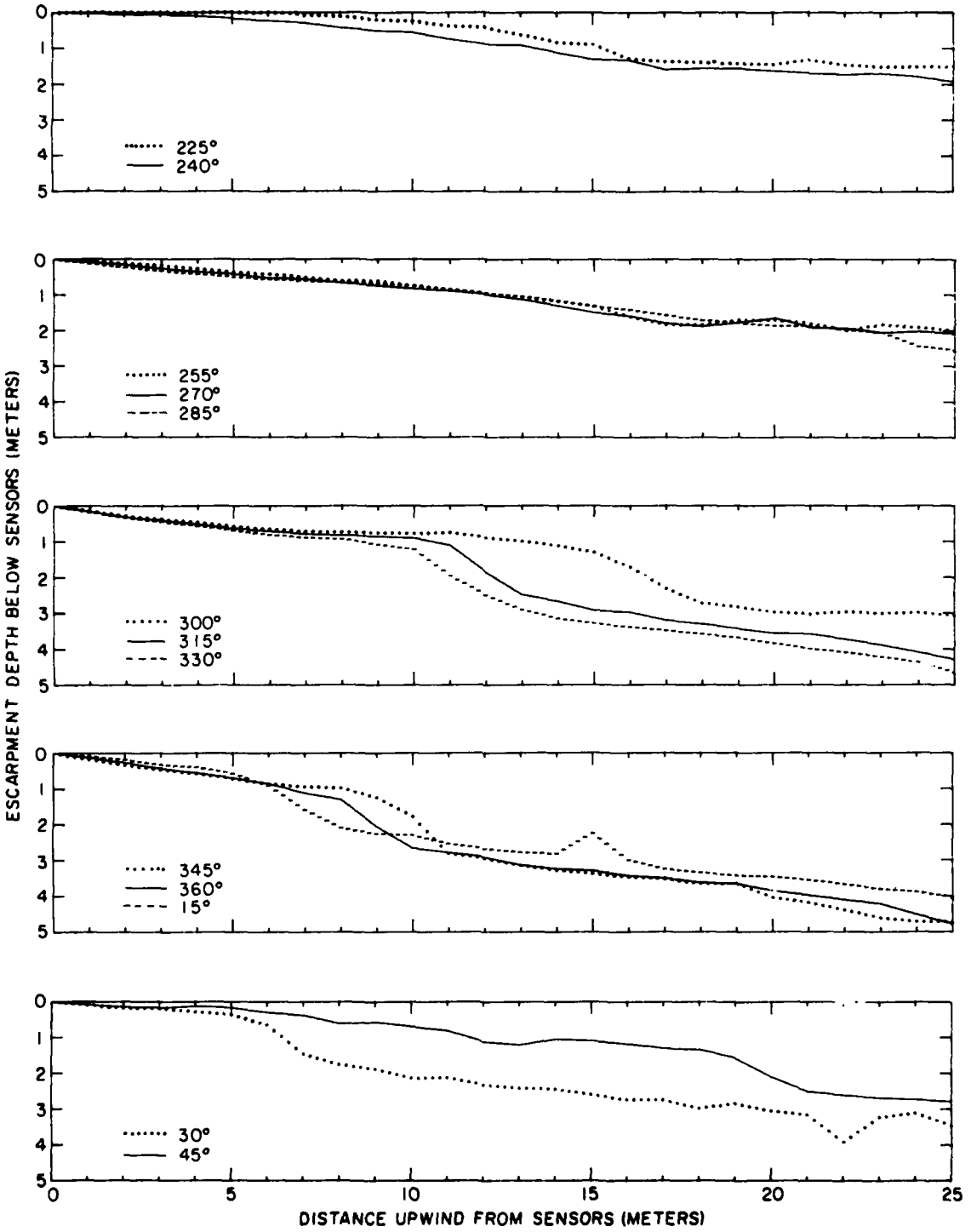

Fig. 9.5 — The measurement site escarpment topography exhibited as a function of the upwind fetch direction (true) with the zero reference point defined as the top of the escarpment located immediately below the profile sensors on the tower. Mean sea level was 4.7 meters below the top of the escarpment.

Fig. 9.6 — View of the upwind rocky shelf exposed at low tide looking west-northwest from the tower

studies of the airflow over a rock field conducted by Mulhearn and Finnigan (1978) would indicate a roughness length of $\sim 0.8 \times 10^{-2}$ meters. Averaging the three estimates to obtain a crude consensus gave a roughness length of about 0.7×10^{-2} meters for the exposed rocky beach upwind of the escarpment.

10. Special Micrometeorological Tower Design and Location of Sensors

The review of measurement platforms and their influence on data (Section 5) showed the necessity of designing a micrometeorological tower as open as possible, with sensors located at least three or four times the tower's aspect width upwind of the structure, to insure a negligible tower influence in the data. The examination of profile sensor placement above the beach (Sections 6 and 7) indicated that the lowest measurement level should be no lower than 9 meters and that the other measurement levels should be located no lower than approximately 17 and 31 meters.

The particular measurement site selected on San Nicolas Island imposed additional constraints on the design of a micrometeorological tower. The site survey conducted by Chern (1977) indicated that the beach escarpment site would be subject to flooding and breaking waves under extreme storm conditions. The geological survey of Vedder & Norris (1963) reported the existence of a pair of geological faults within a few hundred meters of the site. The necessity of locating the tower close to the water on the edge of a three-sided escarpment precluded the use of guy-wires to enhance structural stability. Since the tower would have to be freestanding and capable of withstanding potentially sizable lateral loading, it was decided to limit the height of the structure to 20 meters. The examination of the profile measurement accuracy as a function of the number of measurement levels (Section 8) indicated that the resulting deployment of a two-level system rather than a three-level system could be achieved at the expense of only a 23% reduction in profile measurement accuracy.

The selected design for a main-tower structure consisted of a welded tubular aluminum upper section (13.8 meters) bolted on top of a similar lower section (5.3 meters), resulting in an overall height of 19.1 meters. The basic design configuration could be viewed as a series of 1.5-meter structural cubes stacked on top of each other. Each cube was capable of accommodating a single 6.7-meter, elongated, tetrahedon-shaped instrument-support truss (see Fig. 10.1). The instrument trusses, or sensor arms, were constructed of welded tubular aluminum and were hinged approximately midway out from the tower to facilitate access to the sensors from within the safety of the structure. When the sensor arms are fully extended and the wind is from the northwest, the arms afford a tower aspect width-to-upwind sensor distance ratio greater than 1.4. The diameters of the tower's tubular elements are listed in Table 10.1.

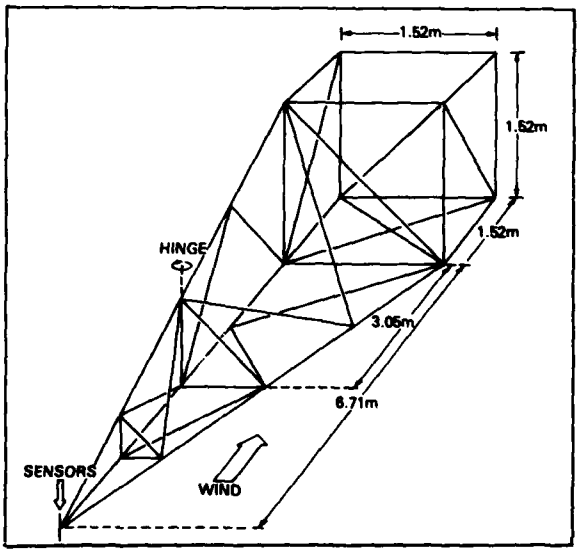

Fig. 10.1 — Basic tower and sensor arm structural element configuration in relation to the prevailing wind direction

Table 10.1 — Diameters of Micrometeorological Tower Main Tubular Elements

Structural Segment	Structural Element Outside Diameter (cm)		
	Vertical	Horizontal	Diagonal
Instrument Arm	4.5	4.5	4.5
Upper Main Tower	7.4	7.4	5.9
Lower Main Tower	7.8	7.8	7.8

Because the measurement site was expected to be flooded occasionally, a 67 m^3 controlled-environment mobile field shelter*, which could be moved to higher ground when the facility was not in use, was provided to house the data-reduction instrumentation and personnel. A view of the tower with instrument arms and mobile field shelter is presented in Fig. 10.2.

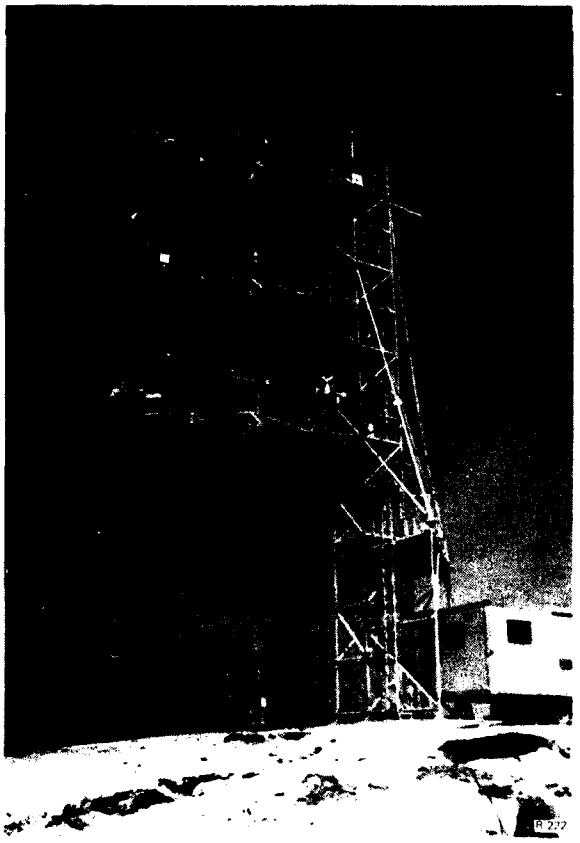

Fig. 10.2 — View of the micrometeorological tower and mobile field shelter taken from the base of the beach escarpment looking east-northeast. Instruments shown midway back on sensor arms were not deployed during the May 1979 experiment.

Three instrument arms located at heights of 8.92, 13.49, and 18.06 meters were used for the May 1979 experiment. The top and bottom arms were employed for the profile measurements. The air temperature, humidity, and wind-speed sensors were vertically offset at the ends of the arms by +0.20, −0.05, and +0.72 meters, respectively, (see Fig. 10.3). This arrangement yielded mean† profile measurement heights of 9.20 and

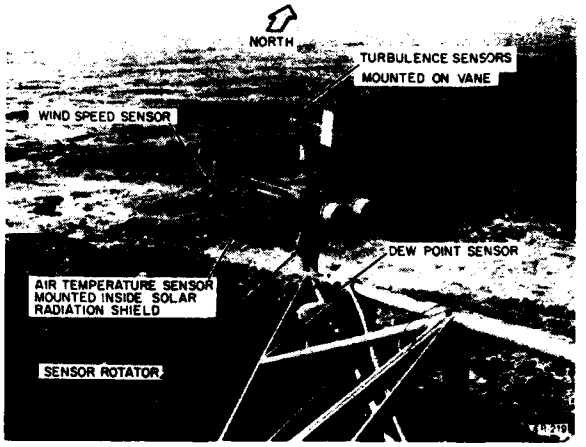

Fig. 10.3 — View from the tower of one level of the profile sensors mounted at the end of an arm. The vane mounted turbulence sensors were not deployed for the May 1979 experiment.

18.35 meters above the beach, as measured from below the fully extended sensor arms. The middle arm was used exclusively for the aerosol measurements; the sensor intake was located at a height of 14.4 meters.

Other sensors were mounted directly on the main tower structure. The barometric-pressure sensor was located on the rear of the tower at 9.9 meters and the solar pyranometer at the top of the tower at 19.8 meters. The wind-direction sensor was mounted on a small forward mast and located at 20.7 meters above the ground. The radon-222 measurements were typically taken on the tower at a height of approximately 5.3 meters above the ground. The bulk-water-temperature, tide-height, inversion-height, and wave-height measurement locations are indicated in Section 9.

As cautioned by Deacon (1980), a structure like the San Nicolas Island tower proved to be an ideal perch for much of the local cormorant population when the tower was unmanned. The ensuing debris which accumulated on the tower between experiments was found to be a considerable nuisance and a potential health hazard to the experiment's personnel. A successful method found to minimize this problem was to place several approximately 40 cm high plastic owl replicas‡ at strategic locations on the tower.

11. Correction of Beach-Escarpment-Induced Accelerations

The section dealing with the influence of a beach on flux data (Section 6) indicated that the acceleration

*8.53 meters long by 3.05 meters wide by 2.59 meters high, exclusive of 0.61 meter high wheels and undercarriage.

†The standard deviation of the sensor height variation about the mean was ±0.29 meters, or 2.2% of the profile-measurement geometric mean height of 12.99 meters.

‡Available from the Huge Co., 7262 Page Blvd., St. Louis, Missouri 63133.

induced in the marine wind field by the local change in elevation inherent in most beaches should be taken into consideration. The survey of the site (Section 9) determined that the top of the beach escarpment upon which the measurement site was located was 4.7 meters above mean sea level and that the local upwind escarpment slope ranged from approximately 1:12 to 1:5, depending upon the wind direction. Additionally, the roughness length of the beach upwind of the escarpment was estimated to be approximately 0.7×10^{-2} meters. The presentation of the micrometeorological tower design rationale (Section 10) indicated that the profile measurements were to be acquired at heights of 9.20 and 18.35 meters above the escarpment surface, representing heights normalized to that of the escarpment of 1.96 and 3.90, respectively.

Over the last decade several papers dealing with the flow over hills have appeared in the literature: Taylor & Gent (1974), Mason & Sykes (1979), Hunt et al. (1979), Sacré (1979), Bradley (1980), and Hunt (1980). However, the authors dealt primarily with flows close to the escarpments at elevations typically less then one normalized height, or they presented their results in a form which was not readily applicable to the requirements of the San Nicolas Island site.

Jensen & Peterson (1978) achieved a major breakthrough in terms of both a conceptual and potentially utilitarian approach. They concluded that the extraordinary steepness of the upper portion of the observed wind profiles (see Fig. 6.3) reported by Echols & Wagner (1972) and others were probably due to large-scale terrain features in addition to the change in roughness. Jensen & Peterson described the influence of the beach escarpment as a height-dependent speedup of the wind profile, for which they could find no systematic dependence due to either stability or wind speed. Peterson et al. (1980) confirmed these findings and concluded that the small variations in surface elevation could, in fact, have a significant influence on observed mean wind profiles.

As noted in the beach survey, it is not uncommon to find an escarpment created by wave erosion close to the high-water mark which drops off with increasing steepness toward the ocean. As a first-order approximation, this type of escarpment can frequently be approximated as being semielliptical with the distance along the wind direction as the major axis and the height of the escarpment as the minor axis. For example, see the escarpment cross-section presented in Fig. 9.5 for the wind direction of 300°. Jensen & Peterson made extensive use of the work of Frost et al. (1974), which presented an investigation of boundary-layer flow over semielliptical escarpments.

Another important factor to be taken into consideration in determining the modification of the wind profile is the ratio of the upwind roughness length to escarpment height. Clearly, the relative roughness and the change in elevation work in combination with each other. Most authors of such studies typically present their results scaled in terms of this ratio. Scaling the measurement-site escarpment height of 4.7 meters to the ratio of 0.001 employed by Jensen & Peterson and by Frost et al., indicated that their results would be applicable for a roughness length of about 0.5×10^{-2} meters—a value very close to the upwind beach roughness estimated for San Nicolas Island in Section 9. Therefore, in terms of both the general escarpment shape and the roughness-to-escarpment height ratio, the Frost et al. findings were well suited to describing the influence of the San Nicolas measurement site (see Fig. 11.1).

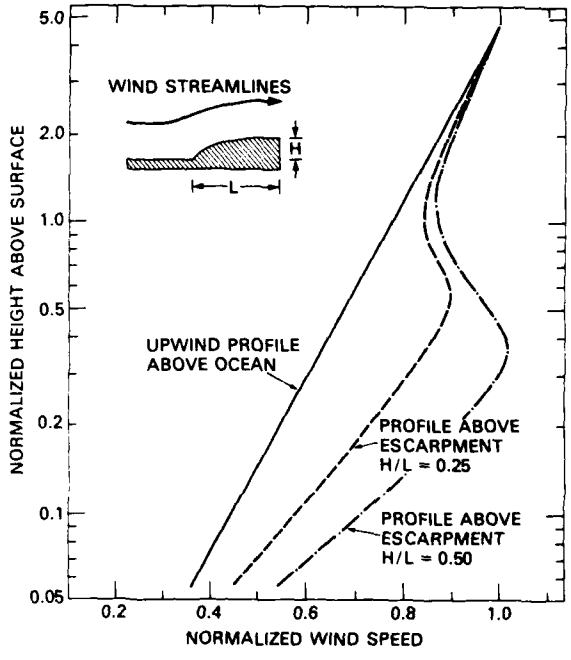

Fig. 11.1 — Composite of Frost et al. (1974) figures showing the speed up of the wind profile on top of two semielliptical escarpments with aspect ratios of 0.25 and 0.50 as compared to the *upstream profile*. The profile height is displayed normalized to the height of the escarpment.

The Frost et al. study examined the modification of a neutrally stable wind profile created by a semielliptical escarpment with an aspect ratio of 0.25 and 0.50, in which the height of the profile was normalized to that of the escarpment. The escarpment aspect ratio is here defined as height:length ratio, or the height/length value, and is considered to be approximately equivalent to the escarpment slope. Frost et al. and others described the modification at the top of the escarpment as a height-dependent speedup occurring up to a height approximately five times that of the escarpment. Since the

lowest normalized height at San Nicolas Island was approximately equal to two, only the upper portion of the Frost et al. results shown in Fig. 11.1 was of interest (see Fig. 11.2). This region was found by Frost et al. to be relatively well behaved and to have the least variability due to changes in upwind roughness.

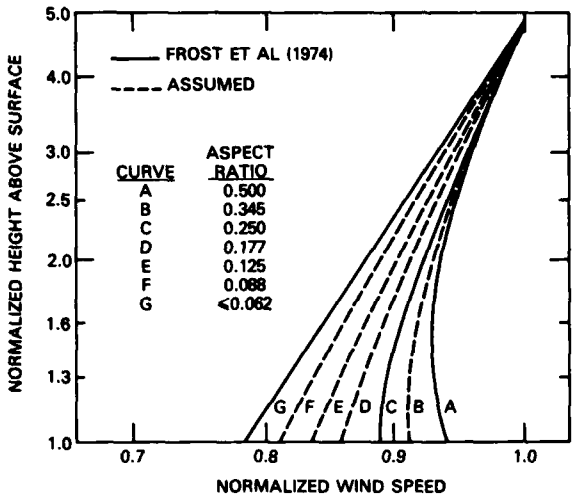

Fig. 11.2 — Upper portion of Frost et al. (1974) profiles presented in Fig. 11.1 with four additional profiles generated by assuming the influence of the escarpment to decrease as a logarithmic function of the aspect ratio

The next step was to infer in a more general sense the influence of the aspect ratio on the wind-profile speedup. If the modification of the wind profile above one normalized height decreased as a linear function of the aspect ratio, the curve for an aspect ratio of 0.25 in Fig. 11.2 would be expected to lie midway between the upstream value (aspect ratio $\cong$ 0) and 0.50. As can be seen from the figure, this is not the case. If, however, the modifications were allowed to decrease as a logarithmic function of the aspect ratio, a family of curves could be generated which would appear to fit the situation quite well. Aspect ratios less then or equal to 0.062 could be viewed, in terms of the measurement uncertainty, as being approximately equal to zero. This would be a reasonable assumption in light of the fact that the highest obtainable accuracy for a wind-speed measurement is about $\pm 1\%$ and that the largest typical speedup anticipated would be about 5%. This would also be consistent with the earlier assumption presented in Section 9, that the local aspect ratios in front of and on top of the measurement-site escarpment (0.037 and 0.025, respectively) had a negligible influence.

Because the influence of an escarpment is contour dependent and is not directly related to the ambient wind speed, it is convenient to express the wind-profile modification in terms of a speedup ratio in which the height dependence is expressed in a coordinate system adjusted to conform to the local topography (see Fig. 11.3). The speedup ratio is known as the wind-speed amplification factor. The air can be portrayed as moving over the escarpment in smooth streamlines in which a measurement made at a given height above the upstream surface is compared to a measurement made at a similar height over the escarpment. Inherent in this portrayal is the assumption that any lateral deformation of the wind streamlines due to the horizontal nonuniformity of the escarpment is negligible.

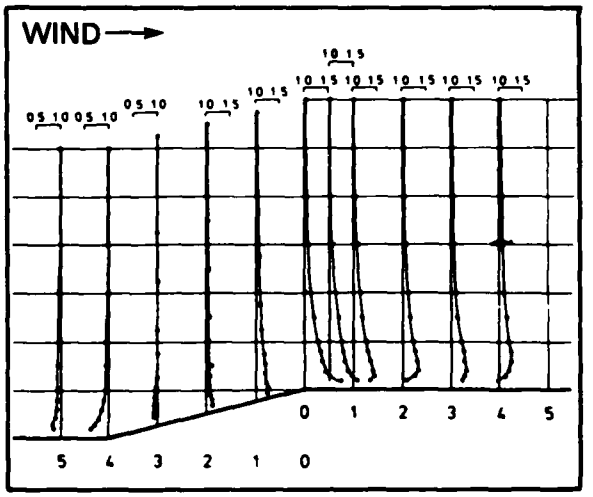

Fig. 11.3 — Figure from wind tunnel studies of Bowen & Lindley (1977) showing the height-dependent variation of the wind-speed amplification along a ramp having an aspect ratio of 0.25 with height displayed on a linear scale normalized to the height of the escarpment

The Frost et al. results and the approximations exhibited in Fig. 11.2 were computed in terms of the wind-speed amplification factor and are presented in Fig. 11.4.

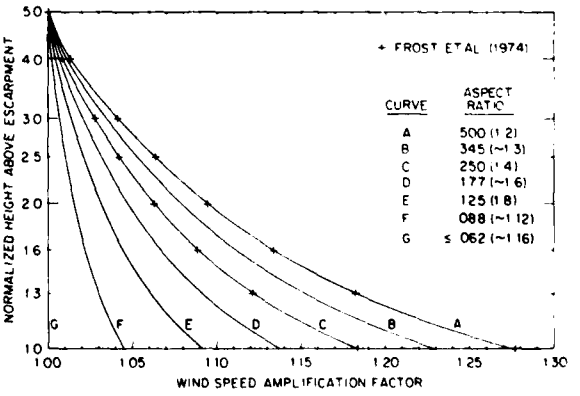

Fig. 11.4 — Same as Fig. 11.2 except the wind profile speedup is expressed in terms of the wind speed amplification factor

To represent mathematically in a more general manner the entire family of possible curves for the wind speed amplification factor (W) as a function of both the escarpment aspect ratio (R) and the normalized height above the top of the escarpment (H), each of the seven curves for R presented in Fig. 11.4 was related to W by a first-order polynomial curve-fit* of the form

$$W = a + b(\log R), \tag{11.1}$$

where the logarithm is expressed to the base of 10. Then eight values of H were chosen so that log H would be approximately equally spaced (H = 1.0, 1.3, 1.6, 2.0, 2.5, 3.0, 4.0, and 5.0) and these values of H were related to the polynomial constant a by a fourth-order polynomial curve-fit* of the form

$$a = c + d(\log H) + e(\log H)^2 + f(\log H)^3 + g(\log H)^4. \tag{11.2}$$

In a similar manner the same eight values of H were related to the polynomial constant b by a fourth order polynomial curve-fit* of the form

$$b = h + i(\log H) + j(\log H)^2 + k(\log H)^3 + l(\log H)^4. \tag{11.3}$$

By this procedure, a form of three-dimensional data smoothing was applied to a grid of 56 data points to generate a mathematical surface that could be used to portray W as a function of R and H (see Fig. 11.5).

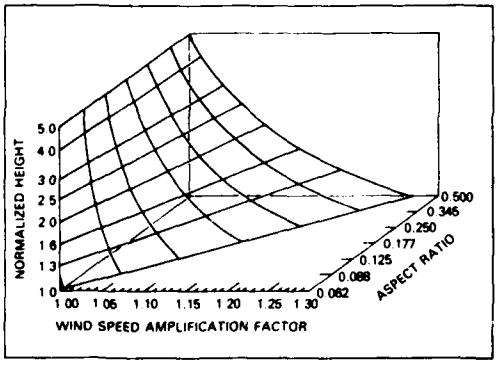

Fig. 11.5 — A three-dimensional representation of the mathematical surface generated to portray the family of curves for the wind-speed amplification factor as a function of the escarpment aspect ratio and the normalized height above the top of the escarpment

*Digital Equipment Corporation DEC system-10 least squares polynomial curve-fit subroutine named LSCF programmed in BASIC, developed by L.C. Semprebon, Radiophysics Laboratory, Dartmouth College, Hanover, New Hampshire.

The values for the ten required polynomial constants were determined to be the following:

c = 1.3668, h = 0.3047,
d = −1.3493, i = −1.1210,
e = 2.7473, j = 2.2843,
f = −3.6841, k = −3.0647,
g = 2.0652, l = 1.7184.

Thus, given any normalized height above the top of the escarpment (H) in the range of 1 to 5 and any escarpment aspect ratio (R) in the range of 0.07 to 0.50, the wind-speed amplification factor (W) could be determined. A table of typical values for the amplification factor computed in this manner as a function of the height and the aspect ratio is presented in Table A.2 of Appendix A. The measurement-site aspect ratio (or slope) was computed by employing a first-order polynomial curve-fit* to the site survey data presented in Fig. 9.5 and Table A.1 of Appendix A. By knowing the aspect ratio as a function of wind direction, it was then possible to correct the observed wind profiles for the influence of the escarpment by knowing only the wind direction and the measurement height above the escarpment. The reciprocal of the amplification factor was defined as the escarpment wind-speed correction coefficient (see Table A.3 of Appendix A).

Wind-profile observations needed for most micrometeorological measurements typically require averaging over an observation period of about 30 minutes. Since it would be unrealistic to assume that the wind direction would remain constant over such a period, it was necessary to integrate the aspect ratio information presented in Table A.3 of Appendix A over an appropriate interval of wind-direction variation. The interval of integration selected for the San Nicolas Island data was ±10° as referenced to the average wind direction for the observation period.

Once the correction technique had been employed to remove the influence of the escarpment, it was necessary to confirm whether the technique had been successful and whether the procedure yielded reasonable values. The review of measurement platforms and their influence on data (Section 5) suggested that the profile method would be about an order of magnitude more sensitive to profile flow distortions than the bulk method. Since one of the parameters most sensitive to profile flow distortion was the Richardson number stability, a comparison of the change brought about between the profile-derived and bulk-derived values was used to judge the relative improvement. Recall from Section 7 that the profile-derived Richardson number (Ri) is an inverse function of the square of the profile wind-speed differential.

Figure 11.6 displays a 48 hour sample of data taken over a wide range of meteorological conditions

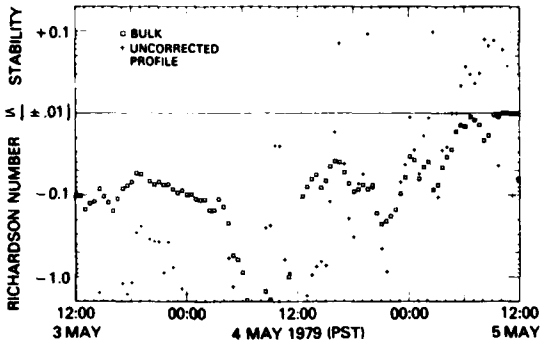

Fig. 11.6 — A comparison of profile-derived and bulk-derived Richardson stability data taken over a wide variety of meteorological conditions from the San Nicolas Island beach before applying the escarpment wind-speed correction

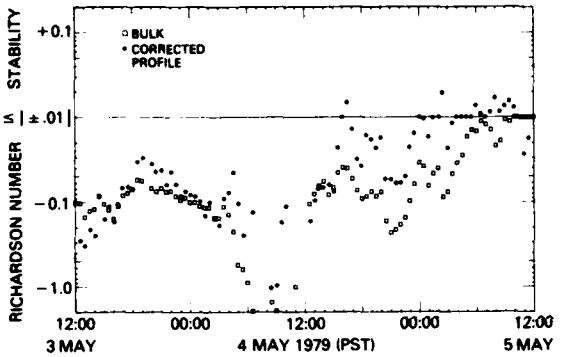

Fig. 11.7 — Same as Fig. 11.6 after applying the escarpment wind-speed correction

without the escarpment correction. Fig. 11.7 shows the same data with the escarpment correction.

Clearly, the improvement is significant. The remaining scatter contained in the profile-derived data presented in Fig. 11.7 is typical of other profile-bulk comparisons of data taken without the presence of an escarpment. For example, see Figs. 5 through 7 in Hasse et al. (1978b).

S. D. Smith (1981) has suggested the possibility that placing the mobile field shelter close to the base of the tower, as can be seen in Fig. 10.2, may have additionally complicated the flow observed upwind on the arms of the tower. A precursory check performed by scaling the wind-tunnel results presented by Bowen & Lindley (1977) for a vertical step-shaped escarpment suggested that the profile measurements reported from the tower were probably forward of the detectable influence of the shelter (see Fig. 11.8).

The top of the shelter was located 3.2 meters above the ground and approximately 9.7 meters

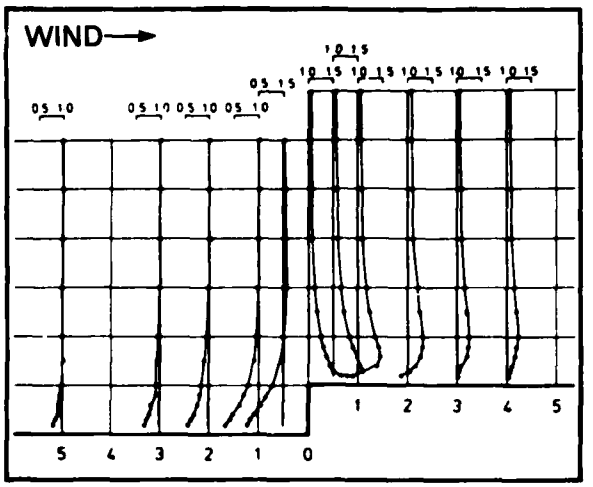

Fig. 11.8 — Figure from wind tunnel studies of Bowen & Lindley (1977) showing the height-dependent variation of the wind speed amplification factor in the vicinity of an abrupt vertical step change in surface in which the height is displayed in terms of a linear scale

downwind of the sensors located at the end of the tower arms. The lowest sensor level was located at 9.2 meters above the ground. Scaling these distances, normalized to the height of the shelter above the ground, would place the lowest sensor in Fig. 11.8 approximately three normalized distances forward of the step change and three normalized distance above the upstream surface. For future experiments, however, prudence would suggest that the shelter be located farther back from the tower.

12. Instrumentation and Measurement Accuracies

When dealing with the calibration of instruments and the resulting measurement accuracies, experimenters are often required to make, consciously or unconsciously, a series of implicit value judgments based on their experience in regard to labyrinth of underlying assumptions and potential sources of error. These judgments vary significantly from experimenter to experimenter and are rarely communicated to the prospective user of the final data. Obviously, this complicates any comparison of one experimenter's data with another's. Much of this section is an effort to remove some of the "black magic" from this procedure. Table 12.1 gives the measurement accuracies of the San Nicolas Island sensors.

The wave-height and wave-period measurements were taken with a Datawell "Waverider" buoy, model 6900,* the inversion-height measurements with National Weather Service model JOO5 radiosondes (modified to take 10 readings/min.),* the aerosol size measurements

*Operated by and data made available courtesy of the Geophysics Division, Pacific Missile Test Center, Point Mugu, California.

Table 12.1 — Measurement Accuracies of the San Nicolas Island Sensor Systems

Sensor Systems	Manufacturer	Model Number	Absolute Accuracy Of Calibration Standard	Typical Measurement Accuracy[a]	Source of Calibration
Air Temperature	Hewlett-Packard	2801A (with 2850A)[b]	±0.001°C[c]	±0.003°C[d]	National Bureau of Standards[e]
Barometric Pressure	YSI-Sostman	2014	±0.34 mb	±0.36 mb[f]	Manufacturer
Dew Point Temperature	EG&G	110-C3[g]	±0.04°C	±0.07°C[h]	National Bureau of Standards[i]
Sky & Solar Radiation	Eppley Laboratory	8-48[j]	±2% of reading	±5% of reading	Manufacturer
Water Temperature (Bulk)	InterOcean Systems	518A[k]	±0.001°C	±0.002°C	National Bureau of Standards[l]
Wind Direction	R. M. Young	12302	±2° True	±5° True	Naval Research Laboratory
Wind Speed	Meteorology Research	1022S (with 12905)[m,n]	±1.0% of reading	±1.2% of reading[o]	National Bureau of Standards[p]

[a]Includes rms error of the polynomial curve-fit to the calibration data required for converting output voltages into meteorological units and the error introduced by any associated amplifier or power supply.

[b]Sensor mounted inside R.M. Young model 43404A solar radiation shield with sensor oscillator and cable shielded from solar radiation. Electronics were set up for a narrow sensing range of 0 to 40°C with 6 digit resolution and 10-sec sampling period.

[c]Calibration was performed in a water bath and was assumed to be applicable to sensors operated in air. No compensation was made for possible increase in self-heating effect of sensor in air due to decreased thermal conductivity of measurement medium.

[d]Manufacturer's stated max. error due to the solar radiation shield was 0.050°C (see note b). Because the measurement sought was a differential temperature, the increase due to solar heating was assumed to be equal at all locations. Therefore, the influence of the radiation shields was not included.

[e]NBS test report No. G-43279.

[f]It was assumed that the acceleration of the air flow over the measurement site escarpment had no significant influence on the ambient reading.

[g]Standard range of device narrowed by manufacturer for −20 to +40° C operation and modified for corresponding −0-10 Vdc output.

[h]To maintain this accuracy, the device must be recalibrated at least once every 8 hours with a special resistance-type secondary standard. See Appendix B. This value includes the error introduced by solar heating of the sensor cables due to the differing lengths and positions of exposure.

[i]NBS test report No. G-43282.

[j]Sensor sensitive to shortwave radiation from 0.28×10^{-6} to 2.8×10^{-6} meter wavelength. Ectron model 616A used as output amplifier.

[k]Device set up for narrow sensing range of 10 to 20 ° C, corresponding to −0-10 Vdc output. Ectron model 616A used as output amplifier.

[l]NBS test report No. G-43675.

[m]Manufacturer modified standard stainless-steel sensor cups for marine use by electron-beam welding each cup to the spoke of the anenometer. The standard solder was found to deteriorate rapidly in the salt air.

[n]Tachometer modified for output time constant of 20 sec. and range narrowed for 0 to 120 Hz operation, corresponding to −0-10 Vdc output.

[o]To minimize polynomial curve-fitting errors at low wind speeds, two polynomial curve-fits were employed: 0 to 5 m sec^{-1}, corresponding to −0-2.5 Vdc and 5 to 20 m sec^{-1}, corresponding to −2.5-10 Vdc output.

[p]NBS test report No. G-43623.

with a Particle Measurements Systems model ASSP,* and the radon-222 measurements with a device* described in Larson (1973). The tide data were taken in October and November of 1976 by the National Oceanographic and Atmospheric Administration (NOAA). The maximum and minimum tide heights were computed† for May 1979 from the NOAA data. From the four daily extreme tide levels the tide height was calculated as a function of day and time by the procedure prescribed in Table 3 of National Ocean Survey (1979).

From the accuracy values of the fundamental measurements indicated in Table 12.1, it was possible to compute the typical accuracies of various calculated meteorological parameters given in Table 12.2.

Of all the measurements taken in the marine environment, an accurate humidity measurement is perhaps the most difficult to obtain. The dew point measurement technique has a distinct advantage of being an absolute measure independent of the errors produced by less than perfect solar radiation shielding of the sensor. As a practical matter, however, the devices used to measure dew point typically employ a three-conductor platinum-wire temperature sensor which can be separated from the electronic bridge by a sensor cable as long as 120 meters. If the sensor cable is not shielded from direct solar radiation, the radiation heating of the cable can alter the resistance of the cable conductors, producing a measurable error in the reading. The sensor cables employed at San Nicolas Island ranged in length from 34 to 46 meters, and no precaution had been taken to protect the cables from solar heating. Subsequent laboratory tests determined that a 10°C increase in the ambient temperature of a typical 40-meter-long sensor cable would produce a 0.009°C decrease in the indicated dew point temperature with the devices used at San Nicolas Island. This source of error was taken into consideration in computing the accuracy values presented in Tables 12.1 and 12.2.

The standard EG&G model 110-C3 chilled-mirror dew point device was specified by the manufacturer in EG&G (1972) to have an accuracy of ±0.28°C over an operating range of −65 to +50°C. A fourfold increase in the measurement accuracy was achieved by narrowing the range of operation to −20 to +40°C and by calibrating the device in a standards laboratory simultaneously in terms of absolute humidity and sensor resistance. The primary source of error with the EG&G model 110-C3 was found to be the combined electronics drift of the bridge and output circuits. Subsequent tests in the field determined that this source of error could be minimized by periodical recalibration, at least once every 8 hours, using a precision resistance secondary dew point standard calibrated at the time of the dew point sensor's primary calibration.

Table 12.2 — Typical Accuracies Expressed in Meteorological Units for the Observed and Calculated Parameters at Each Profile Measurement Level

Parameter	Typical Measurement Accuracy
Absolute Humidity	$\pm 0.067 \times 10^{-3}$ kg m^{-3}
Air Density	±0.0005 kg m^{-3}
Air Temperature	±0.003°C
Barometric Pres.[a]	±0.36 mb
Dew Point Temp.	±0.07°C
Height[b]	±0.29 meter
Latent Heat of Vap.	±6 ITcal. kg^{-1}
Potential Temp.	±0.006°C
Relative Humidity	±0.55%
Saturated Vap. Pres.	±0.007 mb
Sky & Solar Rad.[c]	±25 Watts m^{-2}
Specific Heat	±0.012 ITcal. kg^{-1} °K^{-1}
Specific Humidity	$\pm 0.056 \times 10^{-3}$ kg kg^{-1}
Vapor Pressure	±0.089 mb
Virtual Temp.	±0.013°C
Virtual Pot. Temp.	±0.016°C
Water Temp. (Bulk)[d]	±0.002°C
Wind Direction[e]	±5° True
Wind Speed[f]	±0.02 m sec^{-1}

[a]Barometric pressure was measured at 9.9 meters and calculated for the other levels.

[b]Standard deviation of sensor height variation about the geometric mean value employed in computing profiles.

[c]Value computed for 500 Watts m^{-2}, midvalue for the maximum observed radiation intensity.

[d]See Section 9 for location and depth of sensor.

[e]Ambient wind direction was measured at 20.7 meters and was assumed to be valid for all levels. For a more detailed presentation of what is entailed in this assumption, see Lockhart (1979).

[f]Value indicated was computed for the standard wind speed of 2 m sec^{-1} to facilitate comparison with the other experiments.

The required quality of the precision resistance secondary standard in regard to both resistance stability and reproducibility can not be overemphasized. Typical high-quality laboratory precision-resistance decade devices were found to be unsuitable for this task. Additionally, the calibration device provided by the manufacturer of the dew point sensor was found to be unreliable. The design of a suitable field-calibration device similar to that employed at San Nicolas Island is described in Appendix B.

In addition to the periodic recalibration of the dew point systems, it was generally found to be desirable to inspect all the sensors and clean off salt buildup and moisture condensation, particularly at the air intakes of the temperature and humidity sensors. The EG&G model 110-C3 was found to be potentially susceptible to this problem because the insect screen at the air intake

*Operated by and data made available courtesy of Dr. R. K. Jeck, Experimental Cloud Physics Section, Atmospheric Physics Branch, Naval Research Laboratory.

†See footnote p. 25

tends to collect salt, which can act as a local source or sink for moisture. Vugts (1980) has recently noted what can happen to an experiment if sufficient precautions are not taken to eliminate the problem of condensation on the sensors.

For comparison, it would be extremely interesting to consider the measurement accuracies present in other similar experiments. Four such experiments were selected from those listed in Table 4.1 and are presented in Table 12.3. Although little is presented by the authors as to how their accuracy figures were derived, inspection can reveal some important information.

Mease (1980) has indicated that the wind speed standards of most internationally accepted calibration laboratories are no better then ± 1% of the indicated reading in the range of 1 to 20 m sec^{-1}. It would appear that the stated accuracy of ±0.5% for the GATE experiment is overly optimistic. However, of considerably more importance is what seems to be a consistent and sizeable overestimation of the stated or inferred humidity accuracy of the other experiments. Yaglom (1977) has contended that the role of instrumentation error has often been underestimated in the micrometeorological literature.

Unlike the work at San Nicolas Island, which employed an absolute measure of humidity, the other four experiments listed in Table 12.3 used a wet-bulb technique. This technique gives a relative measure of humidity that is susceptible to a large number of possible sources of error, such as solar radiation heating and salt contamination, particularly in the marine environment. Most experiments which utilize the wet-bulb technique usually do not indicate accuracy in terms of humidity, but rather in terms of the precision to which they can measure the wet-bulb temperature—typically about ±0.01°C. A comparison of the dew point and wet bulb methods is presented in Coantic & Friehe (1980).

Bindon (1965) concluded that the best overall accuracy that could be expected from a wet-bulb measurement with an adequate radiation shield was about ±2%. An ambient specific humidity of about 7×10^{-3} kg kg^{-1} (the mean value observed at San Nicolas Island) would imply an accuracy of $\pm 0.14 \times 10^{-3}$ kg kg^{-1}. Sheppard et al. (1972), in an overwater experiment, reported observing unexplainable errors in differential wet-bulb measurements equivalent to about $\pm 0.08 \times 10^{-3}$ kg kg^{-1}. Smedman-Högström & Högström (1973), in an overland experiment in which two wet-bulb sensors were run side by side for 24 hours, observed on two occasions differences as large as $\pm 0.63 \times 10^{-3}$ kg kg^{-1}. The typical sources of error which must be taken into consideration when employing the wet-bulb technique have been presented by Pande (1970).

Hasegawa (1980) has indicated that the humidity standards of most internationally excepted calibration laboratories are no better then about $\pm 0.03 \times 10^{-3}$ kg kg^{-1} in the −20 to +40°C dew point range. It would appear that the stated accuracies of ±0.02 and $\pm 0.03 \times 10^{-3}$ kg kg^{-1} in Table 12.3 are overly optimistic by at least a factor of 2 or 3. A value no smaller then $\pm 0.06 \times 10^{-3}$ kg kg^{-1}, perhaps even as large as $\pm 0.12 \times 10^{-3}$ kg kg^{-1}, would appear more realistic.

Lastly, consider the accuracy of the air temperature measurements. Like the San Nicolas Island experiment, other experiments have had to be content with assuming that the radiation shields used to house the air-temperature sensors were reasonably effective and that, in any event, it was the temperature differential between the different measurement heights which was important for a profile measurement. It was assumed that the relative inefficiency of the shields and the influence of differing locations on a tower cancelled themselves out. An extensive literature search, however, has been unable to reveal the existence of any experimental effort designed to judge the validity of this assumption.

Lockhart (1975) reported a comparison of temperature measurements taken from three different solar-radiation shields located close to each other. At wind

Table 12.3 — Comparison of Stated Measurement Accuracies for each Measurement Level from Similar Marine Surface Layer Profile Experiments

Source	Experiment (name or location)	Air Temperature (°C)	Specific Humidity (10^{-3} kg kg^{-1})	Wind Speed (% of reading)
Badgley et al. (1972)	Indian Ocean	±0.009	±0.03	±1.5[b]
Paulson et al. (1972)	BOMEX	±0.005	±0.02	±1.0[b]
Krügermeyer (1976)	ATEX	±0.010	±0.02[a]	±1.0
Hasse et al. (1978b)	GATE	±0.010	±0.02[a]	±0.5
This Experiment	San Nicolas Island	±0.003	±0.06	±1.2[b]

[a]Value infered from stated wet bulb temperature accuracy of ±0.01°C.
[b]Value computed for standard wind speed of 2 m sec^{-1}.

speeds in excess of 10 m sec^{-1} he reported observing temperature differences as large as 2°C. Similar findings under high-wind conditions were observed with one type of solar shield, since replaced, which was used in an earlier experiment at San Nicolas Island reported by Blanc (1979). McKay & McTaggart-Cowan (1977), in a comparison of 19 different solar shields, found that most aspirated shields yielded temperature measurements which agreed to within ±0.2°C. Yaglom (1974) has presented an interesting example of the disastrous consequences which can occur with a profile air temperature measurement when only one of the sensor cables was not properly shielded. Moffat (1962) has catalogued many of the precautions which must be taken into consideration when designing an air-temperature sensor and its housing. A review of different temperature sensors is presented by Deacon (1980).

If one were to assume that the temperature measurements made in adequately designed solar shields from the same manufacturer differed by only 5% of the McKay & McTaggart-Cowan (1977) findings (due to manufacturing variation, the placement variation of sensors in shields, the difference in shield locations relative to the ground and the tower structure, etc.), it would suggest a temperature measurement accuracy no better than about ±0.010°C. Suffice it to say that, of the air temperature accuracies presented in Table 12.3, the ±0.010°C value is probably the most realistic.

Clearly what is needed at this time is a detailed study to determine the magnitude of these errors. Experiments such as the Indian Ocean experiment and BOMEX attempted to minimize these problems by employing a scanning-sensor strategy in which the same sensor set is sequentially moved from one measurement level to another. However, this procedure assumes that the atmosphere remains unchanged throughout the period required for a complete vertical scan of the instruments. In essence, this amounts to exchanging one set of assumptions for another. An interesting experiment would be one in which three identical sensor sets are employed. Two sensor sets could be placed at different fixed altitudes and a third could be scanned back and forth between the first two. This would not only allow a comparison of the two measurement strategies, it would allow a determination of the relative measurement accuracy at each level by periodically operating two identical sensor sets side by side. Conducting this type of comparison under a wide variety of atmospheric conditions could go a long way toward resolving some of the uncertainties. Lacking such an experimental determination, the approximate consensus summarized in Table 12.4 will have to suffice. Once the best accuracy realistically obtainable for the measurements in the field was established, it was possible to employ Eqs. 7.1 through 7.3 to obtain the corresponding minimum vertical separation appropriate for the profile measurement levels (see Table 12.4).

Table 12.4 — The Best Accuracy to which the Three Primary Observed Meteorological Parameters can be Realistically Measured in the Field and the Corresponding Minimum Vertical Separation Between Measurement Levels Appropriate for Profile Determination in the Marine Surface Layer as Concluded in Section 7.

Parameter	Best Field Obtainable Accuracy	Minimum Vertical Separation $\Delta ln\ z$ (z in meters)
Air Temperature	±0.010°C	0.399
Specific Humidity	$\pm 0.06 \times 10^{-3}$ kg kg^{-1}	0.429
Wind Speed	±1% of reading	0.619

13. Data Acquisition, Measurement Averaging Period and Availability of Experiment Database

The wind field is the predominant horizontal transport medium for the atmosphere. From the perspective of a fixed point in space, the temporal variation of the wind speed can be said to approximate the statistical variation of the atmosphere. Therefore, an inspection of the wind-speed kinetic energy spectrum should indicate an appropriate period over which an atmospheric measurement should be averaged in order to obtain a statistically independent data sample. Byshev & Ivanov (1969) presented the wind velocity spectra obtained from measurements made in the marine surface layer over the South Atlantic for the frequency range of 1.2×10^{-7} Hz (~96 days) to 5.0×10^{-1} Hz (2 sec). Inspection of Fig. 13.1 suggests that the best averaging period, the region of least variation, should lie somewhere between 3×10^{-4} Hz (~56 min) and 5×10^{-3} Hz (~3 min).

Ivanov & Ordanovich (1973), in a study of velocity and temperature fluctuation spectra taken at heights on the order of 10 meters, found that turbulent flux

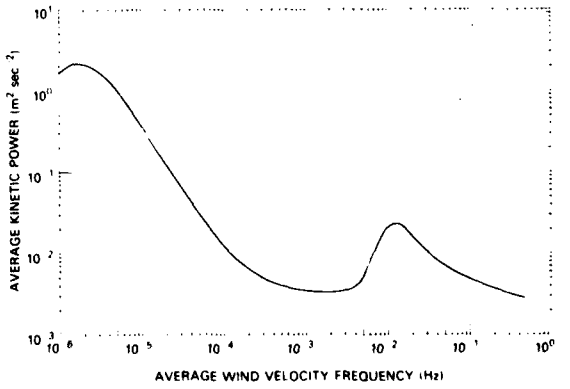

Fig. 13.1 — Byshev & Ivanov (1969) composite average wind velocity power spectrum for the marine surface layer from data taken over the South Atlantic Ocean

processes displayed a characteristic period of about 17 minutes. Chou (1966), in a study to determine the appropriate averaging period for profile measurements of momentum and sensible heat flux at heights on the order of 20 meters, found the optimum averaging period to be approximately 20 minutes. Tennekes & Wyngaard (1972) suggested that for wind speeds of about 5 m sec^{-1} an averaging period of 27 minutes should yield a variance measurement accurate to about 1%. Most of the experiments presented in Table 4.1 employed an averaging period of 10 minutes. Fleagle at al. (1958), Badgley et al. (1972), and Paulson et al. (1972) employed averaging periods of 60, 40, and 48 minutes, respectively. The measurements for the San Nicolas Island experiment were averaged for a period of 30 minutes.

The data acquisition and reduction were performed in the field with the aid of a 24-kilobyte programmable computer equipped with a 1-megabyte dual-magnetic-disk storage system and a high speed printer. Figure 13.2 shows a block diagram of the computer data acquisition system.

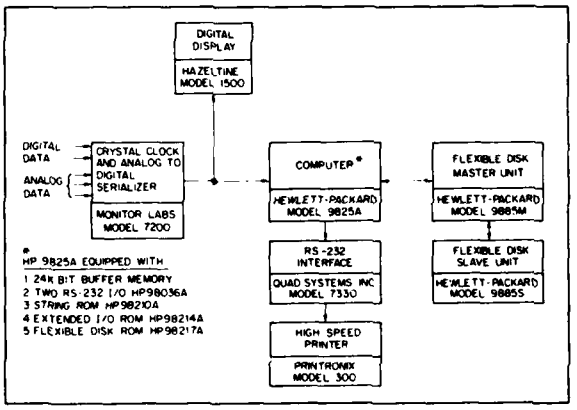

Fig. 13.2 — The computer data acquisition system employed at San Nicolas Island for in situ data reduction

Experience at San Nicolas Island demonstrated the substantial advantage and cost effectiveness of having in situ data reduction available in the field. Without it, several important experimental aspects of the work would have been overlooked and the amount of reliable data would have been reduced by a factor of at least four. Figure 13.3 shows a view of the electronics inside the mobile field shelter.

The various sensor-system analog outputs typically had a dynamic range of 0 to 10 Vdc, with time constants which ranged from approximately 0.2 to 20 seconds. The analog data was digitized with a five-digit resolution accurate to 2 parts in 10^4. The air-temperature system employed a digital output with a six-digit resolution accurate to 3 parts in 10^5 and updated every 10 seconds.

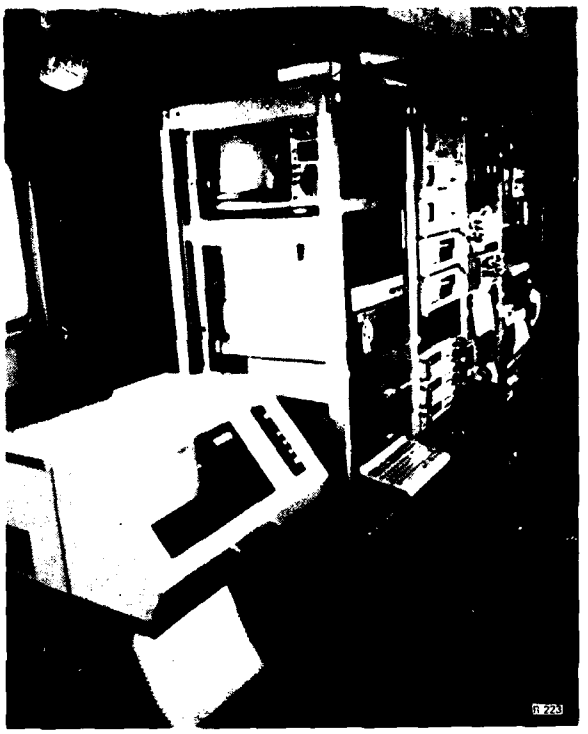

Fig. 13.3 — View inside the mobile field shelter of the computer data acquisition system and the sensor readout electronics

Data from a crystal-controlled clock and all the sensor system outputs were read into the computer once every 10 seconds at the rate of 15 readings per second. A complete set of readings took about 2 seconds. The computer was programmed to average the data from each sensor system for a 30 minute period by accumulating the readings in a series of registers and dividing the total of each register by the number of readings at the end of the averaging period.

At the end of each 30-minute period, while continuing to acquire data for the next period, the computer would perform the various micrometeorological calculations, print out the results, and store the data on magnetic disk. The data stored on magnetic disk was catalogued for future use by a ten-digit run number,* which represented the start time of the averaging period expressed in year, month, day, hour, and minutes in local Pacific Standard Time (PST)† rounded off to the nearest clock half hour.

*For example, data averaged from 1979 May 2, 15:32:20 to 16:02:10 PST, would have a run number of 7905021530.

†Pacific Daylight Saving Time = PST + 1 hour. Greenwich Mean Time = PST + 8 hours.

The analog inputs to the digital serializer were designed for differential operation to ensure a high common mode noise rejection. All sensor and power cables were individually shielded, with all common conductors and shields grounded at a single point, to eliminate the possibility of noise from ground-current loops. Two precision voltage references and two digital numeric references were monitored continuously by the computer to ensure digitizing accuracy. All the electronic instruments were powered from a single active ac power-line conditioner* with the output continuously monitored by the computer to detect any possible power-line frequency and voltage fluctuations.

The micrometeorological data contained in this report, catalogued by run number, is available on Hewlett-Packard model 9885 or Tektronix model 4907 compatible floppy disk upon request to the author. A hard copy of the experiment data base will be made available in a forthcoming Naval Research Laboratory Memorandum Report 4713, Blanc (1982).

14. Outline of Micrometeorological Calculations

As a general rule, the typical formulations employed for the micrometeorological calculations were those viewed by the author to be the most accurate. Since this is a subjective judgment, and because there exists no universally excepted standard method, the following brief overview is presented. A more-detailed presentation is given in Appendix E. The reader should note that the notation used to indicate altitude in this report is the *reverse* of that most commonly found in the literature. In this report, subscript 1 is employed to denote the top measurement level and subscript 2 is employed to denote the bottom measurement level.

The outputs of the air-temperature measurement devices were digital and required no calibration-curve fitting. The outputs of all the other meteorological devices were analog and required up to a third-order polynomial calibration-curve fit in order to convert the voltage output into meteorological units.

The correction of the observed wind speeds due to the influence of the beach escarpment as a function of wind direction and height, the tide height as a function of the day and time, and the upwind distance from the water's edge to the sensors as a function of wind direction and tide height were all calculated from tables stored in the computer. The wind-speed correction and upwind distance tables are summarized in Table A.3 of Appendix A. The tide height table was computed in manner described in Section 12.

*California Instruments Dynamic AC Line Corrector, Model 1360.

The barometric pressure, measured near the lowest measurement level, was calculated for the other levels as a function of elevation. The vapor pressure and saturated vapor pressure were calculated from the dew point and the air temperature, respectively, using the barometric pressure and the Goff-Gratch formulation presented in Table 94 of List (1958). From these parameters the absolute, relative, and specific humidities and the potential, virtual, and virtual potential temperatures were calculated.

To ensure that the profile measurement uncertainty was never larger than the observed differential measurement, minimum limits for acceptable differential values were established based upon the rms of the error values presented in Table 12.2 for wind speed, specific humidity, and potential temperature. The minimum acceptable differential values were set at ± 0.028 m sec^{-1}, $\pm 0.08 \times 10^{-3}$ kg kg^{-1}, and ± 0.008 °C, respectively.

The acceleration constant due to gravity at sea level was computed as a function of the measurement site latitude, as prescribed in Table 167 of List (1958). The partial derivatives with respect to height for the above three profile parameters were computed employing the approximation suggested by Panofsky (1965) and reported by Badgley et al. (1972) which is accurate to about $\pm 3\%$. The partial derivatives of wind speed and potential temperature were used to compute the Richardson-number stability in the general manner defined by Badgley et al.

The Richardson-number formulation of Badgley et al. required modification for practical considerations. The orginal form required the thermal constituent to be defined in terms of virtual potential temperature profile in an effort to incorporate the humidity influence, or buoyancy, into the thermodynamic component of the stability equation. Inspection of Table 12.2 revealed that the ± 0.016°C error associated with each measurement level of the virtual potential temperature, mainly due to the relatively large humidity error, would yield an rms profile error of about ± 0.023°C. This is four times larger than it would be if the potential temperature profile were employed. Such a large measurement uncertainty frequently would have made it impossible to distinguish between a real temperature profile and the "noise" of the profile measurement. This aspect was of particular concern, since it is the temperature profile which governs the determination of a stable or unstable condition.

The application of the Monin-Obukhov similarity theory to the marine surface layer was experimentally verified by Weiler & Burling (1967). Once the Richardson-number stability parameter (Ri) had been calculated, it was then possible to translate it into the Monin-Obukhov stability parameter (z/L or ζ) by employing the Eqs. 26 and 28 of Businger et al. (1971).

Computation of the z/L parameter as a function of Ri required solving two of the Businger et al. equations in reverse. The solution of the unstable condition was achieved by employing the Newton-Raphson (or Newton) method described in Scheid (1968). The solution of the stable condition was achieved by the use of the quadratic solution method. Knowing z/L and the height z, it was then a simple matter to compute the Monin-Obukhov length L. The height z, in this case, was equal to the mean height for which the Ri value was valid, the geometric mean of the two profile measurement levels, 12.99 meters.

The computationally and conceptually convenient log-linear profile relationship described in Section 7 is technically correct only under neutral or near-neutral stability conditions, where $Ri \approx z/L \approx 0$. From Fig. 7.2 it can be seen that the nonlinearity of the wind profile increases with increased stability or instability. A similar, but different, stability-dependent curvature also exists for the temperature and humidity profiles. To correct the observed profiles for this stability dependent nonlinearity, ψ corrections were applied to the profile measurements—ψ_1 for the wind speed profile and ψ_2 for the temperature and humidity profile. The ψ corrections are a function of both L and z, where z, in this case, is the height at which the particular profile measurement was acquired, 9.20 or 18.35 meters. For the unstable case, the Paulson (1970)* ψ equations were used in which, like Businger et al. (1971), Paulson's γ was set equal to 15 for ψ_1 and 9 for ψ_2. For the stable case, the values of ψ_1 and ψ_2 were inferred from Businger et al. Eqs. 29 and 30.

Unlike Businger et al., we set the von Kármán constant equal to 0.4. The rationale for this modification was given in Section 3. It is tantamount to reducing the Businger et al. profile computational scheme equivalent to that of Dyer & Hicks (1970).

Once the profile measurements were corrected for the stability-dependent nonlinearity, with the appropriate ψ correction, it was then possible to compute the slope of the three profiles. The profile slope $[\Delta(\ln z - \psi)/\Delta$ (profile parameter)] was employed to eliminate the confusion which exists in literature between Western and USSR use of the terms gradient and lapse rate.† In this report:

$$\text{slope} = \frac{1}{-\text{lapse rate}} = \frac{1}{\text{gradient (Western)}} = \frac{1}{-\text{gradient (USSR)}}.$$

From the von Kármán constant and the slopes of wind speed, specific humidity, potential temperature the respective scaling parameters were computed. The scaling parameters can be viewed as an artifact of the profile method, which is a conceptually convenient way to represent the slopes or gradients of the various parameters. The wind-speed scaling parameter is more commonly called the friction velocity.

The mean density of the moist air was calculated as a function of barometric pressure and virtual temperature, as prescribed in Table 71 of List (1958). The mean specific heat at constant pressure of moist air was computed as a function of specific humidity and the specific heat of dry air by the approximation suggested by McIntosh (1972), his p. 263, and from Table 70 of List (1958). From these and the scaling parameters, the fluxes of momentum, humidity, heat were computed.

In the literature a negative momentum flux (negative because it is downwards) is frequently called stress, shear stress, surface stress, eddy stress, turbulent stress, or Reynold's stress. In this report humidity flux is defined as humidity mass flux and heat flux is defined as sensible heat flux.

The latent heat of water vapor (L_v) in ITcal kg^{-1} was approximated as a function of air temperature (T) in °C from Table 92 of List (1958) for the temperature range −10 to +40°C by the equation

$$L_v \approx [597.31 - (0.56525\ T)] \times 10^3. \qquad (14.1)$$

Knowing the latent heat of vaporization, it was then possible to compute the latent heat flux from the humidity flux. In the literature latent heat flux is frequently called water vapor flux or vapor pressure flux. The term moisture flux can be used to mean either humidity mass flux or latent heat flux.

The total heat budget flux was approximated by summing the sky & solar short-wave radiation heat flux, the latent heat flux, and the sensible heat flux. A positive sign was used to indicate the upward direction and a negative sign to indicate the downward direction. The Bowen ratio was computed as the value (including signs) of the sensible heat flux divided by the latent heat flux. Thus, a positive Bowen ratio sign indicated that the two fluxes were in the same direction and a negative sign that they were in opposite directions.

The neutral drag coefficient at 10 meters was computed as a function of the friction velocity and wind speed as prescribed by McIntosh & Thom (1973), their Eq. 9.13. The roughness length over the water was computed as a function of the friction velocity by employing a fourth-order polynomial fit to the Sheppard et al. (1972) curve presented in their Fig. 4. The roughness length (z_0) was approximated with an accuracy of about ±20% and the relationship was extended over a wider

*The reader should take care to note that the Paulson (1970) equation indicated for the partial derivative at the bottom of his p. 858 is incorrect.

†For example, see p. 103 of Tverskoi (1965).

range of values as a function of the friction velocity (U_*) by the equation

$$z_0 \approx 10^{-2.501+1.465\log U_* - 6.743(\log U_*)^2 - 10.7(\log U_*)^3 - 6.875(\log U_*)^4} \quad (14.2)$$

A comparison of this approach with other schemes found in the literature is presented in Fig. 14.1.

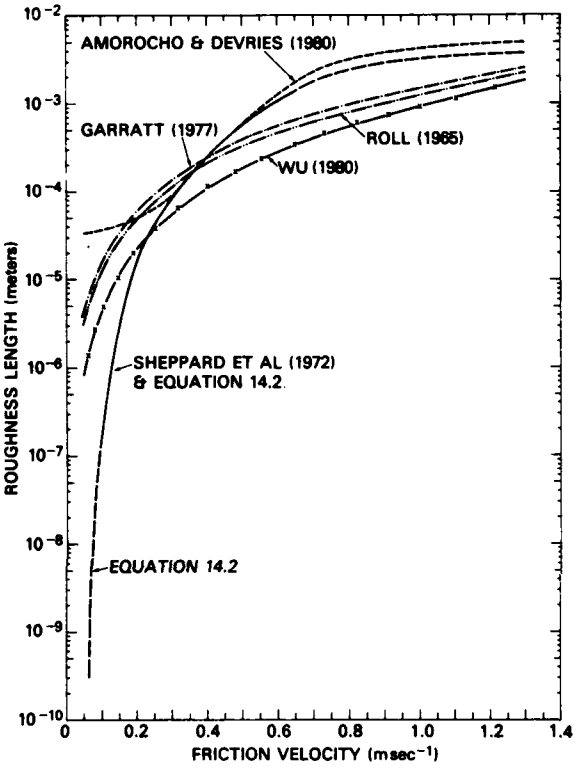

Fig. 14.1 — Sheppard et al. (1972) roughness length approximation, Eq. (14.2), as a function of friction velocity compared to the results of Roll (1965) via Charnock (1955), Garratt (1977) via Charnock (1955), Amorocho & DeVries (1980) via Charnock (1955), and Wu (1980) via Hill (1962) and Condon & Odishaw (1958)

The profile calculations having been completed, it was then necessary to initiate those for the bulk method. To facilitate a comparison with other experiments, it was desirable to compute the bulk parameters based upon measurements taken at the standard height of 10 meters. At the risk of introducing a relatively small error, the values at the 10-meter height were estimated from the measurements taken at 9.20 and 18.35 meters by assuming an idealized log-linear profile.

The bulk parameter calculations for vapor pressure through the latent heat of water vaporization, Eq. 14.1, were done in the same manner as those for the profile parameters. As detailed in Section 3, the bulk method of Friehe & Schmitt (1976) with the drag coefficient scheme of Smith and Banke (1975) was employed to compute the bulk-derived fluxes.

The bulk-derived friction velocity was computed as a function of shear stress (negative momentum flux) and the density of moist air as prescribed by McIntosh and Thom (1973), their Eq. 9.5. The bulk-derived roughness length was computed as a function of the bulk-derived friction velocity in the same manner prescribed for the profile method. The bulk-derived scaling parameters were computed from their respective fluxes by employing the same equations used for computing the profile fluxes.

The bulk-derived Monin-Obukhov length (L) for the height of 10 meters was computed as a function of the friction velocity as defined by Businger et al. (1971), their p. 182. Knowing L, it was a simple procedure to compute the z/L for the geometric mean height, 12.99 meters. The bulk-derived Richardson-number stability was computed as a function of z/L at the geometric mean height by the same equations used for computing the profile-derived z/L, but this time in the forward manner.

15. Error Analysis and a Comparison with Previous Experiments

Yaglom (1974,1977) has suggested that much of the scatter contained in various comparisons of flux data obtained by different techniques is probably due to instrumentation measurement errors. Yet, none of available sources of the flux data listed in Table 4.1 contained anything more than an occasional speculation as to the accuracy of the reported flux measurements. Perhaps L. P. Smith (1970) said it best:

> All too often published meteorological data are accepted at their face value, with a blind faith that is rarely justified by the facts. To use inaccurate data in research is an act of stupidity; to publish misleading information under the guise of truth is a scientific crime. It is no excuse to plead ignorance—ignorance not of the law, but of the inaccuracies. The main unforgivable effect of incompetence is the trouble it causes to other people. A scientist could be expected to correct his own mistakes, but if he has to spend half his time discovering and correcting the errors of others, life becomes impossible.

To compute the flux and stability measurement errors attributable to the instrumentation employed at San Nicolas Island, a method was developed for approximating the influence of the constituent measurement errors listed in Table 12.2. A detailed presentation of the error-analysis computation method is presented in Appendix E. The errors attributable to the measurement uncertainties during each 30-minute-long data run were

computed for the various profile-derived and bulk-derived stability, flux, and scaling parameters, as well as for the drag coefficient and roughness length. They are presented as error bars in the figures in Sections 18 through 20.

As detailed in Section 3, the Wieringa (1980) work served to coalesce the various profile flux schemes into a single unified technique. This has not yet been done for the bulk method. To allow a conclusion to be drawn in regard to the bulk technique in general, and not just to the scheme selected for this experiment, uncertainty values were estimated for the bulk transfer coefficients to reflect these differences. For example, unlike in the bulk scheme employed for the San Nicolas Island work, Krügermeyer (1976) and Liu et al. (1979) have advocated the use of stability-dependent coefficients. Based upon the scatter among the data of various experimenters presented by Friehe & Schmitt (1976), their Figs. 2 and 5, and by Smith & Banke (1976), their Fig. 4, the uncertainties for the bulk coefficients of momentum, moisture, and sensible heat were estimated to be 40%, 25%, and 55%, respectively. Because the bulk water-temperature measurement was employed to approximate the surface temperature, the uncertainty value for the air-water temperature difference was set equal to 0.5°C based upon the estimates of Katsaros (1980a,1980b).

Based upon the rms of the error values presented in Table 12.2, the criterion selected for the specific humidity and potential temperature differential values equivalent to a profile measurement error of 100% were $\pm 0.08 \times 10^{-3}$ kg kg^{-1}, and ± 0.008°C, respectively. For example, an observed specific humidity profile differential measurement of -0.32×10^{-3} kg kg^{-1} would indicate a measurement error of ±25%. A somewhat larger error value than that suggested by Table 12.1 or 12.2 was selected for the wind speed profile, since no attempt had been made to correct the anemometer data for overspeeding. The selected ±2.8% wind speed value was based upon the rms of the 2% accuracy value reported by Meshal (1977) in an experiment performed to measure cup anemometer overspeeding over water. The results of both the profile and bulk error analysis are presented in Table 15.1, where the typical error value has been defined as the average error value for the entire experiment.

The uncertainty values in Table 15.2 were computed from the respective percent error values presented in Table 15.1 and the combined profile-bulk parameter value. The combined parameter value was defined as the mean of the average profile parameter value and the average bulk parameter value, computed for the entire experiment.

It should be emphasized that the uncertainty values presented in Tables 15.1 and 15.2 are those which are attributable only to the instrumentation error and to the variability of the different schemes within a given technique. The tables contain no assessment as to the other sources of error that must be taken into consideration when determining the overall merits of a particular technique. The suitability of the bulk technique will be the topic of Section 24.

From Tables 15.1 and 15.2 it can be concluded that the profile technique is more sensitive to instrumentation error in determining momentum and latent heat

Table 15.1 — Typical Profile and Bulk Technique Flux and Stability Uncertainty Values due to Instrumentation Measurement Error and Scheme Variability Expressed in Percent of Reading. The data is based upon 136 hours of observations acquired under average wind speeds ranging from 2 to 17 m sec^{-1}, air-water temperature differences from −2.1 to +0.6°C, and dew point-water temperature difference from −7.5 to −2.0°C.

Parameter	Profile Technique Mean Error	Bulk Technique Mean Error
Gradient Richardson Stability	±139%	±296%
Monin-Obukhov Stability (at 10 m)	±145%	±297%
Momentum Flux	±117%	±46%
Latent Heat Flux	±165%	±44%
Sensible Heat Flux	±116%	±225%
Total Heat Budget Flux	±78%	±23%
Bowen Ratio	±280%	±269%
Drag Coefficient (at 10 m)	±7%	±40%
Roughness Length	±78%	±43%
Friction Velocity	±58%	±23%
Scaling Specific Humidity	±106%	±67%
Scaling Potential Temperature	±57%	±248%

Table 15.2 — Typical Profile and Bulk Technique Flux and Stability Uncertainty Values due to Instrumentation Measurement Error and Scheme Variability Expressed in Meteorological units. The data is based Upon 136 hours of observations acquired under average wind speeds ranging from 2 to 17 m sec^{-1}, air-water temperature differences from −2.1 to +0.6°C, and dew point-water temperature differences from −7.5 to −2.0°C.

Parameter	Profile Technique Mean Error	Bulk Technique Mean Error
Gradient Richardson Stability	±0.18	±0.38
Monin-Obukhov Stability (10 m)	±0.14	±0.30
Momentum Flux	±0.27 Nt. m^{-2}	±0.11 Nt. m^{-2}
Latent Heat Flux	±118 Watts m^{-2}	±32 Watts m^{-2}
Sensible Heat Flux	±8 Watts m^{-2}	±16 Watts m^{-2}
Total Heat Budget Flux	±134 Watts m^{-2}	±56 Watts m^{-2}
Bowen Ratio	±0.25	±0.24
Drag Coefficient (10 m)	$\pm 2.0 \times 10^{-3}$	$\pm 0.7 \times 10^{-3}$
Roughness Length	$\pm 3.0 \times 10^{-4}$ m	$\pm 1.6 \times 10^{-4}$m
Friction Velocity	±0.21 m sec^{-1}	±0.08 m sec^{-1}
Scaling Specific Humidity	$\pm 0.067 \times 10^{-3}$ kg kg^{-1}	$\pm 0.042 \times 10^{-3}$kg kg^{-1}
Scaling Potential Temperature	±0.003°C	±0.012°C

flux than is the bulk technique and that the bulk technique is more sensitive to instrumentation error in determining stability and sensible heat flux. As described in Section 14, the sensible heat flux is of particular importance in determining stability. It not only plays a roll in determining the magnitude of the stability, it is the sole determinant for distinguishing between a stable and unstable situation. These results would tend to suggest that because the uncertainty associated with the bulk-derived stability is so large, little would be gained by employing stability-dependent bulk coefficients unless the bulk technique were supplemented with an auxiliary technique for determining stability.

As can be seen from Tables 15.1 and 15.2, the relatively large bulk technique measurement error in determining sensible heat flux could explain the poor correlation between the bulk-derived and profile-derived derived sensible heat fluxes reported by Dunckel et al. (1974) and others. As discussed in Section 3, the problem is due almost exclusively to the inherent difficulty of measuring the water surface temperature accurately enough to be of practical use with the existing bulk technique.

Because the various constituent instrumentation measurement errors which go into making up the profile flux and stability error interact in a rather complex fashion (the scheme variability for the profile technique is comparatively negligible), a study was undertaken to determine the variation of the error as a function of the observed parameter magnitude. A study was conducted for each of the profile-derived flux and stability related parameters and is presented in Figs. 15.1 through 15.12.

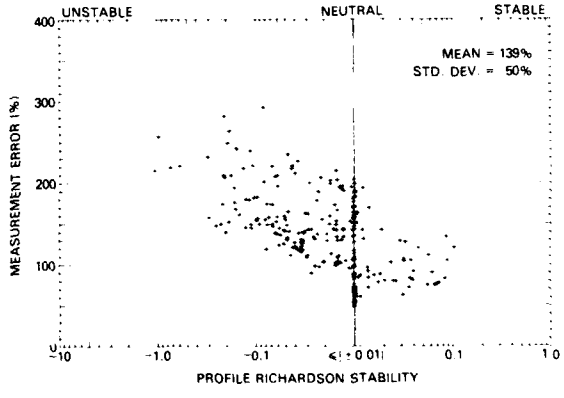

Fig. 15.1 — Results of the error analysis for profile-derived Richardson number stability

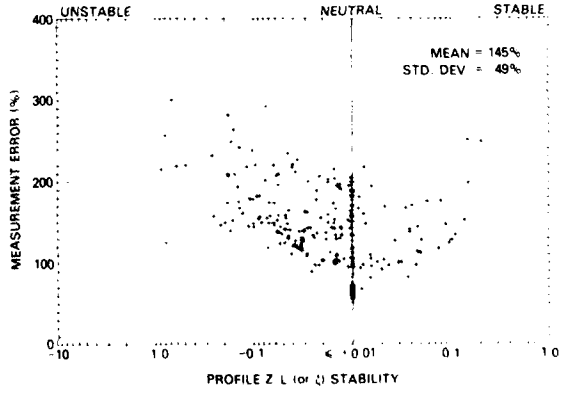

Fig. 15.2 — Results of the error analysis for profile-derived Monin-Obukhov stability

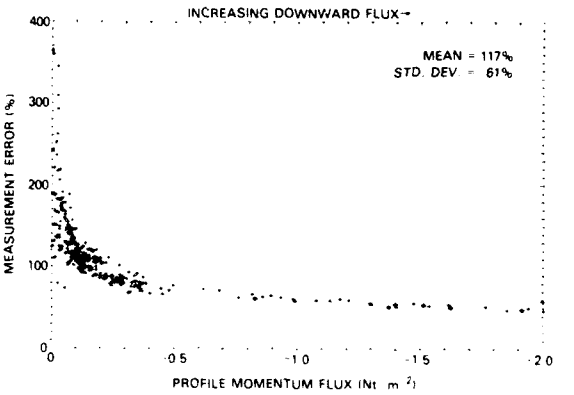

Fig. 15.3 — Results of the error analysis for profile-derived momentum flux

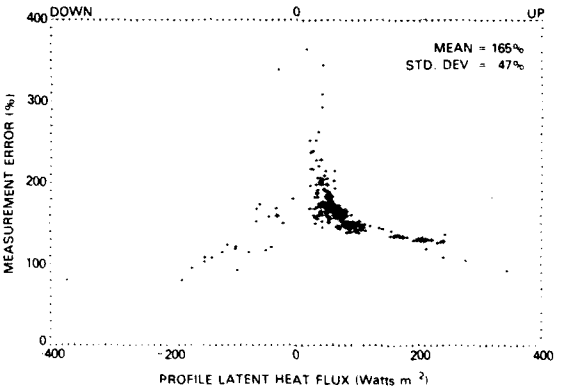

Fig. 15.4 — Results of the error analysis for profile-derived latent heat flux

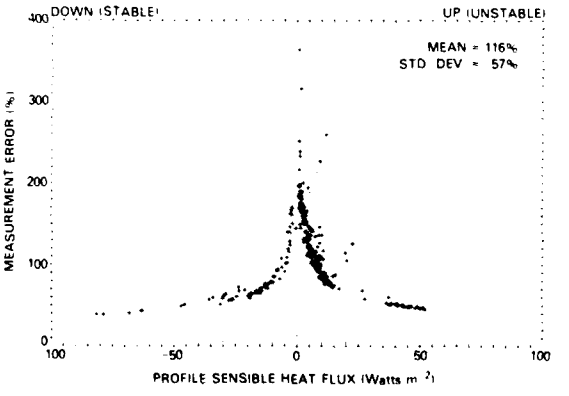

Fig. 15.5 — Results of the error analysis for profile-derived sensible heat flux

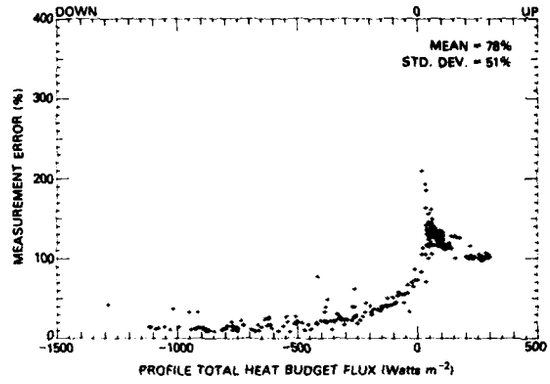

Fig. 15.6 — Results of the error analysis for profile-derived total heat budget flux

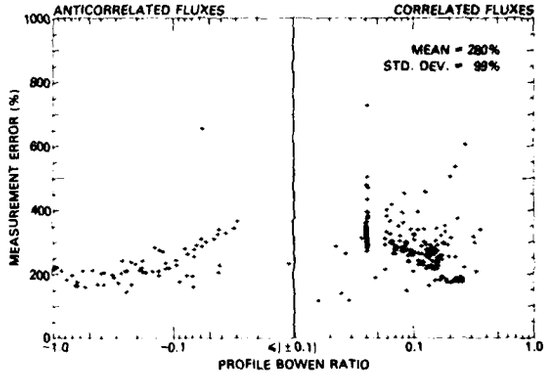

Fig. 15.7 — Results of the error analysis for profile-derived Bowen ratio

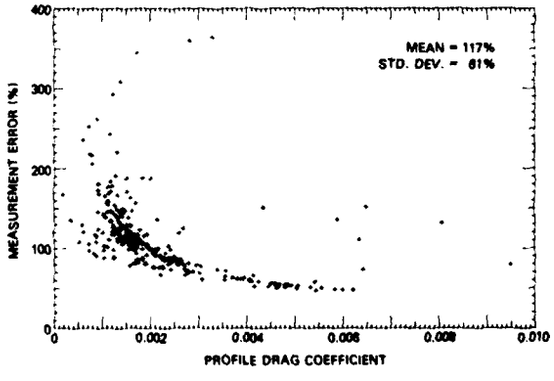

Fig. 15.8 — Results of the error analysis for profile-derived neutral drag coefficient for 10-meter height

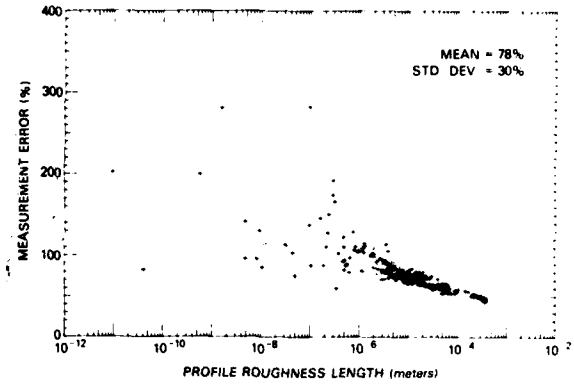

Fig. 15.9 — Results of the error analysis for profile-derived roughness length computed via Eq. 14.2

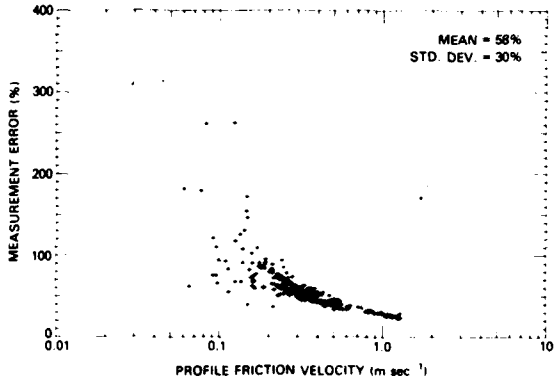

Fig. 15.10 — Results of the error analysis for profile-derived friction velocity

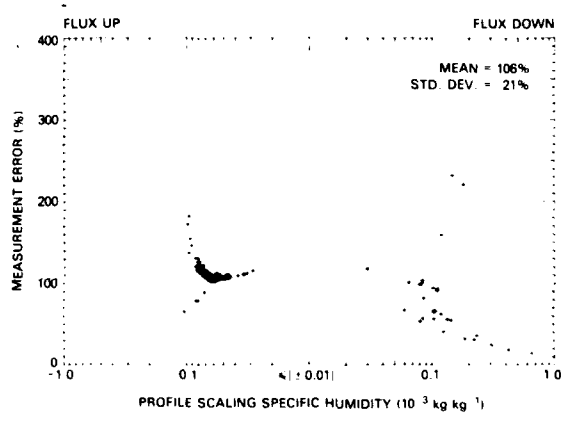

Fig. 15.11 — Results of the error analysis for profile-derived scaling specific humidity

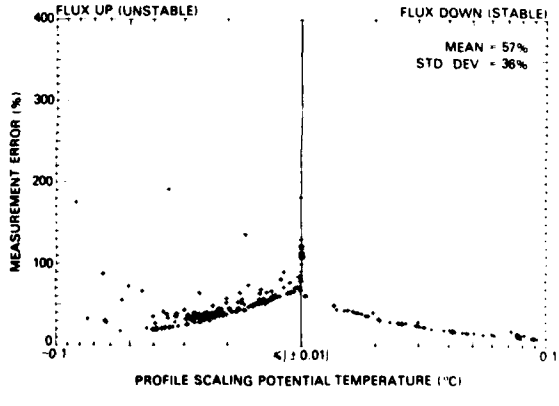

Fig. 15.12 — Results of the error analysis for profile-derived scaling potential temperature

Table 15.3 — Comparison of Marine Surface-Layer Profile Experiment Instrumentation Arrangements Presented in Terms of the Number of Measurement Levels (No.) and the Average Vertical Logarithmic Separation Between Adjacent Levels ($\overline{\Delta \ln z}$), where z is in Meters.

Source	Experiment (name or location)	Wind Speed		Air Temp.		Humidity	
		No.	$\overline{\Delta \ln z}$	No.	$\overline{\Delta \ln z}$	No.	$\overline{\Delta \ln z}$
Hoeber (1969)	Equatorial Atlantic	4	0.570	4	0.583	4	0.583
Badgley et al. (1972)	Indian Ocean	6	0.329	6	0.329	6	0.329
Paulson et al. (1972)	BOMEX	4	0.568	4	0.568	4	0.568
Krügermeyer (1976)	ATEX	7	0.315	4	0.608	4	0.608
Hasse et al. (1978b)	GATE	7	0.281	5	0.496	5	0.496
This Experiment	San Nicolas Island	2	0.690	2	0.690	2	0.690

Table 15.4 — Comparison of Marine Surface-Layer Profile Experiment Instrumentation Arrangements Relative Profile Measurement Accuracy Scaled in Terms of the Number of Measurement Levels and the Vertical Separation Between Levels. The larger the scaling coefficient, the higher the relative accuracy.

Source	Experiment (name or location)	Profile Accuracy Scaling Coefficients		
		Wind Speed	Air Temp.	Humidity
Hoeber (1969)	Equatorial Atlantic	1.302	2.067	1.922
Badgley et al. (1972)	Indian Ocean	0.921	1.429	1.329
Paulson et al. (1972)	BOMEX	1.298	2.014	1.873
Krügermeyer (1976)	ATEX	0.951	2.155	2.005
Hasse et al. (1978b)	GATE	0.849	1.967	1.829
This Experiment	San Nicolas Island	1.115	1.729	1.608

The error analysis of the two-level profile flux and stability data indicated that the measurement uncertainties were considerably larger than had been originally anticipated. It, therefore, was of interest to determine if the profile error values summarized in Table 15.1 might be typical of other profile experiments had their data been acquired under similar meteorological conditions.

From Table 4.1 it can be seen that previous profile experiments conducted in the marine surface layer employed various numbers of measurement levels distributed over a range of altitude configurations. Five instrumentation arrangements were selected for comparison with the San Nicolas Island array and are summarized in Table 15.3.

Earlier parts of this report presented a rationale for determining the minimum vertical spacing appropriate for sensors of a given accuracy (Section 7) and demonstrated the influence the number of sensors had on the accuracy in determining the profile (Section 8). A comparison of the instrumentation employed in previous profile experiments (Section 12) concluded that the instrumentation employed in the other experiments was probably no more accurate than that used at San Nicolas Island. Scaling the product of the influence of the number of measurement levels (Table 8.1) and the influence of the vertical separation (Table 12.4) to the information presented in Table 15.3 resulted in the profile accuracy scaling coefficients of Table 15.4.

Normalizing the accuracy coefficient to the San Nicolas Island values; scaling the results to the friction velocity, scaling potential temperatures, and scaling specific-humidity mean-error profile values (Table 15.1); and computing the subsequent error values for the fluxes yielded Table 15.5. From this table it can be seen that, in terms of the three primary fluxes, the other instrumentation arrangements would have yielded uncertainty values no better than 0.84 times the San Nicolas Island error results and no worse than 1.30 times them had they acquired data under similar meteorological conditions, exclusive of any island or escarpment influence.

16. Statistical Distribution of Observations and the Presentation Format

The May 1979 San Nicolas Island experiment was conducted over a 10 day period under a wide range of meteorological conditions as illustrated in Figs. 16.1 through 16.6. Two hundred seventy-two 30-minute-long measurement periods were obtained, totaling 136 hours of data.

The figures used to illustrate the observations as a function of experiment time in Sections 17 through 20 are exhibited in terms of the day and hour of the data acquisition initiation, expressed in local Pacific Standard Time (PST) rounded off to the nearest clock half hour. The error bars exhibited in the figures were computed for each data run in the manner described in Section 15; they are based upon constituent measurement uncertainties attributable to instrumentation and the computational-scheme variability within the given measurement technique. In those figures in which both the profile data and the bulk data are displayed with error bars, the respective data points were offset slightly to the side of each other in order to minimize overlapping.

Table 15.5 — Comparison of Flux and Stability Measurement Errors of Various Marine Surface-Layer Profile Experiments Attributable to Constituent Instrumentation Measurement Uncertainty, as Scaled to the Errors Computed for the San Nicolas Island Results. The values presented are the mean error values the experiments would have encountered had data been acquired under the same meteorological conditions experienced at San Nicolas Island. The analysis assumes that instruments of equivalent accuracy had been employed in all experiments and takes into consideration the number of sensors and their vertical separation. Values are approximate and valid only for comparative purposes.

Parameter	Mean Measurement Uncertainties					
	This Experiment San Nicolas Island	Hoeber (1969) Equatorial Atlantic	Badgley et al. (1972) Indian Ocean	Paulson et al. (1972) BOMEX	Krügermeyer (1976) ATEX	Hasse et al. (1978b) GATE
Gradient Richardson Stability	139%	119%	168%	120%	155%	172%
Monin-Obukhov Stability (10 m)	145%	124%	175%	125%	162%	179%
Momentum Flux	117%	100%	140%	100%	136%	152%
Latent Heat Flux	165%	139%	198%	141%	153%	169%
Sensible Heat Flux	116%	98%	139%	99%	114%	126%
Total Heat Budget Flux[a]	78%	66%	94%	67%	72%	80%
Bowen Ratio	280%	237%	337%	240%	267%	295%
Drag Coefficient (10 m)	117%	100%	140%	100%	136%	152%
Roughness Length[b]	78%	70%	90%	70%	88%	96%
Friction Velocity	58%	50%	70%	50%	68%	76%
Scaling Specific Humidity	106%	89%	128%	91%	85%	93%
Scaling Potential Temperature	57%	48%	69%	49%	46%	50%

[a]Assumes other experiments would have had an equivalent type of sky and solar radiation instrumentation.

[b]Assumes other experiments would have employed Eq. 14.2 to compute roughness length as a function of friction velocity.

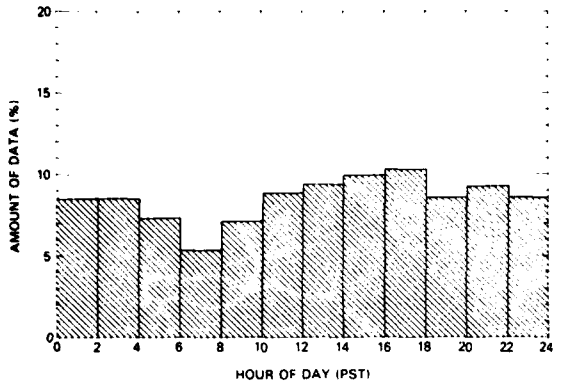

Fig. 16.1 — Statistical distribution of the meteorological observations as a function of the hour of day in local standard time

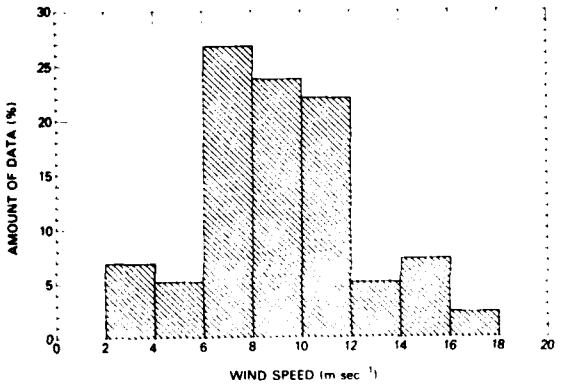

Fig. 16.2 — Statistical distribution of the meteorological observations as a function of 30-minute-average wind speed at 10-meter height

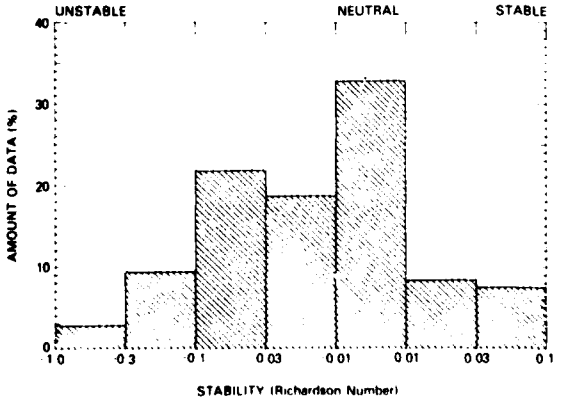

Fig. 16.3 — Statistical distribution of the meteorological observations as a function of the profile-derived stability

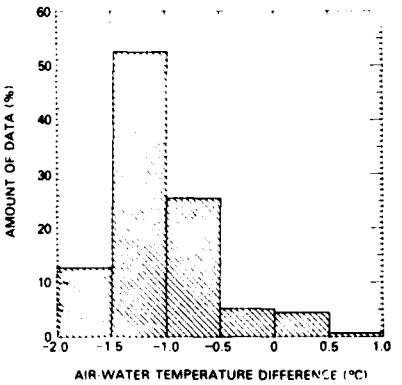

Fig. 16.4 — Statistical distribution of the meteorological observations as a function of the air temperature at 10-meter height and the bulk water temperature difference

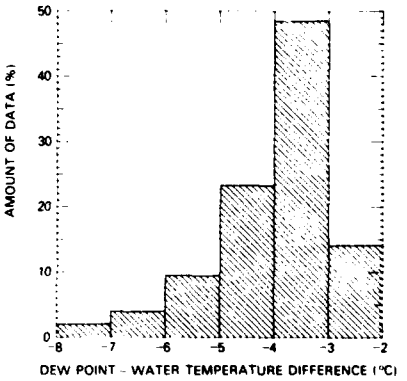

Fig. 16.5 — Statistical distribution of the meteorological observations as a function of the dew-point temperature at 10-meter height and the bulk water temperature difference

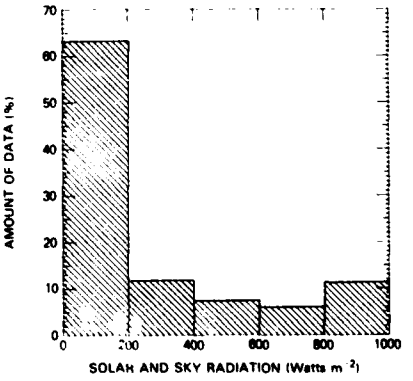

Fig. 16.6 — Statistical distribution of the meteorological observations as a function of the incoming shortwave solar and sky radiation

17. Meteorological, Oceanographic, and Aerosol Observations

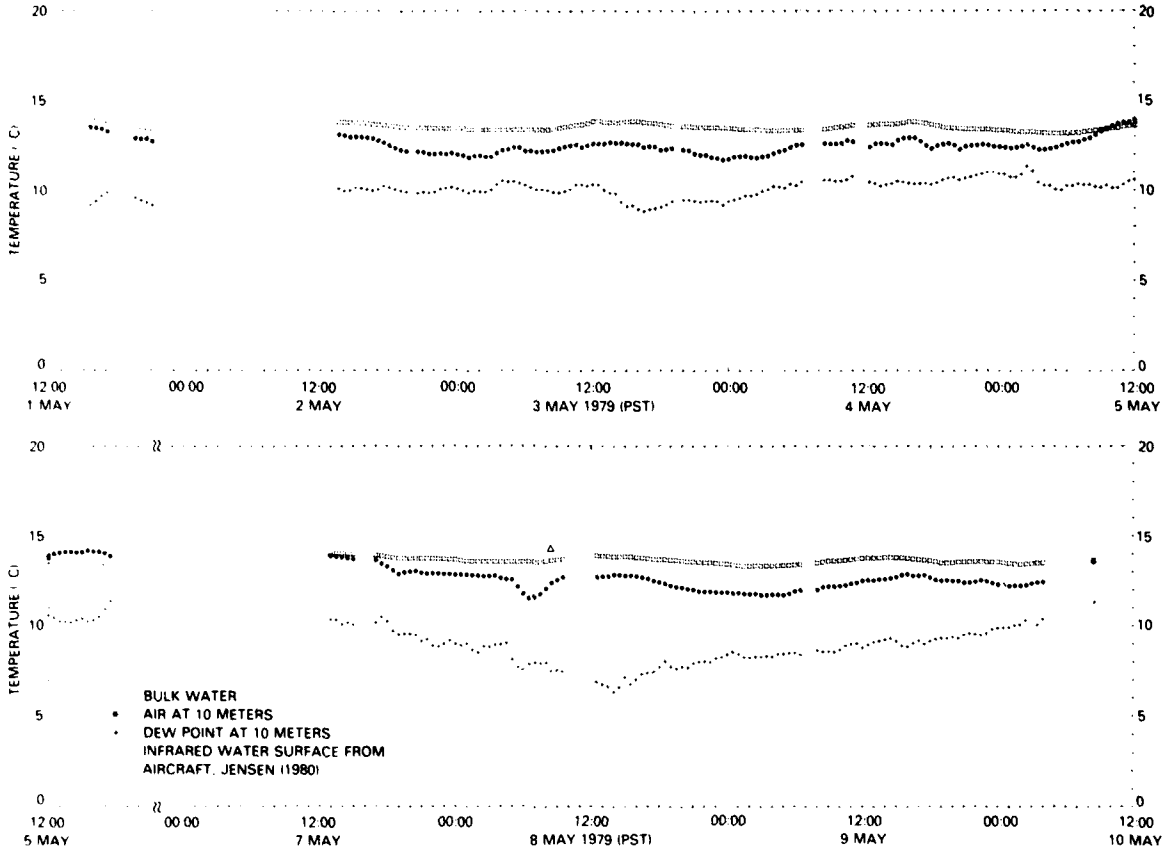

Fig. 17.1 — Thirty-minute-average bulk water, air, and dew point temperatures displayed as a function of time. The aircraft infrared-water-surface temperature reading was averaged over a 15-minute period and was taken at a 15-meter altitude over the bay ranging 0 to 4 km east-northeast of the tower site, along a path approximately perpendicular to the wind direction. The aircraft measurement is believed to be accurate to $\sim \pm 0.5$°C.

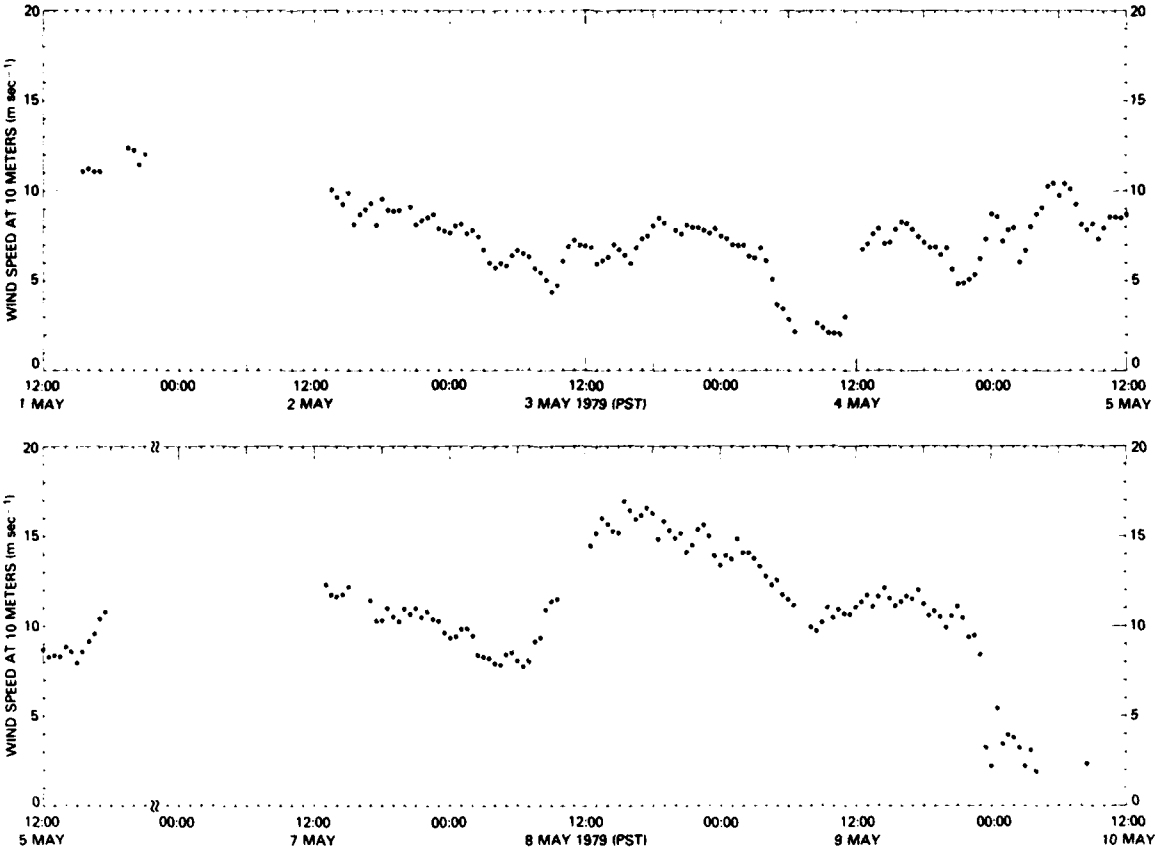

Fig. 17.2 — Thirty-minute-average wind speed at 10-meter height displayed as a function of time

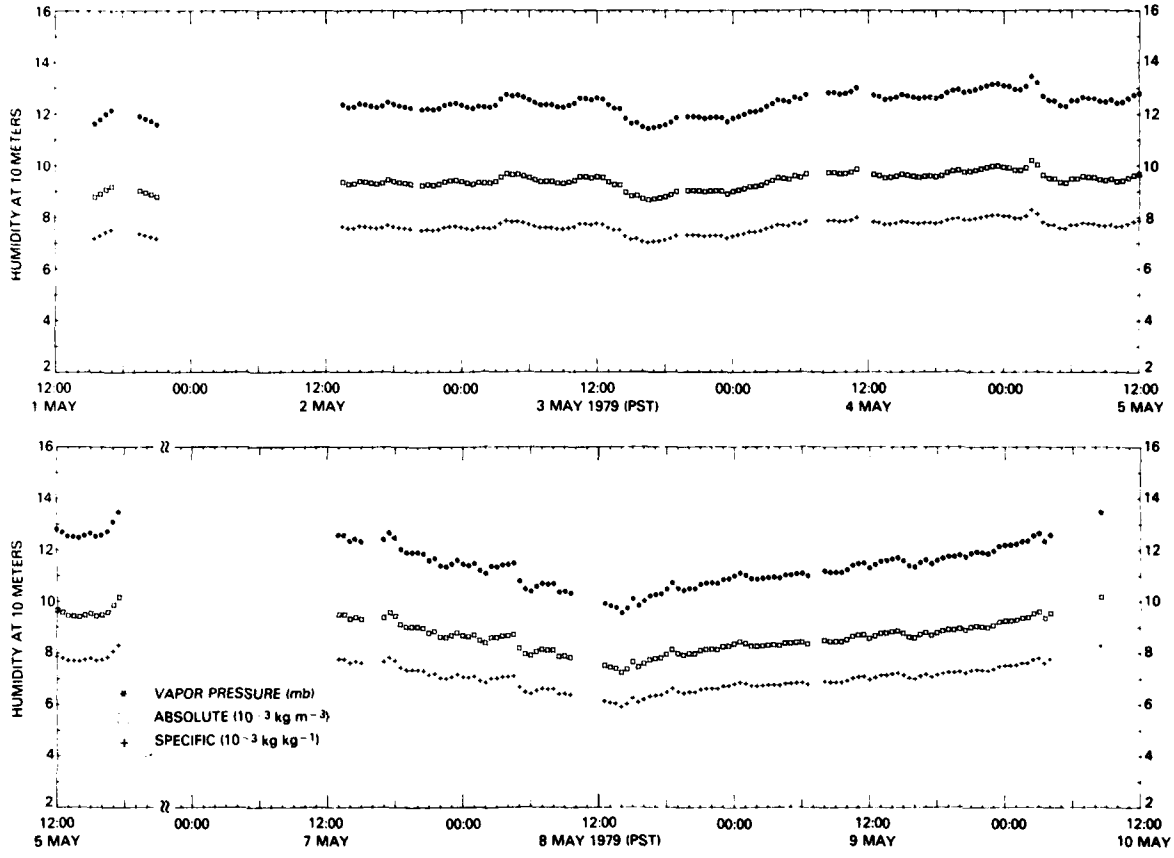

Fig. 17.3 — Thirty-minute-average vapor pressure, absolute humidity, and specific humidity at 10-meter height displayed as a function of time

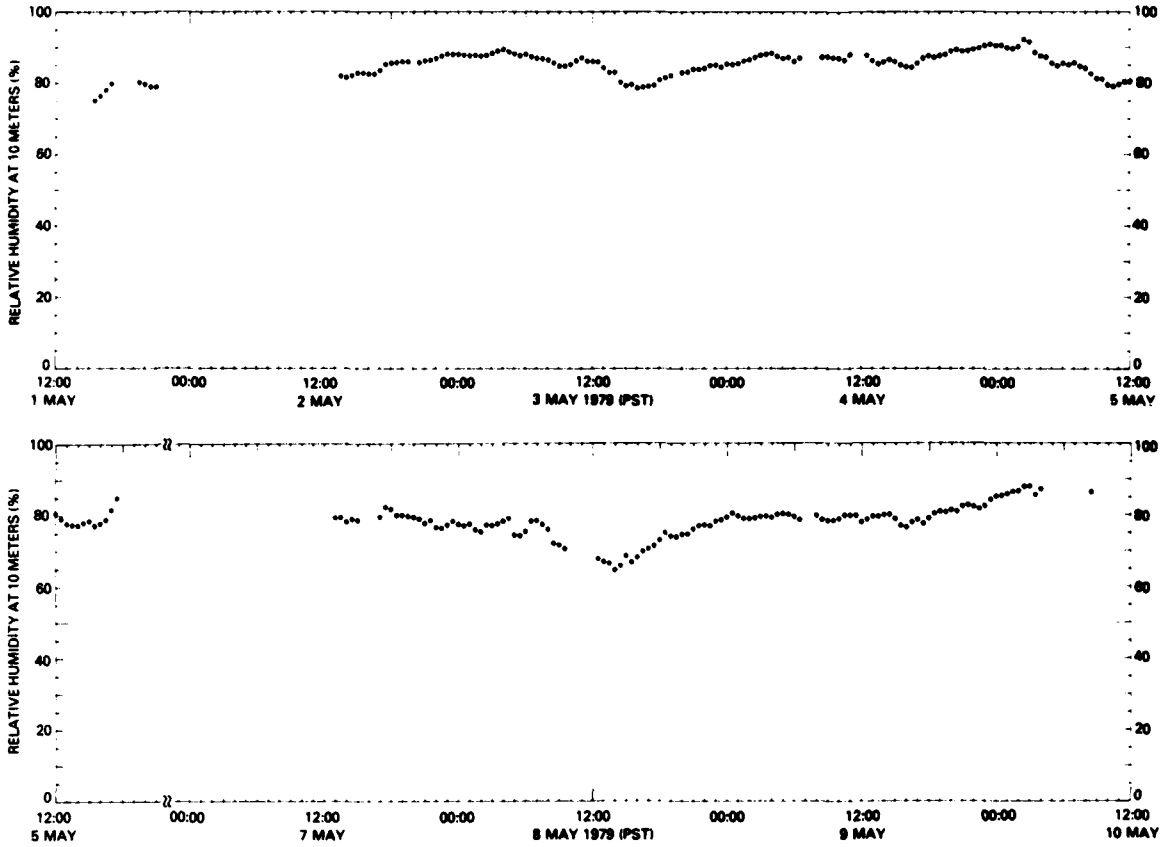

Fig. 17.4 — Thirty-minute-average relative humidity at 10-meter height displayed as a function of time

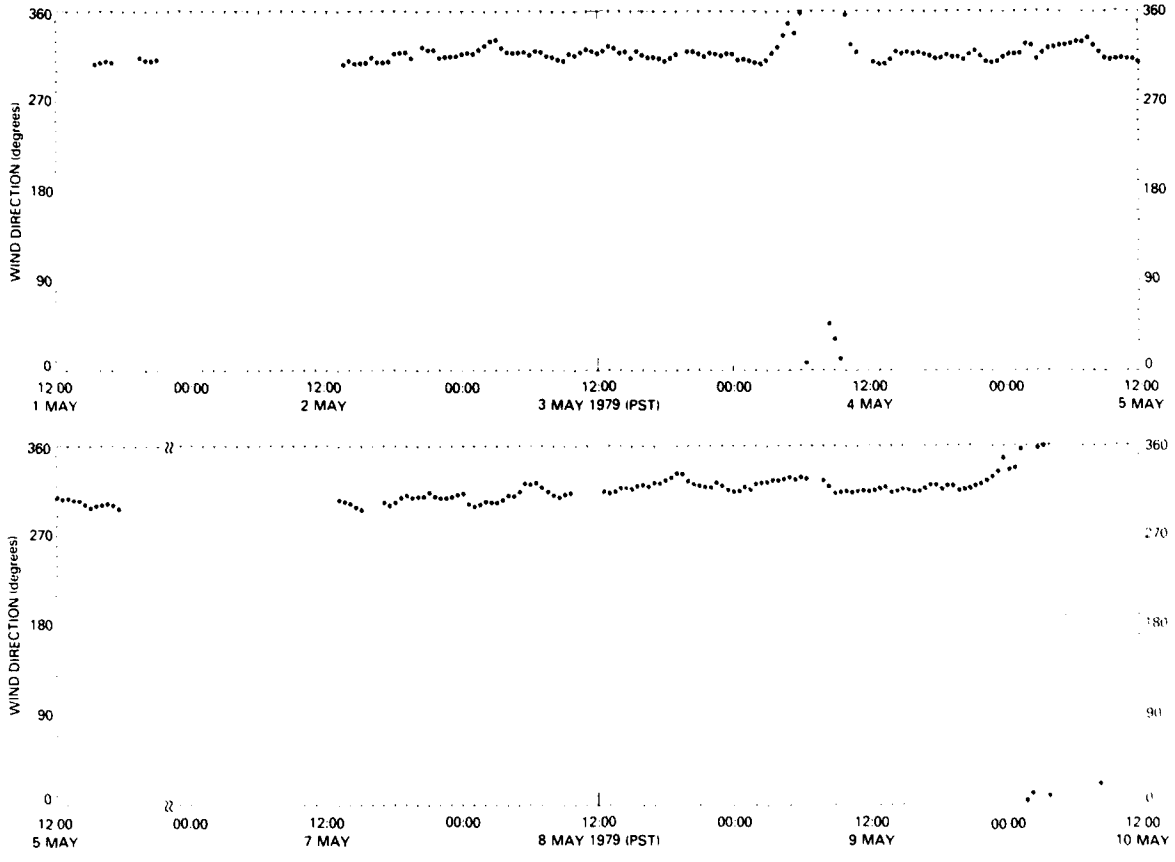

Fig. 17.5 — Thirty-minute-average wind direction (true) at 20.7-meter height displayed as a function of time

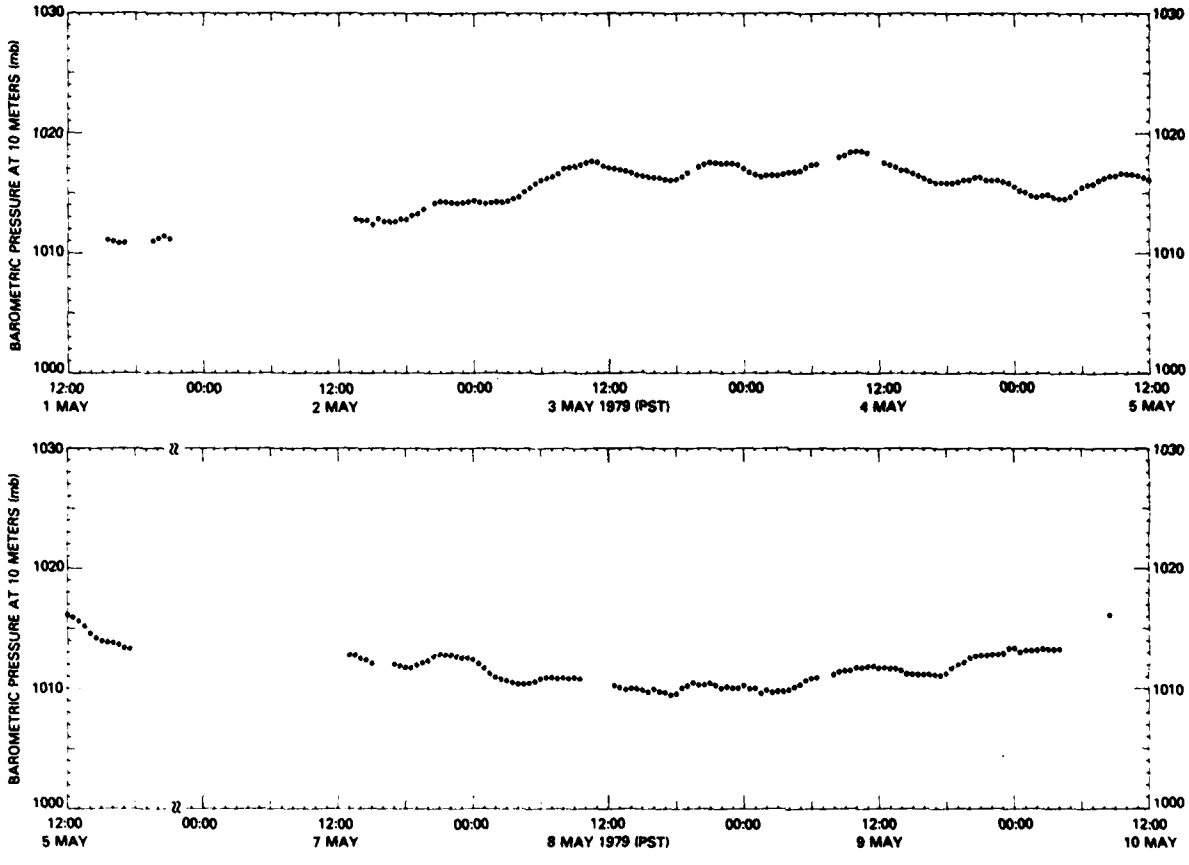

Fig. 17.6 — Thirty-minute-average barometric pressure at 10-meter height displayed as a function of time

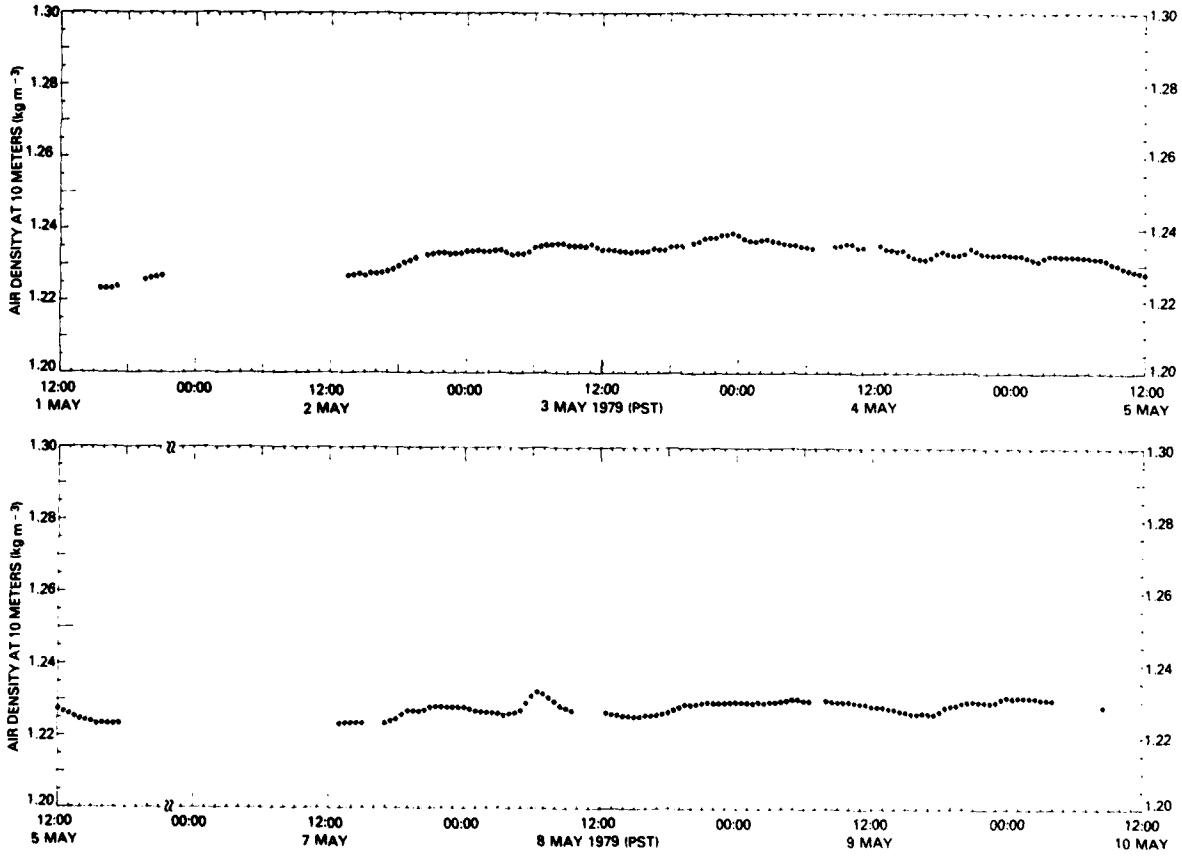

Fig. 17.7 — Thirty-minute-average density of moist air at 10-meter height displayed as a function of time

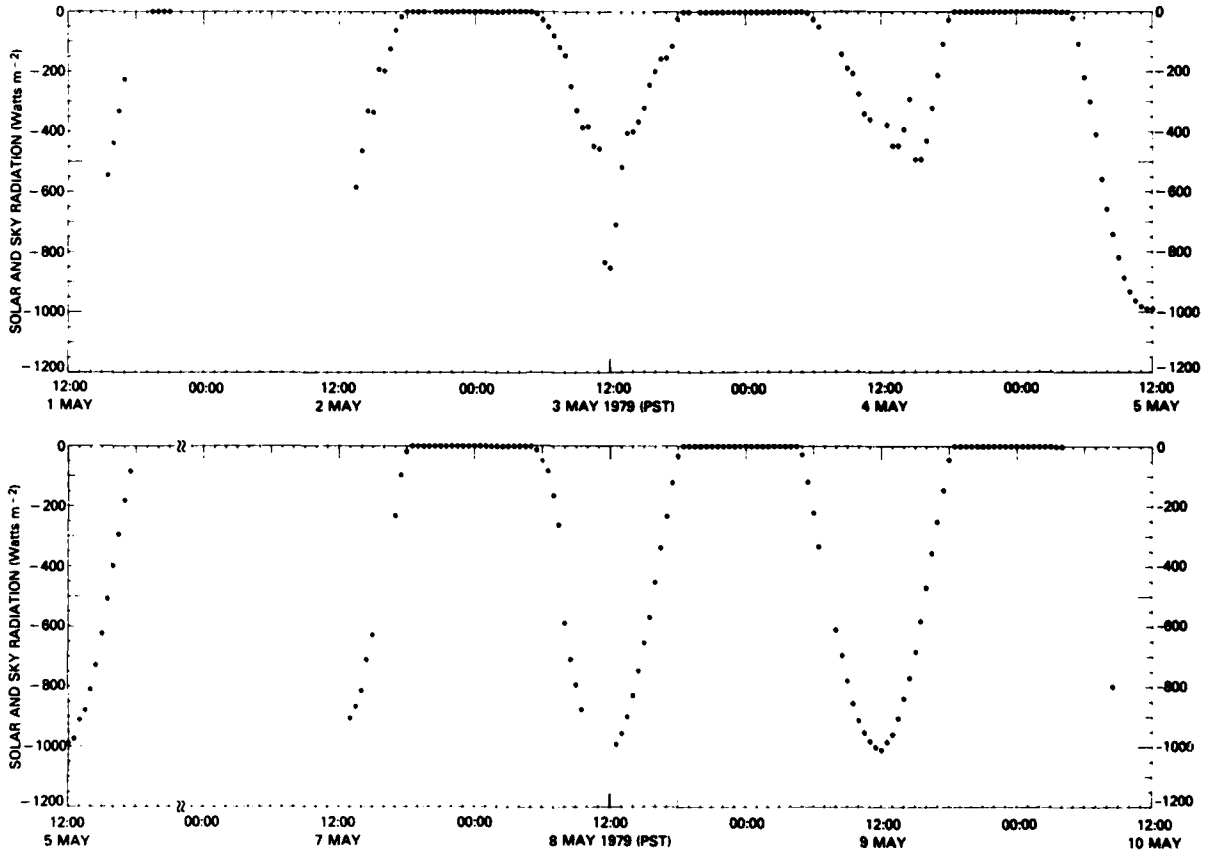

Fig. 17.8 — Thirty-minute-average incoming shortwave solar and sky radiation displayed as a function of time. Negative sign denotes downward direction. Sensor located at a height of 19.8 meters.

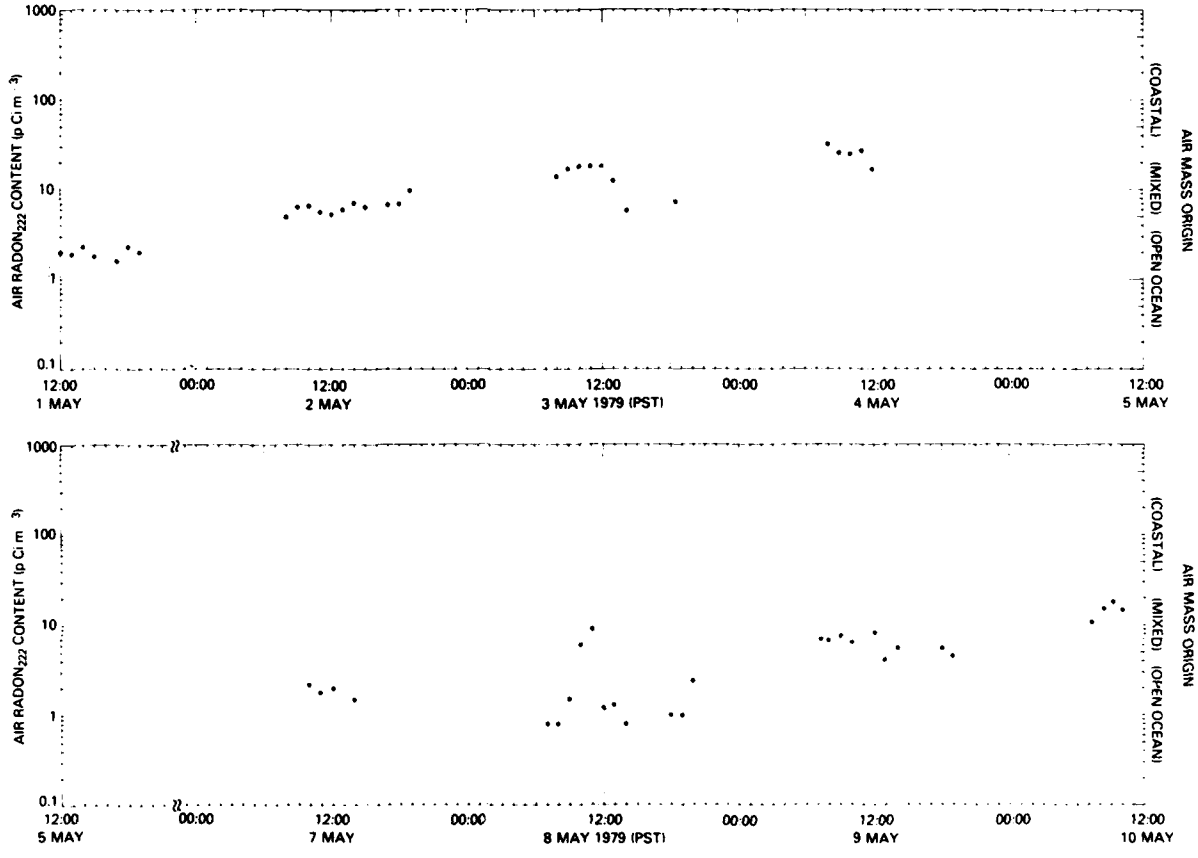

Fig. 17.9 — Twenty-minute-average radon content of the air at 5.3-meter height displayed as a function of time. Readings less than 5 pCi m^{-3} typically indicate an air mass of open ocean origin and readings greater then 50 pCi m^{-3} typically indicate an air mass of coastal origin. Data from Larson (1979).

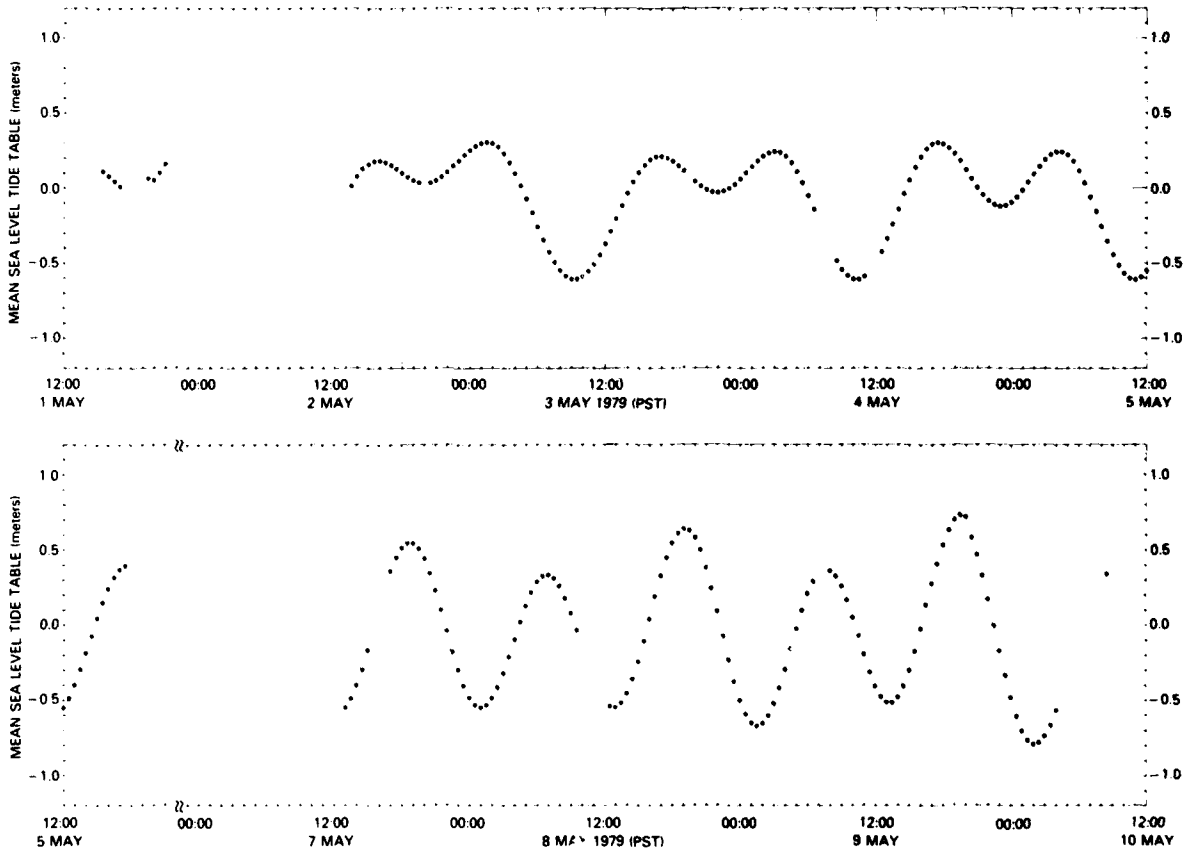

Fig. 17.10 — Thirty-minute-average tide height referenced to mean sea level and displayed as a function of time. Values were calculated from daily high- and low-tide table values in the manner prescribed by the National Ocean Survey (1979).

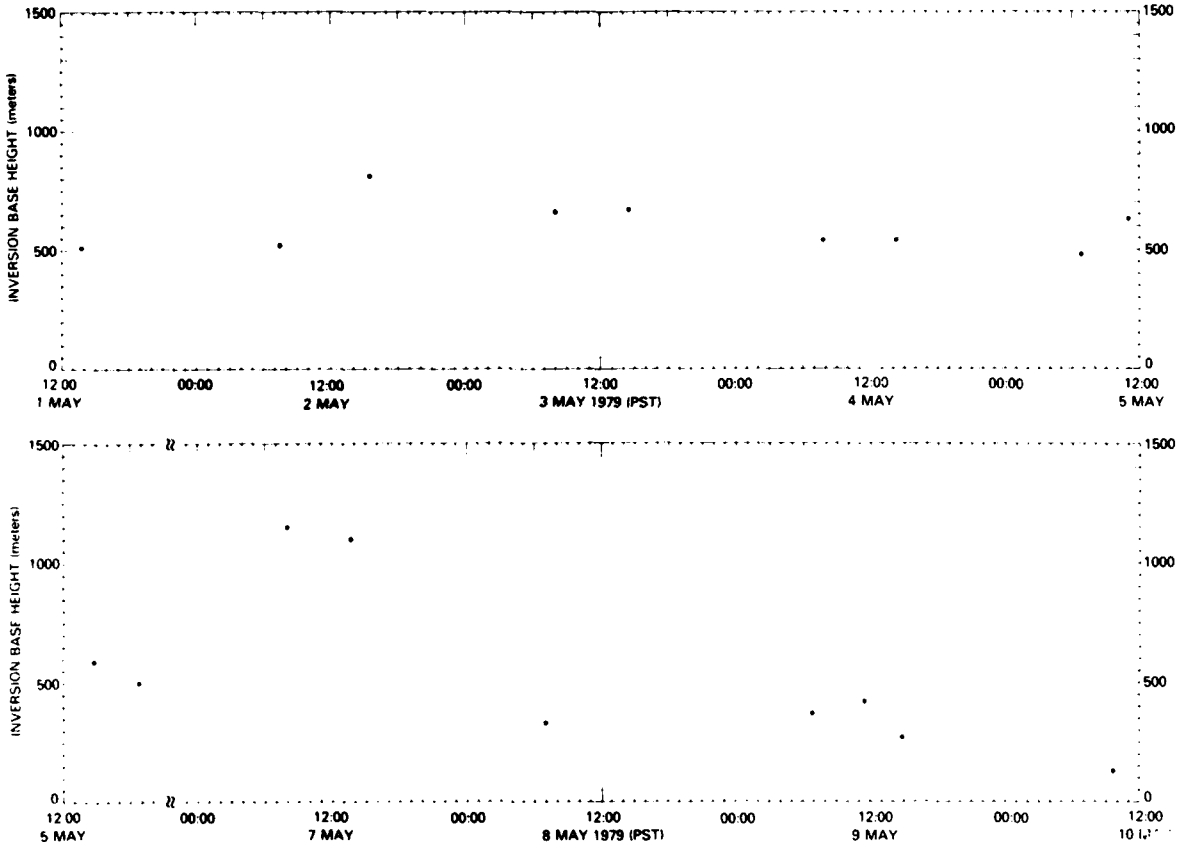

Fig. 17.11 — Inversion-base height observed by high-resolution radiosonde displayed as a function of time. The launch site for the radiosondes was located 2.1-km south-southeast and downwind of the tower site. Data courtesy of de Violini (1980).

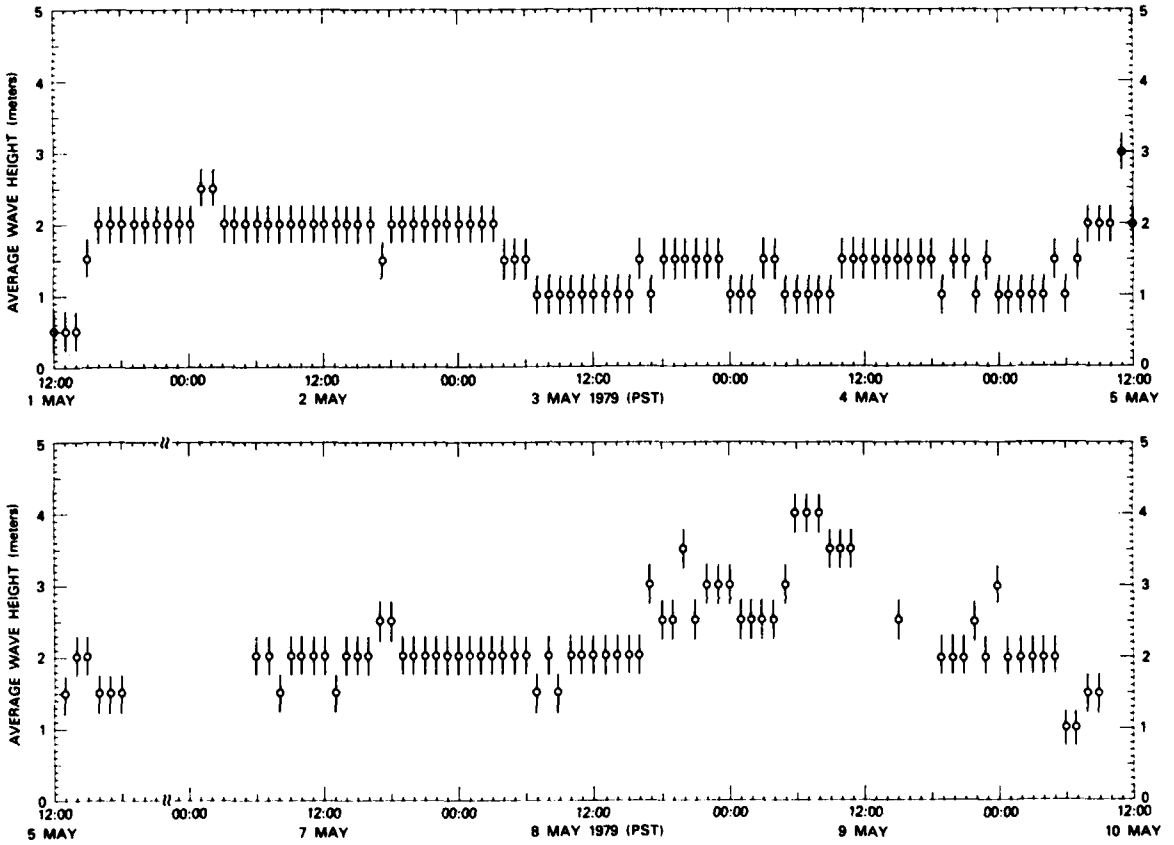

Fig. 17.12 — Three-minute-average wave height (recorded in increments of 0.5 meters) displayed as a function of time, as observed by a Waverider buoy located 15.6-km northwest and upwind of the island tower site in ~ 100 meter deep water. Data courtesy of de Violini (1980).

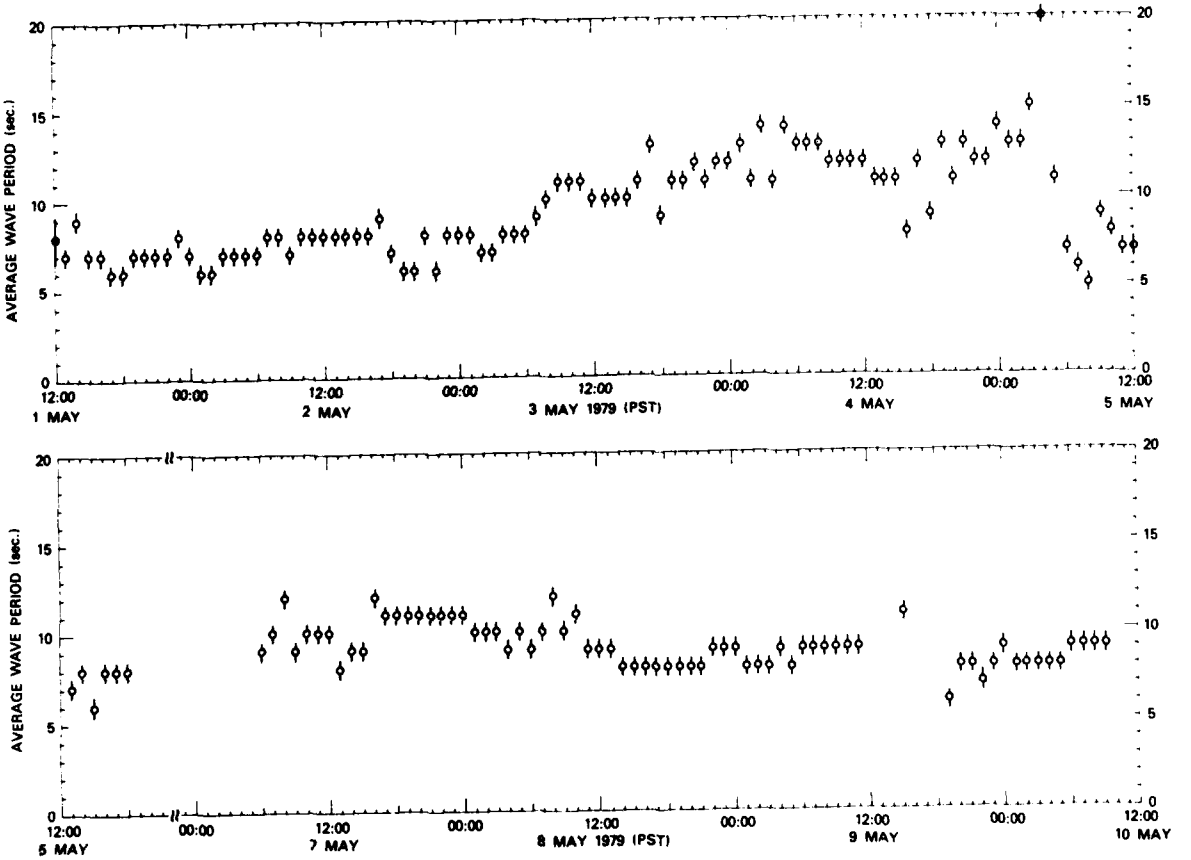

Fig. 17.13 — Three-minute-average wave period (recorded in increments of 1 second) displayed as a function of time, as observed by a Waverider buoy located 15.6-km northwest and upwind of the island tower site in ~ 100 meter deep water. Data courtesy of de Violini (1980).

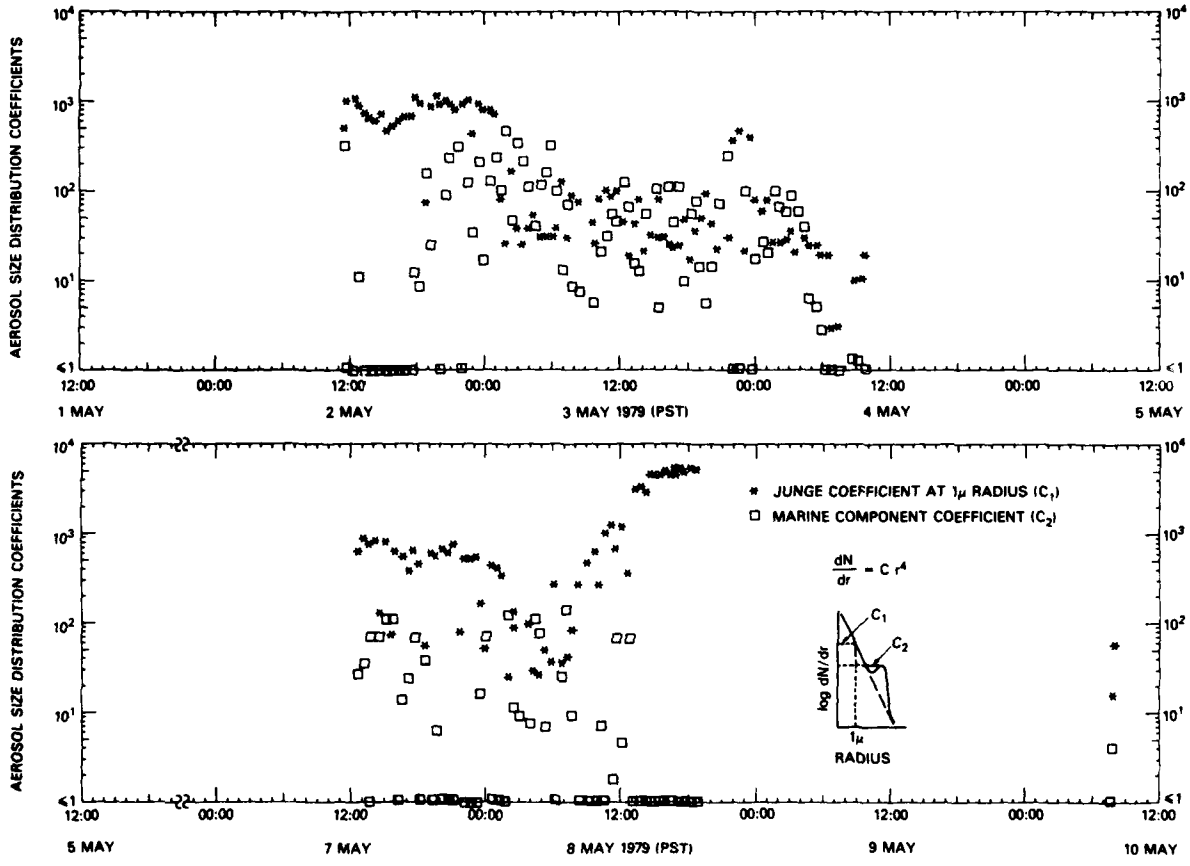

Fig. 17.14 — Thirty-minute-average aerosol size distribution at 14.4-meter height displayed as a function of time for particle sizes ranging from 0.3 to 14.0 μm radius. Data courtesy of Gathman & Jeck (1981).

18. Flux and Stability Observations

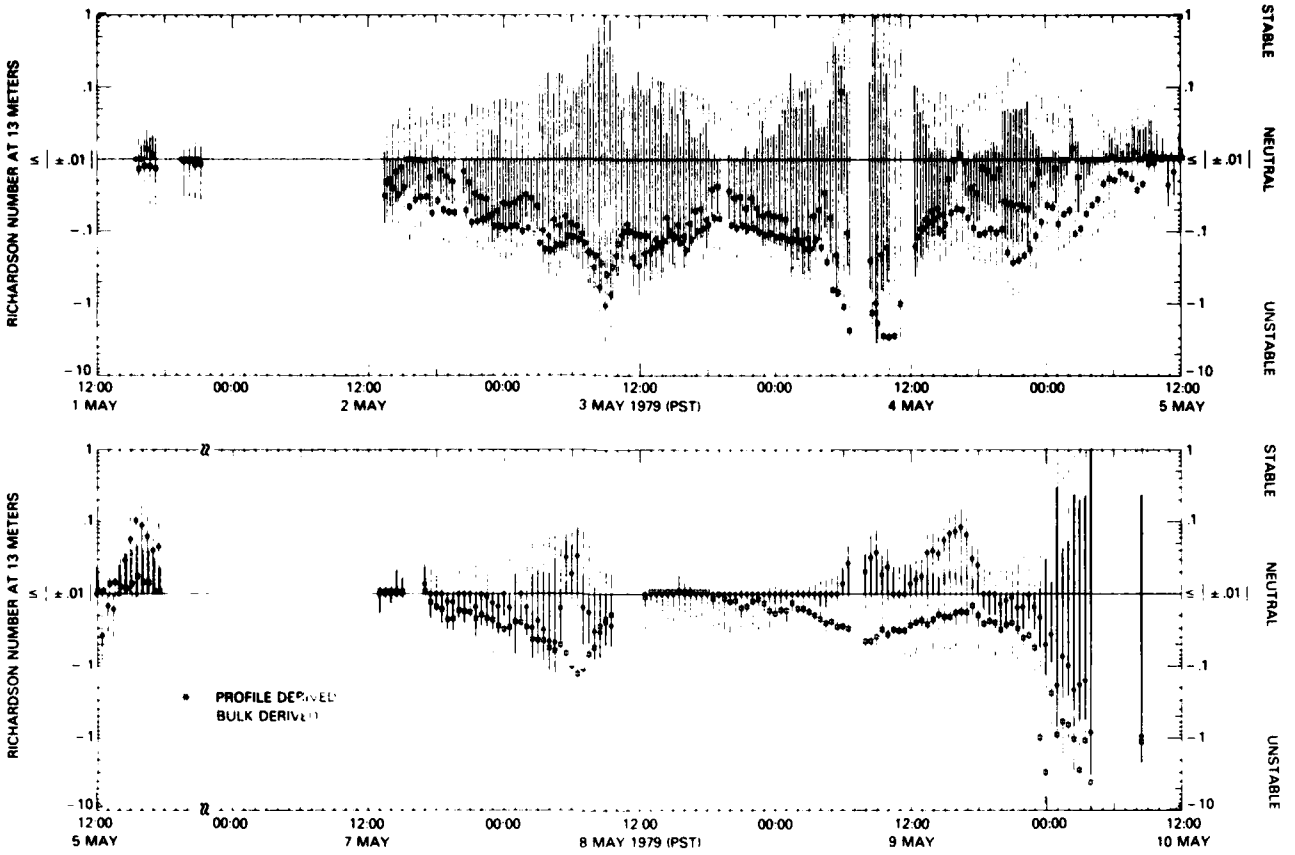

Fig. 18.1 — Thirty-minute-average profile- and bulk-derived gradient Richardson number stability at the geometric mean measurement height displayed with error bars as a function of time

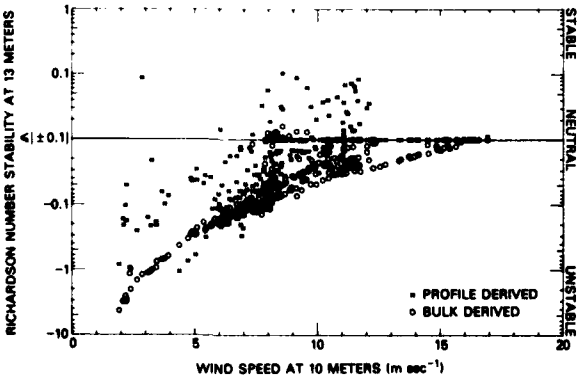

Fig. 18.2 — Profile- and bulk-derived gradient Richardson number stability at the geometric mean measurement height displayed as a function of 30-minute-average wind speed at 10-meter height, typical stability error values are ±139% and ±296%, respectively

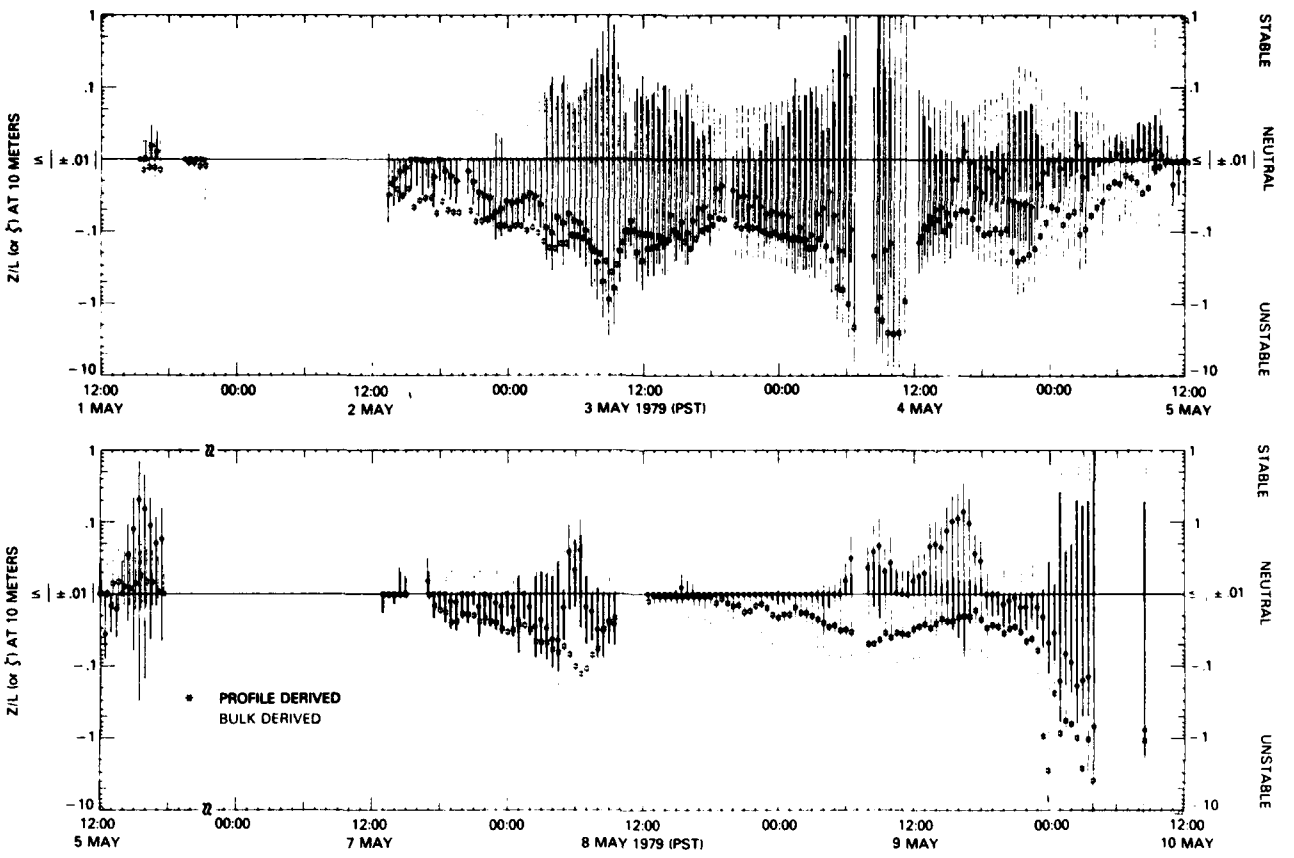

Fig. 18.3 — Thirty-minute-average profile- and bulk-derived Monin-Obukhov stability at 10-meter height displayed with error bars as a function of time

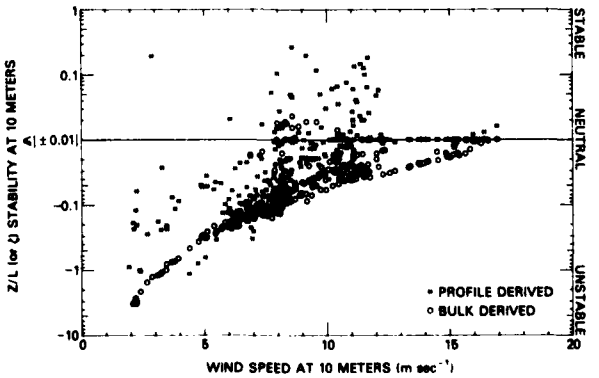

Fig. 18.4 — Profile- and bulk-derived Monin-Obukhov stability at 10-meter height displayed as a function of 30-minute-average wind speed at 10-meter height, typical stability error values are ±145% and ±297%, respectively

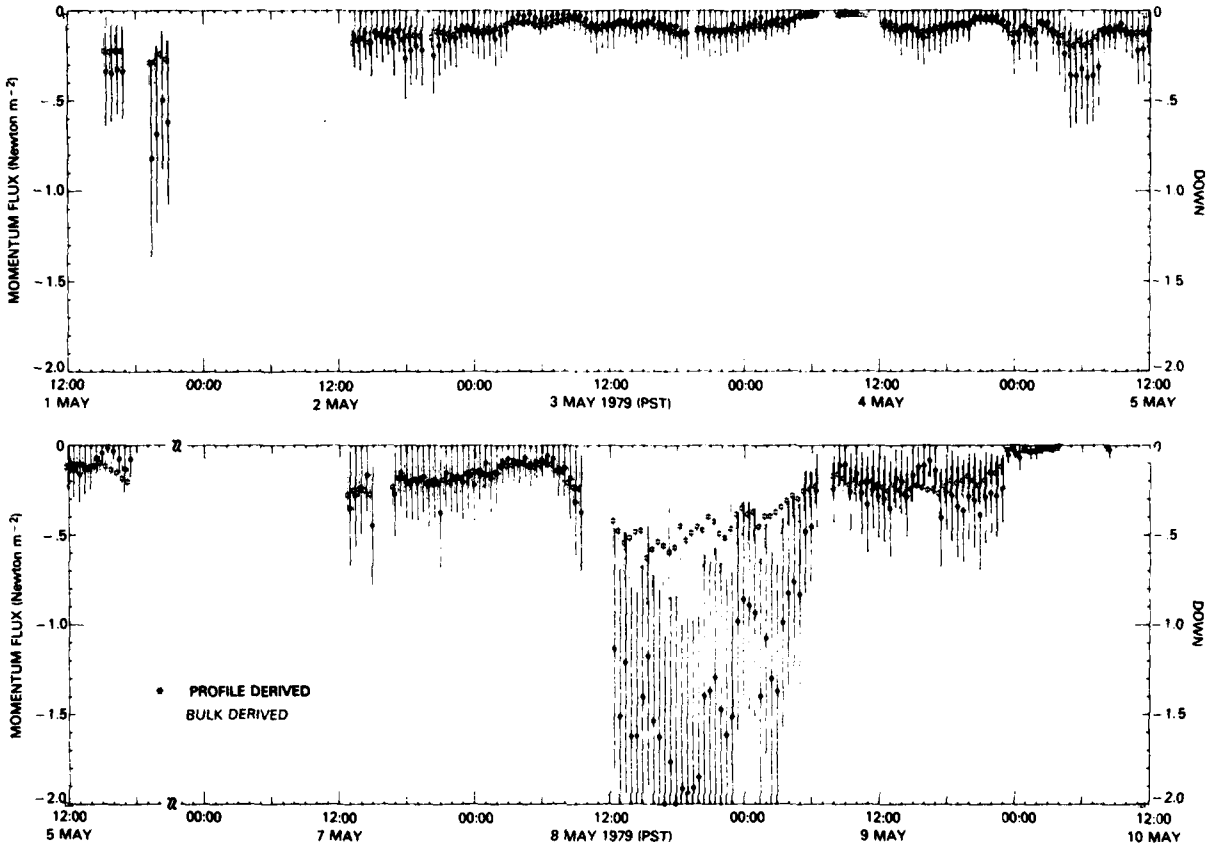

Fig. 18.5 — Thirty-minute-average profile- and bulk-derived momentum flux displayed with error bars as a function of time

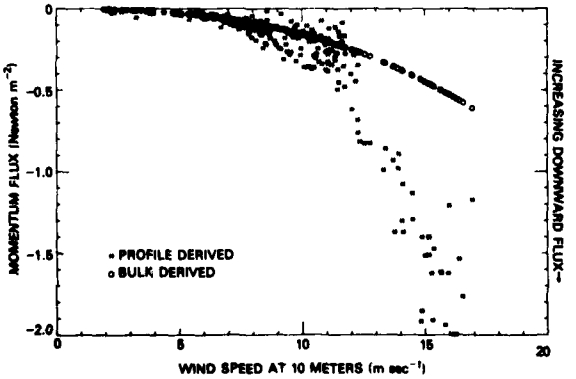

Fig. 18.6 — Profile- and bulk-derived momentum flux displayed as a function of 30-minute-average wind speed at 10-meter height, typical flux error values are ± 0.27 Nt. m^{-2} and ± 0.11 Nt. m^{-2}, respectively

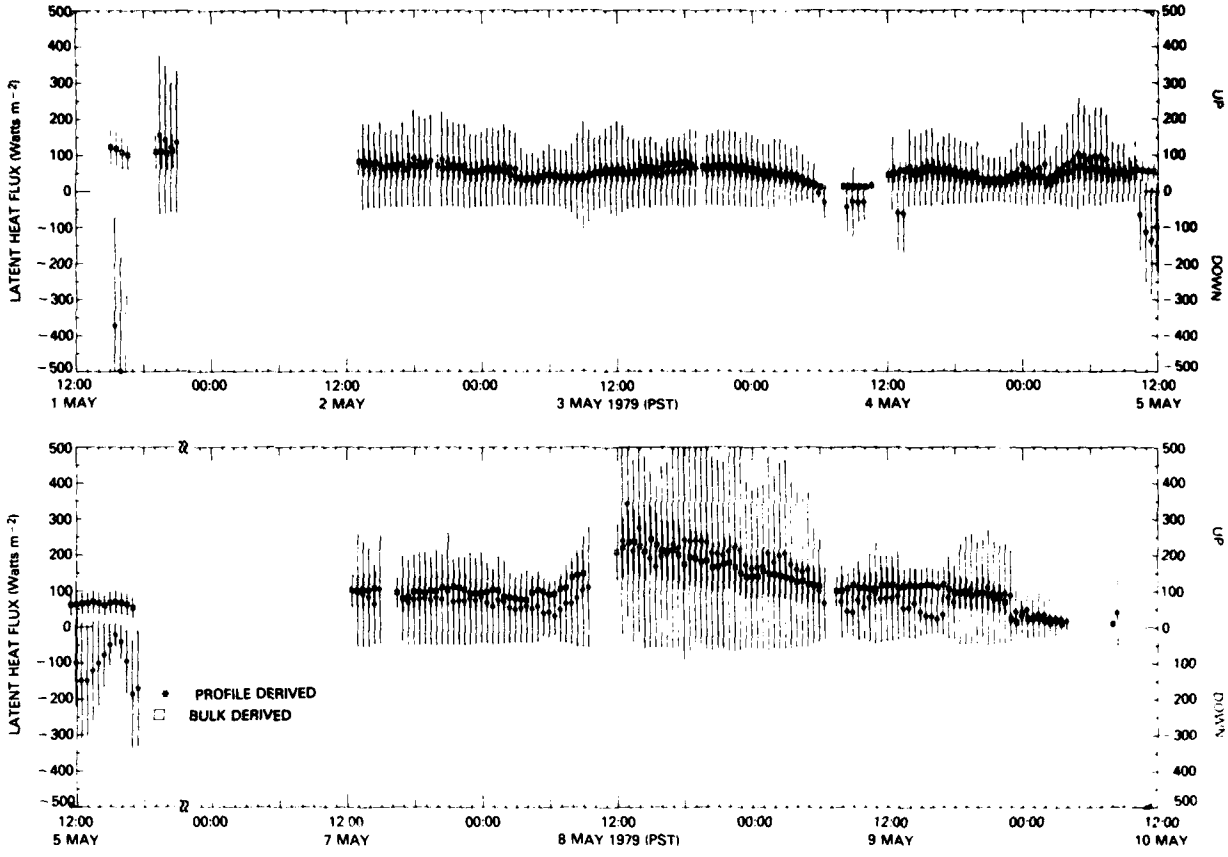

Fig. 18.7 — Thirty-minute-average profile- and bulk-derived latent heat flux displayed with error bars as a function of time

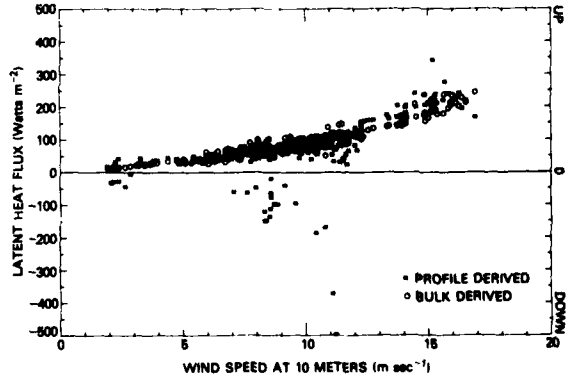

Fig. 18.8 — Profile- and bulk-derived latent heat flux displayed as a function of 30-minute-average wind speed at 10-meter height, typical flux error values are ±118 Watts m^{-2} and ±32 Watts m^{-2}, respectively

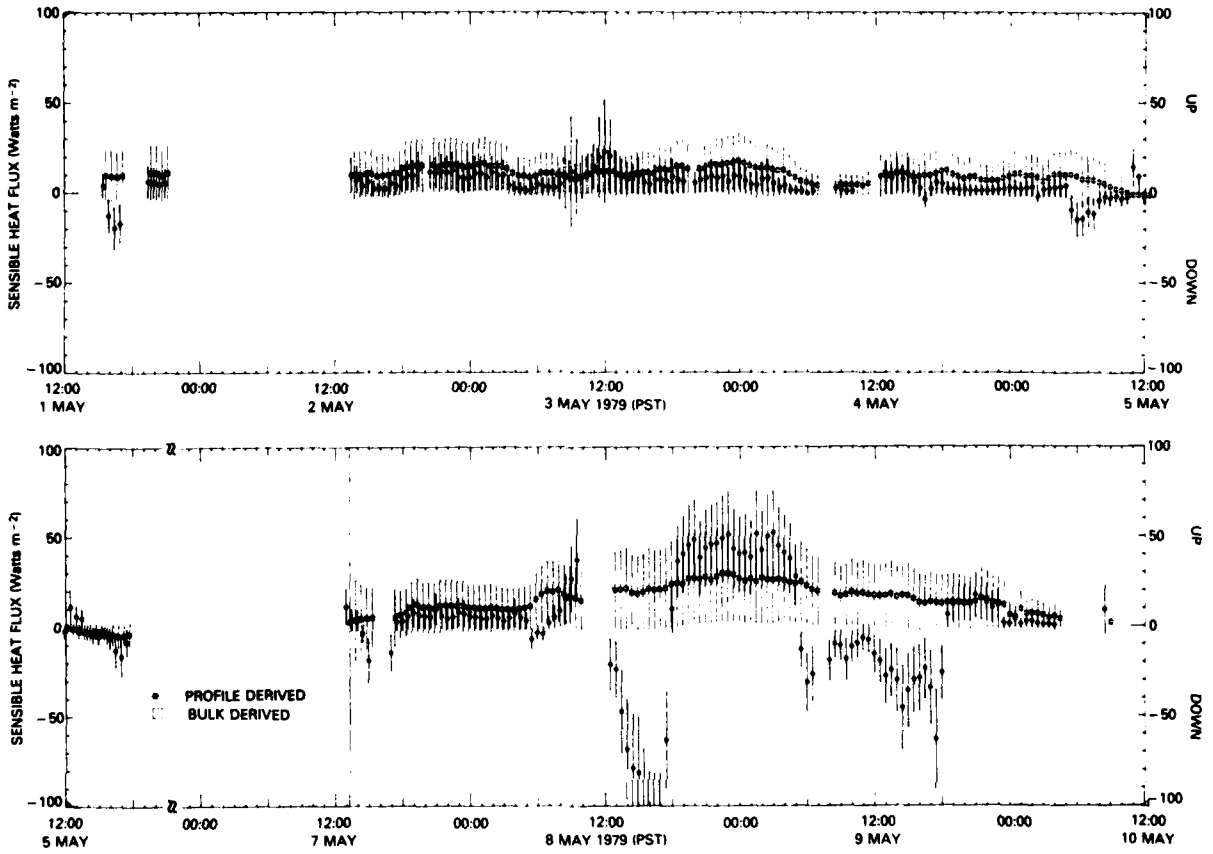

Fig. 18.9 — Thirty-minute-average profile- and bulk-derived sensible heat flux displayed with error bars as a function of time

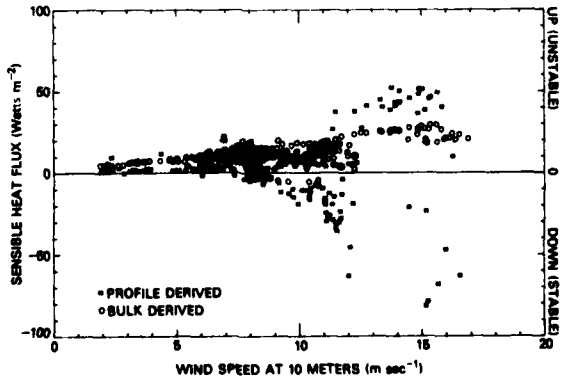

Fig. 18.10 — Profile- and bulk-derived sensible heat flux displayed as a function of 30-minute-average wind speed at ten-meter height, typical flux error values are ±8 Watts m^{-2} and ±16 Watts m^{-2}, respectively

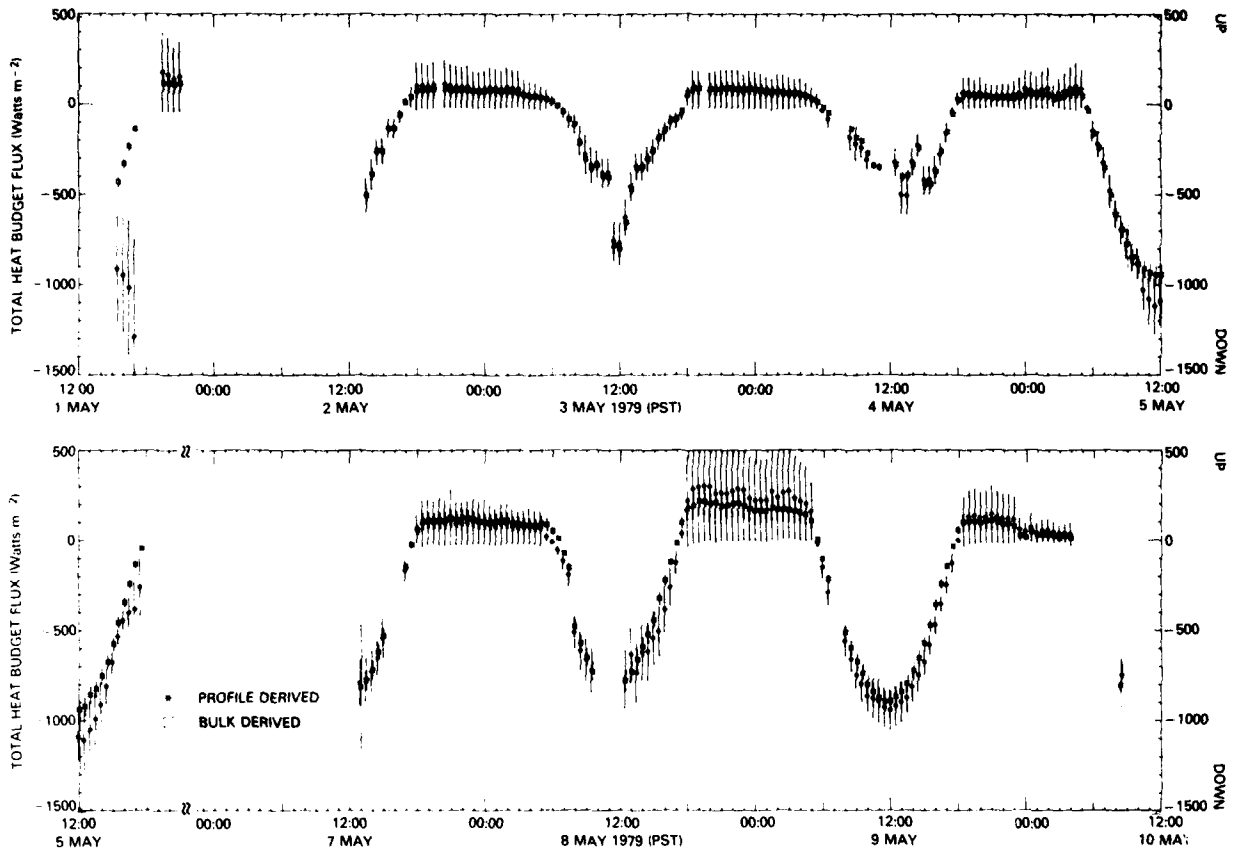

Fig. 18.11 — Thirty-minute-average profile- and bulk-derived total heat budget flux displayed with error bars as a function of time

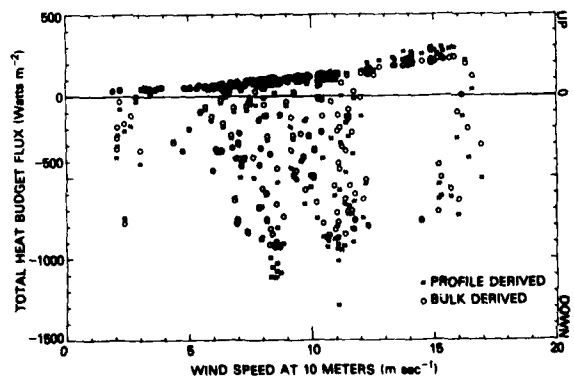

Fig. 18.12 — Profile- and bulk-derived total heat budget flux displayed as a function of 30-minute-average wind speed at 10-meter height, typical flux error values are ±134 Watts m^{-2} and ±56 Watts m^{-2}, respectively

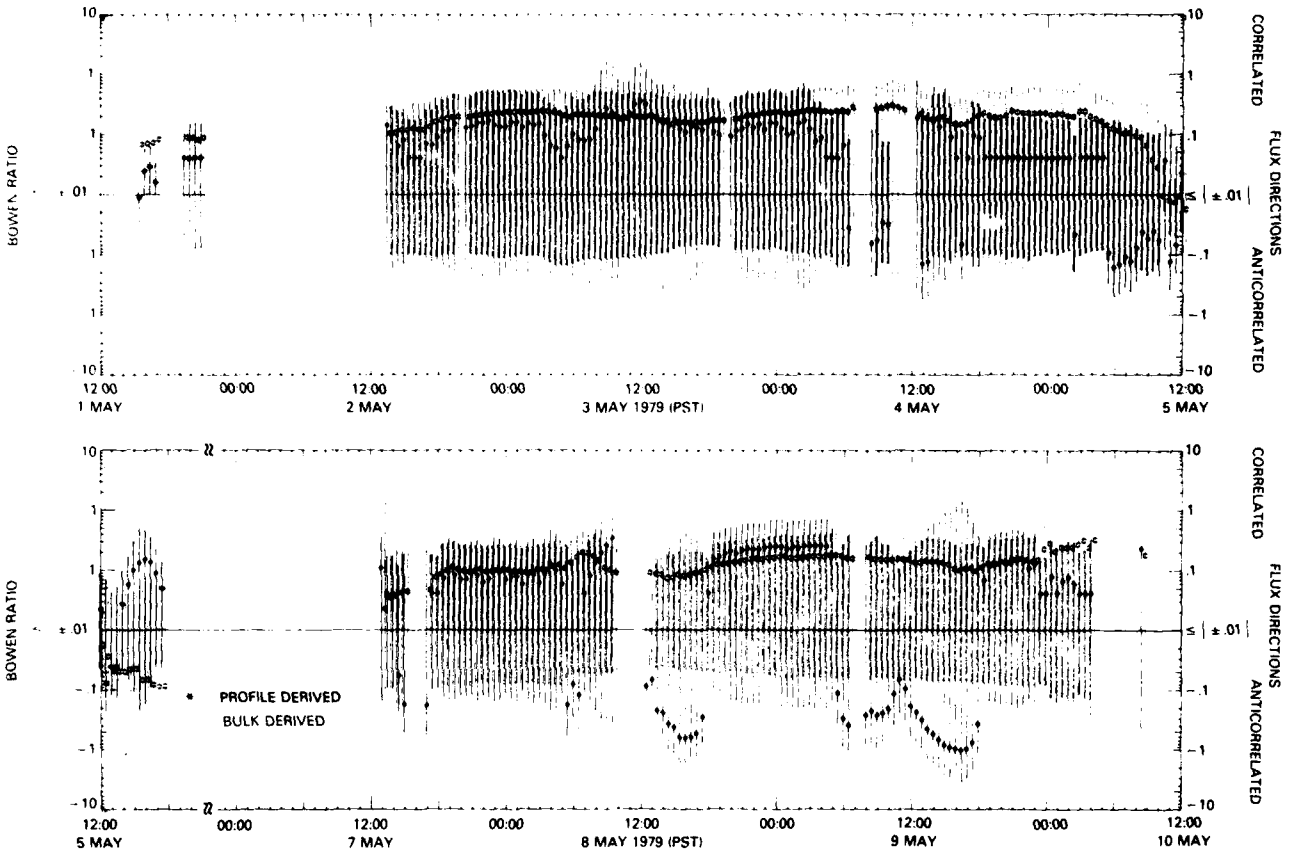

Fig. 18.13 — Thirty-minute-average profile- and bulk-derived Bowen ratio displayed with error bars as a function of time

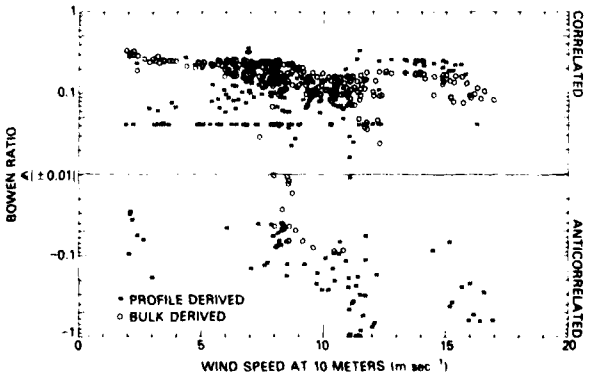

Fig. 18.14 — Profile- and bulk-derived Bowen ratio displayed as a function of 30-minute-average wind speed at 10-meter height, typical ratio error values are ±0.25 and ±0.24, respectively

19. Drag Coefficient and Roughness Length Observations

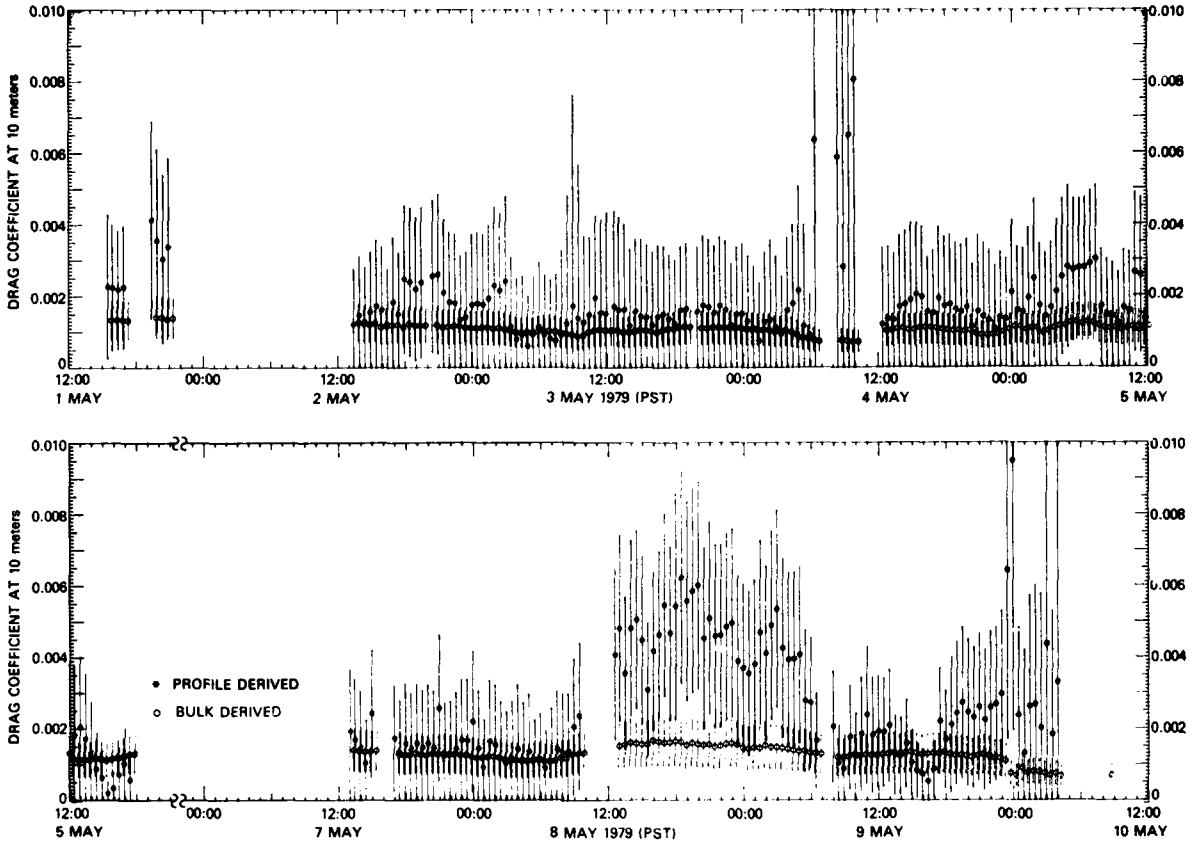

Fig. 19.1 — Thirty-minute-average profile- and bulk-derived neutral drag coefficient for 10-meter height displayed with error bars as a function of time, bulk drag coefficient via Smith & Banke (1975)

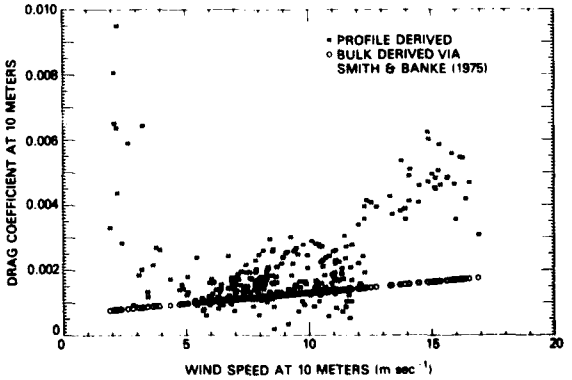

Fig. 19.2 — Profile- and bulk-derived neutral drag coefficient for 10-meter height displayed as a function of 30-minute-average wind speed at 10-meter height, typical drag error values are $\pm 2.0 \times 10^{-3}$ and $\pm 0.7 \times 10^{-3}$, respectively, bulk drag coefficient via Smith & Banke (1975)

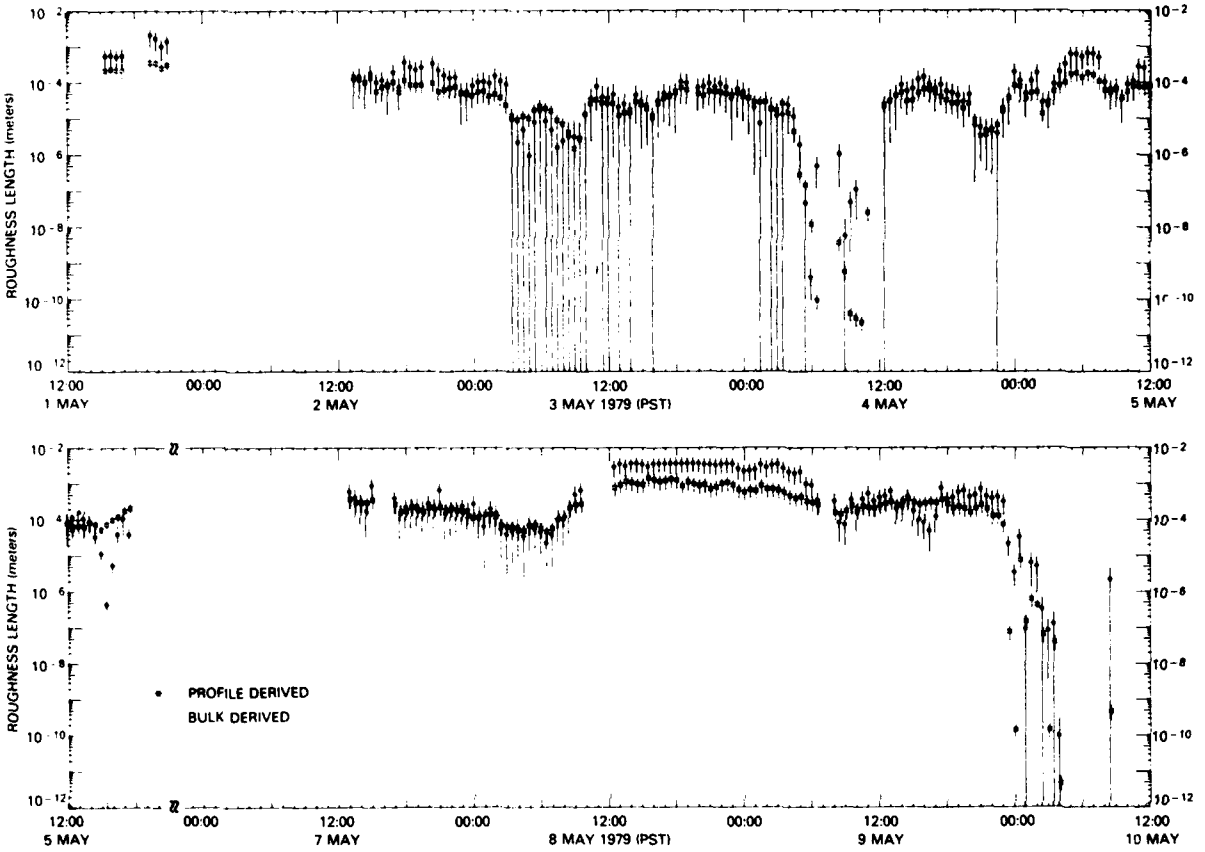

Fig. 19.3 — Thirty-minute-average profile- and bulk-derived roughness length computed via Eq. (14.2) displayed with error bars as a function of time

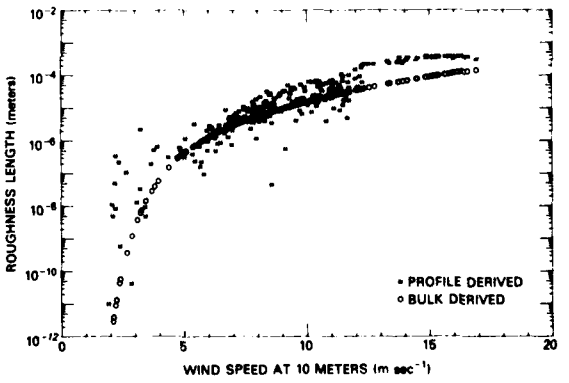

Fig. 19.4 — Profile- and bulk-derived roughness length computed via Eq. (14.2) displayed as a function of 30-minute-average wind speed at 10-meter height, typical roughness error values are $\pm 3.0 \times 10^{-4}$m and $\pm 1.6 \times 10^{-4}$m, respectively

20. Friction Velocity and Other Scaling Parameter Observations

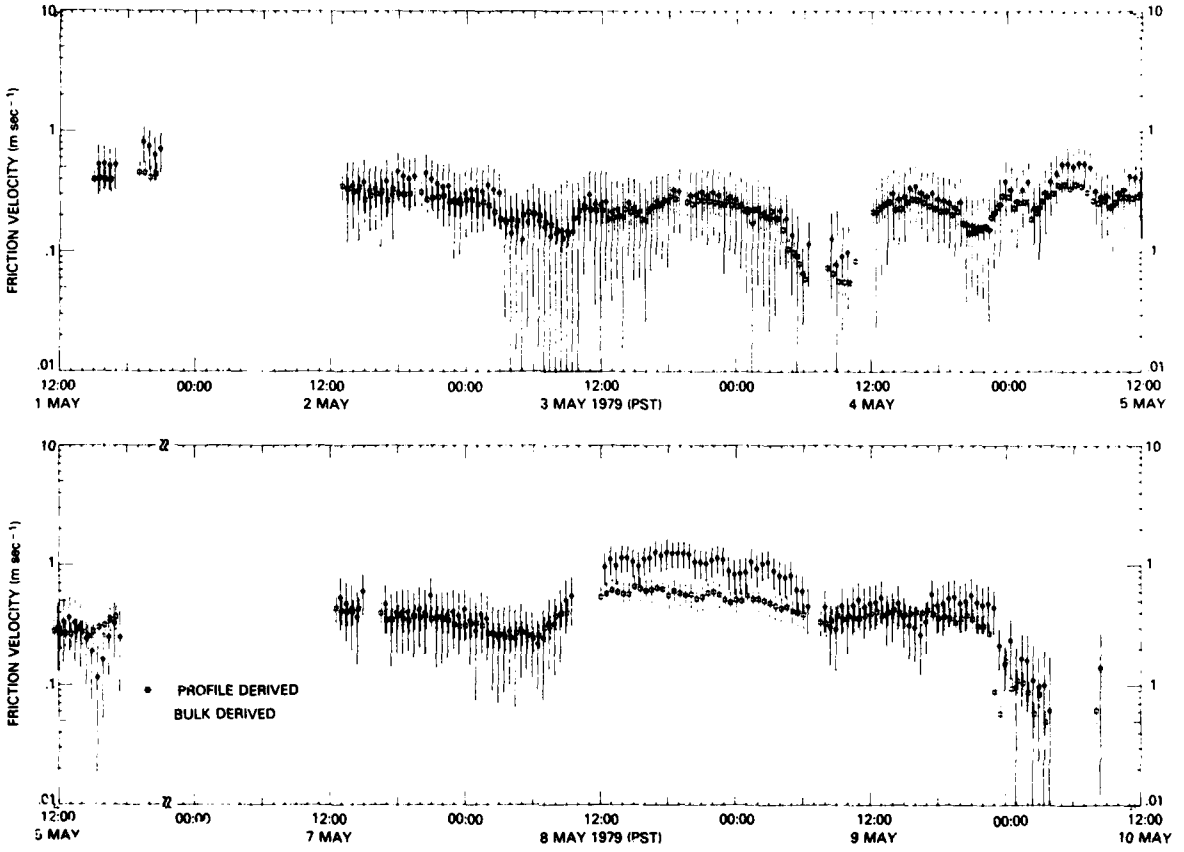

Fig. 20.1 — Thirty-minute-average profile- and bulk-derived friction velocity displayed with error bars as a function of time

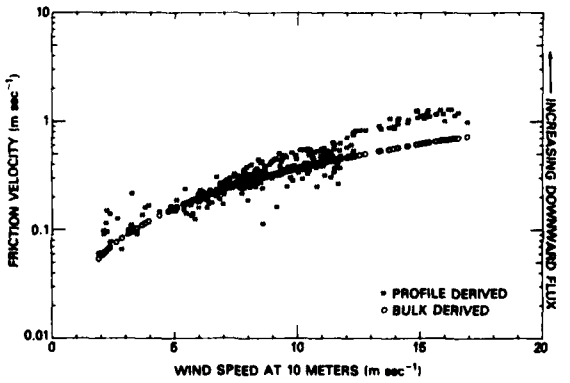

Fig. 20.2 — Profile- and bulk-derived friction velocity displayed as a function of 30-minute-average wind speed at 10-meters height, typical friction velocity error values are ± 0.21 m sec^{-1} and ± 0.08 m sec^{-1} respectively

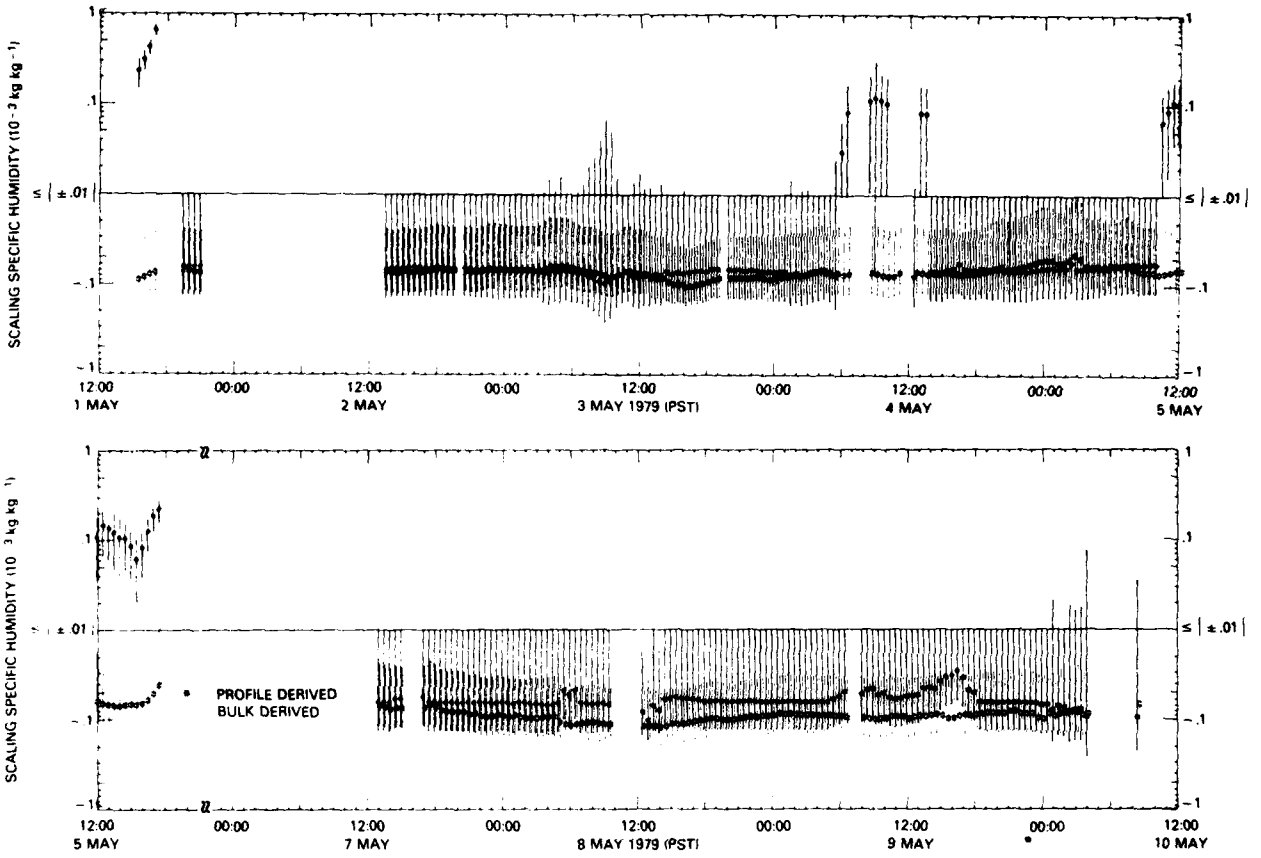

Fig. 20.3 — Thirty-minute-average profile- and bulk-derived scaling specific humidity displayed with error bars as a function of time

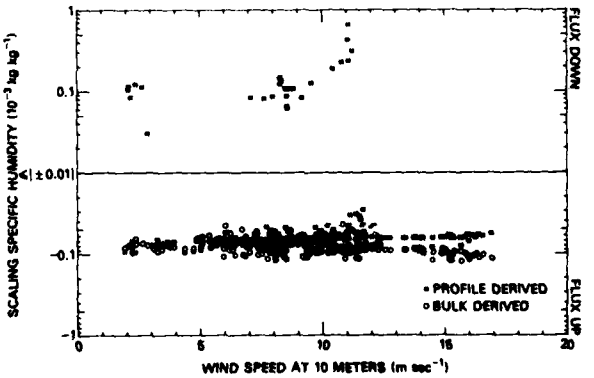

Fig. 20.4 — Profile- and bulk-derived scaling specific humidity displayed as a function of 30-minute-average wind speed at 10-meter height, typical scaling error values are $\pm 0.067 \times 10^{-3}$ kg kg^{-1} and $\pm 0.042 \times 10^{-3}$ kg kg^{-1}, respectively

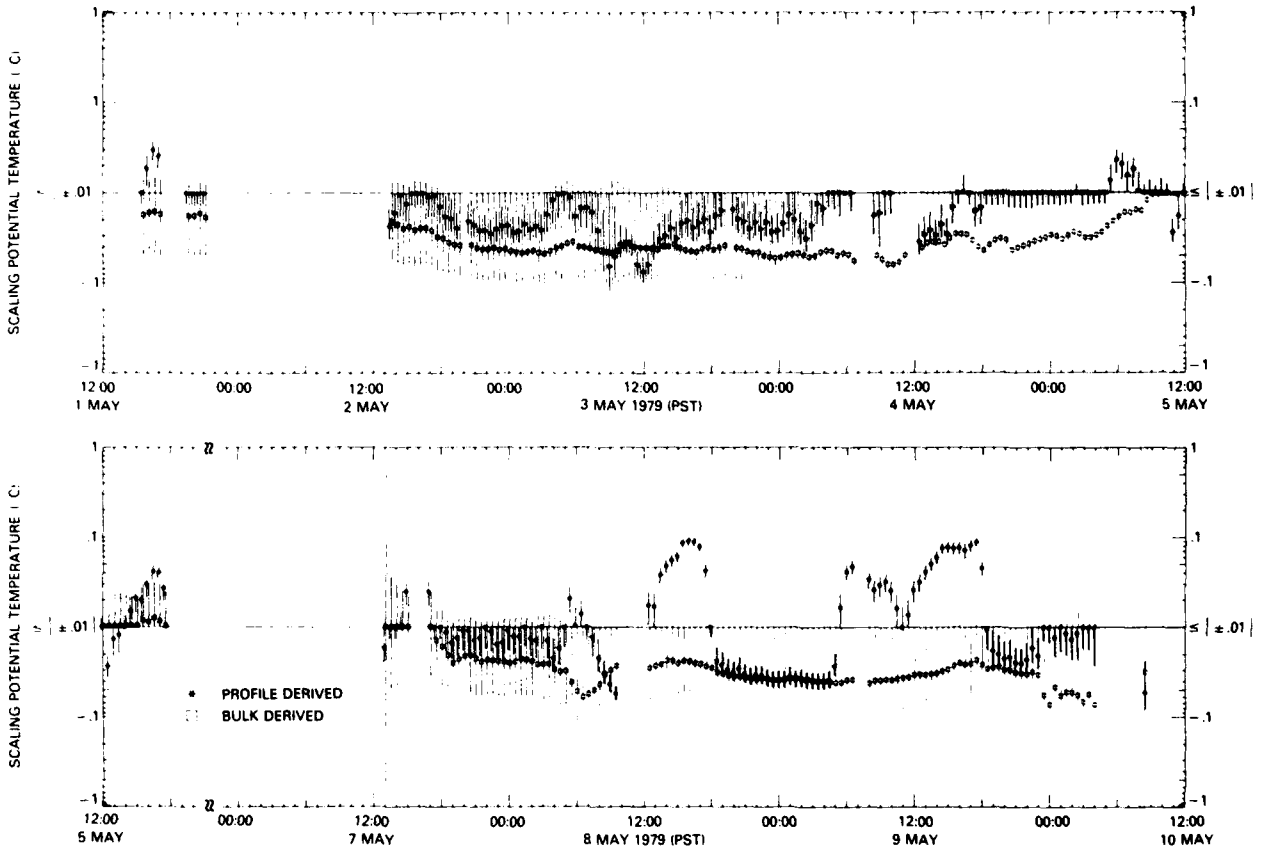

Fig. 20.5 — Thirty-minute-average profile- and bulk-derived scaling potential temperature displayed with error bars as a function of time

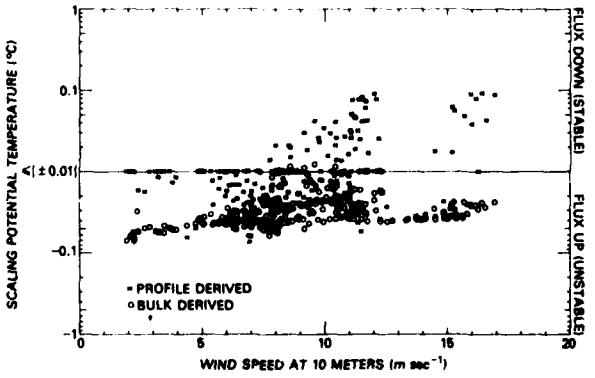

Fig. 20.6 — Profile- and bulk-derived scaling potential temperature displayed as a function of 30-minute-average wind speed at 10-meter height, typical scaling error values are ±0.003°C and ±0.012°C, respectively

21. Tests for Island Influence in the Flux and Stability Data

In the determination of the minimum measurement height above the beach (Section 6) it was contended that if the flux and stability measurements were made above 9 meters that they would be sufficiently high in altitude and close enough to the water to be outside of the internal boundary layer formed by the island. From that, it was inferred that these measurements would be unaffected by the island-generated surf, spray, and breaking waves. Further, a method was devised (Section 11) which purported to correct the acceleration induced in the marine wind profile by the beach escarpment located immediately upwind of the measurement tower. An essential part of any data analysis would be devising a method to test these hypotheses. The determination of whether the aerosol measurements, made at a height of 14.4 meters, were unaffected by the locally generated surf and spray is beyond the scope of the present report.

Obviously, the best procedure for an independent verification would have been to take, simultaneously with these measurements, the identical type of measurements far enough upwind of the island to be unaffected by its influence. However, as is usually the case with experiments of this type, reliable upwind measurements are rarely available. When measurements are available, they too are often suspected of being distorted by the observation platform as in the case of the *Acania* data reported in Section 5. One is rapidly led to the conclusion that there is a sort of Heisenberg uncertainty principle in marine micrometeorology—the results one obtains depend to a large extent upon the measurement technique employed and the platform from which the observations are made.

One test which could be used to help alleviate this inherent dilemma would be to measure the difference between the profile-derived and bulk-derived flux values taken from the island and compare the results with similar profile-bulk comparisons made with data acquired from other types of platforms. From this, it could be determined if the island distorted the data, on the average, to a greater or lesser extent than did the other platforms. This "differential" approach was particularly appealing because, although much of the data input into the two techniques was from the same instrumentation, the computational procedures and the underlying assumptions are sufficiently different that, for all intent and purposes, the two techniques could be considered independent determinations of the same parameters. For example, if the lowest-level wind-speed sensor observed a 4% increase in wind speed due to the presence of the beach escarpment (a typical value suggested in Section 11) and was uncorrected, the profile-derived momentum flux would be 55% too low and the bulk-derived flux would be 8% too high, an almost sevenfold difference in magnitude. Such a comparison is presented in Table 21.1.

From the Table 21.1 it can be concluded that, under similar wind-speed conditions, the measurements made from the San Nicolas Island tower were, on the average, no worse than those previously taken from other ocean platforms. Additionally, the table would tend to support the arguments that employing a profile-measurement system of more than two or three levels (Section 8) or stability-dependent bulk coefficients (Section 15) would yield little in the way of improved flux measurement accuracy. Consider, for example, the comparison of Liu et al. (1979), which compares a complex stability-dependent bulk-coefficient method with a four-level profile measurement, and this experiment, which compares a simple fixed valued bulk-coefficient method with a two-level profile measurement. To place the results of Table 21.1 in perspective, it should be noted that Friehe & Gibson (1978) have estimated that the typical rms differences between eddy-correlation (or direct) and bulk flux determinations to be 0.025 Nt. m^{-2},

Table 21.1 — Comparison of the (Approximate) RMS Differences Observed Between Profile and Bulk Determinations of Fluxes from Different Types of Platforms Over the Ocean for Wind Speeds Ranging from Approximately 2 to 10 m sec^{-1}.

Source	Experiment[e] (name or location)	Types of Comparison		Type of Platform	Momentum Flux (Nt m^{-2})	Latent Heat Flux (Watts m^{-2})	Sensible Heat Flux (Watts m^{-2})
		Profile Method	Bulk Method				
Krügermeyer (1976)[a]	ATEX	4 & 7 Levels	Stability Dependent	Buoy	0.026	25	1.5
Fujita (1978)[b]	AMTEX '75	2 Levels	Wind Speed Dependent	Offshore Tower[f]	0.018	29	5.2
Hasse et al. (1978b)[c]	GATE	5 & 7 Levels	Fixed Coefficient	Buoy	0.016	19	4.4
Liu et al. (1979)[d]	BOMEX	4 Levels	Stability Dependent	Stabilized Ship	0.011	22	4.5
This Experiment	San Nicolas Island	2 Levels	Fixed Coefficient	San Nicolas Island	0.016	15	3.3

[a]Values were estimated from Krügermeyer (1976), his Figs. 7, 10, and 13

[b]Fujita (1978), his Table 2, could technically be considered not to be a profile-bulk technique comparison

[c]Values were estimated from Hasse et al. (1978b), their Figs. 5, 6, and 7

[d]Average values from Liu et al. (1979), their Tables 4, 5, and 6 for Paulson et al. (1972) data.

[e]AMTEX '75 = Air Mass Transformation Experiment held in 1975 over the East China Sea. The definitions for the other experiment acronyms are given in Table 4.1

[f]From Fujita (1978) it is not completely clear if the AMTEX '75 data used in the comparison were taken from the tower offshore of Trarma Island

17 Watts m^{-2}, and 8.4 Watts m^{-2}, listed in the order of appearance in the table.

In light of the comparison of the profile-derived and bulk-derived momentum flux values presented in Fig. 18.6, it is unfortunate that no other profile-bulk comparisons exist for wind speeds above 10 or 12 m sec^{-1}. Since none of the published studies dealing with wind flow over escarpments (Sections 6 and 11) have been able to determine any wind-speed dependence of the escarpment influence, it would seem unlikely that the discrepancy between the profile-derived and bulk-derived momentum fluxes observed for wind speeds in excess of 12 m sec^{-1} was due to either the beach escarpment or the manner employed in this experiment to correct the wind profile. If, however, a discrepancy between a profile-derived and a bulk-derived parameter could be correlated to a parameter which was uniquely demonstrative of the island, like the distance between the water and the sensors, then a direct causal connection could be demonstrated.

In an analysis specifically designed to detect the influence of the island, three parameters were selected which were thought to be the most likely candidates to demonstrate any potential island influence. The parameters were the upwind distance between the water's edge and the sensors, which varied from 35 to 155 meters; the slope of the beach escarpment, which varied from 0.12 to 0.21; and the tide height, which varied from −0.79 to +0.73 meters. The analysis, which attempted to correlate the profile-bulk discrepancies (defined in Section 22) in stability, momentum flux, latent heat flux, sensible heat flux, drag coefficient, and roughness length with these three island parameters, revealed the existence of no discernible relationships. The results are presented in graphic form in Appendix C.

22. Comparison of Profile and Bulk Observations

Once a calculation procedure had been devised for computing the measurement uncertainties for the flux and stability parameters (Section 15), it is possible, with enough data runs, to make a distinction between the measurement "noise" and the statistically meaningful correlations between various parameters. Because the measurement error could vary by more than an order of magnitude in some instances, depending upon the meteorological conditions, it was necessary to compute the errors for each 30-minute long data run.

As was demonstrated in the previous section, it is very useful to have an objective comparison between the various profile-derived and bulk-derived parameters as an analytical tool. The usual procedure for such a comparison would have been to select one measurement technique as a reference and compare the other against it. Since this would have required selecting one technique over the other, a more rational and objective procedure would be to weigh each of the derived parameters inversely as a function of its measurement error and to compute the mean of the two weighted values as a reference—a parameter we shall define as the profile-bulk weighted mean:

$$\text{Weighted Mean} \equiv \frac{\dfrac{\text{Profile Value}}{\text{Profile Error (\%)}} + \dfrac{\text{Bulk Value}}{\text{Bulk Error (\%)}}}{\dfrac{1}{\text{Profile Error (\%)}} + \dfrac{1}{\text{Bulk Error (\%)}}}.$$

In this manner, a derived parameter value having half the measurement error compared to the other would be twice as important in computing the reference.

Additionally, a lower limit for the absolute value of the weighted-mean reference would need to be selected, particularly in cases where the parameter is represented in terms of a log scale or where the two derived values could be of opposite sign. This would eliminate the possibility of having to deal with a logarithm of zero or a weighted-mean reference unrealistically small. The lower limits for the various weight means were selected as conservative estimates of realistic thresholds, based upon the results of Table 15.2. For example, if the profile stability were +0.04, the bulk stability −0.03, and both had equal error values, the weighted mean reference would equal +0.005. However, based upon prior experience, values smaller than |±0.02| are known to be unrealistic in terms of the measurement uncertainty. In such a case, the weighted mean would be set equal to +0.02, taking care to conserve the sign. The lower limits selected for the various weighted means are indicated in Appendix E.

It is then possible to compare the profile-derived and bulk-derived parameters in terms of their standard deviation from the weighted-mean reference—a parameter we shall define as the profile-bulk discrepancy:

$$\text{Discrepancy} \equiv \left| \frac{(\text{Profile Value} - \text{Weighted Mean})^2 + (\text{Bulk Value} - \text{Weighted Mean})^2}{2} \right|^{1/2}.$$

This new parameter not only affords an objective measure of the difference between the two derived values, it effectively removes the substantial and variable influence of the measurement errors from the comparison.

Although the observations input into the profile calculations and the bulk calculations are from many of the same sensors, the computational procedures, the underlying assumptions, and the relative effect of measurement errors are so drastically different that the two methods can be considered to be virtually independent determinations of the same parameter. The availability of two simultaneously independent measurements of the same parameter can be a very useful tool in understanding the relative limitations of either measurement technique.

In the following analysis the profile-derived Richardson number was selected to portray stability, because its measurement error was typically half that of the bulk error (see Table 15.1). Additionally, no distinction was made between the Richardson number and Monin-Obukhov stability The use of either yielded results virtually identical in detail. For example, compare Figs. 18.1 and 18.3. The symbol $\bar{U}_{10}$ was employed to denote the 30-minute-average wind speed at 10 meters. Stable atmospheric conditions were defined as having a stability value greater than $+0.02$; neutral as less than $|\pm 0.02|$; and unstable, as less than -0.02. All measurements are 30-minute averages, and all air temperature, dew-point, and wind-speed values are expressed for an altitude of 10 meters.

The following figures portray graphically the results of the profile-bulk comparison and the subsequent conclusions. Many of the parameter interactions are rather complex. The analysis required a substantial effort to unscramble and dissect the influence of the various constituent components.

Stability

Figure 22.1 reveals that the profile-bulk stability discrepancy tended to increase with increasing stability and was typically one or two times greater under stable conditions.

Figure 22.2 demonstrates that there was no systematic relationship between the stability discrepancy and wind speed.

Figure 22.3 indicates that under neutral stability conditions the air-bulk water temperature difference was typically -1°C instead of the anticipated ~ 0°C. This suggested that the local bulk water temperature employed to approximate the integrated upwind water surface temperature was, on the average, reading ~ 1°C too warm.

Figure 22.4 demonstrates that the bulk stability technique indicated a stable atmosphere substantially less often than the profile technique. The bulk technique consistently overestimated the size of the instability when compared to the profile technique.

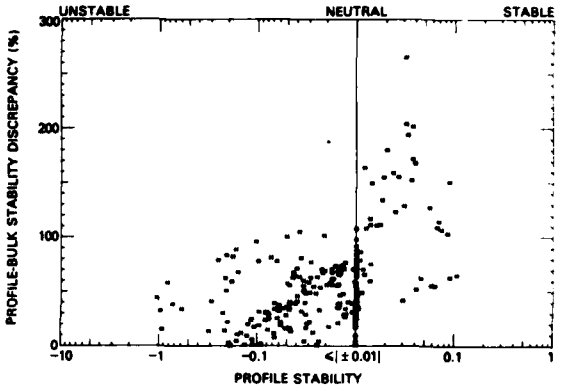

Fig. 22.1 — Discrepancy between profile- and bulk-derived stabilities displayed as a function of profile stability

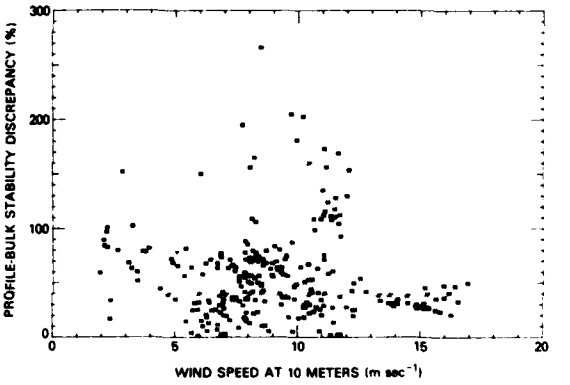

Fig. 22.2 — Discrepancy between profile- and bulk-derived stabilities displayed as a function of 30-minute-average wind speed at 10-meter height

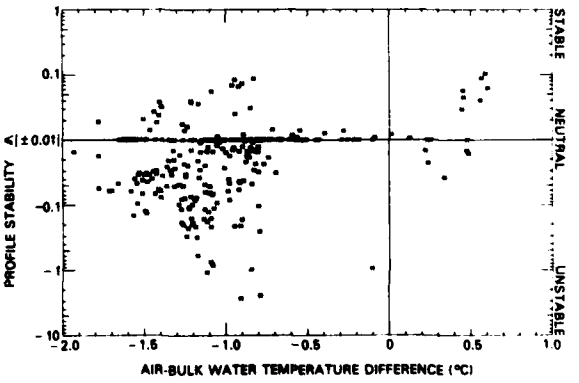

Fig. 22.3 — Profile- derived stability displayed as a function of the difference between the air temperature at 10-meter height and the bulk-water temperature, typical error values are ± 139% and ±0.5°C, respectively

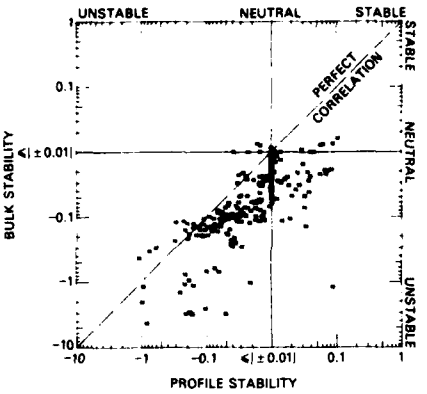

Fig. 22.4 — Correlation of profile- and bulk-derived stabilities, typical error values are ±139% and ±296%, respectively

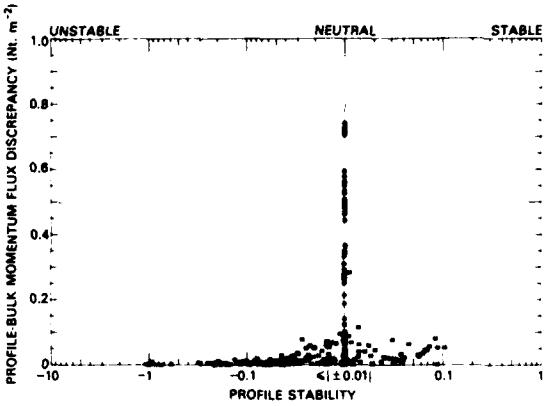

Fig. 22.6 — Discrepancy between profile- and bulk-derived momentum fluxes displayed as a function of profile stability

Momentum Flux

Figure 22.5 reveals that the profile-bulk momentum flux discrepancy tended to increase systematically with increasing wind speed and that it was most acute at wind speeds in excess of 12 m sec^{-1}.

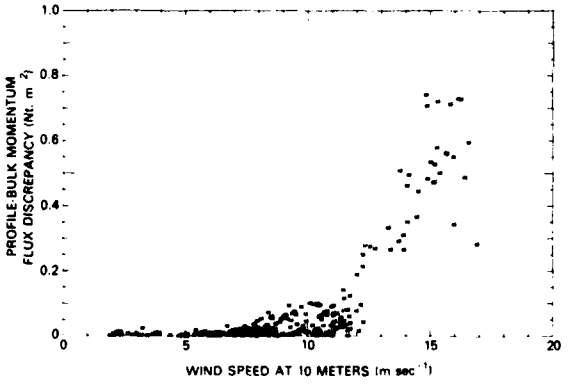

Fig. 22.5 — Discrepancy between profile- and bulk-derived momentum fluxes displayed as a function of 30-minute-average wind speed at 10-meter height

Figure 22.6 indicates that the momentum flux discrepancy was as much as four times greater under neutral stability conditions. From the results indicated in Fig. 22.5 this was not surprising, since high wind speeds normally imply neutral stability. The converse, however, is not necessarily true.

Figure 22.7 demonstrates that for wind speeds greater than 12 m sec^{-1} the profile technique systematically indicated a higher momentum flux than did the bulk technique, which was not attributable to the measurement uncertainty. Figures C.6 through C.8 of

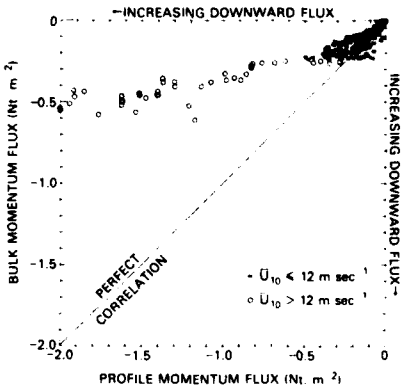

Fig. 22.7 — Correlation of profile- and bulk-derived momentum fluxes for two ranges of 30-minute-average wind speed at 10-meter height ($\bar{U}_{10}$), typical flux error values are ±0.27 Nt. m^{-2} and ±0.11 Nt. m^{-2}, respectively

Appendix C demonstrated that there was no systematic correlation between the profile-bulk momentum flux discrepancy and the various beach parameters. Jensen & Peterson (1978) found no systematic wind-speed dependence in the influence of an escarpment. Anderson & Smith (1981) recently reported that eddy-correlation momentum-flux measurements made from above an island beach displayed a similar increase at high wind speeds when compared to the bulk measurements. It was concluded that the higher momentum flux observed *with the profile technique was real and that it was not* due to the beach escarpment, nor was it an artifact of the profile technique.

Latent Heat Flux

Figure 22.8 reveals that the largest profile-bulk latent heat flux discrepancy occurred when the profile

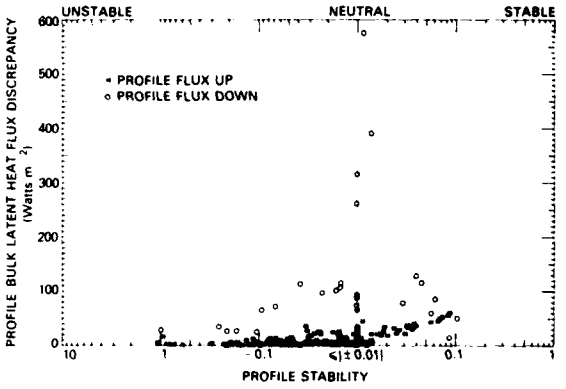

Fig. 22.8 — Discrepancy between profile- and bulk-derived latent heat fluxes displayed as a function of profile stability for both upward and downward profile-determined latent heat flux conditions

technique indicated a downward humidity flux (condensation). Otherwise the discrepancies were found to be relatively small, tending to increase slightly with increasing stability. It further reveals that the downward flux occurred over a wide range of stabilities and that the magnitude of the discrepancy was up to four times greater under neutral stability conditions.

Figure 22.9 demonstrates that the downward humidity flux discrepancy and the other discrepancies occurred over a wide range of wind speeds. Figure 22.8 revealed a sizable increase in the discrepancy due to the downward flux under neutral stability conditions. It would be incorrect to conclude that the increase indicated in Fig. 22.9 was necessarily associated with an increased wind speed, since neutral stability conditions are not necessarily accompanied by high wind speeds.

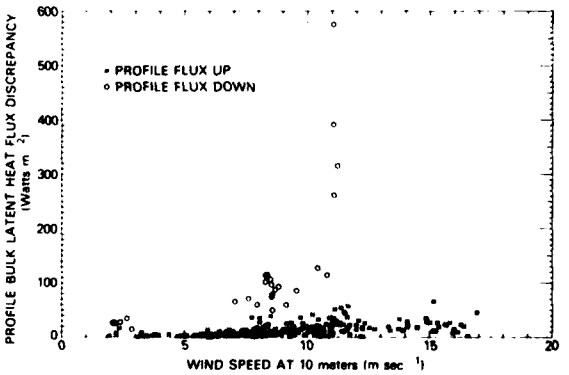

Fig. 22.9 — Discrepancy between profile- and bulk-derived latent heat fluxes displayed as a function of 30-minute-average wind speed at 10-meter height for both upward and downward profile-determined latent heat flux conditions

Figure 22.10 indicates that there was no apparent relationship between the latent heat flux discrepancy and the 10-meter dew point-bulk water temperature difference. The bulk techniques estimated the humidity at the water surface by assuming that the dew-point temperature was equal to the bulk water temperature. This is equivalent to assuming that the relative humidity at the surface is 100% and that the surface can be approximated by the bulk water temperature. The use of the bulk water temperature to approximate the surface conditions appeared to have no systematic influence upon the latent heat flux discrepancy.

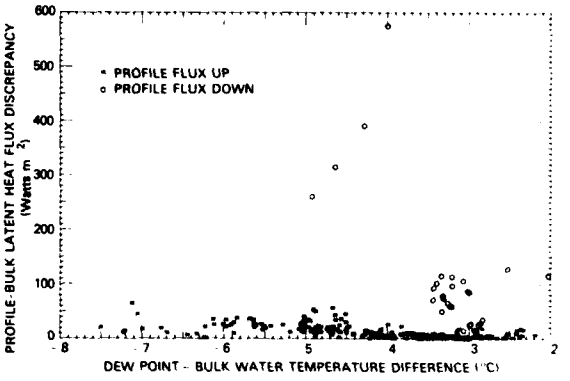

Fig. 22.10 — Discrepancy between profile- and bulk-derived latent heat fluxes displayed as a function of the difference between the dew-point temperature at 10-meter height and the bulk-water temperature for both upward and downward profile-determined latent heat flux conditions

Figure 22.11 demonstrates that solar heating of the upwind segment of beach between the measurement site and the water had no discernible influence upon either the latent heat flux discrepancy or the profile-observed downward humidity flux.

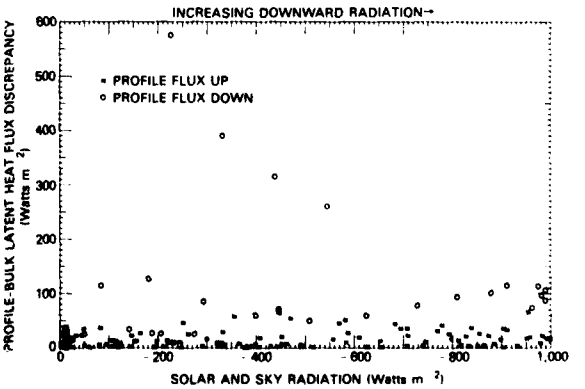

Fig. 22.11 — Discrepancy between profile- and bulk-derived latent heat fluxes displayed as a function of incoming shortwave solar and sky radiation for both upward and downward profile-determined latent heat flux conditions

Figure 22.12 reveals that over a wide range of stabilities the bulk technique systematically indicated an upward latent heat flux (evaporation), even for the 10% of the time when the profile indicated a downward flux (condensation). The topic of a downward humidity flux will be considered in more detail in Section 26.

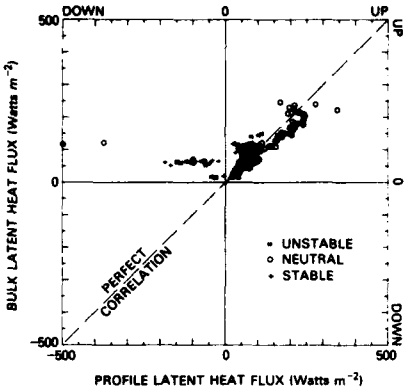

Fig. 22.12 — Correlation of profile- and bulk-derived latent heat fluxes for three general classes of stability, typical flux error values are ±118 Watts m^{-2} and ±32 Watts m^{-2}, respectively

Sensible Heat Flux

Figure 22.13 suggests that the profile-bulk sensible heat flux discrepancy frequently increased with increasing wind speed. Anderson & Smith (1981) recently reported that eddy-correlation sensible heat flux measurement, made from above an island beach, displayed a similar increase at high wind speed when compared to the bulk method. It was concluded that the profile-observed higher heat flux was real and that it was not an artifact of the profile technique.

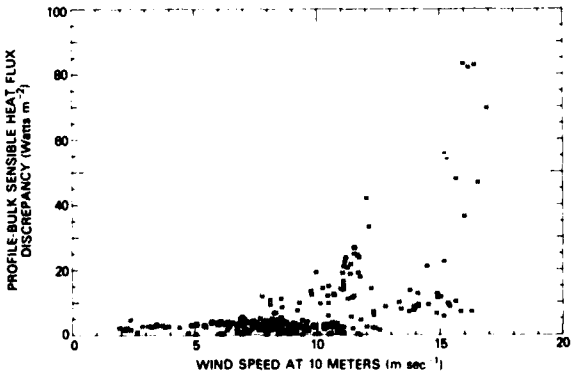

Fig. 22.13 — Discrepancy between profile- and bulk-derived sensible heat fluxes displayed as a function of 30-minute-average wind speed at 10-meter height

Figure 22.14 indicates that the sensible heat flux discrepancy was significantly increased under stable conditions and that the maximum discrepancy occurred under neutral stability conditions.

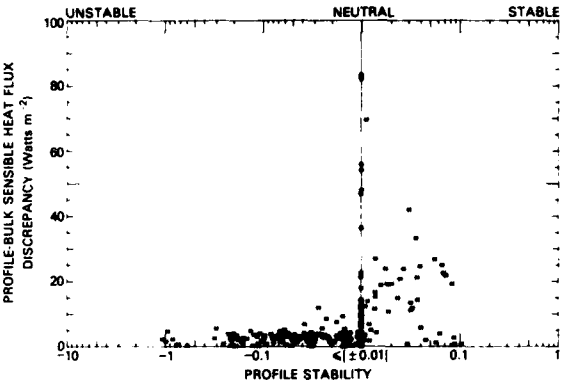

Fig. 22.14 — Discrepancy between profile- and bulk-derived sensible heat fluxes displayed as a function of profile stability

Figure 22.15 demonstrates that solar heating of the upwind segment of beach between the sensors and water had no discernible effect upon the sensible heat flux discrepancy. In conjunction with Fig. C.12 through C.14 of Appendix C, the figures demonstrate that there was no discernible influence of either the beach or the island in the air-temperature measurements. Therefore, any major discrepancy with the air-bulk water temperature difference must be due to the water-temperature measurement.

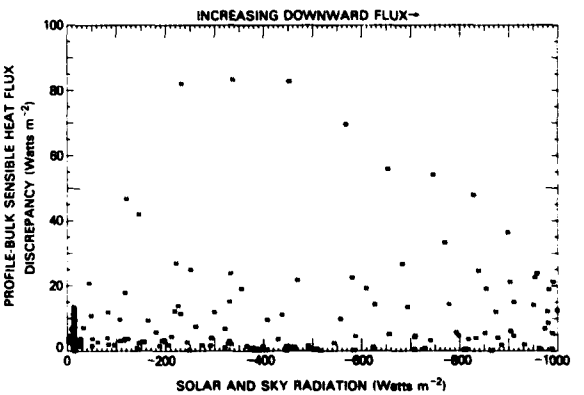

Fig. 22.15 — Discrepancy between profile- and bulk-derived sensible heat fluxes displayed as a function of incoming shortwave solar and sky radiation

Figure 22.16 in conjunction with the above indicates that the local bulk water temperature used to approximate the integrated upwind surface temperature was on the average, −1°C too warm. Since the use of the bulk water temperature to approximate the surface

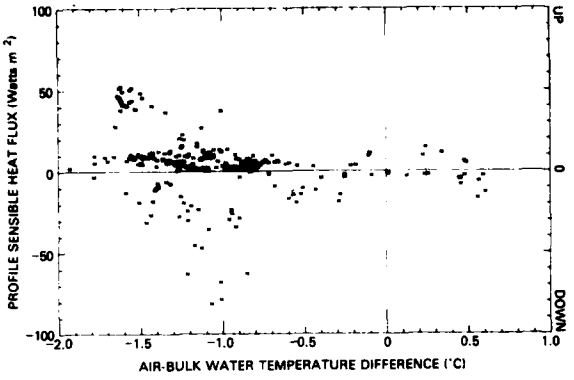

Fig. 22.16 — Profile-derived sensible heat flux displayed as a function of the difference between the air temperature at 10-meter height and the bulk water temperature, typical error values are ±8 Watts m^{-2} and ±0.5°C, respectively

temperature should have introduced an error of typically ±0.5°C, an approximately zero sensible heat flux should have been centered about an air-bulk water temperature difference of approximately 0°C within ±0.5°C. The much larger magnitude of the inferred average discrepancy portrayed in Fig. 22.16 graphically demonstrates an inherent problem, described in Section 3, which occurs when one attempts to apply the bulk method to a local mesoscale situation. The water near the island measurement site was on the average about 0.5°C warmer than integrated surface temperature of the upwind footprint. It is not really the water temperature observed in the immediate vicinity of the air-temperature measurement which is relevant, but rather the integrated effective surface temperature along the wind fetch trajectory. Figure C.14 of Appendix C indicated that this problem was not the result of the tide changing the depth of the bulk water temperature sensor. As elaborated in Section 3 there are other inherent experimental difficulties in attempting to measure the surface temperature accurately. Some experimenters, when confronted with these problems, simply "correct" for the difference by an average amount. However, like the San Nicolas Island data, most other experimental data were obtained under predominately unstable conditions (the water warmer than the air), and any average offset would favor that direction. For example, durring an evening with under stable conditions (the water cooler than the air) the bulk water temperature would be cooler than the surface* and the "correction" would need to be of the opposite sign. The same phenomenon can happen during the daytime as well; for example, see Grassl & Hinzpeter (1975), Schooley (1977), and Reuter & Raschke (1977). It may, also, be related to the surface waves; for example, see Shifrin (1974) and Witting (1972). This is of course a somewhat oversimplified view of a very complex heat transfer mechanism. A more detailed view is presented by Katsaros (1980b). This is particularly critical, since it is the direction of the sensible heat flux which is the primary determinant in characterizing the stability. To make a determination as to the offset and its sign, either an *a posteriori* assumption must be made about stability, in effect predetermining the answer, or the bulk technique must be accompanied by an independent technique for determining the stability. Unlike the latent heat flux, the sensible heat flux is more sensitive to the error introduced by employing the bulk water temperature to approximate the surface condition because the temperature differences are typically much smaller.

Figure 22.17 demonstrates that, in the majority of cases in which the profile technique had detected a downward sensible heat flux, the bulk technique indicated it as upward. Because of this, the profile technique indicated a stable atmosphere more frequently than did the bulk technique.

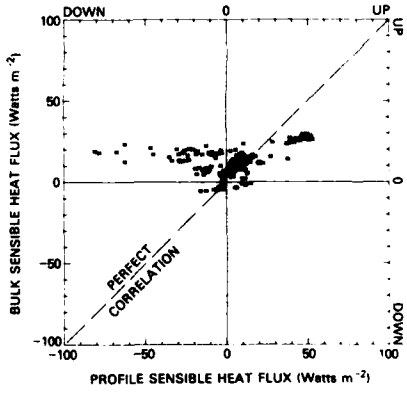

Fig. 22.17 — Correlation of profile- and bulk-derived sensible heat fluxes, typical error values are ±8 Watts m^{-2} and ±16 Watts m^{-2}, respectively

Total Heat Flux

Figure 22.18 indicates that the profile-derived and bulk-derived total heat fluxes agreed reasonably well, except for those cases in which the profile technique indicated a large downward latent heat flux. Additionally, the figure reveals that, even for those cases in which the humidity flux was not large enough to dominate the total flux, the downward humidity flux (condensation) never occurred when the total heat flux was in the upward direction. The total heat flux was upward for approximately 50% of the observations.

*In this report the following heat flux and stability sign convention has been adopted. Heat can be viewed as flowing from areas of high concentration (warm) to areas of low concentration (cool). Heat flow up (+) from below the surface (the bulk water) to the air implies that the surface must be cooler than the bulk and this is indicative of an unstable atmosphere (−). Heat flow down (−) from the air to below the surface (the bulk water) implies that the surface must be warmer than the bulk and this is indicative of a stable atmosphere (+).

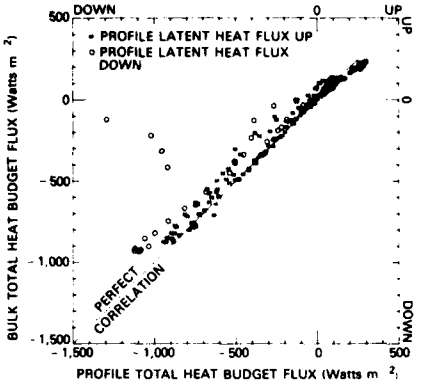

Fig. 22.18 — Correlation of profile- and bulk-derived total heat budget fluxes for both upward and downward profile-determined latent heat flux conditions, typical total heat flux error values are ±134 Watts m^{-2} and ±56 Watts m^{-2}, respectively

Bowen Ratio

Figure 22.19 reveals that the major disagreements between the profile-derived and the bulk-derived Bowen ratios was not due to the discrepancy caused by the profile technique indicating a downward latent heat flux, but it was rather due to the inability of the bulk technique to detect a downward sensible heat flux. The latter condition was more frequent than the former condition.

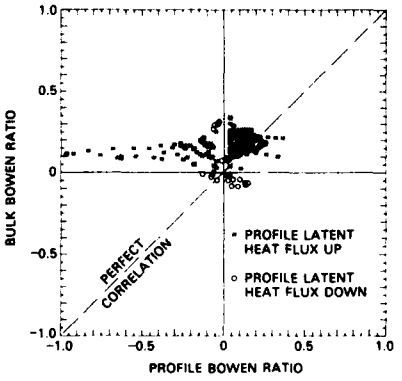

Fig. 22.19 — Correlation of profile- and bulk-derived Bowen ratios for both upward and downward profile-determined latent heat flux conditions, typical ratio error values are ±0.25 and ±0.24, respectively

Drag Coefficient

Figure 22.20 reveals that in the wind speed range of 4 to 12 m sec^{-1} the profile-bulk drag coefficient discrepancy was relatively small. For wind speeds under 4 m sec^{-1} and over 12 m sec^{-1}, the discrepancy ranged from two to four times larger.

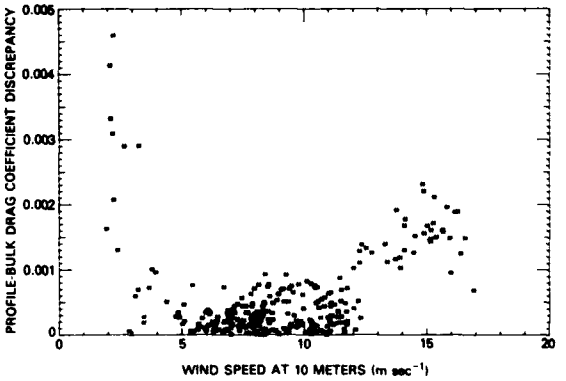

Fig. 22.20 — Discrepancy between profile- and bulk-derived neutral drag coefficients for 10-meter height displayed as a function of 30-minute-average wind speed at 10-meter height, bulk drag coefficient via Smith & Banke (1975)

Figure 22.21 reveals that the drag coefficient discrepancy was substantially larger under neutral and unstable conditions than it was under stable conditions.

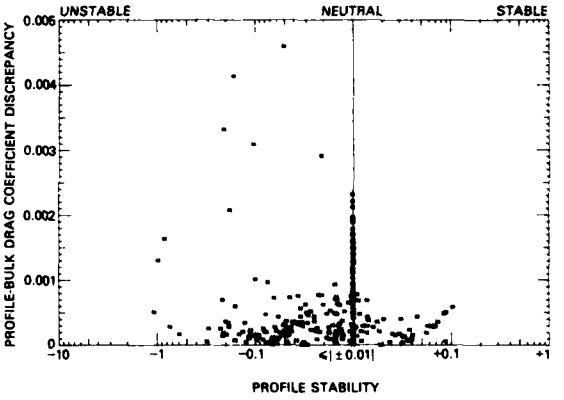

Fig. 22.21 — Discrepancy between profile- and bulk-derived neutral drag coeffficients for 10-meter height displayed as a function of profile stability, bulk drag coefficient via Smith & Banke (1975)

Figure 22.22 demonstrates that for wind speeds below 4 m sec^{-1} and above 12 m sec^{-1} the profile technique indicated a substantially larger drag coefficient than does the bulk technique. This would account for the underestimation by the bulk technique, as compared to the profile technique, of the bulk momentum flux at wind speeds above 12 m sec^{-1}, as shown in Fig. 22.7. The effect at wind speeds below 4 m sec^{-1} would be lost in the computation uncertainty of the momentum flux, and it would not be expected to be apparent due to the difference of the respective formulations. For example, compare profile-derived data in Fig. 19.2 with Fig. 18.6. The topic of an increased drag coefficient at both high and low wind speeds will be considered in more detail in Section 23.

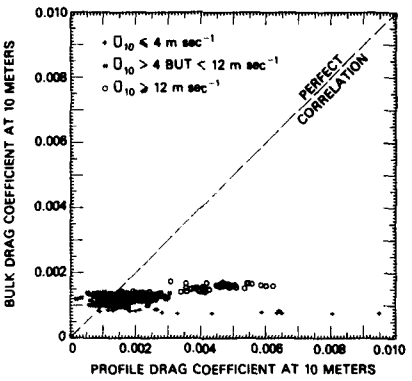

Fig. 22.22 — Correlation of profile- and bulk-derived neutral drag coefficients for 10-meter height for three ranges of 30-minute-average wind speeds at 10-meter height ($\bar{U}_{10}$), bulk drag coefficient via Smith & Banke (1975), typical drag error values are $\pm 2.0 \times 10^{-3}$ and $\pm 0.7 \times 10^{-3}$, respectively

Roughness Length

Figure 22.23 indicates that the profile-derived and the bulk-derived roughness lengths computed by Eq. 14.2 agree well, except for wind speeds below 4 m sec^{-1}, and that under those conditions the bulk technique tended to indicate smaller values than did the profile technique.

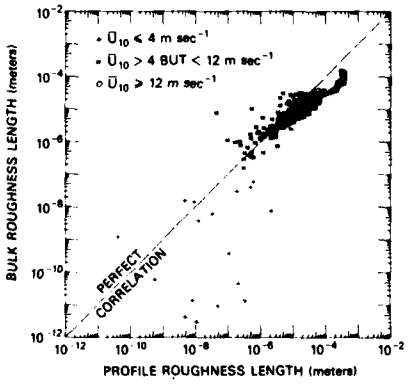

Fig. 22.23 — Correlation of profile- and bulk-derived roughness lengths for three ranges of 30-minute-average wind speeds at 10-meter height ($\bar{U}_{10}$) with roughness computed via Eq. 14.2 and typical error values of $\pm 3.0 \times 10^{-4}$ m and $\pm 1.6 \times 10^{-4}$ m, respectively

Friction Velocity and Other Scaling Parameters

Figures 22.24 through 22.26 are essentially a reiteration of the results presented in Figs. 22.7, 22.12, and 22.17, respectively, but expressed in terms of the scaling parameters.

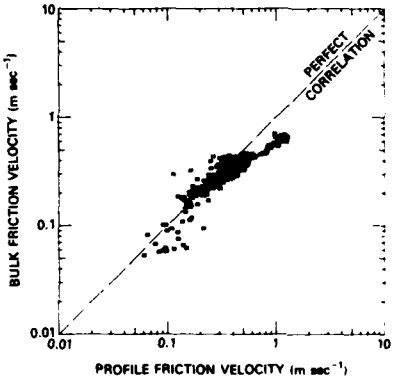

Fig. 22.24 — Correlation of profile- and bulk-derived friction velocities, typical friction velocity error values are ± 0.21 m sec^{-1} and ± 0.08 m sec^{-1}, respectively

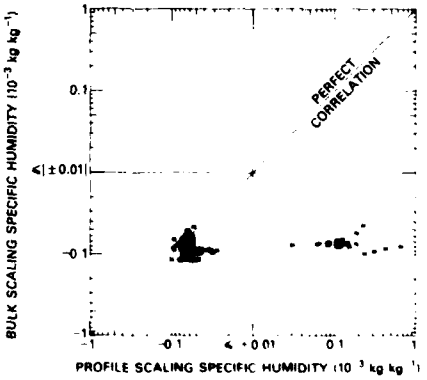

Fig. 22.25 — Correlation of profile- and bulk-derived scaling specific humidities, typical scaling error values are $\pm 0.067 \times 10^{-3}$ kg kg^{-1} and $\pm 0.042 \times 10^{-3}$ kg kg^{-1}, respectively

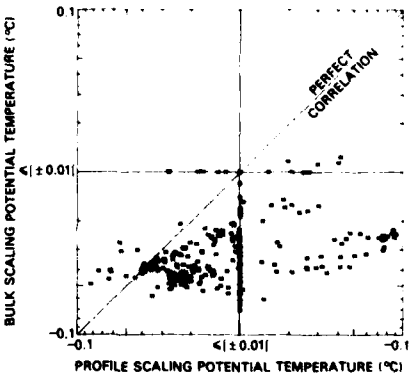

Fig. 22.26 — Correlation of profile- and bulk-derived scaling potential temperatures, typical scaling error values are ± 0.003°C and ± 0.012°C, respectively

Table 22.1—Typical Profile-Bulk Discrepancy Parameter Values for the Flux and Stability Parameters Expressed in Meteorological Units. The data is based upon 136 hours of observations acquired under average wind speeds ranging from 2 to 17 $msec^{-1}$, air-water temperature differences from −2.1 to +0.6°C, and dew point-water temperature differences from −7.5 to −2.0°C.

Parameter	Discrepancy Parameter Mean Value	Discrepancy Parameter Standard Deviation
Gradient Richardson Stability	0.07	0.23
Monin-Obukhov Stability (10 m)	0.06	0.19
Momentum Flux	0.08 Nt. m^{-2}	0.16 Nt. m^{-2}
Latent Heat Flux	23 Watts m^{-2}	52 Watts m^{-2}
Sensible Heat Flux	7 Watts m^{-2}	12 Watts m^{-2}
Total Heat Budget Flux	28 Watt m^{-2}	59 Watts m^{-2}
Bowen Ratio	0.09	0.10
Drag Coefficient (10 m)	0.6×10^{-3}	0.7×10^{-3}
Roughness Length	1.9×10^{-4} m	3.9×10^{-4} m
Friction Velocity	0.06 m sec^{-1}	0.07 m sec^{-1}
Scaling Specific Humidity	0.022×10^{-3} kg kg^{-1}	0.042×10^{-3} kg kg^{-1}
Scaling Potential Temperature	0.016°C	0.016°C

Summary of the Analysis

The bulk sensible heat flux method is more likely than the profile method to indicate an upward flux, because of the inherent necessity of approximating the integrated upwind surface temperature from the local bulk water temperature measurement. This accounts for the bulk technique being less likely to detect a stable atmosphere, and it is the reason why the bulk technique consistently overestimates the magnitude of unstable conditions. It also demonstrates the inherent difficulty of attempting to use the bulk method for determining fluxes in a local mesoscale situation. Additionally, at wind speeds above 12 m sec^{-1} the bulk technique tends to underestimate the momentum flux significantly.

Except for those circumstances in which the profile technique detected a downward latent heat flux (condensation), the profile technique and the bulk technique agreed well in regard to humidity flux. The profile-derived downward latent heat flux was observed over a wide range of stabilities and wind speeds, but it was most pronounced under neutral stability conditions, and it accounted for the major differences between the profile-derived and the bulk-derived total heat fluxes. Even in those cases when the downward humidity flux was not large enough to dominate the total heat flux, it was observed only when the total flux was in the downward direction.

Solar heating of the upwind segment of the beach between the measurement site and the water was shown to have no influence upon the sensible or latent heat flux measurements. The majority of differences in the profile-derived and the bulk-derived Bowen ratios was shown to be due to the difference in the direction of the sensible heat flux. At wind speeds below 4 m sec^{-1} and above 12 m sec^{-1} the bulk technique substantially underestimated the drag coefficient. At wind speeds below 4 m sec^{-1} the bulk technique indicated, typically, smaller roughness length values than did the profile technique. It was demonstrated, in conjunction with the results presented in Appendix C, that it was unlikely that any of these findings were influenced by either the island's internal boundary layer or by the beach escarpment upward of the measurement site. The typical profile-bulk discrepancy parameter values were computed, their mean value and standard deviations are given in Table 22.1.

23. Comparison of Drag Coefficient Results With Other Experiments

Comparison of Figs. 18.6, 18.8, 18.10, and 19.2 revealed that the major discrepancies between the profile flux data and the bulk flux data occurred at wind speeds greater than 12 m sec^{-1}, at which speeds the profile parameters increased more rapidly with increasing wind speed than did the corresponding bulk values. Inspection of the figures revealed that the increase in the discrepancy was greater for the momentum flux and the drag coefficient than for the latent and sensible heat fluxes. Since the friction velocity is the only parameter common to all four, and it is squared in both the momentum flux and the drag coefficient formulas, it was the principle candidate for a potential common source of the discrepancy. When one compares profile-derived and bulk-derived friction velocities, it is convenient to express the comparison in terms of the drag coefficients, since the discrepancy between the friction velocities is

enhanced and its normalized to the ambient wind speed. As noted earlier (Section 22) the drag coefficient discrepancy at low wind speeds is of little consequence when it is expressed in terms of the momentum flux because of the difference in the respective formulations.

Reviews of much of the existing drag-coefficient (C_D) observations as a function of the average wind speed at 10 meters ($\bar{U}_{10}$) have been presented by Smith & Banke (1975), by Garratt (1977), by Augstein (1979), and by Amorocho & DeVries (1980). Most of the observations cited in the various reviews were made at wind speeds ranging from approximately 2 to 20 m sec^{-1}. Although there was a great deal of scatter in the data, these observations generally portrayed a drag coefficient which increased moderately in some fashion with increased wind speed. The Smith & Banke (1975) formula was based upon approximately 56 hours of eddy-correlation observations made at windspeeds ranging from 3 to 21 m sec^{-1}, and it was used for computing the bulk-derived drag coefficient, momentum flux, and friction velocity values presented in various figures of Sections 18 through 20. S. D. Smith (1980a), using approximately 42 hours of eddy-correlation data taken under wind speeds ranging from 6 to 22 m sec^{-1} over the open ocean (about 60 meter deep), substantially verified the Smith & Banke findings. The Smith & Banke (1975) formula is

$$C_D = (0.63 + 0.066\,\bar{U}_{10}) \times 10^{-3},\ \pm 0.23 \times 10^{-3}. \quad (23.1)$$

A somewhat different conceptual approach was described by Kitaigorodskii (1973). He noted that most studies of drag coefficient presupposed the existence of an empirical relationship between the coefficient and the wind speed. Those studies presumed that the scatter in the experimental data for a given wind speed was due solely to the imperfections of the various measurements. Kitaigorodskii contended that, in addition to the measurement uncertainty, the averaging of coefficient data for a given wind speed should also be considered equivalent to averaging over an entire ensemble of the most varied stages of surface-wave development under similar wind-speed and stability conditions. He determined that the scatter of such drag-coefficient values was random and very large—he observed variations on the order of hundreds of percent. Kitaigorodskii concluded that the most appropriate approach for analyzing drag-coefficient data would be to consider data ranged over narrow bands of wind speeds and to use the tools statistical analysis on each discrete segment.

Kuznetsov (1970) employed the statistical ensemble approach described by Kitaigorodskii in the analysis of approximately 200 hours of profile measurements taken from buoys in deep ocean water and ranging in wind speed from 2 to 20 m sec^{-1}. The sensors were distributed from 0.4 to 3.0 meters above the sea surface, employing four or five measurement levels. For wind speeds greater than 20 m sec^{-1}, Kuznetsov utilized the hurricane data of Myers (1959). Kuznetsov analyzed his data employing wind-speed bandwidths of 1 and 5 m sec^{-1}. He found the drag coefficient to increase dramatically for wind speeds in excess of 11.4 m sec^{-1}, very close to the increase noted in the San Nicolas Island data at approximately 12 m sec^{-1}. A similar abrupt increase, although much less pronounced, has also been reported by Amorocho & DeVries (1980)* at approximately 11 m sec^{-1}. Because the Myers data have not been independently substantiated, the validity of the Kuznetsov findings for wind speeds greater than 20 m sec^{-1} may be somewhat in question. The Kuznetsov findings are shown in Fig. 23.1 overlying the San Nicolas Island profile-derived neutral drag coefficient values.

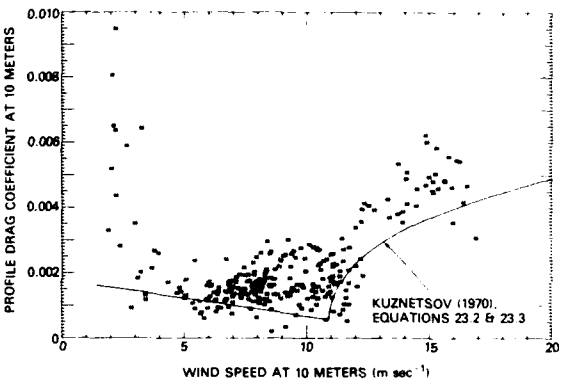

Fig. 23.1 — Profile-derived neutral drag coefficient for 10-meter height displayed as a function of 30-minute-average wind speed at 10-meter height overlying Kuznetsov (1970) bulk curve, typical profile drag error value is $\pm 2.0 \times 10^{-3}$

The Kuznetsov (1970) findings yielded the following formulas for computing the bulk-derived derived drag coefficient: for $\bar{U}_{10} < 11.4$ m sec^{-1},

$$C_D = (1.72 - 0.98\,\bar{U}_{10}) \times 10^{-3},\ \pm 0.12 \times 10^{-3}; \quad (23.2)$$

and for $\bar{U}_{10} > 11.4$ m sec^{-1},

$$C_D = [1.0 + 1.26\,(\bar{U}_{10} - 11)^{1/2}] \times 10^{-3},\ \pm 0.47 \times 10^{-3}. \quad (23.3)$$

For wind speeds above 4 m sec^{-1} the Kuznetsov bulk drag coefficient formulas fitted the San Nicolas Island profile data rather well, considering that the typical measurement error (Table 15.2) was $\pm 2 \times 10^{-3}$.

Kondo & Fujinawa (1972) described the various sources of error which must be taken into consideration when attempting to measure drag coefficient with the profile technique at wind speeds below 4 m sec^{-1}. They concluded that the error created by the over-speeding of mechanical anemometers due to wave-induced wind

*Also see, S. D. Smith (1981b).

fluctuations was of considerable magnitude, increasing in importance as the ambient wind speed decreased. Because the Kuznetsov (1970) data were acquired at an altitude below 3 meters, this would have resulted in a significant underestimation of the drag coefficients below 4 m sec^{-1}. The San Nicolas Island profile results should have been unaffected, since they had been acquired at a height greater than 9 meters.

Mitsuta & Tsukamoto (1978) reported more than 95 hours of drag-coefficient observations made with a sonic anemometer at heights of 1.5 and 5.6 meters with the eddy-correlation technique. The measurements were made over shallow water* in two large inland lakes of Japan; 60% of the measurements were acquired at wind speeds between 0.4 and 4.0 m sec^{-1}. Mitsuta & Tsukamoto, like Kuznetsov, reported drag coefficients which increased moderately with decreased wind speed between 4 and 9 m sec^{-1}. However, at wind speeds below 4 m sec^{-1} they observed drag coefficients which were typically one to four times greater than Kuznetsov's. Nine data runs with drag coefficients below 0.6×10^{-3} (less than 5% of the total) were rejected as being unrealistic; the remaining Mitsuta & Tsukamoto data were curve fitted by eye with the intention of mating it to the Kuznetsov results at 12 m sec^{-1}. The resulting curve is shown overlying the Mitsuta & Tsukamoto data in Fig. 23.2.

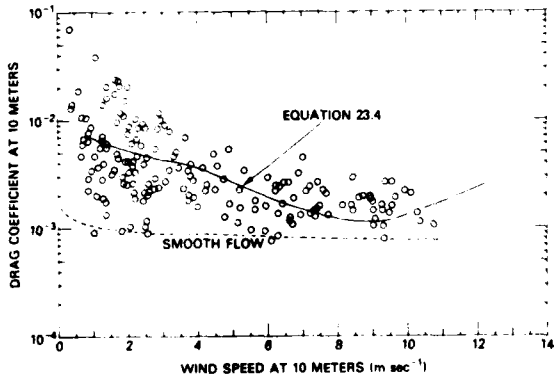

Fig. 23.2 — Figure from Mitsuta & Tsukamoto (1978) showing eddy-correlation measurements made over shallow water with overlying curve fit represented by Eq. (23.4), the nine data points falling below 0.6×10^{-3} in value are not shown

The curve fitted to the Mitsuta & Tsukamoto data was approximated by the relationship

$$C_D = \left[\frac{\sin(4.2 + 0.059\,\bar{U}_{10}) + 1.0}{0.018} + 1.2 \right] \times 10^{-3}. \qquad (23.4)$$

Employing Eq. 23.4 to represent the bulk drag coefficient for wind speeds between 1 and 12 m sec^{-1} and Eq. 23.3 for wind speeds between 12 and 18 m sec^{-1} yielded the curve in Fig. 23.3 shown overlying the San Nicolas Island profile results. The combined Mitsuta & Tsukamoto data and Kuznetsov data appear to fit the profile results exceptionally well. The same equations were used in computing the bulk momentum flux and friction velocity curves presented in Figs. 23.4 and 23.5, respectively. They are displayed overlying the San Nicolas Island profile results. The results of all three computations are summarized in Table 23.1.

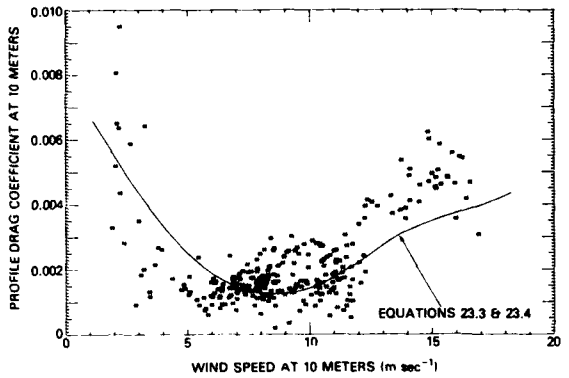

Fig. 23.3 — Profile-derived neutral drag coefficient for 10-meter height displayed as a function of 30-minute-average wind speed at 10-meter height overlying curve fit [Eq. (23.4)] of Mitsuta & Tsukamoto (1978) data mated at 12 m sec^{-1} to the bulk-curve [Eq. (23.3)] of Kuznetsov (1970), typical profile drag error value is $\pm 2.0 \times 10^{-3}$

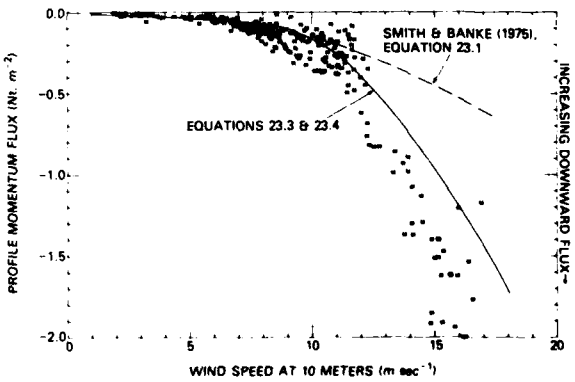

Fig. 23.4 — Profile-derived momentum flux displayed as a function of 30-minute-average wind speed at 10-meter height overlying the Smith & Banke (1975) bulk curve and the bulk curve formed by the combination of Mitsuta & Tsukamoto (1978) and Kuznetsov (1970) results, typical profile flux error value is ± 0.27 Nt. m^{-2}

*Unfortunately, Mitsuta & Tsukamoto (1978) do not indicate the depth of the water over which the measurements were taken. An effort is being made to obtain that information from the authors.

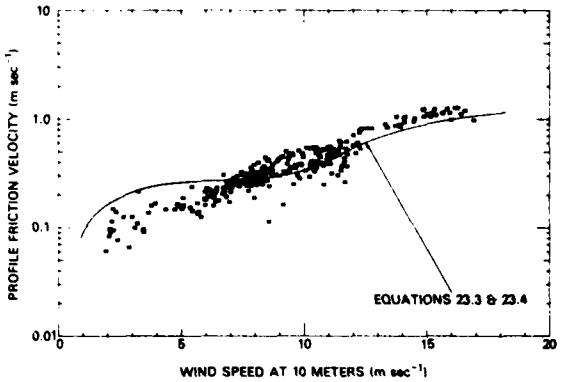

Fig. 23.5 — Profile-derived friction velocity displayed as a function of thirty-minute-average wind speed at 10-meter height overlying the bulk curve formed by the combination of Mitsuta & Tsukamoto (1978) and Kuznetsov (1970) results. Both the profile data and the bulk data were computed via Eq. (14.2). A typical profile friction velocity error value is ± 0.21 m sec^{-1}.

Table 23.1 — Results of Employing the Curve Fitted to the Mitsuta & Tsukamoto (1978) Data [Eq. 23.4] for Wind Speeds Between 1 and 12 m sec^{-1} and the Kuznetsov (1970) Findings [Eq. 23.3] for Wind Speeds Between 12 and 18 m sec^{-1} to Compute the Bulk-Derived Drag Coefficient

30 Minute Average Wind Speed at 10 meters	Bulk-Derived Neutral Drag Coefficient at 10 meters ($\times 10^{-3}$)	Bulk-Derived Momentum Flux[a] (Nt m^{-2})	Bulk-Derived Friction Velocity (m sec^{-1})
1	6.81	−0.008	0.083
2	5.46	−0.027	0.148
3	4.30	−0.048	0.197
4	3.31	−0.065	0.230
5	2.51	−0.077	0.250
6	1.90	−0.084	0.262
7	1.47	−0.089	0.268
8	1.25	−0.098	0.283
9	1.21	−0.121	0.313
10	1.37	−0.169	0.370
11	1.72	−0.256	0.456
12	2.26	−0.400	0.570
13	2.78	−0.578	0.685
14	3.18	−0.767	0.789
15	3.52	−0.974	0.890
16	3.82	−1.203	0.989
17	4.09	−1.454	1.087
18	4.33	−1.726	1.184

[a]Computed for an average moist-air density of 1.23 kg m^{-3}.

It is of interest to note, in comparing Figs. 23.3 and 19.2, that the Smith & Banke bulk formula (Eq. 23.1) and Eqs. 23.4 and 23.3 agree, within the limits of experimental error, for wind speeds between 4 and 12 m sec^{-1}.

Charnock (1955) proposed a "constant" (α) for a relationship relating the roughness length (z_0) to the friction velocity (U_*) and the acceleration due to gravity (g), where

$$z_0 = \frac{\alpha U_*^2}{g}. \tag{23.5}$$

From McIntosh & Thom (1973), the elementary equation relating the drag coefficient to the friction velocity and average wind speed is

$$C_D = \frac{U_*^2}{\bar{U}_{10}^2}. \tag{23.6}$$

Amorocho & DeVries (1980) present an equation representing the drag coefficient at 10 meters as a function of average wind speed,

$$C_D = 0.0015\left\{1 + \exp\left[-\frac{\bar{U}_{10} - 12.5}{1.56}\right]\right\}^{-1} - 0.00104. \tag{23.7}$$

They combined Eqs. 23.5 through 23.7 to compute the Charnock α parameter as a function of wind speed. Their resulting figure has been reproduced in Fig. 23.6. The Amorocho & DeVries results presented in Fig. 23.6 for the Charnock parameter bears an uncanny resemblance in the wind speed range of 1 to 18 m sec^{-1} to the drag-coefficient curve presented in Fig. 23.3.

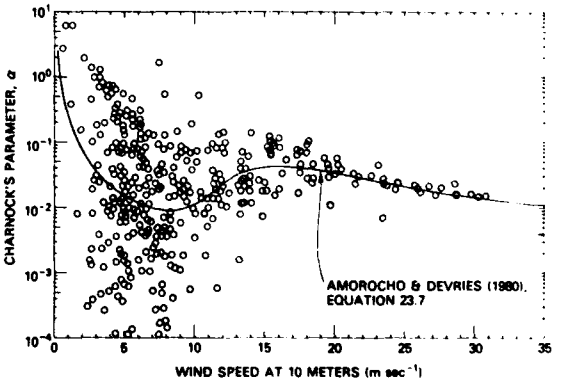

Fig. 23.6 — Figure from Amorocho & DeVries (1980) of Charnock's parameter, α, displayed as a function of average wind speed at 10-meter height

As indicated in Section 22, Anderson & Smith (1981) had observed a similar increase in momentum and sensible heat flux at high wind speeds for measurements made from the beach of a small island with the eddy-correlation technique. They speculated that the increase was probably due to the breaking waves and surf in the vicinity of the island. Like the San Nicolas Island

experiments, their measurements were made at a height above 9 meters. However, from the criteria suggested by Krügermeyer et al. (1978) and Hasse et al. (1978a) for determining the height of the wave influence in profile measurements, it is unlikely that the breaking waves and surf would have affected the San Nicolas Island profile measurements unless they were of amplitudes greater than 3 meters.

S. D. Smith (1981a) has suggested that, since the Smith & Banke (1975) results have been independently substantiated with measurements over deep water (~60 meters) by the recent work of Large & Pond (1981)*, which utilized the dissipation technique, that the San Nicolas Island findings may be indicative of the shallow-water situation. The fact that the low wind speed profile data fitted the Mitsuta & Tsukamoto (1978) findings over shallow water would tend to lend credence to this suggestion.

Employing the 1:20 height-to-fetch criterion (Section 6) of Shir (1972) to determine the region of the water surface which would influence the profile wind-speed measurements, would center the measurement footprint at a distance of 260 meters† upwind of the tower, or about 160 meters from the mean water mark on the beach. From the data presented in Table 9.1, this would suggest that the water which most influenced the San Nicolas Island results had a depth of approximately 4 or 5 meters.

The S. D. Smith (1981a) suggestion is further supported by the work of Wieringa (1974), which reported profile-drag coefficient measurements made over a shallow lake, approximately 4 meters deep. Wieringa found, at wind speeds between 5 and 15 m sec^{-1}, that the higher the profile measurements were above the water, the greater the wind-speed-dependent increase of drag coefficient computed for 10 meters. If the Wieringa profile-derived increases in drag coefficient as a function of wind speed for the geometric mean heights of 2.8 and 5.8 meters were scaled to the geometric mean height of the San Nicolas Island experiment, the scaled Wieringa results would agree very well with the island profile values (see Fig. 23.7).

If the S. D. Smith (1981a) suggestion is correct, it would imply that water depth will be required as an input parameter in future improved bulk methods. In light of a general understanding of the influence waves have upon drag coefficient and the modification of ocean waves in shallow water, this would hardly seem surprising. An alternative interpretation is presented in Section 24.

*Also see, Large (1979).

†The geometric mean height for the San Nicolas Island profile array was ~13 meters.

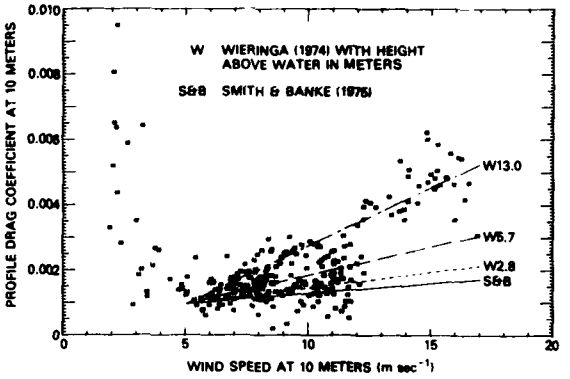

Fig. 23.7 — Profile-derived neutral drag coefficient for 10-meter height displayed as a function of 30-minute-average wind speed at 10-meter height overlying the Smith & Banke (1975) bulk results for deep water and the results of Wieringa (1974) for shallow water. The Wieringa results are shown for profile geometric mean measurement heights of 2.8 and 5.7 meters. Scaling the change in the Wieringa results as a function of height to the geometric mean height of the San Nicolas Island measurements, 13.0 meters, yielded curve W 13.0. A typical island profile drag coefficient error value is $\pm 2.0 \times 10^{-3}$.

24. Merits of the Bulk Technique

When one considers the overall quality and suitability of a flux measurement technique, there are essentially five sources of uncertainty which must be taken into account:

- *Instrumentation Error* — The uncertainty introduced by the measurement inaccuracy of the various sensor instruments and the data processing procedures.
- *Computation Variation* — The uncertainty introduced by employing one computation scheme, as opposed to another, within a given measurement technique; for example, by using the Friehe & Schmitt (1976) bulk scheme instead of those of Krügermeyer (1976) or Kondo (1975).
- *Platform Influence* — The distortions introduced by the presence of an observation platform or an instrument support structure upon the atmospheric and oceanic fields to be observed.
- *Hypothesis Quality* -- The uncertainty introduced by the underlying assumptions inherent within a technique. For example, when employing the bulk technique it is necessary to assume that the water surface temperature can be determined with the necessary degree of accuracy.

- *Data Base Limitation* — The uncertainty introduced by employing a technique under atmospheric conditions for which there is only a limited amount of reliable verifying data.

In comparing the relative profile and bulk measurement error values presented in Table 15.1, an inexperienced observer might conclude that the bulk technique was typically more accurate than the profile technique for determining several of the flux parameters. However, the error values indicated in the table are only those attributed to the first two of the five possible sources of uncertainty. The typical bulk error values indicated in Table 15.1 have been restated in Table 24.1.

Table 24.1 — Results of the Bulk Technique Flux and Stability Error Analysis (Section 15) Expressed in Percent of Indicated Parameter Value. Errors are those attributable to constituent instrument measurement uncertainties and to the computational scheme variability within the technique. Error values are based upon 136 hours of observations acquired at a height of 10 meters with average wind speeds ranging from 2 to 17 m sec^{-1}, air-water temperature differences from −2.1 to +0.6°C, and dew point-water temperature difference from −7.5 to −2.0°C.

Bulk-Derived Parameter	Bulk Technique Mean Error
Gradient Richardson Stability	296%
Monin-Obukhov Stability (10 m)	297%
Momentum Flux	46%
Latent Heat Flux	44%
Sensible Heat Flux	225%
Total Heat Budget Flux	23%
Bowen Ratio	269%
Drag Coefficient (10 m)	40%
Roughness Length	43%
Friction Velocity	23%
Scaling Specific Humidity	67%
Scaling Potential Temperature	248%

In terms of platform influence, although a great deal of information has recently come to light about the contamination of profile and eddy-correlation measurements, little has been available in the main stream of the literature about the bulk measurements. However, Hoeber (1977) and others (Section 5) have reported that observation platforms such as ships have been found to introduce errors in the order of 100% in the bulk-derived fluxes. These errors are in addition to the values already indicated in Table 24.1.

As for hypothesis quality, the comparison (Section 22) of the profile-derived and the bulk-derived sensible heat flux and stability determinations demonstrate that the bulk-technique assumption that the water surface temperature could be determined within the necessary degree of accuracy introduced an average bulk uncertainty of 101% for sensible heat flux and 54% for stability.* These errors are in addition to the values already indicated in Table 24.1.

As for the data base limitation, it should be recalled that the bulk technique is a semiempirical method, based upon a conglomerate of profile, dissipation, and eddy-correlation flux measurements. The significant discrepancies observed at wind speeds greater than 12 m sec^{-1} between the profile method and the original bulk method may simply portray the decreased conformation afforded by the decreased amount of reliable observations at high wind speeds. This might also account for the similar discrepancy reported by Anderson & Smith (1981). Like the bulk method, the profile and dissipation methods are themselves semiempirical. The flux and stability error analysis (Section 15) demonstrated that the typical profile-derived parameter measurement error was on the order of ±130%. There is little reason to believe that the dissipation method is any more accurate. If the bulk technique is to be improved, prudence would suggest that it be based primarily upon eddy-correlation measurements. It would be unrealistic to expect the bulk technique to be better than the data employed to develop the method. The amount of existing eddy-correlation measurements reported for wind speeds above 12 m sec^{-1} is presented in Table 24.2.

Table 24.2 suggests that the amount of eddy-correlation data available to develop the bulk method at wind speeds above 12 m sec^{-1} is statistically small and that relatively little of it is the best quality data. If the measurements acquired with questionable mechanical momentum flux sensors† were rejected and only the data acquired with sonic or thrust anemometers‡ accepted§, the data base would shrink to 44.5 hours for momentum flux, no data for latent heat flux, and 3 hours for sensible heat flux.

*The uncertainty values were estimated from the ratio of the mean profile-bulk discrepancy (Table 22.1) and the combined profile-bulk average parameter value (Section 15) computed in percent, in which the profile technique was used as the reference standard.

†For examples of some of the typical problems encountered with the mechanical propeller and trivane momentum flux devices refered to here, see McBean (1972), Horst (1973) and Francey & Sahashi (1979).

‡The accuracy of the thrust anemometer was successfully verified in the field where it was compared against a sonic anemometer, see S. D. Smith (1980b).

§With the eddy-correlation technique, the vertical velocity fluctuation determined with the momentum flux sensor is also used in computing the sensible and latent heat fluxes.

Table 24.2 — Existing Eddy-Correlation Flux Measurements Taken in the Marine Surface Layer at Wind Speeds Greater than 12 m sec^{-1}.

Source	Flux Measured	Sensors	Approximate Amount of Data Taken at Wind Speeds Greater than 12 m sec^{-1} (hours)	Approximate Maximum 30-Minute Average Wind Speed (m sec^{-1})
S. D. Smith (1970)	Momentum	Thrust Anemometer	2.5	16
DeLeonibus (1971)	Momentum	Propeller Anemometer	10.5	15
Wieringa (1974)	Momentum	Mechanical Trivane	2.5	15
Garratt & Hyson (1975)	Momentum	Propeller Anemometer	25.5	15
	Latent Heat	IR Hygrometer	25.5	15
	Sensible Heat	Bead Thermistor	13.5	15
Smith & Banke (1975)	Momentum	Sonic & Thrust Anemometers	6	21
Naito (1978)	Momentum	Sonic Anemometer	3	15
	Sensible Heat	Small Thermocouple	3	15
S. D. Smith (1980a)	Momentum	Thrust Anemometer	33	22

Comparing the bulk method with the other flux methods is a little like comparing apples and oranges. As elaborated in Section 3 and Fig. 22.16, the bulk method is appropriate for synoptic macroscale climatological studies and the other methods are appropriate for local mesoscale investigations. The bulk method is also different because it can be viewed as being a method of statistical forecasting, particularly in light of the Kitaigorodskii (1973) interpretation presented in Section 23. Whereas the other flux methods yield an in situ determination of a particular observation, the bulk method can be viewed as yielding the statistically most probable observation, a statistical probability based upon the aggregate of past experience. Because the previously existing data base which forms the aggregate experience contains comparatively little data taken under stable atmospheric conditions (estimated to be ~2%) and because phenomenon like a downward humidity flux occurs relatively infrequently over the ocean (estimated to be ~5% in Section 26), the bulk method is considerably less likely to detect such conditions and then only under the most extreme circumstances.

From a utilitarian perspective, the bulk method differs from the other flux methods in two principle aspects:

- The bulk method selects only the most probable flux value from among a large number of possible determinations which could be valid under exactly the same synoptic conditions.
- The bulk method is a viable technique only when it is employed to evaluate an average situation integrated over an appropriately large spatial scale. It is of questionable validity under realistic ocean conditions if it is used to determine fluxes and stability for relatively small planetary scales such as a few kilometers.

25. Recommendations for the Bulk Technique

In the absence of additonal eddy-correlation verification at both high and low wind speed conditions over various depths of water, and in the absence of a more accurate method to determine the sea surface temperature, the San Nicolas Island experiment has demonstrated that the following precautions should be taken whenever the bulk technique is utilized:

- The bulk measurements should always be accompanied by an independent determination of sensible heat flux and stability (Table 24.1).
- Local water depth and/or surface wave characteristics, as well as incoming solar and sky radiation, should be measured with an eye to possible future inclusion into the bulk technique (Sections 23 and 22).
- Great care should be taken to select a location for the bulk sensors which will not be affected by the influence of the observation platform or the instrument support structure (Section 5).
- It should be emphasized that the bulk method is unlikely to detect relatively

Table 25.1 — Example of the Estimated Average Confidence to be Gained by Employing a Two-Level Profile Measurement in Combination with the Bulk Method. The profile and bulk determinations are considered to be independent measurements of the same parameters.

Parameter	Profile Mean Error	Bulk Mean Error	Combined Profile-Bulk Mean Error* (E)	Profile-Bulk Mean Discrepancy† (D)	Approximate Ratio D/E
Gradient Richardson Stability	139%	296%	231%	56%	1/4
Monin-Obukhov Stability (10 m)	145%	297%	234%	55%	1/4
Momentum Flux	117%	46%	89%	21%	1/4
Latent Heat Flux	165%	44%	121%	42%	1/3
Sensible Heat Flux	116%	225%	179%	72%	1/2
Total Heat Budget Flux	78%	23%	58%	15%	1/4
Bowen Ratio	280%	269%	275%	63%	1/4
Drag Coefficient (10 m)	117%	40%	87%	31%	1/3
Roughness Length	78%	43%	63%	28%	1/2
Friction Velocity	58%	23%	44%	12%	1/4
Scaling Specific Humidity	106%	67%	89%	35%	1/3
Scaling Potential Temperature	57%	248%	180%	56%	1/3

*Combined Measurement Error = $\frac{\sqrt{(\text{Profile Errror})^2 + (\text{Bulk Error})^2}}{\sqrt{(\text{Number of Independent Measurements}}}$

†The profile-bulk discrepancy is defined in Section 22.

infrequent atmospheric phenomia, for example downward humidity flux, because the method tends to average out statistically the occurrence of such phenomena (Section 24).

The measurement of solar and sky radiation was included in the above recommendation for future bulk measurements in the belief that it might be possible to determine the sea surface temperature more accurately if one knows the incoming radiation, the wave characteristics, and the bulk water temperature. In future analyses, it may be possible to use the San Nicolas Island profile-derived sensible heat flux to infer the water surface temperature in an attempt to relate the surface-bulk temperature difference as a function of the incoming solar radiation and the wind speed.

Previous sections of this report have clearly demonstrated the advantages, and often the necessity, of accompanying the bulk measurements with an independent determination of the fluxes. An example of the relative confidence to be gained by employing a two-level profile measurement in combination with the bulk method is presented in Table 25.1. Various other types of two-level profile-bulk combinations have been previously proposed by Okamoto et al. (1968), Fujita (1978), and Itier (1980). An example of a flux parameter determined by such a combination of methods is presented in Appendix D for the latent heat flux, where the mutually determined value is portrayed in terms of the weighted mean (Section 22) and the error bars are expressed in terms of the profile-bulk discrepancy. Compare Fig. D.1 of Appendix D and Fig. 18.7 of Section 18.

26. Downward Humidity Fluxes Over the Ocean

At San Nicolas Island a downward humidity flux (condensation) was observed without the presence of rain or fog about 10% of the time. A precurrsory search of the literature revealed that the occurence of downward humidity flux may be more common than was previously thought. The findings of the literature search are presented in Table 26.1. This table should not be considered a comprehensive listing, since authors frequently do not note such observations and they do not present detailed tables listing uninterpreted data. It is possible that many of the observations of downward humidity flux are in fact due to measurement errors. However, when Table 26.1 is considered as an aggregate, it would suggest that the occurrence of such downward flux is not uncommon. If the nine experiments listed in Table 4.1 for which there is no record of a downward flux were combined with the results of Table 26.1, one might venture a guess from the combination that, on the average, condensation occurs in the marine surface layer about 5% of the time.

At first it was thought that the profile-derived downward humidity flux was due to some undetected influence of the island or the surf. A check of the instrumentation in the field determined that it was not due to a sensor malfuntion. However, the analysis presented in Sections 21 and 22 revealed that there was no discernable correlation between the phenomenon and those parameters thought most likely to be a measure of the possible influence of the island. Section 22 demonstrated that the downward flux was observed over a wide range of stabilities and wind speeds, but it was most pro-

Table 26.1 — Instances of Marine Surface Layer Downward Humidity Flux Observed or Inferred from Published Data.

SOURCE	Experiment[g] (Name or Location)	Observation Method[h]	Platform	Approximate Observation Time (hours)	Approx. Percent of Total Observations
Takahashi (1956)[a]	Kagoshima Bay	Profile	Anchored Boat	4.5	7%
Hoeber (1969)[b]	Equatorial Atlantic	Profile	Buoy	10.5	4%
Phelps & Pond (1971)[c]	BOMEX	Eddy-Correlation	Stabilized Ship	2.5	4%
Krechmer et al. (1972)	Black Sea	Eddy-Correlation	Ship	< 0.5	10%
S.D. Smith (1974)[d]	Lake Ontario	Bulk	Offshore Tower	0.8	3%
Krügermeyer (1976)[e]	ATEX	Profile	Buoy	18.5	10%
Schmitt et al. (1979)[f]	NORPAX '74	Eddy-Correlation	Stabilized Ship	4.0	17%
Schmitt et al. (1979)	NORPAX '74	Bulk	Stabilized Ship	20.0 (?)	5% (?)
Anderson & Smith (1981)	Sable Island	Eddy-Correlation	Onshore Tower	4.5	27%
This Experiment	San Nicolas Island	Profile	Onshore Tower	13.5	10%

[a]Based upon Takahashi (1956) water vapor measurements made at 2 and 4 meters.
[b]Estimated from Hoeber (1979), his Fig. 18.
[c]Estimated from Phelps & Pond (1971), their Fig. 5a.
[d]Inferred from S.D. Smith (1974), his Table V.
[e]Approximated by Krügermeyer (1976) to be 10%, see his p. 61..
[f]Estimated from Schmitt et al (1979), their Fig. 2, see also their p. 607.
[g]NORPAX '74 = North Pacific Experiment held in 1974. The definitions for the other experiment acronyms are given in Table 4.1.
[h]The dissipation method is incapable of detecting a downward humidity flux by itself.

nounced under neutral stability conditions. It further revealed that, even in those cases in which the humidity flux was not large enough to dominate the total heat-budget flux, the downward flux was observed only when the total heat-budget flux was also in the downward direction. The downward humidity flux was observed only during daylight hours.

Fehn & Fehn (1979) conducted a series of rudimentary humidity measurements at less then 1 meter above a beach, ranging from the water's edge to 600 meters inland. Their findings were of little practical assistance, since they were conducted well within the internal boundary layer formed by the beach. However, their article referenced a study conducted by Tuller (1972) of the microclimate energy balance of a coastal beach almost exactly ten years before this experiment, to the day, on a beach located approximately 130 km from the San Nicolas Island site.

Tuller found, from measurements made at 0.8 meters above the beach, that the wet-sand region of the beach (the region between the previous high-tide mark and the current high-water mark) represented a transition region between the moisture extremes of the wet ocean and the dry beach. Section 9 described the upwind beach material at San Nicolas Island as sand stone. Tuller further determined that, during the daytime, because of the enchanced evaporation from the wet beach due to solar heating, the upward humidity flux was typically three times greater over the wet beach then over the surf zone. If the measurements at San Nicolas Island were made above and forward of both the transition region and the internal boundary formed by the beach (as demonstrated in Section 21), the enhanced evaporation of the wet beach would have no effect upon the humidity flux measurements. If, however, the profile measurements were made forward of the internal boundary layer but within the transition region, the Tuller findings would suggest that the humidity flux would more likely be enhanced in the upward direction. Section 6 demonstrated that the profile measurements were not made within the internal boundary formed by the beach. Therefore, it was concluded that the profile-detected downward humidity flux was real and was not due to the presence of the upwind beach.

The existence of a downward humidity would be expected to be of significant importance in understanding the generation and maintainance of marine aerosols and, therefore, in the optical transmission of the maritime atmosphere.

27. Horizontal Homogeneity and the Optical Measurements

The micrometeorological measurements made at San Nicolas Island were primarily intended to characterize the marine atmosphere for simultaneous integrated-path infrared-transmission measurements made between the island promotories visible to the left in Fig. 9.1. The principal end of the optical path was located 180 meters downwind from the micrometeorological site on the major promontory and extended to either of the island's two lesser promontories located to the east-northeast.

This arrangement enabled optical measurements to be made principally upwind of the island surf at distances of 2.508 and 4.067 km over water. The paths ranged from 0.2- to 1.0- km upwind of the beach between the promontories. The mean-sea-level average water depth was 12.4 meters for the short optical path and 11.2 meters for the long path. Both optical paths were approximately 15 meters above mean sea level and they ran approximately perpendicular (laterally) to the prevailing mean wind direction. A point of considerable interest, therefore, was how well an essentially single-point micrometeorological measurement integrated over time could be expected to characterize a horizontal atmospheric optical measurement integrated over both time and lateral distance.

Dyer & Hicks (1972) reported, as the result of measurements separated by up to 0.15 km over land, that the horizontal homogeneity of momentum and sensible-heat fluxes was on the order of ±10%. Naito & Kondo (1974) studied horizontally separated wind-fluctuation measurements over water. They found, for altitudes up to 20 meters and lateral distances of up to 16.5 meters, that the small-scale structure of the marine wind field could be viewed as cells ranging in lateral size from about 1.4 to 16.5 meters.

Hasse et al. (1975) reported simultanous eddy-correction and profile flux measurements, separated by distances of 0.2 to 11 km, made over the open ocean during GATE. They observed differences as large as 0.08 Nt. m^{-2}, 60 Watts m^{-2}, and 25 Watts m^{-2} for momentum, latent heat, and sensible heat fluxes, respectively. Yaglom (1974, 1977) has suggested that many of the discrepancies observed between various simultaneous measurements made at horizontally separated locations were probably due to instrument measurement error. The results of Section 15 would tend to substantiate Yaglom's contention.

Mickle & Davison (1979) reported, from boundary-layer tethered-balloon measurements made during GATE from two ships maintained 4 km crosswind of each other, that the large-scale structures of the wind and humidity fields were markedly different in shape for windward distances of several tens of kilometers. Their measurements indicated that wind-field observations made along the mean wind direction (longitudinally) showed good correlation and could be portrayed as large cellular structures about 4 km by 4 km in size. The humidity field, however, was found to be characterized by a cellular structure elongated in the longitudinal direction, with ratios in excess of 5:1 in comparison to the lateral direction, suggesting cellular structures in excess of 20 km by 4 km in size.

The marked elongation of the large-scale humidity cellular structure observed by Mickle & Davison suggested that the humidity values measured at one location and integrated in time could not be as readily extrapolated in the lateral direction as in the longitudinal direction. The measurements made at San Nicolas Island were averaged 30-minute periods at an average 10-meter altitude wind speed of 9 m sec^{-1}, corresponding to an average longitudinal distance of 16.2 km. This gave a ratio of about 4:1 for the average longitudinal path length compared to the maximum lateral optical path length of 4.1 km.

From high-resolution infrared transmission measurements made at 3.6- to 3.7-μm wavelength at San Nicolas Island, Dowling et al. (1981) were able to measure the mean integrated humidity vapor pressure along the 4.1-km optical path. Although it was not possible to verify directly the flux homogeneity for the lateral path, it was possible to compare simultaneous point and integrated-path humidity measurements (see Fig. 27.1).

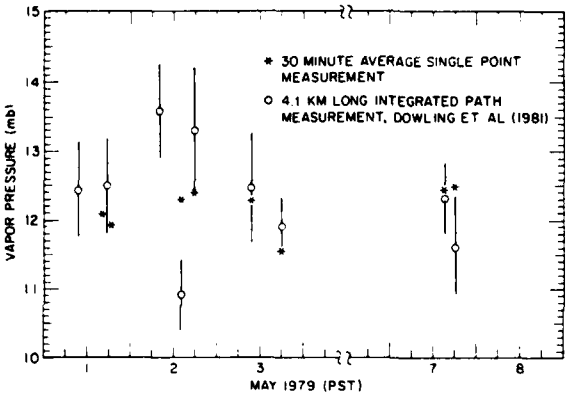

Fig. 27.1 — Dowling et al. (1981) 4.1-km-long integrated-path infrared humidity measurements, made approximately perpendicular to the prevailing wind direction, compared to single-point measurements. The typical single point measurement error was <0.1 mb.

The Dowling et al. measurements required approximately 15 minutes of observation and were made at an altitude of approximately 15 meters above mean sea level. The single-point meteorological measurements were averaged for 30 minutes at an altitude of 10 meters. Figure 27.1 demonstrates that the measurements agreed well for six of the seven occasions when direct comparisons were possible.

28. Summary and Conclusions

A search for a suitable open-ocean marine surface layer experiment site located within the limits of the continental United States determined that the upwind vicinity of San Nicolas Island, California, was virtually an ideal location (Table 2.1) in terms of the variety of meteorological conditions. Because flux and stability

measurements would be required in a salt-laden environment on a continuous basis, for periods as long as several hundreds of hours, the profile method was determined (Section 3) to be the most practical in terms of data quality, the state of instrumentation development, and cost effectiveness.

A review of the literature (Table 4.1) revealed the existence of only about 2,100 hours of previous profile measurements taken in the marine surface layer in which all three of the primary fluxes had been measured. Of those data, approximately 85% had been acquired in the equatorial region of the Atlantic Ocean. It was further determined that only about 1% of the entire previous profile data base had been acquired under stable atmospheric conditions and that there existed virtually no reliable profile data taken at wind speeds in excess of 12 m sec^{-1}.

An analysis (Section 16) of the distribution of the 136 hours of micrometeorological observations made at San Nicolas Island revealed that over a ten-day period a wide variety of conditions were observed in which the average wind speed ranged from 2 to 17 m sec^{-1}, air-water temperature difference from -2.1 to $+0.6$°C, and dew point-water temperature difference from -7.5 to -2.0°C. Subsequently, 10% of the data were acquired under stable atmospheric conditions and 15% at wind speed in excess of 12 m sec^{-1}.

As a first choice, a fixed structure located in the water was considered to be the most desirable type of observation platform. However, an engineering survey revealed that a structure of sufficient integrity to withstand the frequently hostile environment of the area would have been beyond the fiscal resources of the project. Subsequently, the location of the measurements was changed to the extreme tip of a 1.5-km-long, low-profile, narrow island promontory which pointed directly into the prevailing wind direction.

A review of the influence that various platforms have upon meteorological measurements (Section 5) revealed that measurements made from ships, even those equipped with instrumentation mounted on forward booms, could produce errors on the order of 100% in fluxes computed with the relatively insensitive bulk method. Compared to the flow distortions (Section 6) introduced by the presence of a complex structure, such as a ship or large ocean tower, the influence of a beach was found considerably less complex and better understood. The existing body of literature strongly suggested that the discrepancy observed between the simultaneous measurements made for the island promontory and a ship was probably due to locally induced distortion of the shipboard measurements and not a distortion of the island-based measurements, as speculated by Fairall et al. (1979b) and Noonkester et al. (1980).

From existing theoretical and experimental studies made for beach-type situations, it was determined (Section 6) that the minimum measurement altitude appropriate for the San Nicolas Island measurement site was 9 m. It was further demonstrated (Section 7) that, knowing the measurement accuracy of the various sensor instruments, it was possible to establish general rules for determining the appropriate minimum vertical separation ($\Delta \ln z$) between adjacent profile measurement levels. As a result, it was determined that

$$\Delta \ln z \geqslant 39.903\, A_t,$$

$$\Delta \ln z \geqslant 7157.0\, A_q,$$

and

$$\Delta \ln z \geqslant 0.61922\, A_u,$$

where z is the vertical distance in meters, A_t is the accuracy of the air temperature sensors in °C, A_q is the accuracy of the humidity sensors in kg kg^{-1} of the specific humidity, and A_u is the accuracy of the wind speed sensors in average percent of reading for the entire operating range of the experiment. In addition, it was determined (Section 8) that increasing the number of profile-measurement levels beyond the minimum two or three was not an efficient technique for increasing the profile-measurement accuracy.

Based upon the field studies of Jensen & Peterson (1978) and the theoretical study of Frost et al. (1974), a generalized equation (Eq. 11.1) was developed to portray the wind flow modification induced by the change in elevation inherent in many beaches (see Fig. 28.1). The generalized solution subsequently allowed the correction of the observed wind profile measurement for the beach escarpment.

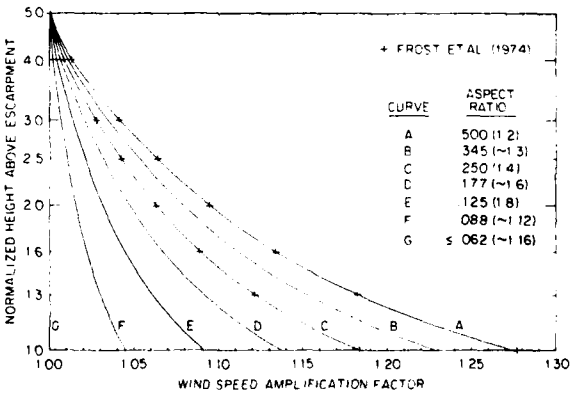

Fig. 28.1 — Beach-escarpment-induced wind-profile modification represented by Eq. (11.1) presented in terms of the normalized height above the escarpment and the escarpment aspect ratio

Comparison (Section 12) of the instrumentation with that employed in previous profile experiments indicated that the San Nicolas Island instruments were at least as accurate as those employed elsewhere. Because

the humidity profile measurement uncertainty was determined to be, typically, three times larger than had been estimated by previous experimenters, it was found to be impractical (Section 14) to incorporate the influence of buoyancy into the thermodynamic component of the stability equation. Subsequently, the conventional overland measurement of the potential temperature profile was used to determine the thermodynamic constituent in the stability formulation.

A conservative analysis (Table 15.1) to determine the magnitude of realistic measurement errors revealed that the average flux and stability uncertainties, which were attributable to instrumentation inaccuracy and computation scheme-variations, were typically on the order of 130% for the profile method and 150% for the bulk. The largest single errors were found to be in the bulk-derived sensible heat flux and stability. The substantial size of the average bulk stability error (~300%) suggested that, unless an independent measurement technique to determine stability accompanied the bulk method, little could be gained by using the existing stability-dependent bulk-coefficient schemes. A comparison (Table 21.1) with other experiments which used stability dependent bulk coefficients confirmed this suggestion.

A comparison (Tables 15.3 and 15.4) of the San Nicolas Island profile instrumentation arrangement was made with the typical configuration used in other marine surface layer experiments. Taking into consideration the number of measurement levels and their separation, the comparison (Table 15.5) determined that, if the other configurations had been used under similar meteorological conditions, they would have yielded flux and stability measurement uncertainties no better than 0.84 times and no worse than 1.30 times those determined for San Nicolas Island, exclusive of any island or escarpment influence.

A comparison (Table 21.1) made with other similar overwater experiments demonstrated that the San Nicolas Island results were, typically, as good as profile experiments conducted from buoys and offshore towers. An extensive analysis was conducted which was specifically designed to detect the possible distortions introduced by the presence of the island or the use of the wind-profile escarpment correction. That analysis (Appendix C) revealed no discernable distortions in the data which were attributable to the presence of either the island or the beach escarpment.

A detailed comparison (Section 22) of profile-derived and bulk-derived flux and stability values demonstrated that, because the bulk water temperature measurement was used to determine the sea surface temperature, the bulk method was more likely to indicate an upward sensible heat flux. Consequently, this resulted in a diminished ability of the bulk method to detect a stable atmospheric condition. Further analysis revealed that if an average offset had been employed to "correct" for the average anticipated difference between the bulk water temperature and the surface water temperature, this in effect would have statistically diminished the ability of the bulk method to detect stable atmospheric conditions except under the most extreme circumstances. Clearly the most serious impediment to a rational implementation of the bulk method is the inherent dilemma present in the water temperature technique. At this time there is no instrument which can directly measure the sea surface temperature under routine ocean conditions any more accurately than the estimated typical bulk-surface temperature difference, about ± 0.5°C.

The profile-bulk comparison further revealed that, at wind speeds greater than 12 m sec^{-1}, the Smith & Banke (1975) bulk scheme tended to underestimate the observed momentum flux as compared with the profile method. Solar heating of the upwind segment of the island beach was shown to have no discernable influence upon either the sensible heat flux or the latent heat flux measurements. Except under those circumstances (about 10% of the time) in which the profile method detected a downward humidity flux (condensation), the profile and bulk humidity methods agreed well. The downward humidity flux was observed unaccompanied by rain or fog under a wide range of stability and wind speed conditions, but it was found to be largest under neutral conditions. Although 50% of the overall data base was acquired under conditions in which the total heat budget flux was in the upward direction even when the latent heat flux was not large enough to dominate the total, the downward humidity flux was observed only when the total flux was, also, in the downward direction. A precursory search of the literature (Table 26.1) identified nine instances in which a downward humidity flux had been detected over water. Based upon the results of this search, a rough estimate suggested that the phenomenon occurs about 5% of the time.

An analysis of the difference between the profile data and the bulk data demonstrated that the largest flux discrepancies occurred at wind speeds greater than 12 m sec^{-1}, where the profile-derived parameters tended to increase more rapidly with increasing wind speed than did the corresponding bulk parameters using the computational schemes of Friehe & Schmitt (1976) for sensible and latent heat and Smith & Banke (1975) for momentum. Inspection revealed that the wind-speed-dependent discrepancies were more pronounced for momentum flux and drag coefficient than for sensible and latent heat fluxes. Because the friction velocity was the only parameter common to all four and is squared in both the momentum flux and drag coefficient formulas, it was concluded to be the major source of the discrepancy. Earlier analysis (Section 21) had demonstrated that the friction velocity discrepancy was not due to either the

island or the manner employed to correct the wind profile for the presence of the escarpment. The search for the source of the difference between the two methods was then shifted to an analysis (Section 23) of the drag coefficients, since the manifestation of the friction velocity discrepancy would be enhanced and would be normalized to the wind speed.

Although the Smith & Banke bulk drag coefficient scheme worked well in the 4- to 12-m sec^{-1} wind-speed range, a different bulk scheme was required for the high and low wind speed cases. The Kuznetsov (1970) scheme fit the data very well, except for wind speeds below 4 m sec^{-1}. A bulk scheme developed from the special overwater low-wind-speed eddy-correlation experiment of Mitsuta & Tsukamoto (1978) was found to fit the data well for both the low and intermediate wind speed cases (see Fig. 28.2).

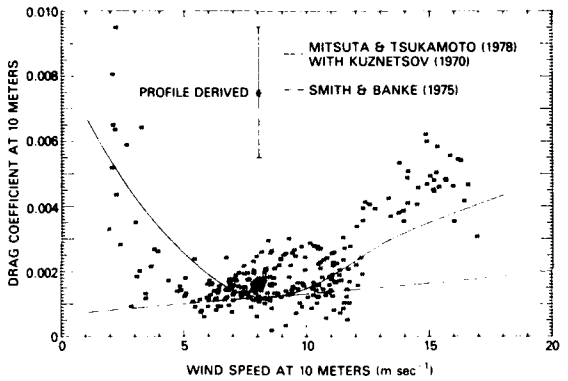

Fig. 28.2 — Profile-derived neutral drag coefficient for 10-meter height displayed as a function of 30-minute-average wind speed at 10-meter height overlying the Smith & Banke (1975) results and the proposed combination of the Mitsuta & Tsukamoto (1978) and Kuznetsov (1970) results

Consequently, the Friehe & Schmitt bulk sensible heat coefficient (C_H) and bulk moisture coefficient (C_E) scheme, in combination with the bulk drag coefficient (C_D) scheme developed from Mitsuta & Tsukamoto, worked well for wind speeds between 1 and 12 m sec^{-1}, and in combination with the bulk drag coefficient scheme of Kuznetsov, worked well for wind speeds between 12 and 18 m sec^{-1}. As a result, it was determined that, for $1 \leqslant \bar{U}_{10} \leqslant 12$ m sec^{-1},

$$C_D = \left[\frac{\sin(4.2 + 0.59\,\bar{U}_{10}) + 1.0}{0.018} + 1.2\right] \times 10^{-3},$$

$$C_E = 1.32 \times 10^{-3},$$

and

$$C_H = 0.92 \times 10^{-3};$$

and for $12 \geqslant \bar{U}_{10} \geqslant 18$ m sec^{-1},

$$C_D = [1.0 + 1.26(\bar{U}_{10} - 11)^{1.2}] \times 10^{-3},$$

$$C_E = 1.32 \times 10^{-3},$$

and

$$C_H = 0.92 \times 10^{-3},$$

where $\bar{U}_{10}$ is the 30-minute-average wind speed at the 10-meter altitude.

In the search (Section 23) for an explanation of the wind-speed-dependent discrepancy between the San Nicolas Island drag-coefficient results and those of Smith & Banke, circumstantial evidence was presented which would suggest that the island results might be indicative of conditions over shallow ocean water. If this interpretation is correct, it would imply strongly that future bulk schemes will need to incorporate the water depth in some fashion as an input parameter.

An alternative interpretation (Section 24) for the increasing discrepancy above 12 m sec^{-1} as a function of increasing wind speed is that it may simply portray the decreasing confirmation afforded by the increasing scarcity of reliable observations. This view would tend to be substantiated by a literature search (Table 24.2) which revealed that for wind speeds greater than of 12 m sec^{-1} there were less then 45 hours of reliable eddy-correlation observations for momentum flux, none for latent heat flux, and only 3 hours for sensible heat flux. Clearly, more high-wind-speed eddy-correlation measurements are required. Smith & Katsaros (1981) have recently proposed such an experiment.

The increasing discrepancy between the San Nicolas Island drag-coefficient results and those of Smith & Banke below 4 m sec^{-1}, as a function of decreasing wind speed, could be explained in a similar manner to the high-wind-speed case, or it could be explained in terms of the increased measurement uncertainty inherent in low-wind-speed observations. In either event, the source of the low-wind-speed drag-coefficient discrepancy is academic when expressed in terms of the fluxes, since the flux discrepancies at low wind speeds are small when compared to the overall flux measurement uncertainty.

The future implementation of bulk measurements (Section 25) is discussed and a simple two level combined profile-bulk technique is proposed. The combined method could reduce the average flux and stability measurement error by a factor of approximately 3.

A comparison of the various flux methods (Section 3) suggested that the bulk method was most appropriate for macroscale climatological investigations and that the other flux methods were better suited for investigations involving smaller spatial scales. In light of the Kitaigorodskii (1973) interpretation (Section 23), the

bulk method is also different because it can be viewed as a method of statistical forecasting. Where the other flux methods yield in situ determinations of a particular observation, the bulk method can be thought of as determining the statistically most probable observation, a statistical probability based upon the aggregate of past experience. Because the existing data base which forms the aggregate experience of past observations contains comparatively few data taken under stable atmospheric conditions, and because phenomena like downward humidity fluxes occur relatively infrequently, the bulk method is considerably less likely to detect such conditions and, then, only under the most extreme circumstances.

From a utilitarian perspective, the bulk method differs from the other flux methods in two principal aspects. First, the bulk method selects only the most probable flux value from among a large number of possible determinations which could be valid under exactly the same synoptic conditions. Second, it is a viable technique only when it is employed to evaluate a general situation averaged over an appropriately large spatial scale. It is of questionable validity under realistic ocean conditions if it is used to determine fluxes and stability for relatively small planetary scales such as a few kilometers.

In an elementary test (Section 27) to judge the horizontal homogeneity of the marine surface layer forward of the upwind edge of the island, an integrated optical humidity measurement, made over a path 4.1 km long approximately lateral to the prevailing wind direction, was compared to a single-point humidity measurement. In six of the seven cases in which a direct comparison was possible, the two measurements agreed within the limits of the experimental error.

The May 1979 San Nicolas Island experiment data base is available on magnetic floppy disk (Section 13) to interested parties upon request to the author. A hard copy of the experiment data base will be available in a forthcoming Naval Research Laboratory Memorandum Report 4713, Blanc (1982).

29. Acknowledgments

An experiment such as that undertaken at San Nicolas Island is, of course, accomplished due to the concerted effort of many people. The author wishes to thank Lothar Ruhnke, head of the Atmospheric Physics Branch, for his steadfast moral support, even under the most adverse circumstances; Jon Wunderlich and his predecessor Lowell Wilkins, of the U.S. Navy's Optical Signatures Program, for their advocacy in the optical community of a systematic and rational approach to the study of the influence of the marine atmosphere upon the operation of optical systems; Arvid Severson, of Meteorology Research Incorporated, for his assistance in the design and construction of the San Nicolas Island instrument system and tower; Carl Friehe, John Willett, Tom Lockhart, Lutz Hasse, Stuart Smith, and Ken Davidson for their suggestions, encouragement, and criticism; Bob deViolini, Jay Rosenthal, and Darwin Tolzin, of the Pacific Missile Test Center, for the acquisition of the island climatological and oceanographic observations and for the logistical support on the island; Stuart Gathman, Bud Larson, Doug Jensen, Jim Dowling, and Richard Jeck for contributing auxiliary data to the report; Mike Romeo and Deane Blazie, of Maryland Computer Services, for the extensive computer programming required for the data acquisition and analysis; Chuck Morgan, Bruce Rosenwasser, Horst Koster, Mark Bahu, Ron Beattie, and Ben Julian, who served as temporary field technicians on various occasions; Fred Rettenmaier, of the Library Reference Section, for his diligent effort in obtaining many of the more obscure sources which frequently proved to be so helpful; Dora Wilbanks and the Computerized Technical Composition Section for their handling and arrangement of the final manuscript; and Stanley Weintraub for his diligent editing.

The author also wishes to thank the NATO Air-Sea Interaction Program for the 1980-1981 Study Visit Grant which made possible the author's interaction with other research scientists conducting similar investigations in Europe and Canada. Their criticism and suggestions have proven most useful in the interpretation of the data. The San Nicolas Island experiment was funded as part of the Electro-Optics Meteorology Program of the United States Navy.

30. Bibliography

Amorocho, J., & J.J. DeVries, 1980: "A New Evaluation of the Wind Stress Coefficient Over Water Surfaces," J. Geophys. Res. **85** (C1), 433-442.

Anderson, R.J., & S.D. Smith, 1981: "Evaporation Coefficient for the Sea Surface from Eddy Flux Measurements,". J. Geophys. Res. **86** (C1), 449-456.

Angell, J.K., & A.B. Bernstein, 1976: "Evidence for a Reduction in Wind Speed on the Upwind Side of a Tower," J. Appl. Meteorol. **15**, 186-188.

Augstein, E., 1979: "The Atmospheric Boundary Layer Over the Tropical Oceans," *Meteorology Over the Tropical Oceans*, ed. by D.B. Shaw, Royal Meteorological Society, Bracknell, England, pp. 73-103.

Augstein, E., H. Hoeber, & L. Krügermeyer, 1974a: "Errors of Temperature, Humidity, and Wind Speed Measurements on Ships in Tropical Latitudes," "Meteor" Forschungsergeb. (Berlin), Reihe B, No. 9, 1-10 (Naval Intelligence Support Center translation No. 6375, Washington, D.C.).

Augstein, E., H. Schmidt, & F. Ostapoff, 1974b: "The Vertical Structure of the Atmospheric Planetary Boundary Layer in Undisturbed Trade Winds

over the Atlantic Ocean," Boundary-Layer Meteorol. **6**, 129-149.

Augstein, E., & J. Wucknitz, 1969: "The Quality of Wind Speed Measurements on a Semistabilized Buoy," "Meteor" Forschungsergeb. (Berlin), Reihe B, No. 3, 27-32.

Badgley, F.I., C.A. Paulson, & M. Miyake, 1972: *Profiles of Wind, Temperature, and Humidity over the Arabian Sea*, International Indian Ocean Expedition Meteorological Monograph No. 6, The University Press of Hawaii, Honolulu.

Barenblatt, G.I., G.S. Golitsyn, A.M. Obukhov, & A.M. Yaglom, 1975: "G.I. Taylor (1886-1975)," Izv. Acad. of Sci., USSR, Atmos. Oceanic Phys. **11**, 687-688 (English translation).

Bill, R.G., Jr., A.F. Cook, L.H. Allen, Jr., & J.F. Bartholic, 1980: "Predicting Fluxes of Latent and Sensible Heat of Lakes From Surface Water Temperatures," J. Geophys. Res. **85** (C1), 507-512.

Bindon, H.H., 1965: "A Critical Review of Tables and Charts used in Psychrometry," *Humidity and Moisture, Measurement and Control in Science and Industry*, ed. by A. Wexler & R.E. Ruskin, Reinhold Publishing, New York, Vol. 1, pp. 3-15.

Blanc, T.V., 1979: "The Marine Surface Layer Micrometeorological Experiments at San Nicolas Island, California," *Preprints, Second Conference on Coastal Meteorology, Los Angeles, California*, American Meteorological Society, Boston, Mass., pp. 76-83.

Blanc, T.V., 1982: "Data Base for the May 1979 Marine Surface Layer Micrometeorological Experiment at San Nicolas Island, California," NRL Memorandum Report 4713, Washington, D.C., in preparation.

Bogorodskiy, M.M., 1964: "Investigation of Tangential Friction, Vertical Turbulent Heat Exchange and Evaporation under Open Sea Conditions," Okeanologiya **4**, 19-26 (in Russian).

Bogorodskiy, M.M., 1966: "A Comparison of Gradient Observations of Wind Velocity by Means of the Froude Spear-Buoy and a Shipboard Gradient Installation," Oceanol. Acad. Sci. USSR, **6**, 283-288 (English translation).

Bowen, A.J. & D. Lindley, 1977: "A Wind-Tunnel Investigation of the Wind Speed and Turbulence Characteristics Close to the Ground over Various Escarpment Shapes," Boundary-Layer Meteorol. **12**, 259-271.

Bradley, E.F., 1980: "An Experimental Study of the Profiles of Wind Speed, Shearing Stress and Turbulence at the Crest of a Large Hill," Quart. J. R. Meteorol. Soc. **106**, 101-123.

Bruce, J.P., D.V. Anderson, & G.K. Rodgers, 1961: "Temperature, Humidity and Wind Profiles over the Great Lakes," Great Lakes Research Division, Institute of Science and Technology, The University of Michigan, Publication No. 7, pp. 65-70.

Buck, A.L., 1976: "The Variable-Path Lyman-Alpha Hygrometer and its Operating Characteristics," Bull. Am. Meteorol. Soc. **57**, 1113-1118.

Burt, W.V., 1979: "The Oceanography Program at the Royal Netherlands Meteorological Institute," European Scientific Notes, Office of U.S. Naval Research, London **ESN 33-9**, 350-354.

Businger, J.A., J.C. Wyngaard, Y. Izumi, & E.F. Bradley, 1971: "Flux-Profile Relationships in the Atmospheric Surface Layer," J. Atmos. Sci. **28**, 181-189.

Byshev, V.I., & Yu. A. Ivanov, 1969: "The Time Spectra of Some Characteristics the Atmosphere above the Ocean," Izv. Acad. Sci., Atmos. Oceanic Phys. **5**, 8-13 (English translation).

Camp, D.W. & J.W. Kaufman, 1970: "Comparison of Tower Influence on Wind Velocity for NASA's 150-Meter Meteorological Tower and a Wind Tunnel Model of the Tower," J. Geophys. Res. **75**, 1117-1121.

Campbell, G.S., B.D. Tanner, & E.C. Campbell, 1981: "A Portable Eddy Correlation System for Near-Surface Flux Measurements," Bull. Am. Meteorol. Soc. **62**, 147 (Abstract only).

Campbell, G.S., & M.H. Unsworth, 1979: "An Inexpensive Sonic Anemometer for Eddy Correlation," J. Appl. Meteorol., **18**, 1072-1077.

Champagne, F.H., C.A. Friehe, J.C. LaRue, & J.C. Wyngaard, 1977: "Flux Measurements, Flux Estimation Techniques, and Fine-Scale Turbulence Measurements in the Unstable Surface Layer Over Land," J. Atmos. Sci., **34**, 515-[illegible]

Charnock, H., 1955: "Wind Stress on a Water Surface," Quart. J. Roy. Meteorol. Soc. **81**, 639-640.

Chern, C., 1977: "Project METEOR," Ocean Engineering and Construction Project Office, Chesapeake Division, Naval Facilities Engineering Command, Washington, D.C., Report No. FPO-1-77 (17).

Ching, J.K.S., 1976: "Ship's Influence on Wind Measurements Determined from BOMEX Mast and Boom Data," J. Appl. Meteorol. **15** 102-106.

Chou, Min-Yui, 1966: "The Optimum Averaging Periods for Measurements of Meteorological Fields," Izv. Acad. Sci. USSR, Atmos. Oceanic Phys. **2**, 291-295 (English translation).

Coantic, M., & C.A. Friehe, 1980: "Slow-Response Humidity Sensors," *Air-Sea Interaction Instruments and Methods*, ed. by F. Dobson, L. Hasse, & R. Davis, Plenum Press, New York, pp. 399-411.

Condon, E.U., & H. Odishaw, 1958: *Handbook of Physics*, McGraw-Hill, New York, p. 5-97 (surface tension of water at 20°C).

Deacon, E.L., 1962: "Aerodynamic Roughness of the Sea," J. Geophys. Res. **67**, 3167-3172.

Deacon, E.L., 1980: "Slow-Response Temperature Sensors," *Air-Sea Interaction Instruments and Methods*, ed. by F. Dobson, L. Hasse, & R.

Davis, Plenum Press, New York, pp. 255-267.

Deacon, E.L., P.A. Sheppard, & E.K. Webb, 1956: "Wind Profiles over the Sea and the Drag at the Sea Surface," Austr. J. Phys. **9**, 511-541.

DeLeonibus, P.S., 1971: "Momentum Flux and Wave Spectra Observations from an Ocean Tower," J. Geophys. Res. **76**, 6506-6527.

deViolini, R., 1974: "Climatic Handbook for Point Mugu and San Nicolas Island, Part 1, Surface Data," Technical Publication PMR-TP-74-1, Pacific Missile Test Center, Geophysics Division, Point Mugu, California.

deViolini, R., 1980: Private communication (Atmospheric Sciences Branch, Geophysics Division, Pacific Missile Test Center, Point Mugu, California).

Dobson, F., L. Hasse, & R. Davis, 1980: *Air-Sea Interaction Instruments and Methods*, Plenum Press, New York, pp. 1-10.

Dowling, J., S.T. Hanley, G.M. Truby, J.A. Curcio, C.O. Gott, G.B. Mathews, & A. Ackermann, 1981: Results of Laser Calibrated High Resolution Transmission Measurements and Comparison of Broadband Transmissometer Data; San Nicolas Island, California, May 1979," Private communication of June 1981. (Present address for J. Dowling: Optimetrics Inc., Las Cruces, New Mexico).

Dunckel, M., L. Hasse, L. Krügermeyer, D. Schriever, & J. Wucknitz, 1974: "Turbulent Fluxes of Momentum, Heat and Water Vapor in the Atmospheric Surface Layer at Sea during ATEX," Boundary-Layer Meteorol. **6**, 81-106.

Dyer, A.J., 1974: "A Review of Flux-Profile Relationships," Boundary-Layer Meteorol. **7**, 363-372.

Dyer, A.J., & J.R. Garratt, 1978: "The Variation of Eddy Fluxes with Height and Fetch in an Unstable Atmosphere," J. Meteorol. Soc. Japan **56**, 19-24.

Dyer, A.J., & B.B. Hicks, 1970: "Flux-Gradient Relationships in the Constant Flux Layer," Quart. J.R. Meteorol. Soc. **96**, 715-721.

Dyer, A.J., & B.B. Hicks, 1972: "The Spatial Variability of Eddy Fluxes in the Constant Flux Layer," Quart. J.R. Meteorol. Soc. **98**, 206-212.

Echols, W.T., 1970: "Modification in Surface Boundary Layer Wind Structure with Onshore Flow," Atmospheric Science Group, College of Engineering, The University of Texas, Austin, Report No. 23.

Echols, W.T., & N.K. Wagner, 1972: "Surface Roughness and Internal Boundary Layer Near a Coastline," J. Appl. Meteorol. **11**, 658-662.

EG&G, 1972: "Cambridge Systems Dew Point Hygrometer Error Analysis," Report DP-2, EG&G, Environmental Equipment Division, Waltham, Mass. 02154.

Elliott, W.P., 1958: "The Growth of the Atmospheric Internal Boundary Layer," Trans. Am. Geophys. Union **39**, 1048-1054.

Fairall, C.W., K.L. Davidson, & G.E. Schacher, 1979a: "Humidity Effects and Sea Salt Contamination of Atmospheric Temperature Sensors," J. Appl. Meteorol. **18**, 1237-1239.

Fairall, C.W., G.E. Schacher, K.L. Davidson, & T.M. Houlihan, 1979b: "Atmospheric Marine Boundary Layer Measurements in the Vicinity of San Nicolas Island During CEWCOM-78," *Preprints, Second Conference on Coastal Meteorology, Los Angeles, Calif. held in January 1980.* American Meteorological Society, Boston, Mass., pp. 71-75.

Fleagle, R.G., J.W. Deardorff, & F.I. Badgley, 1958: "Vertical Distribution of Wind Speed, Temperature and Humidity above a Water Surface," J. Marine Res. **17**, 141-155.

Francey, R.J., & K. Sahashi, 1979: "Gill Propeller Anemometer Frequency Response over the Sea," J. Appl. Meteorol **18**, 1083-1086.

Freymuth, P., 1978: "A Bibliography of Thermal Anemometry," TSI Incorporated, St. Paul, Minnesota 55164.

Friehe, C.A., 1978: Private communication dated 16 May 1978. (Present address: National Center for Atmospheric Research, Boulder, Colorado)

Friehe, C.A., 1979: Private communication dated 6 May 1979. (Present address: see above.)

Friehe, C.A., & C.H. Gibson, 1978: "Estimates of the Surface Fluxes Over the Ocean," *Turbulent Fluxes Through the Sea Surface, Wave Dynamics, & Prediction*," ed. by A. Favre and K. Hasselmann, Plenum Press, New York, pp. 67-79.

Friehe, C.A., C.H. Gibson, F.H. Champagne, & J.C. LaRue, 1975: "Turbulence Measurements in the Marine Boundary Layer," *Atmospheric Technology*, National Center for Atmospheric Research, Boulder, Colorado, No. 7, pp. 15-22.

Friehe, C.A., & S.E. Pazan, 1978: "Performance of an Air-Sea Interaction Buoy," J. Appl. Meteorol. **17**, 1488-1497.

Friehe, C.A., & K.F. Schmitt, 1976: "Parameterization of Air-Sea Interface Fluxes of Sensible Heat and Moisture by the Bulk Aerodynamic Formulas," J. Phys. Oceanogr. **6**, 801-809.

Frost, W., J.R. Maus, & G.H. Fichtl, 1974: "A Boundary-Layer Analysis of Atmospheric Motion over a Semi-Elliptical Surface Obstruction," Boundary-Layer Meteorol. **7**, 165-184.

Fujita, T., 1978: "Determination of Turbulent Flux by the Bulk Method Using Measurements at Two Levels," Papers in Meteorol. and Geophys. (Japan) **29**, 1-15.

Garratt, J.R., 1972: "Studies of Turbulence in the Surface Layer over Water (Lough Neagh). Part II. Production and Dissipation of Velocity and Temperature Fluctuations," Quart. J. R. Meteorol. Soc. **98**, 642-657.

Garratt, J.R., 1977: "Review of Drag Coefficients over Oceans and Continents," Mon. Weather Rev.

AD-A110 488 NAVAL RESEARCH LAB · WASHINGTON DC F/G 4/2
REPORT AND ANALYSIS OF THE MAY 1979 MARINE SURFACE LAYER MICROM--ETC(U)
DEC 81 T V BLANC
UNCLASSIFIED NRL-8363 NL

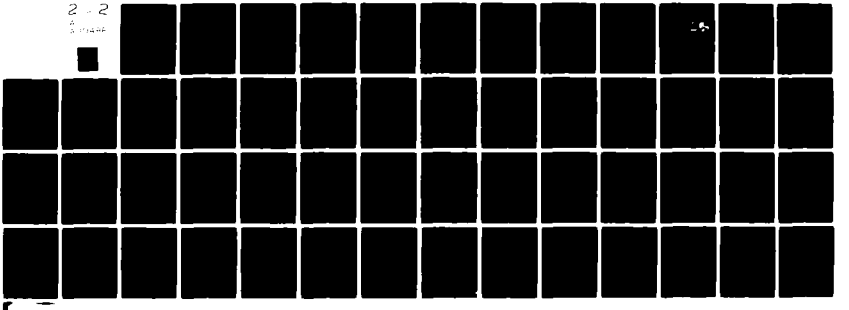

END
DATE FILMED
3 82
DTIC

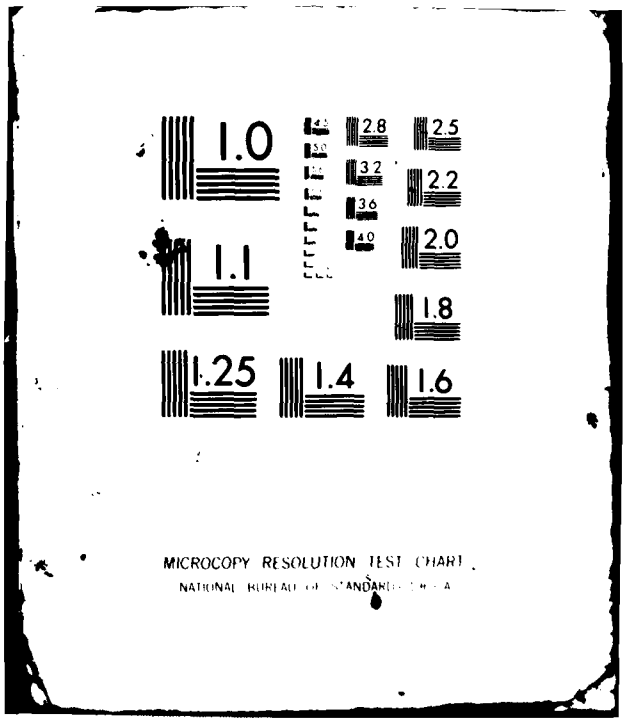
1.0
1.1
1.25
2.8
3.2
3.6
4.0
2.5
2.2
2.0
1.8
1.4
1.6
MICROCOPY RESOLUTION TEST CHART
NATIONAL BUREAU OF STANDARDS

105, 915-929.

Garratt, J.R., & P. Hyson, 1975: "Vertical Fluxes of Momentum, Sensible Heat and Water Vapour During the Air Mass Transformation Experiment (AMTEX) 1974," J. Meteorol. Soc. Japan **53**, 149-160.

Gathman, S.G., & R.K. Jeck, 1981. Private communication (Atmospheric Physics Branch, Naval Research Laboratory, Washington, D.C.).

Gill, G.C., L.E. Olsson, J. Sela, & M. Suda, 1967: "Accuracy of Wind Measurements on Towers or Stacks," Bull. Am. Meteorol. Soc. **48**, 665-674.

Goerss, J.S., & C.E. Duchon, 1980: "Effect of Ship Heating on Dry-Bulb Temperature Measurements in GATE," J. Phys. Oceanogr. **10**, 478-479.

Grassl, H., & H. Hinzpeter, 1975: "The Cool Skin of the Ocean," Global Atmospheric Research Program, GATE Report 14, Vol. II, pp. 229-236.

Hasegawa, S., 1980: Private communication of November 1980 (Humidity Section, Thermal Processes Division, National Bureau of Standards, Gaithersburg, Maryland).

Hasse, L., M. Grünewald, & D.E. Hasselmann, 1978a: "Field Observations of Air Flow above the Waves," *Turbulent Fluxes Through the Sea Surface, Wave Dynamics, and Prediction*, ed. by A. Favre & K. Hasselmann, Plenum Press, New York, pp. 483-494.

Hasse, L., M. Grünewald, J. Wucknitz, M. Dunckel, & D. Schriever, 1978b: "Profile Derived Turbulent Fluxes in the Surface Layer under Disturbed and Undisturbed Conditions during GATE," "Meteor" Forschungsergeb. (Berlin), Reihe B, No. 13, Berlin. 24-40.

Hasse, L., J. Wucknitz, G. Kruspe, V.N. Ivanov, A.A. Shuskov, I.V. Nekrasov, J.A. Volkov, B.M. Koprov, L.G. Elagina, J. Müller-Glewe, & H. Hinzpeter, 1975: "Preliminary Report on Determination of Fluxes by Direct and Profile Method during Intercomparison IIa," Global Atmospheric Research Program, GATE Report No. 14, Vol. II, pp. 267-277.

Hay, D.R., 1980: "Fast-Response Humidity Sensors," *Air-Sea Interaction Instruments and Methods*, ed. by F. Dobson, L. Hasse, & R. Davis, Plenum Press, New York, pp. 413-432.

Hill, M.N., ed. 1962: *The Sea: Ideas and Observations on Progress in the Study of the Seas*, Vol. 1, *Physical Oceanography*, Interscience Publishers, John Wiley & Sons, New York, p. 27 (dynamic viscosity of sea water at 20°C from Table V).

Hinzpeter, H., 1967: "The Diurnal Variation of the Water Surface Temperature in the Vicinity of the Equator," "Meteor" Forschungsergeb. Berlin, Reihe B, No. 1, 41-44 (Naval Intelligence Support Center translation no. 6376, Washington, D.C.)

Hoeber, H., 1969: "Wind, Temperature, and Humidity Profiles in the Atmospheric Surface Layer over the Equatorial Atlantic," "Meteor" Forschungsergeb. (Berlin), Reihe B, No. 3, 1-25 (Naval Intelligence Support Center translation no. 6378, Washington, D.C.).

Hoeber, H., 1977: "Accuracy of Meteorological Observations on the Ocean," Der Seewart (Hamburg) **38**, 204-213 (in German).

Horst, T.W., 1973: "Corrections for Response Errors in a Three-Component Propeller Anemometer," J. Appl. Meteorol. **12**, 716-725.

Hsu, S.-A., 1971: "Measurement of Shear Stress and Roughness Length on a Beach," J. Geophys. Res. **76**, 2880-2885.

Hsu, S.-A., 1973: "Dynamics of the Sea Breeze in the Atmospheric Boundary Layer: A Case Study of the Free Convection Regime," Mon. Weather Rev. **101**, 187-194.

Hsu, S.-A., 1977: "Boundary-Layer Meteorological Research in the Coastal Zone," Geoscience and Man **18**, 99-111.

Hunt, J.C.R., 1980: "Wind over Hills," *Workshop on Planetary Boundary Layer*, ed. by J.C. Wyngaard, American Meteorological Society, Boston, pp. 107-146.

Hunt, J.C.R., J.S. Puttock, & W.H. Snyder, 1979: "Turbulent Diffusion from a Point Source in Stratified and Neutral Flows around a Three-Dimensional Hill—Part I. Diffusion Equation Analysis," Atmos. Environ. **13**, 1227-1239.

Hupfer, P., T. Foken, & U. Bachstein, 1976: "Fine Structure of the Internal Boundary Layer in the Near-Shore Zone of the Sea," Boundary-Layer Meteorol. **10**, 503-505.

Huschke, R.E., 1959: *Glossary of Meteorology*, American Meteorological Society, Boston.

Hyson, P., J.R. Garratt, & R.J. Francey, 1977: "Algebraic and Electronic Corrections of Measured *uw* Covariance in the Lower Atmosphere," J. Appl. Meteorol. **16**, 43-47.

Itier, B., 1980: "Une Méthode Simplifiée Pour La Mesure Du Flux De Chaleur Sensible," J. Rech. Atmos. **14**, 17-34.

Ivanov, V.N., & A. Ye. Ordanovich, 1973: "Mesoscale Structure of the Atmospheric Boundary Layer and Its Interaction with Small-Scale Turbulence," Izv. Acad. of Sci. USSR, Atmos. Oceanic Phys. **9**, 387-393 (English translation).

Izumi, Y., & M.L. Barad, 1970: "Wind Speeds as Measured by Cup and Sonic Anemometers and Influenced by Tower Structure," J. Appl. Meteorol. **9**, 851-856.

Jackson, P.S., & J.C.R. Hunt, 1975: "Turbulent Wind Flow over a Low Hill," Quart. J. R. Meteorol. Soc. **101**, 929-955.

James, R.W., & P.T. Fox, 1972: "Comparative Sea-Surface Temperature Measurements," World Meteorological Organization Reports on Marine Science Affairs, No. 5, WMO-No. 336.

Jehn, K.H., & M.S. Jehn, 1979: "Beach Atmosphere,"

Weather **34**, 223-232.

Jensen, D.R., 1980: "San Nicolas Island CEWCOM-79 Data Report, Ground-Based and Airborne Aerosol-Size Distribution Measurements in the Marine Boundary Layer," Technical Note 798, Naval Ocean System Center, San Diego, California, pp. 760-763.

Jensen, N.O., & E.W. Peterson, 1978: "On the Escarpment Wind Profile," Quart. J. R. Meteorol. Soc. **104**, 719-728.

Kaimal, J.C., 1969: Measurement of momentum and heat flux variations in the surface boundary layer. Radio Sci., Vol. 4, 1147-1153.

Kaimal, J.C., 1975: "Sensors and Techniques for Direct Measurement of Turbulent Fluxes and Profiles in the Atmospheric Surface Layer," *Atmospheric Technology*, National Center for Atmospheric Research, Boulder, Colorado, No. 7, pp. 7-14.

Kaimal, J.C., 1980: "Sonic Anemometers," *Air-Sea Interaction Instruments and Methods*, ed. by F. Dobson, L. Hasse, & R. Davis, Plenum Press, New York, pp. 81-96.

Kaimal, J.C., & J.A. Businger, 1963: "A Continuous-Wave Sonic Anemometer-Thermometer," J. Appl. Meteorol. **2**, 156-164.

Kaimal, J.C., & D.A. Haugen, 1969: "Some Errors in the Measurement of Reynolds Stress," J. Appl. Meteorol. **8**, 460-462.

Kaimal, J.C., & D.A. Haugen, 1971: "Comments on 'Minimizing the Levelling Error in Reynolds Stress Measurement by Filtering,'" J. Appl. Meteorol. **10**, 337-339.

Kaimal, J.C., D.A. Haugen, & J.T. Newnan, 1966: "A Computer-Controlled Mobile Micrometeorological Observation System," J. Appl. Meteorol. **5**, 411-420.

Katsaros, K., 1980a: "Radiative Sensing of Sea Surface Temperature," *Air-Sea Interaction: Instruments and Methods*, ed. by F. Dobson, L. Hasse, & R. Davis, Plenum Press, New York, pp. 293-317.

Katsaros, K.B., 1980b: "The Aqueous Thermal Boundary Layer," Boundary-Layer Meteorol., **18**, 107-127.

Kidwell, K.B., & W.R. Seguin, 1978: "Comparison of Mast and Boom Wind Speed and Direction Measurements on U.S. GATE B-Scale Ships," National Oceanic and Atmospheric Administration Technical Report EDS28, Washington, D.C.

Kitaigorodskii, S.A., 1973: *The Physics of Air-Sea Interaction*, Israel Program for Scientific Translations, Jerusalem (English translation).

Kondo, J., 1975: "Air-Sea Bulk Transfer Coefficients in Diabatic Conditions," Boundary-Layer Meteorol. **9**, 91-112.

Kondo, J., 1977: "Comparison of the Kondo's Bulk Transfer Coefficient with the Recently-Made Direct Observations of Fluxes on the Sea Surface," J. Meteorol. Soc. Japan **55**, 319-323.

Kondo, J., & Y. Fujinawa, 1972: "Errors in Estimation of Drag Coefficient for Sea Surface in Light Winds," J. Meteorol. Soc. Japan **50**, 145-149.

Krechmer, S.I., G.N. Panin, & V.V. Ipatov, 1972: Measurement of humidity pulsations above the sea. Izvestiya, USSR Academy of Sciences, Atmos. & Oceanic Phys., Vol. 8, 448-450 (English translation).

Krügermeyer, L., 1976: "Vertical Transports of Momentum, Sensible and Latent Heat from Profiles at the Tropical Atlantic during ATEX," "Meteor" Forschungsergeb. (Berlin), Reihe B, No. 11, 51-77.

Krügermeyer, L., M. Grünewald, & M. Dunckel, 1978: "The Influence of Sea Waves on the Wind Profile," Boundary-Layer Meteorol. **14**, 403-414.

Kuznetsov, O.A., 1970: "Results of an Experimental Investigation of Airflow Above the Sea Surface," Izv., Acad. Sci. USSR, Atmos. Oceanic Phys., **6**, 469-472 (English translation).

Large, W.G., 1979: "The Turbulent Fluxes of Momentum and Sensible Heat Over the Open Sea During Moderate to Strong Winds," Ph.D. Thesis, Department of Physics, Institute of Oceanography, The University of British Columbia, Vancouver, Canada (Document No. ADA081392, Defense Technical Information Center, Alexandria, Va.).

Large, W.G., & S. Pond, 1981: "Open Ocean Momentum Flux Measurements in Moderate to Strong Winds," J. Phys. Oceanogr. **11**, 324-336.

Larsen, S.E., F.W. Weller, & J.A. Businger, 1979: "A Phase-Locked Loop Continuous Wave Sonic Anemometer-Thermometer," J. Appl. Meteorol. **18**, 562-568.

Larsen, S.E., J. Højstrup, & C.H. Gibson, 1980: "Fast-Response Temperature Sensors," *Air-Sea Interaction: Instruments and Methods*, ed. by F. Dobson, L. Hasse, & R. Davis, Plenum Press, New York, pp. 269-292.

Larson, R.E., 1973: "Measurements of Radioactive Aerosols using Thin Plastic Scintillators," Nucl. Instrum. Methods **108**, 467-470.

Larson, R.E., 1978: "Radon 222 Measurements During Marine Fog Events off Nova Scotia," J. Geophys. Res. **83** (C1), 415-418.

Larson, R.E., 1979: "Atmospheric ^{222}Rn Measurements at San Nicolas Island," Naval Research Laboratory Memorandum Report 4099, Washington, D.C.

LaRue, J.C., T. Deaton, & C.H. Gibson, 1975: "Measurement of High-Frequency Turbulent Temperature," Rev. Sci. Instrum. **46**, 757-764.

List, R.J., 1958: *Smithsonian Meteorological Tables*, Publication No. 4014, sixth revised ed., Smithsonian Institution, Washington, D.C.

Liu, W.T., K.B. Katsaros, & J.A. Businger, 1979: "Bulk Parameterization of Air-Sea Exchanges of Heat and Water Vapor Including the Molecular Constraints at the Interface," J. Atmos. Sci. **36**,

1722-1735.

Lo, A.K., 1977: "Boundary Layer Flow over Gentle Curvilinear Topography with a Sudden Change in Surface Roughness, Quart. J. R. Meteorol. Soc. **103**, 199-209.

Lo, A.K., & G.A. McBean, 1978: "On the Relative Errors in Methods of Flux Calculations," J. Appl. Meteorol. **17**, 1704-1711.

Lockhart, T.J., 1975: "Variable Errors in Operational Data Networks," *Third Symposium on Meteorological Observations and Instrumentation, Washington, D.C.*, American Meteorological Society, Boston, Mass., pp.

Lockhart, T.J., 1979: "Representativeness of Wind Measurements in Coastal Transitional Flow," *Preprints, Second Conference on Coastal Meteorology, Los Angeles, Calif., held in January 1980*, American Meteorological Society, Boston, Mass., pp. 227-232.

Makita, H., & R. Kikuchi, 1977: "Distribution of Air Temperature on the Sand Beach," Japanese Progress in Climatology, Tokyo, Nov. 1977, 47-56.

Mason, P.J., & R.I. Sykes, 1979: "Flow over an Isolated Hill of Moderate Slope," Quart. J. R. Meteorol. Soc. **105**, 383-395.

McBean, G.A., 1972: "Instrument Requirements for Eddy Correlation Measurements," J. Appl. Meteorol. **11**, 1078-1084.

McGavin, R.E., & M.J. Vetter, 1965: "Radio Refractometry and Its Potential for Humidity Studies," *Humidity and Moisture Measurement and Control in Science and Industry*, ed. by A. Wexler & E.J. Amdur, Reinhold Publishing, New York, Vol. 2, pp. 553-560.

McIntosh, D.H., 1972: *Meteorological Glossary*, 5th ed., Chemical Publishing, New York, p. 263.

McIntosh, D.H., and A.S. Thom, 1973: *Essentials of Meteorology*, Wykeham Publishers, London.

McKay, D.J., & J.D. McTaggart-Cowan, 1977: "An Intercomparison of Radiation Shields for Auto Stations," *World Meteorological Organization Technical Conference on Instrumentation and Methods of Observation* (Hamburg), WMO Report No. 480, pp. 208-213.

Mease, N., 1980: Private communication of November 1980 (Wind Tunnel Calibration Section, Fluid Engineering Division, National Bureau of Standards, Gaithersburg, Maryland).

Meshal, A.M., 1977: Comparison of Drag Coefficients Over Water Measured Directly and Determined by Wind Profile," Atmosphere **15**, 166-177.

Meyer, S.L., 1975: *Data Analysis for Scientists and Engineers*, John Wiley & Sons, New York, p. 22.

Mickle, R.E., & D.S. Davison, 1979: "Differences in Kilometer-Scale Wind and Humidity Boundary-Layer Structure at GATE," Atmosphere-Ocean **17**, 36-45.

Mitsuta, Y., 1966: "Sonic Anemometer-Thermometer for General Use," J. Meteorol. Soc. Japan **44**, 12-23.

Mitsuta, Y., & T. Fujitani, 1974: "Direct Measurements of Turbulent Fluxes on a Cruising Ship," Boundary-Layer Meteorol. **6**, 203-217.

Mitsuta, Y., N. Monji, & O. Tsukamoto, 1979: "Calibration of Anemometers on the Tarama Tower during AMTEX," J. Meteorol. Soc. Japan **57**, 93-95.

Mitsuta, Y., & O. Tsukamoto, 1978: "Drag Coefficients in Light Wind," Bull. Disaster Prev. Res. Inst. Kyoto Univ. (Japan) **28**, part 2, No. 255, 25-32.

Miyake, M., M. Donelan, G. McBean, C. Paulson, F. Badgley, & E. Leavitt, 1970a: "Comparison of Turbulent Fluxes over Water Determined by Profile and Eddy Correlation Techniques," Quart. J. R. Meteorol. Soc. **96**, 132-137.

Miyake, M., R.W. Stewart, & R.W. Burling, 1970b: "Spectra and Cospectra Turbulence over Water," Quart. J. R. Meteorol. Soc. **96**, 138-143.

Moffat, R.J., 1962: "Gas Temperature Measurement," *Temperature, Its Measurement and Control in Science and Industry*, ed. by C.M. Herzfeld & A.I. Dahl, Reinhold publishing, New York, Vol. 3, Part 2, pp. 553-571.

Mollo-Christensen, E., 1979: "Upwind Distortion Due to Probe Support in Boundary-Layer Observation," J. Appl. Meteorol. **18**, 367-370.

Moses, H., & H.G. Daubek, 1961: "Errors in Wind Measurements Associated with Tower-Mounted Anemometers," Bull. Am. Meteorol. Soc. **42**, 190-194.

Mulhearn, P.J., & J.J. Finnigan, 1978: "Turbulent Flow over a Very Rough, Random Surface," Boundary-Layer Meteorol. **15**, 109-132.

Myers, V.A., 1959: "Surface Friction in a Hurricane," Mon. Weather Rev. **87**, 307-311.

Naito, G., 1978: "Direct Measurements of Momentum and Sensible Heat Fluxes at the Tower in the Open Sea," J. Meteorol. Soc. Japan **56**, 25-34.

Naito, G., & J. Kondo, 1974: "Spatial Structure of Fluctuating Components of the Horizontal Wind Speed over the Ocean," J. Meteorol. Soc. Japan [illegible]-399.

National Ocean Survey, 1978: "San Nicolas Island Chart 18755," National Oceanic and Atmospheric Administration, U.S. Department of Commerce, Washington, D.C.

National Ocean Survey, 1979: *Tide Tables for the West Coast of North America*, U.S. Government Printing Office, Washington, D.C.

Naval Weather Service Environmental Detachment, 1971: "Climatological Study: Southern California Operating Area," Naval Weather Service Command, National Climatic Center, Asheville, North Carolina.

Neumann, G., 1959: "Notes on the Stress of Light Winds on the Sea," Bull. Am. Meteorol. Soc. **40**, 146-148.

Nicholls, S., & C.J. Readings, 1979: "Aircraft Observa-

tions of the Structure of the Lower Boundary Layer over the Sea," Quart. J. R. Meteorol. Soc. **105**, 785-802.

Noonkester, V.R., C.N.K. Mooers, and D.F. Leipper, 1980: "Second Conference on Coastal Meteorology, American Meteorological Society, 30 January — 11 February 1980, Los Angeles, California, Bull. Am. Meteorol. Soc. **61**, 1429-1436.

Okamoto, M., H. Uotsu, & T. Furukawa, 1968: "An Estimation of the Heat Flux and the Water Vapour Flux by the Bulk Aerodynamic Method," Papers in Meteorol. and Geophys. (Japan) **19**, 231-241.

Pande, A., 1970: *Modern Hygrometry*, Somaiya, Bombay, India, pp. 19-31.

Panofsky, H.A., 1965: "Reanalysis of Swinbank's Kerange Observations," Report No. AFCRL-65-531, "Flux of Heat and Momentum in the Planetary Boundary Layer," pp 66-76, Pennsylvania State University Department of Meteorology, University Park, Pennsylvania. Report prepared for the Air Force Cambridge Research Laboratory, Bedford, Massachusetts under contract no. AF(604)-6641. Copies available via Defense Technical Information Center, Alexandria, Va. 22314.

Panofsky, H.A., & A.A. Townsend, 1964: "Change of Terrain Roughness and the Wind Profile," Quart. J. R. Meteorol. Soc. **90**, 147-155.

Paulson, C.A., 1970: "The Mathematical Representation of Wind Speed and Temperature Profiles in the *Unstable Atmospheric Surface Layer*," J. Appl. Meteorol. **9**, 857-861.

Paulson, C.A., E. Leavitt, & R.G. Fleagle, 1972: "Air-Sea Transfer of Momentum, Heat and Water Determined from Profile Measurements During BOMEX," J. Phys. Oceanogr. **2**, 487-497.

Pedersen, K., & G. Bφyum, 1980: "Turbulent Flux of Heat and Water Vapor from the Ocean," *Tellus* **32**, 320-325.

Peterson, E.W., 1969: "Modification of Mean Flow and Turbulent Energy by a Change in Surface Roughness under Conditions of Neutral Stability," Quart. J. R. Meteorol. Soc. **95**, 561-575.

Peterson, E.W., 1975: "The Risφ Profiles: A Study of Wind and Temperature Data from the 123 m Tower at Risφ, Denmark," Quart. J. R. Meteorol. Soc. **101**, 107-117.

Peterson, E.W., N.O. Jensen, & J. Hφjstrup, 1979: "Observations of Downwind Development of Wind Speed and Variance Profiles at Bognaes and Comparison with Theory," Quart. J. R. Meteorol. Soc. **105**, 521-529.

Peterson, E.W., P.A. Taylor, J. Hφjstrup, N.O. Jensen, L. Kristensen, & E.L. Petersen, 1980: "Risφ 1978: Further Investigation into the Effects of Local Terrain Irregularities on Tower-Measured Wind Profiles," Boundary-Layer Meteorol. **19**, 303-313.

Phelps, G.T., & S. Pond, 1971: "Spectra of the Temperature and Humidity Fluctuations and of the Fluxes of Moisture and Sensible Heat in the Marine Boundary Layer," J. Atmos. Sci. **28**, 918-928.

Pond, S., D.B. Fissel, & C.A. Paulson, 1974: "A Note on Bulk Aerodynamic Coefficients for Sensible Heat and Moisture Fluxes," Boundary-Layer Meteorol. **6**, 333-339.

Pond, S., W.G. Large, M. Miyake, & R.W. Burling, 1979: "A Gill Twin Propeller-Vane Anemometer for Flux Measurements during Moderate and Strong Winds," Boundary-Layer Meteorol. **16**, 351-364.

Pond, S., G.T. Phelps, J.E. Paquin, G. McBean, & R.W. Stewart, 1971: "Measurements of the Turbulent Fluxes of Momentum, Moisture and Sensible Heat over the Ocean," J. Atmos. Sci. **28**, 901-917.

Raupach, M.R., 1978: "Infrared Fluctuation Hygrometry in the Atmospheric Surface Layer," Quart. J. R. Meteorol. Soc. **104**, 309-322.

Raynor, G.S., S. Sethuraman, & R.M. Brown, 1979: "Formation and Characteristics of Coastal Internal Boundary Layers during Onshore Flows," Boundary-Layer Meteorol. **16**, 487-514.

Reed, R.K., 1978: "An Example of Shipboard Air Temperature Errors," Mariners Weather Log **22**, 13-14.

Reuter, U., & E. Raschke, 1977: "Solar Heating of the Upper Ocean Layers," *International Symposium on Radiation in the Atmosphere, August 1976, Proceedings*, Science Press, Princeton, New Jersey, pp. 289-291.

Roll, H.U., 1965: *Physics of the Marine Atmosphere*, Academic Press, New York.

Sacré, C., 1979: "An Experimental Study of the Airflow over a Hill in the Atmospheric Boundary Layer," Boundary-Layer Meteorol. **17**, 381-401.

Saunders, P.M., 1967: "The Temperature at the Ocean-Air Interface," J. Atmos. Sci. **24**, 269-273.

Scheid, F., 1968: *Schaum's Outline of Theory and Problems of Numerical Analysis*, McGraw-Hill, New York.

Schmitt, K.F., C.A. Friehe, & C.H. Gibson, 1978: "Humidity Sensitivity of Atmospheric Temperature Sensors by Salt Contamination," J. Phys. Oceanogr. **8**, 151-161.

Schmitt, K.F., C.A. Friehe, & C.H. Gibson, 1979: "Structure of Marine Surface Layer Turbulence," J. Atmos. Sci. **36**, 602-618.

Schooley, A.H., 1977: "Temperature of Ocean Skin Related to Cloud Shadows," J. Phys. Oceanogr. **7**, 486-488.

Shaw, R.H., G. Kidd, & G.W. Thurtell, 1973: "A Miniature Three-Dimensional Anemometer for Use within and above Plant Canopies," Boundary-Layer Meteorol. **3**, 359-380.

Sheppard, P.A., D.T. Tribble, & J.R. Garratt, 1972: "Studies of Turbulence in the Surface Layer over Water (Lough Neagh): Part 1. Instrumentation,

Programme, Profiles," Quart. J. R. Meteorol. Soc. **98**, 627-641.

Shifrin, K.S., 1974: "Influence of Wind on the Effective Radiation of the Ocean," Izv. Acad. Sci., USSR, Atmos. Oceanic Phys. **10**, 495-496 (English translation).

Shir, C.C., 1972: "A Numerical Computation of Air Flow over a Sudden Change of Surface Roughness," J. Atmos. Sci. **29**, 304-310.

Simpson, J.J., & C.A. Paulson, 1980: "Small-Scale Sea Surface Temperature Structure," J. Phys. Oceanogr. **10**, 399-410.

Smedman-Högström, A.-S., & U. Högström, 1973: "The Marsta Micrometeorologicai Field Project. Profile Measurement System and Some Preliminary Data," Boundary-Layer Meteorol. **5**, 259-273.

Smith, L.P., 1970: "The Difficult Art of Measurement," editorial, Agricultural Meteorol. **7**, 281-283.

Smith, S.D., 1970: "Thrust-Anemometer Measurements of Wind Turbulence, Reynolds Stress, and Drag Coefficient over the Sea," J. Geophys. Res. **75**, 6758-6770.

Smith, S.D., 1974: "Eddy Flux Measurements over Lake Ontario," Boundary-Layer Meteorol. **6**, 235-255.

Smith, S.D., 1980a: "Wind Stress and Heat Flux over the Ocean in Gale Force Winds," J. Phys. Oceanogr. **10**, 709-726.

Smith, S.D., 1980b: "Evaluation of the Mark 8 Thrust Anemometer-Thermometer for Measurement of Boundary-Layer Turbulence," Boundary-Layer Meteorol. **19**, 273-292.

Smith, S.D., 1981a: Private communications of April and May 1981. (Bedford Institute of Oceanography, Dartmouth, Nova Scotia, Canada)

Smith, S.D., 1981b: "Comment on 'A New Evaluation of the Wind Stress Coefficient Over Water Surfaces'," J. Geophys. Res. 86, C5, 4307-4308.

Smith, S.D., & E.G. Banke, 1975: "Variation of the Sea Surface Drag Coefficient with Wind Speed," Quart. J. R. Meteorol. Soc. **101**, 665-673.

Smith, S.D. & K.B. Katsaros, 1981: "HEXOS — Humidity Exchange Over the Sea, An Experiment Proposal," Bedford Institute of Oceanography Report BI-R-81-17, Dartmouth, Nova Scotia, Canada.

Sutton, O.G., 1953: *Micrometeorology, a Study of Physical Processes in the Lowest Layers of the Earth's Atmosphere*, McGraw-Hill, New York.

Takahashi, T., 1958: "Micrometeorological Observations and Studies over the Sea," Mem. Fac. Fish. Kagoshima Univ. (Japan) **6**, 1-46.

Taylor, P.A., 1970: "A Model of Airflow above Changes in Surface Heat Flux, Temperature, and Roughness for Neutral and Unstable Conditions," Boundary-Layer Meteorol. **1**, 18-39.

Taylor, P.A., 1977: "Some Numerical Studies of Surface Boundary-Layer Flow above Gentle Topography," Boundary-Layer Meteorol. **11**, 439-465.

Taylor, P.A., & P.R. Gent, 1974: "A Model of Atmospheric Boundary-Layer Flow above an Isolated Two-Dimensional 'Hill'; An Example of Flow above 'Gentle Topography'," Boundary-Layer Meteorol. **7**, 349-362.

Tennekes, H., & J.C. Wyngaard, 1972: "The Intermittent Small-Scale Structure of Turbulence: Data-Processing Hazards," J. Fluid Mech. **55**, 93-103.

Thornthwaite, C.W., W.J. Superior, and R.T. Field, "Disturbance of Airflow around Argus Island Tower near Bermuda," J. Geophys. Res. **70**, 6047-6052 (1965).

Tuller, S.E., 1972: "Energy Balance Microclimatic Variations on a Coastal Beach," Tellus **24**, 260-270.

Tverskoi, P.N., 1965: *Physics of the Atmosphere, a Course in Meteorology*, Israel Program for Scientific Translations, Jerusalem (English translation).

Vedder, J.G., & R.M. Norris, 1963: "Geology of San Nicolas Island, California," Geological Survey Professional Paper 369, U.S. Department of the Interior, Washington, D.C.

Vugts, H.F., 1980: "A Study of Terrain Inhomogeneity," Bull. Am. Meteorol. Soc. **61**, 568-569.

Vugts, H.F., & J.A. Businger, 1977: "Air Modification Due to a Step Change in Surface Temperature, Boundary-Layer Meteorol. **11**, 295-305.

Waletzko, J.A., 1975: "A New Ion Displacement System to Measure the Two Dimensional Wind Vector," TSI Incorporated, St. Paul, Minnesota 55164.

Warner, J., 1971: "Observations of the Eddy Fluxes of Heat and Vapour over the Sea," Quart. J. R. Meteorol. Soc. **97**, 540-547.

Warner, J., 1972: "The Structure and Intensity of Turbulence in the Air over the Sea," Quart. J. R. Meteorol. Soc. **98**, 175-186.

Weiler, H.S., & R.W. Burling, 1967: "Direct Measurements of Stress and Spectra of Turbulence in the Boundary Layer Over the Sea," J. Atmos. Sci. **24**, 653-664.

Wieringa, J., 1974: "Comparison of Three Methods for Determining Strong Wind Stress over Lake Flevo," Boundary-Layer Meteorol. **7**, 3-19.

Wieringa, J., 1980: "A Reevaluation of the Kansas Mast Influence on Measurements of Stress and Cup Anemometer Overspeeding," Boundary-Layer Meteorol. **18**, 411-430.

Witting, J., 1972: "Temperature Fluctuations at an Air-Water Interface Caused by Surface Waves," J. Geophys. Res. **77**, 3265-3269.

Wood, D.H., 1978: "Calculation of the Neutral Wind Profile Following a Large Step Change in Surface Roughness," Quart. J. R. Meteorol. Soc. **104**, 383-392.

Wu, J., 1980: "Wind-Stress Coefficients over Sea Surface Near-Neutral Conditions — A Revisit," J. Phys. Oceanogr. **10**, 727-740.

Wucknitz, J., 1977: "Disturbance of Wind Profile Measurements by a Slim Mast," Boundary-Layer Meteorol. **11**, 155-169.

Wucknitz, J., 1980: "Flow Distortion by Supporting Structures," *Air-Sea Interaction Instruments and Methods*, ed. by F. Dobson, L. Hasse, & R. Davis, Plenum Press, New York, pp. 605-626.

Wüst, G., 1920: "Die Verdunstung auf dem Meere," Veröffentl. Inst. Meereskunde Univ. Berlin, No. 6.

Wylie, D.P., & C.F. Ropelewski, 1980: "The GATE Boundary Layer Instrumentation System (BLIS)," Bull. Am. Meteorol. Soc. **61**, 1002-1011.

Yaglom, A.M., 1974: "Data on Turbulence Characteristics in the Atmospheric Surface Layer," Izv., Acad. of Sci., USSR, Atmos. Oceanic Phys. **10**, 341-352 (English translation).

Yaglom, A.M., 1977: "Comments on Wind and Temperature Flux-Profile Relationships," Boundary-Layer Meteorol. **11**, 89-102.

Appendix A

ESCARPMENT AND WIND SPEED CORRECTION TABLES

Table A.1 — Measurement Site Nearfield Escarpment Survey. The values indicated are the height[a] of the escarpment as measured from its top expressed in negative meters. The top of the escarpment was located vertically below the sensors on the fully extended arms of the tower.

Upwind Distance (meters)	Wind Direction (True)[b]												
	225°	240°	255°	270°	285°	300°	315°	330°	345°	360°	15°	30°	45°
0	0	0	0	0	0	0	0	0	0	0	0	0	0
1	0	0.03	0.06	0.08	0.12	0.14	0.16	0.17	0.17	0.13	0.09	0.08	0.08
2	0	0.06	0.13	0.17	0.24	0.28	0.32	0.33	0.33	0.27	0.18	0.17	0.15
3	0	0.06	0.18	0.27	0.34	0.37	0.41	0.45	0.45	0.43	0.33	0.18	0.17
4	0	0.10	0.27	0.36	0.42	0.46	0.52	0.56	0.57	0.56	0.39	0.28	0.13
5	0	0.17	0.38	0.43	0.51	0.58	0.64	0.69	0.71	0.70	0.57	0.36	0.17
6	0	0.24	0.42	0.53	0.57	0.65	0.71	0.81	0.86	0.86	0.91	0.65	0.30
7	0.05	0.29	0.51	0.56	0.61	0.71	0.79	0.89	0.94	1.12	1.59	1.46	0.38
8	0.11	0.43	0.61	0.67	0.65	0.74	0.83	0.93	0.98	1.31	2.10	1.75	0.62
9	0.20	0.51	0.61	0.75	0.69	0.75	0.86	1.08	1.24	2.06	2.26	1.88	0.57
10	0.24	0.56	0.74	0.83	0.75	0.77	0.90	1.22	1.78	2.67	2.30	2.13	0.69
11	0.37	0.74	0.84	0.89	0.85	0.75	1.11	1.96	2.82	2.79	2.54	2.12	0.81
12	0.41	0.89	0.97	0.99	0.94	0.89	1.87	2.49	2.95	2.92	2.68	2.32	1.12
13	0.61	0.91	1.09	1.13	1.04	0.99	2.48	2.90	3.15	3.14	2.78	2.41	1.21
14	0.83	1.12	1.17	1.31	1.16	1.12	2.67	3.15	3.28	3.25	2.82	2.44	1.05
15	0.89	1.31	1.32	1.50	1.32	1.30	2.92	3.28	3.38	3.30	2.25	2.59	1.07
16	1.28	1.32	1.61	1.59	1.41	1.71	2.97	3.38	3.47	3.44	3.00	2.73	1.18
17	1.36	1.59	1.83	1.80	1.57	2.31	3.20	3.48	3.52	3.51	3.25	2.74	1.30
18	1.38	1.55	1.83	1.88	1.71	2.72	3.30	3.58	3.66	3.63	3.35	2.98	1.33
19	1.42	1.56	1.70	1.77	1.78	2.82	3.43	3.68	3.66	3.66	3.43	2.84	1.57
20	1.45	1.63	1.70	1.65	1.87	2.97	3.56	3.84	4.05	3.86	3.47	3.05	2.10
21	1.33	1.70	1.80	1.91	1.88	3.02	3.58	3.99	4.19	3.99	3.56	3.16	2.51
22	1.46	1.73	1.99	1.94	1.98	2.96	3.73	4.09	4.39	4.11	3.68	2.92	2.61
23	1.51	1.70	1.83	2.06	2.06	3.00	3.89	4.22	4.61	4.22	3.81	3.23	2.69
24	1.51	1.78	1.91	2.02	2.44	2.98	4.09	4.37	4.72	4.52	3.89	3.11	2.73
25	1.50	1.92	1.99	2.08	2.54	3.06	4.29	4.65	4.72	4.78	4.03	3.45	2.79

[a]Accurate to ±4% of indicated value.
[b]Accurate to ±2° of indicated true direction.

Table A.2 — Wind Speed Amplification Factor for the Top of a Semielliptical Shaped Escarpment Computed via Eq. 11.1.

ESCARPMENT ASPECT RATIO (height/length)

NORMALIZED HEIGHT ABOVE ESCARPMENT

	0.01	0.02	0.03	0.04	0.05	0.06	0.07	0.08	0.09	0.10	0.11	0.12	0.13	0.14	0.15	0.16	0.17	0.18	0.19	0.20	0.21	0.22	0.23	0.24	0.25
5.0							1.000	1.000	1.000	1.000	1.000	1.000	1.000	1.000	1.000	1.000	1.000	1.000	1.000	1.000	1.000	1.000	1.000	1.000	1.000
4.9							1.000	1.000	1.000	1.000	1.000	1.000	1.000	1.000	1.000	1.000	1.000	1.001	1.001	1.001	1.001	1.001	1.001	1.001	1.001
4.8							1.000	1.000	1.000	1.000	1.000	1.000	1.001	1.001	1.001	1.001	1.001	1.001	1.001	1.001	1.001	1.001	1.001	1.001	1.001
4.7							1.000	1.000	1.000	1.001	1.001	1.001	1.001	1.001	1.001	1.001	1.001	1.001	1.001	1.002	1.002	1.002	1.002	1.002	1.002
4.6							1.000	1.000	1.001	1.001	1.001	1.001	1.001	1.001	1.002	1.002	1.002	1.002	1.002	1.002	1.002	1.002	1.002	1.002	1.003
4.5							1.000	1.000	1.001	1.001	1.001	1.001	1.002	1.002	1.002	1.002	1.002	1.003	1.003	1.003	1.003	1.003	1.003	1.003	1.003
4.4							1.000	1.001	1.001	1.001	1.002	1.002	1.002	1.002	1.003	1.003	1.003	1.003	1.003	1.004	1.004	1.004	1.004	1.004	1.004
4.3							1.000	1.001	1.001	1.002	1.002	1.002	1.003	1.003	1.003	1.004	1.004	1.004	1.004	1.004	1.005	1.005	1.005	1.005	1.005
4.2							1.000	1.001	1.002	1.002	1.002	1.003	1.003	1.004	1.004	1.004	1.004	1.005	1.005	1.005	1.005	1.006	1.006	1.006	1.006
4.1							1.000	1.002	1.002	1.002	1.002	1.003	1.004	1.004	1.005	1.005	1.005	1.006	1.006	1.006	1.006	1.007	1.007	1.007	1.007
4.0							1.001	1.001	1.002	1.003	1.003	1.004	1.005	1.005	1.005	1.006	1.006	1.007	1.007	1.007	1.008	1.008	1.008	1.008	1.009
3.9							1.001	1.002	1.003	1.003	1.004	1.005	1.005	1.006	1.006	1.007	1.007	1.008	1.008	1.008	1.009	1.009	1.010	1.010	1.010
3.8							1.001	1.002	1.003	1.004	1.005	1.005	1.006	1.007	1.007	1.008	1.008	1.009	1.009	1.010	1.010	1.011	1.011	1.011	1.012
3.7							1.001	1.002	1.003	1.004	1.005	1.006	1.007	1.008	1.008	1.009	1.009	1.010	1.011	1.011	1.012	1.012	1.012	1.013	1.013
3.6							1.001	1.003	1.004	1.005	1.006	1.007	1.008	1.009	1.009	1.010	1.011	1.011	1.012	1.012	1.013	1.014	1.014	1.014	1.015
3.5							1.001	1.003	1.004	1.006	1.007	1.008	1.009	1.010	1.011	1.011	1.012	1.013	1.013	1.014	1.015	1.015	1.016	1.016	1.017
3.4							1.001	1.003	1.005	1.006	1.008	1.009	1.010	1.011	1.012	1.013	1.013	1.014	1.015	1.016	1.016	1.017	1.017	1.018	1.019
3.3							1.002	1.004	1.005	1.007	1.008	1.010	1.011	1.012	1.013	1.014	1.015	1.016	1.017	1.018	1.019	1.019	1.019	1.020	1.021
3.2							1.002	1.004	1.006	1.008	1.009	1.011	1.012	1.013	1.014	1.015	1.016	1.017	1.018	1.019	1.020	1.021	1.022	1.023	1.023
3.1							1.002	1.004	1.007	1.008	1.010	1.012	1.013	1.015	1.016	1.017	1.018	1.019	1.020	1.021	1.022	1.023	1.024	1.024	1.025
3.0							1.002	1.005	1.007	1.009	1.011	1.013	1.015	1.016	1.017	1.019	1.020	1.021	1.022	1.023	1.024	1.025	1.026	1.027	1.028
2.9							1.002	1.005	1.008	1.010	1.012	1.014	1.016	1.017	1.019	1.020	1.022	1.023	1.024	1.025	1.026	1.027	1.028	1.029	1.030
2.8							1.003	1.006	1.009	1.011	1.013	1.015	1.017	1.019	1.021	1.022	1.024	1.025	1.026	1.028	1.029	1.030	1.031	1.032	1.033
2.7							1.003	1.006	1.009	1.012	1.015	1.017	1.019	1.021	1.023	1.024	1.026	1.027	1.029	1.030	1.031	1.033	1.034	1.035	1.036
2.6							1.003	1.007	1.010	1.013	1.016	1.018	1.021	1.023	1.025	1.026	1.028	1.030	1.031	1.033	1.034	1.035	1.037	1.038	1.039
2.5							1.003	1.007	1.011	1.014	1.017	1.020	1.022	1.025	1.027	1.029	1.030	1.032	1.034	1.035	1.037	1.038	1.040	1.041	1.042
2.4							1.004	1.008	1.012	1.015	1.019	1.021	1.024	1.027	1.029	1.031	1.033	1.035	1.037	1.038	1.040	1.042	1.043	1.044	1.046
2.3							1.004	1.009	1.013	1.017	1.020	1.023	1.026	1.029	1.031	1.034	1.036	1.038	1.040	1.042	1.043	1.045	1.047	1.048	1.050
2.2							1.004	1.009	1.014	1.018	1.022	1.025	1.028	1.031	1.034	1.036	1.039	1.041	1.043	1.045	1.047	1.049	1.050	1.052	1.054
2.1							1.005	1.010	1.015	1.020	1.024	1.027	1.031	1.034	1.037	1.039	1.042	1.044	1.047	1.049	1.051	1.053	1.055	1.056	1.058
2.0							1.005	1.011	1.016	1.021	1.026	1.030	1.033	1.037	1.040	1.043	1.045	1.048	1.050	1.053	1.055	1.057	1.059	1.061	1.063
1.9							1.006	1.012	1.018	1.023	1.028	1.032	1.036	1.040	1.043	1.046	1.049	1.052	1.055	1.057	1.060	1.062	1.064	1.066	1.068
1.8							1.006	1.013	1.020	1.025	1.030	1.035	1.039	1.043	1.047	1.050	1.054	1.057	1.060	1.062	1.065	1.068	1.070	1.072	1.074
1.7							1.007	1.014	1.021	1.027	1.033	1.038	1.043	1.047	1.051	1.055	1.059	1.062	1.065	1.068	1.071	1.074	1.076	1.079	1.081
1.6							1.007	1.016	1.023	1.030	1.036	1.042	1.047	1.052	1.056	1.060	1.064	1.068	1.071	1.075	1.078	1.081	1.084	1.086	1.089
1.5							1.008	1.017	1.026	1.033	1.040	1.046	1.052	1.057	1.062	1.066	1.071	1.075	1.079	1.082	1.086	1.089	1.092	1.095	1.098
1.4							1.009	1.019	1.029	1.037	1.044	1.051	1.057	1.063	1.069	1.074	1.079	1.083	1.087	1.091	1.095	1.099	1.102	1.106	1.109
1.3							1.010	1.022	1.032	1.041	1.050	1.057	1.064	1.071	1.077	1.083	1.088	1.093	1.098	1.102	1.106	1.111	1.114	1.118	1.122
1.2							1.011	1.024	1.036	1.047	1.056	1.065	1.073	1.080	1.087	1.093	1.099	1.105	1.110	1.116	1.120	1.125	1.129	1.134	1.138
1.1							1.013	1.028	1.041	1.053	1.064	1.074	1.083	1.092	1.100	1.107	1.114	1.120	1.126	1.132	1.138	1.143	1.148	1.153	1.158
1.0							1.015	1.033	1.048	1.062	1.075	1.086	1.097	1.107	1.116	1.124	1.132	1.140	1.147	1.154	1.160	1.166	1.172	1.178	1.183

ESCARPMENT ASPECT RATIO (height/length)

NORMALIZED HEIGHT ABOVE ESCARPMENT

	0.26	0.27	0.28	0.29	0.30	0.31	0.32	0.33	0.34	0.35	0.36	0.37	0.38	0.39	0.40	0.41	0.42	0.43	0.44	0.45	0.46	0.47	0.48	0.49	0.50
5.0	1.000	1.000	1.000	1.000	1.000	1.000	1.000	1.000	1.000	1.000	1.000	1.000	1.000	1.000	1.000	1.000	1.000	1.000	1.000	1.000	1.001	1.001	1.001	1.001	1.001
4.9	1.001	1.001	1.001	1.001	1.001	1.001	1.001	1.001	1.001	1.001	1.001	1.001	1.001	1.001	1.001	1.001	1.001	1.001	1.001	1.001	1.001	1.001	1.001	1.001	1.001
4.8	1.001	1.001	1.001	1.001	1.001	1.001	1.001	1.001	1.001	1.001	1.001	1.001	1.001	1.001	1.001	1.001	1.002	1.002	1.002	1.002	1.002	1.002	1.002	1.002	1.002
4.7	1.002	1.002	1.002	1.002	1.002	1.002	1.002	1.002	1.002	1.002	1.002	1.002	1.002	1.002	1.002	1.003	1.003	1.003	1.003	1.003	1.003	1.003	1.003	1.003	1.003
4.6	1.003	1.003	1.003	1.003	1.003	1.003	1.003	1.003	1.003	1.003	1.003	1.003	1.003	1.003	1.003	1.004	1.004	1.004	1.004	1.004	1.004	1.004	1.004	1.004	1.004
4.5	1.003	1.004	1.004	1.004	1.004	1.004	1.004	1.004	1.004	1.004	1.004	1.004	1.004	1.004	1.005	1.005	1.005	1.005	1.005	1.005	1.005	1.005	1.005	1.005	1.005
4.4	1.004	1.004	1.005	1.005	1.005	1.005	1.005	1.005	1.005	1.005	1.005	1.006	1.006	1.006	1.006	1.006	1.006	1.006	1.006	1.006	1.006	1.006	1.006	1.006	1.006
4.3	1.005	1.006	1.006	1.006	1.006	1.006	1.006	1.006	1.006	1.007	1.007	1.007	1.007	1.007	1.007	1.007	1.007	1.007	1.007	1.007	1.008	1.008	1.008	1.008	1.008
4.2	1.006	1.007	1.007	1.007	1.007	1.007	1.007	1.008	1.008	1.008	1.008	1.008	1.008	1.008	1.008	1.009	1.009	1.009	1.009	1.009	1.009	1.009	1.009	1.009	1.010
4.1	1.008	1.008	1.008	1.008	1.008	1.009	1.009	1.009	1.009	1.009	1.009	1.010	1.010	1.010	1.010	1.010	1.010	1.011	1.011	1.011	1.011	1.011	1.011	1.011	1.011
4.0	1.009	1.009	1.009	1.010	1.010	1.010	1.010	1.011	1.011	1.011	1.011	1.011	1.011	1.012	1.012	1.012	1.012	1.012	1.012	1.013	1.013	1.013	1.013	1.013	1.013
3.9	1.010	1.011	1.011	1.011	1.011	1.012	1.012	1.012	1.012	1.013	1.013	1.013	1.013	1.013	1.014	1.014	1.014	1.014	1.014	1.015	1.015	1.015	1.015	1.015	1.015
3.8	1.012	1.012	1.013	1.013	1.013	1.013	1.014	1.014	1.014	1.014	1.015	1.015	1.015	1.015	1.016	1.016	1.016	1.016	1.016	1.017	1.017	1.017	1.017	1.017	1.017
3.7	1.014	1.014	1.014	1.015	1.015	1.015	1.016	1.016	1.016	1.016	1.017	1.017	1.017	1.017	1.018	1.018	1.018	1.018	1.019	1.019	1.019	1.019	1.019	1.020	1.020
3.6	1.015	1.016	1.016	1.017	1.017	1.017	1.018	1.018	1.018	1.019	1.019	1.019	1.019	1.020	1.020	1.020	1.021	1.021	1.021	1.021	1.022	1.022	1.022	1.022	1.022
3.5	1.017	1.018	1.018	1.019	1.019	1.019	1.020	1.020	1.020	1.021	1.021	1.021	1.022	1.022	1.022	1.023	1.023	1.023	1.024	1.024	1.024	1.024	1.025	1.025	1.025
3.4	1.019	1.020	1.020	1.021	1.021	1.022	1.022	1.022	1.023	1.023	1.024	1.024	1.024	1.025	1.025	1.025	1.026	1.026	1.026	1.027	1.027	1.027	1.027	1.028	1.028
3.3	1.021	1.022	1.022	1.023	1.023	1.024	1.024	1.025	1.025	1.026	1.026	1.027	1.027	1.027	1.028	1.028	1.028	1.029	1.029	1.030	1.030	1.030	1.030	1.031	1.031
3.2	1.024	1.024	1.025	1.025	1.026	1.026	1.027	1.027	1.028	1.028	1.029	1.029	1.030	1.030	1.031	1.031	1.031	1.032	1.032	1.033	1.033	1.033	1.034	1.034	1.034
3.1	1.026	1.027	1.027	1.028	1.028	1.029	1.030	1.030	1.031	1.031	1.032	1.032	1.033	1.033	1.034	1.034	1.035	1.035	1.035	1.036	1.036	1.037	1.037	1.037	1.038
3.0	1.028	1.029	1.030	1.031	1.031	1.032	1.033	1.033	1.034	1.034	1.035	1.035	1.036	1.036	1.037	1.037	1.038	1.038	1.039	1.039	1.040	1.040	1.041	1.041	1.041
2.9	1.031	1.032	1.033	1.033	1.034	1.035	1.036	1.036	1.037	1.038	1.038	1.039	1.039	1.040	1.040	1.041	1.042	1.042	1.043	1.043	1.043	1.044	1.044	1.045	1.045
2.8	1.034	1.035	1.036	1.036	1.037	1.038	1.039	1.040	1.040	1.041	1.042	1.042	1.043	1.044	1.044	1.045	1.045	1.046	1.046	1.047	1.047	1.048	1.048	1.049	1.049
2.7	1.037	1.038	1.039	1.040	1.041	1.041	1.042	1.043	1.044	1.045	1.045	1.046	1.047	1.047	1.048	1.049	1.049	1.050	1.050	1.051	1.052	1.052	1.053	1.053	1.054
2.6	1.040	1.041	1.042	1.043	1.044	1.045	1.046	1.047	1.048	1.048	1.049	1.050	1.051	1.051	1.052	1.053	1.054	1.054	1.055	1.055	1.056	1.057	1.057	1.058	1.058
2.5	1.043	1.045	1.046	1.047	1.048	1.049	1.050	1.051	1.052	1.052	1.053	1.054	1.055	1.056	1.057	1.057	1.058	1.059	1.059	1.060	1.061	1.061	1.062	1.063	1.063
2.4	1.047	1.048	1.049	1.051	1.052	1.053	1.054	1.055	1.056	1.057	1.058	1.059	1.060	1.060	1.061	1.062	1.063	1.064	1.064	1.065	1.066	1.067	1.067	1.068	1.069
2.3	1.051	1.052	1.054	1.055	1.056	1.057	1.058	1.059	1.061	1.062	1.063	1.064	1.065	1.065	1.066	1.067	1.068	1.069	1.070	1.071	1.071	1.072	1.073	1.074	1.074
2.2	1.055	1.057	1.058	1.059	1.061	1.062	1.063	1.064	1.066	1.067	1.068	1.069	1.071	1.072	1.073	1.074	1.075	1.076	1.077	1.078	1.079	1.080	1.081	1.082	1.083
2.1	1.060	1.061	1.063	1.064	1.066	1.067	1.068	1.070	1.071	1.072	1.073	1.075	1.076	1.077	1.078	1.079	1.080	1.081	1.082	1.083	1.084	1.085	1.085	1.086	1.087
2.0	1.065	1.066	1.068	1.070	1.071	1.073	1.074	1.076	1.077	1.078	1.080	1.081	1.082	1.083	1.084	1.085	1.087	1.088	1.089	1.090	1.091	1.092	1.093	1.094	1.095
1.9	1.070	1.072	1.074	1.076	1.077	1.079	1.081	1.082	1.084	1.085	1.086	1.088	1.089	1.090	1.092	1.093	1.094	1.095	1.096	1.097	1.098	1.100	1.101	1.102	1.103
1.8	1.076	1.079	1.080	1.082	1.084	1.086	1.088	1.089	1.091	1.092	1.094	1.095	1.097	1.098	1.100	1.101	1.102	1.104	1.105	1.106	1.107	1.108	1.109	1.111	1.112
1.7	1.084	1.086	1.088	1.090	1.092	1.094	1.096	1.097	1.099	1.101	1.103	1.104	1.106	1.107	1.109	1.110	1.112	1.113	1.114	1.116	1.117	1.118	1.119	1.121	1.122
1.6	1.092	1.094	1.096	1.099	1.101	1.103	1.105	1.107	1.109	1.111	1.112	1.114	1.116	1.118	1.119	1.121	1.122	1.124	1.125	1.127	1.128	1.130	1.131	1.132	1.134
1.5	1.101	1.104	1.106	1.109	1.111	1.113	1.116	1.118	1.120	1.122	1.124	1.126	1.128	1.130	1.131	1.133	1.135	1.136	1.138	1.140	1.141	1.143	1.144	1.146	1.147
1.4	1.112	1.115	1.118	1.120	1.123	1.126	1.128	1.131	1.133	1.135	1.137	1.140	1.142	1.144	1.146	1.148	1.150	1.151	1.153	1.155	1.157	1.158	1.160	1.162	1.163
1.3	1.125	1.129	1.132	1.135	1.138	1.141	1.143	1.146	1.149	1.151	1.154	1.156	1.159	1.161	1.163	1.165	1.167	1.169	1.171	1.173	1.175	1.177	1.179	1.181	1.183
1.2	1.142	1.145	1.149	1.152	1.156	1.159	1.162	1.165	1.168	1.171	1.174	1.177	1.179	1.182	1.184	1.187	1.189	1.192	1.194	1.196	1.198	1.200	1.203	1.205	1.207
1.1	1.162	1.166	1.171	1.175	1.178	1.182	1.186	1.189	1.193	1.196	1.199	1.202	1.205	1.208	1.211	1.214	1.217	1.219	1.222	1.225	1.227	1.229	1.232	1.234	1.237
1.0	1.189	1.194	1.198	1.203	1.207	1.212	1.216	1.220	1.224	1.228	1.232	1.235	1.239	1.242	1.246	1.249	1.252	1.255	1.258	1.261	1.264	1.267	1.270	1.272	1.275

Table A.3 — Summary of Nearfield Escarpment Slopes, Escarpment Wind Speed Corrections, and Upwind Beach Path Length as a Function of Average Wind Direction and Tide Height

Wind Direction (True)	Surveyed Escarpment Slope	Laterally Interpolated Escarpment Slope	Integrated (±10°) Escarpment Slope	Normalized Height = 3.90		Normalized Height = 1.96		Est. Upwind Beach Path Length (meters)			Average (±5°) Wind Direction (True)
				Wind Speed Amplification Factor	Wind-Speed Correction Coefficient	Wind Speed Amplification Factor	Wind-Speed Correction Coefficient	Observed Extreme High Water Mark	Interpolated Mean Sea Level	Observed Extreme Low Water Mark	
225°	0.083							30	52½	75	
230°		0.0850									
235°		0.0870	0.087	1.002	0.998	1.015	0.985	30	49	68	235°
240°	0.089										
245°		0.0893	0.089	1.002	0.998	1.016	0.984	30	47½	65	245°
250°		0.0897									
255°	0.090		0.090	1.002	0.998	1.017	0.983	32	48	64	255°
260°		0.0900									
265°		0.0900	0.090	1.002	0.998	1.017	0.983	36	48½	61	265°
270°	0.090										
275°		0.0917	0.092	1.003	0.997	1.018	0.982	39	49½	60	275°
280°		0.0933									
285°	0.095		0.103	1.003	0.997	1.024	0.977	38	55	72	285°
290°		0.1100									
295°		0.1250	0.125	1.005	0.995	1.032	0.969	41	76	111	295°
300°	0.140										
305°		0.1567	0.157	1.007	0.993	1.043	0.959	34	111	188	305°
310°		0.1733									
315°	0.190		0.183	1.008	0.992	1.050	0.952	27	109½	192	315°
320°		0.1947									
325°		0.1993	0.199	1.008	0.992	1.054	0.949	21	78½	136	325°
330°	0.204										
335°		0.2063	0.206	1.009	0.991	1.056	0.947	19	62½	106	335°
340°		0.2087									
345°	0.211		0.207	1.009	0.991	1.056	0.947	16	51	86	345°
350°		0.2063									
355°		0.2017	0.201	1.008	0.992	1.055	0.948	16	44½	73	355°
0°	0.197										
5°		0.1870	0.186	1.008	0.992	1.051	0.951	17	45½	74	5°
10°		0.1770									
15°	0.167		0.168	1.007	0.993	1.046	0.956	19	43½	68	15°
20°		0.1593									
25°		0.1517	0.152	1.006	0.994	1.042	0.960	20	45	70	25°
30°	0.144										
35°		0.1357	0.136	1.006	0.994	1.036	0.965	20	49½	79	35°
40°		0.1273									
45°	0.119							23	49½	76	

Appendix B

DEW POINT FIELD CALIBRATION DEVICE

Laboratory tests conducted on the manufacturer-provided field-calibration device revealed that four improvements would need to be incorporated in the design to make it a more reliable resistance-type secondary dew-point standard:

- Improved reproducibility of the contact resistance for the value-selection switch and the electronic connector used to mate the device to the sensor cable.
- Improved accuracy of the selected resistance values.
- Improved stability of the resistances employed for the device.
- Deployment of resistance values in increments equivalent to about 10°C dew point.

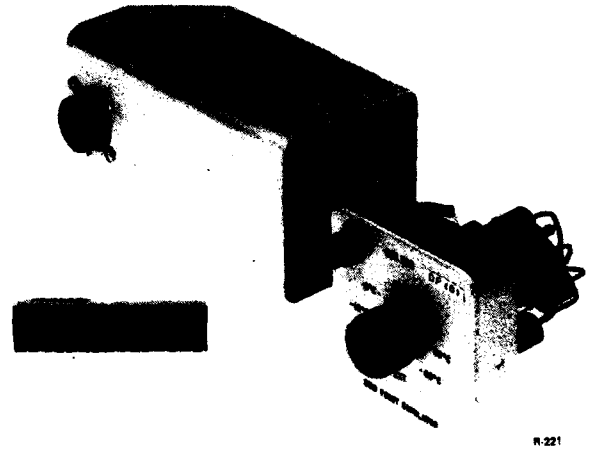

R-221

Fig. B.1 — Photograph of the dew-point field-calibration device opened to show rotary switch and special resistors

Suitable field-calibration devices were constructed with one device provided for each sensor. The calibrators were equipped with sensor cable mating connectors (Bendix connector type PT02A-16-26P) identical to those used on the actual sensor. Seven resistance values were selected from the National Bureau of Standards sensor calibration of dew point vs. sensor resistance. The switching of the resistance values to simulate the dew-point readings was achieved with a military specification type MIL-3786 multiposition six-deck rotary switch, (Grayhill switch type 44MS45-06-1-08N.) in which the six contacts at a given rotary position were connected in parallel to minimize contact resistance. Custom made 0.5 watt wire-wound resistors (Imperial Astronics resistor type SA04, Imperial Astronics Company, 20428 Corisco Street, Chatsworth, California 91311.) were used to match exactly the NBS-determined resistance values to a tolerance of 0.005%, a stability of 0.002% per year, and a temperature coefficient of 5 parts per million/C°.

Approximately once a year the field-calibration device accompanies its sensor back to the National Bureau of Standards for a sensor recalibration.

Appendix C

BEACH OBSERVATIONS AND TESTS FOR ISLAND INFLUENCE

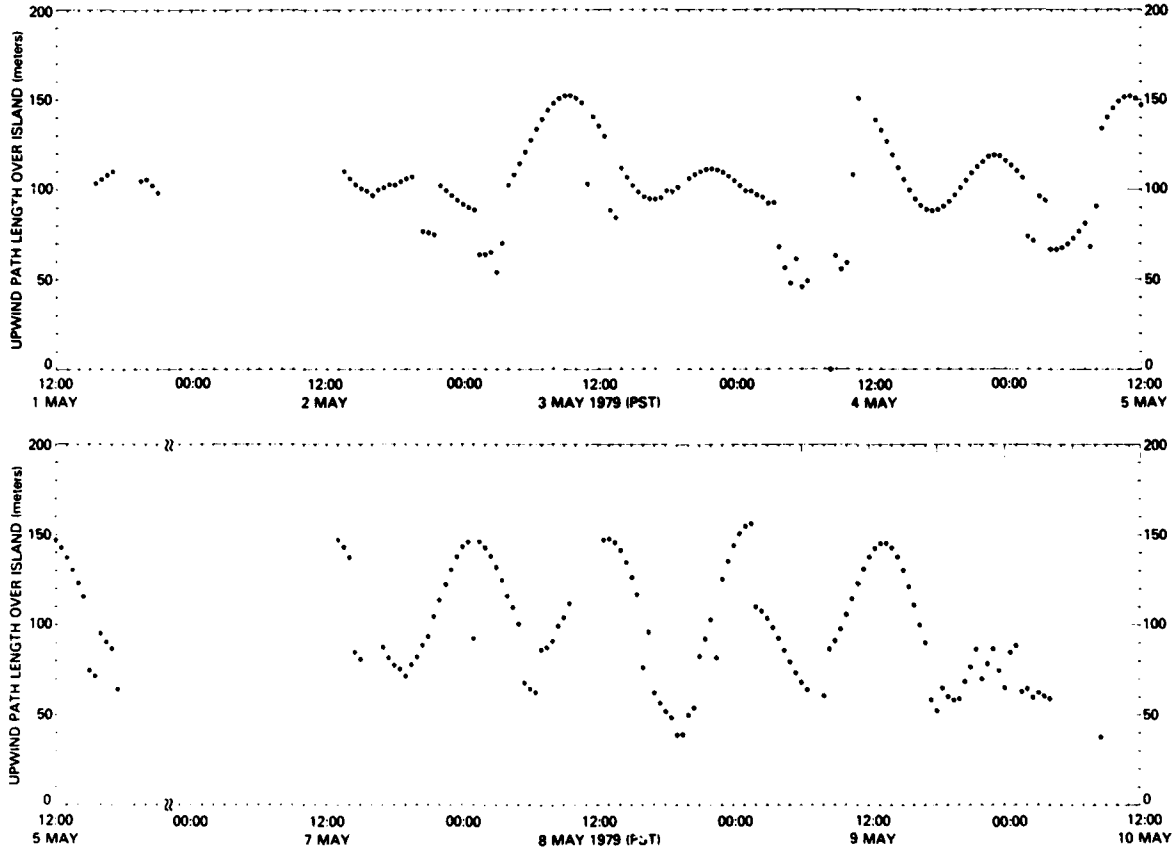

Fig. C.1 — Thirty-minute-average fetch length over the beach upwind of the island measurement site displayed as a function of time

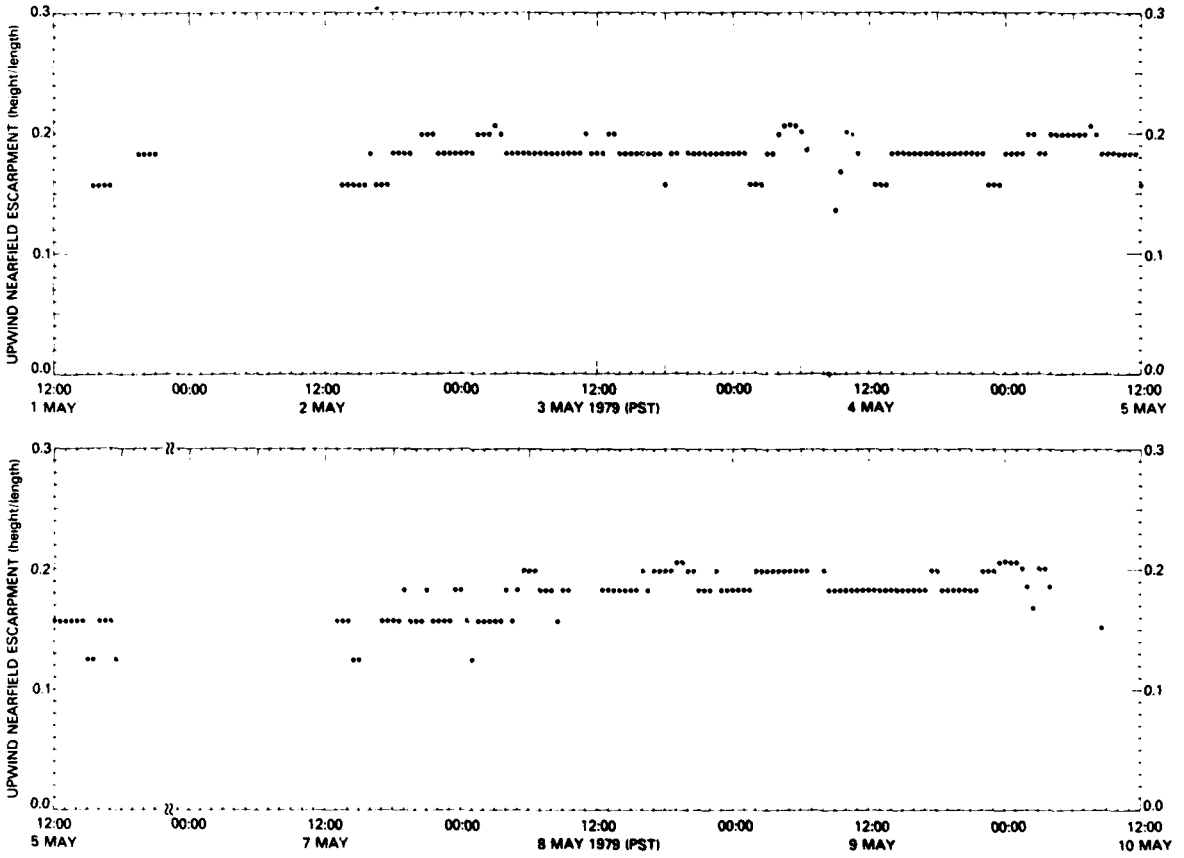

Fig. C.2 — Thirty-minute-average local beach escarpment aspect ratio upwind of the island measurement site displayed as a function of time

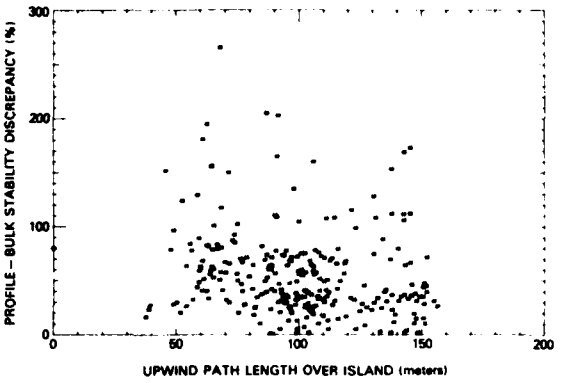

Fig. C.3 — Discrepancy between profile- and bulk-derived stabilities displayed as a function of the fetch length over the beach upwind of the island measurement site.

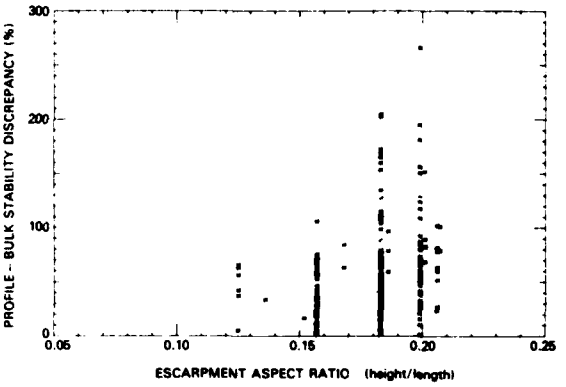

Fig. C.4 — Discrepancy between profile- and bulk-derived stabilities displayed as a function of the local beach escarpment aspect ratio upwind of the island measurement site

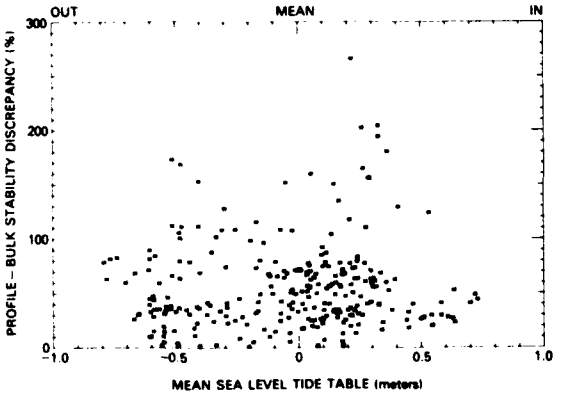

Fig. C.5 — Discrepancy between profile- and bulk-derived stabilities displayed as a function of the tide height

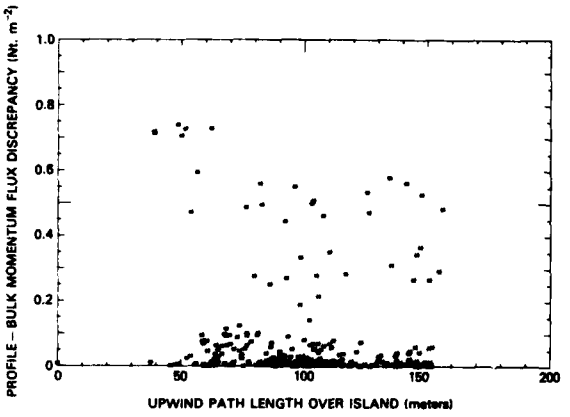

Fig. C.6 — Discrepancy between profile- and bulk-derived momentum fluxes displayed as a function of the fetch length over the beach upwind of the island measurement site

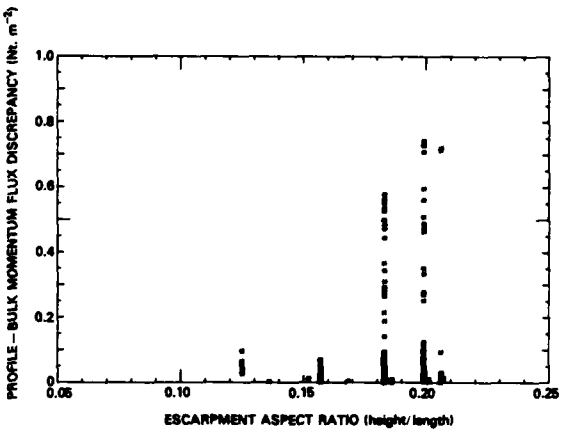

Fig. C.7 — Discrepancy between profile- and bulk-derived momentum fluxes displayed as a function of the local beach escarpment aspect ratio upwind of the island measurement site

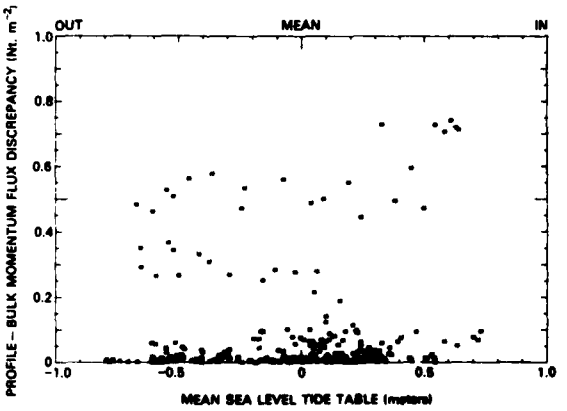

Fig. C.8 — Discrepancy between profile- and bulk-derived momentum fluxes displayed as a function of the tide height

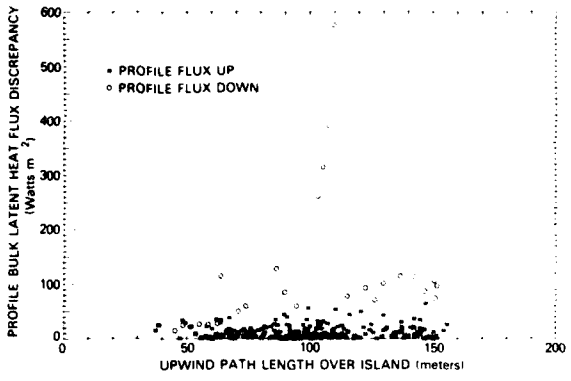

Fig. C.9 — Discrepancy between profile- and bulk-derived latent heat fluxes displayed as a function of the fetch length over the beach upwind of the island measurement site for both upward and downward profile-determined latent heat flux conditions

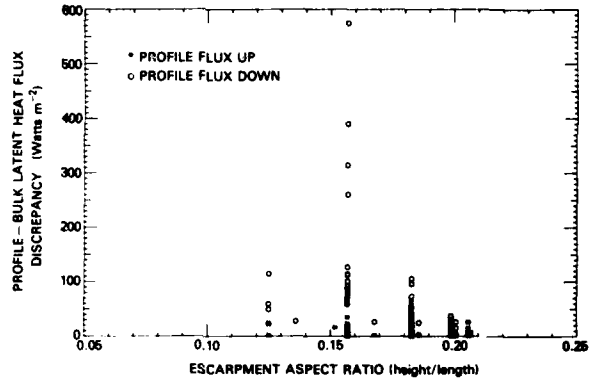

Fig. C.10 — Discrepancy between profile- and bulk-derived latent heat fluxes displayed as a function of the local beach escarpment aspect ratio upwind of the island measurement site for both upward and downward profile-determined latent heat flux conditions

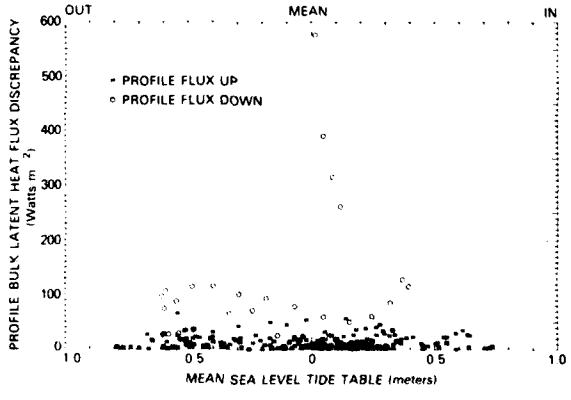

Fig. C.11 — Discrepancy between profile- and bulk-derived latent heat fluxes displayed as a function of tide height for both upward and downward profile-determined latent heat flux conditions

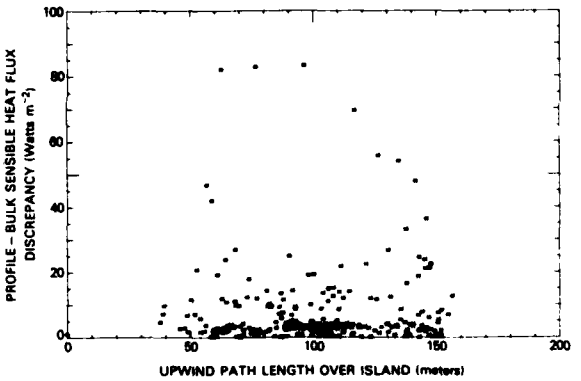

Fig. C.12 — Discrepancy between profile- and bulk-derived sensible heat fluxes displayed as a function of the fetch length over the beach upwind of the island measurement site

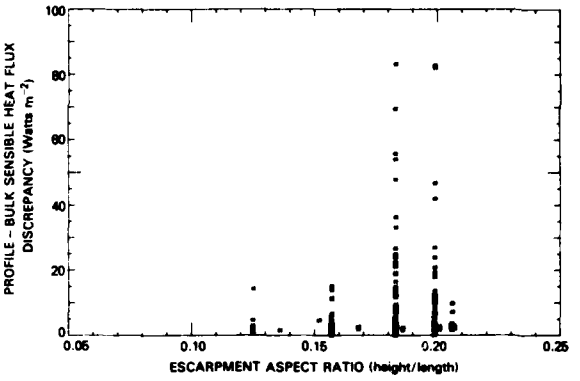

Fig. C.13 — Discrepancy between profile- and bulk-derived sensible heat fluxes displayed as a function of the local beach escarpment aspect ratio upwind of the island measurement site

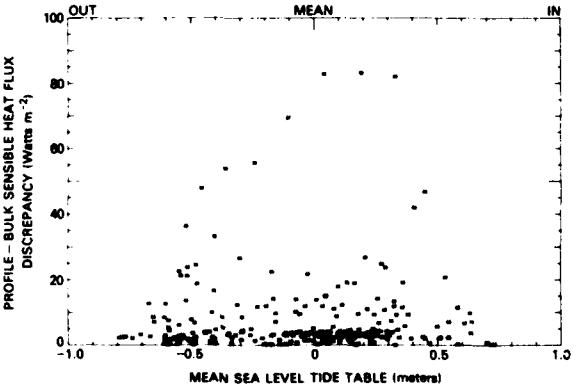

Fig. C.14 — Discrepancy between profile- and bulk-derived sensible heat fluxes displayed as a function of the tide height

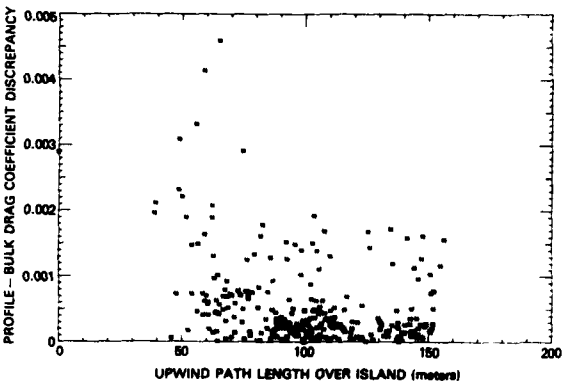

Fig. C.15 — Discrepancy between profile- and bulk-derived neutral drag coefficients for 10-meter height displayed as a function of the fetch length over the beach upwind of the island measurement site, bulk drag coefficient via Smith & Banke (1975)

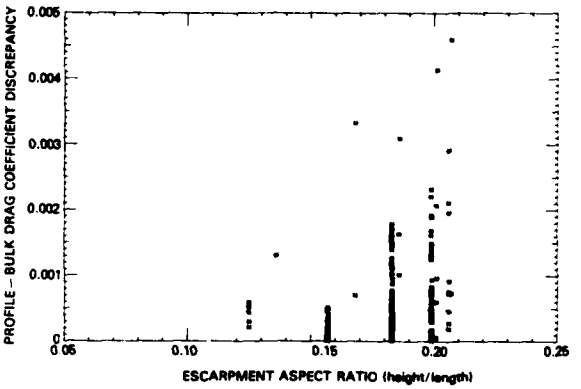

Fig. C.16 — Discrepancy between profile- and bulk-derived neutral drag coefficients for 10-meter height displayed as a function of the local beach escarpment aspect ratio upwind of the island measurement site, bulk drag coefficient via Smith & Banke (1975)

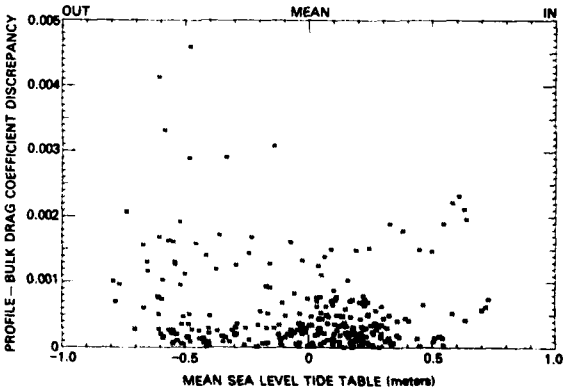

Fig. C.17 — Discrepancy between profile- and bulk-derived neutral drag coefficients for 10-meter height displayed as a function of the tide height, bulk drag coefficient via Smith & Banke (1975)

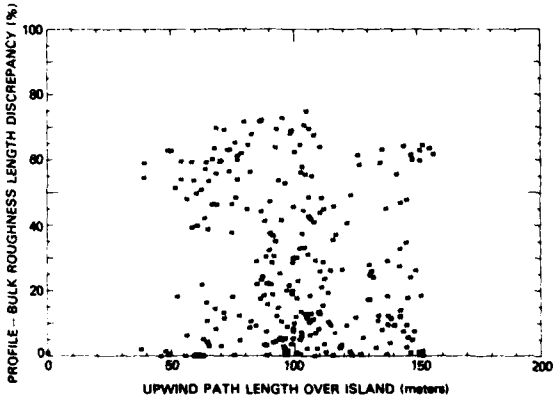

Fig. C.18 — Discrepancy between profile- and bulk-derived roughness lengths displayed as a function of the fetch length over the beach upwind of the island measurement site, both roughness lengths computed via Eq. 14.2

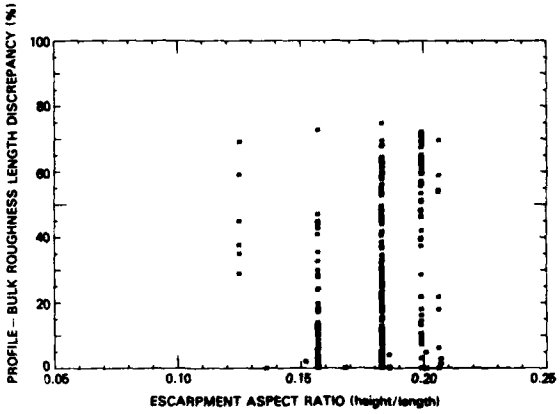

Fig. C.19 — Discrepancy between profile- and bulk-derived roughness lengths displayed as a function of the local beach escarpment aspect ratio upwind of the island measurement site, both roughness lengths computed via Eq. 14.2

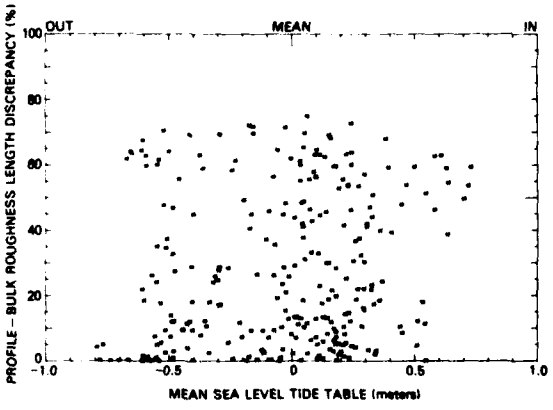

Fig. C.20 — Discrepancy between profile- and bulk-derived roughness lengths displayed as a function of the tide height, both roughness lengths computed via Eq. 14.2

Appendix D

EXAMPLE OF COMBINED TWO LEVEL PROFILE–BULK FLUX METHOD

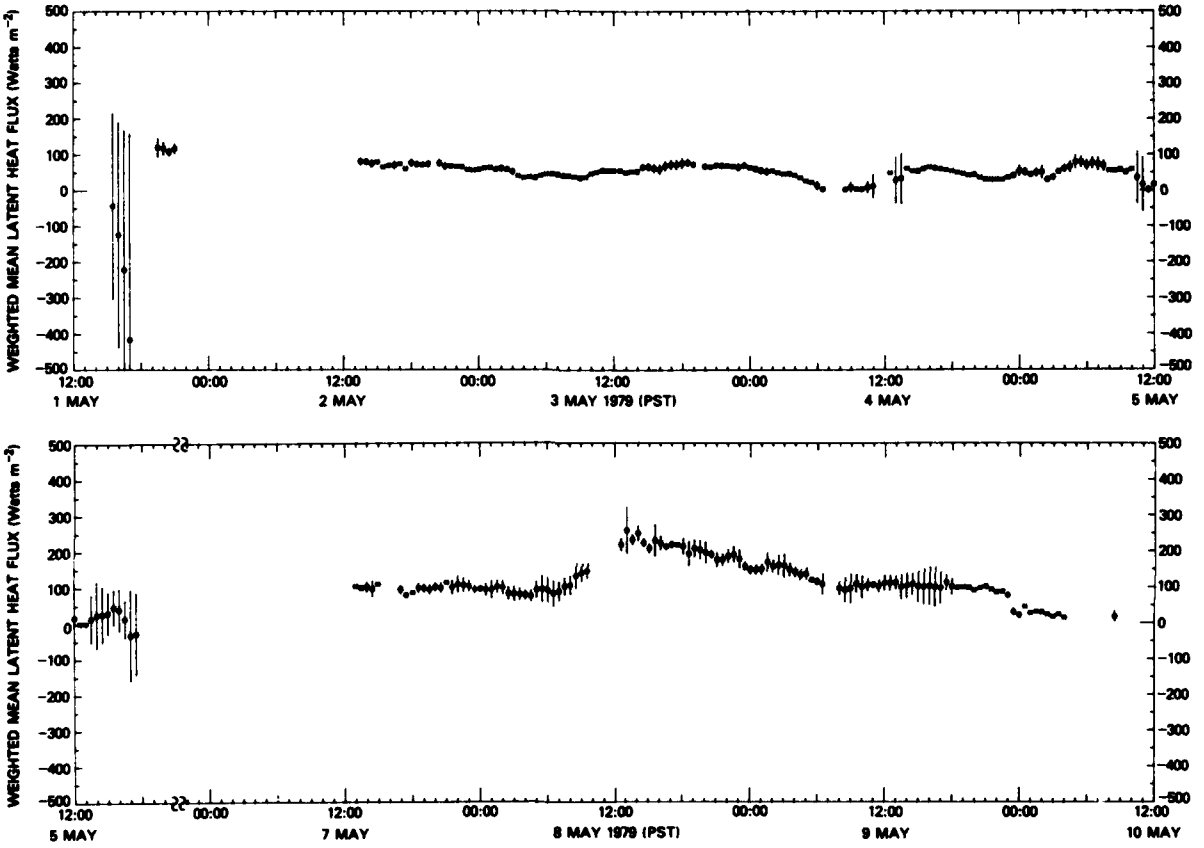

Fig. D.1 — Thirty-minute-average combined profile- and bulk-derived weighted-mean latent heat flux displayed as a function of time, with the error bars set equal to the discrepancy between profile- and bulk-derived values

Appendix E

CALCULATIONS

[May 1979 Data]

General Rules for Notation

AIRD	AIR Density
AH	Absolute Humidity
AT	Air Temperature
BP	Barometric Pressure
BR	Bowen Ratio
D□ □ □	Incremental change in □ □ □ equivalent to the calculated error.
D □ □ DZ	$\frac{\partial \square\square}{\partial Z}$, the partial derivative of □ □ with respect to height (z)
DF □ □ □	Difference betweeen the profile and bulk derived □ □ □ values as computed by the standard deviation from the composite error weighted mean.
DP	Dew Point in °C
DRAG	DRAG coefficient (neutral) computed for 10 m altitude
E □ □ □	Error (approximate) as computed from constituent measurement uncertainties for □ □ □.
FRICV or FRIC	FRICtion Velocity
GGC □ □	Goff-Gratch Constant □ □
GMH	Geometric Mean Height
HEFLX or HEFX	HEat (sensible) FLuX
HUFLX or HUFX	HUmidity FLuX
LHFLX or LHFX	Latent Heat FLuX
LHV	Latent Heat of Vaporization
MOFLX or MOFX	MOmentum FLuX
MOL	Monin-Obukhov Length
$N(\ )_n$	digital channel Number ( ), character n
OPTIR	OPTical Refractive Index (C_n^2)
PSI1Z□	ψ_1, wind speed log profile stability correction at Z□ height
PSI2Z□	ψ_2, temperature and humidity log profile stability correction at height Z□
PT	Potential Temperature in °C
RH	Relative Humidity
RI	RIchardson (gradient) number stability
RUFL	Roughness Length
SCL □ □ □ or SL □ □ □	SCaLing □ □ □ parameter.
SD □ □ □	Standard Deviation of the profile and bulk derived □ □ □ values from the composite error weighted mean.
SH	Specific Humidity
SPHEAT	SPecific HEAT
SR	Sky and solar short wave Radiation heat flux
SVP	Saturated Vapor Pressure
THFLX or THFX	Total Heat budget FLuX (sky & solar + sensible + latent)
TUR	microthermal TURbulence temperature structure parameter (C_t^2)
V( )	average raw data Voltage for analog channel ( )
V'( )	average field calibration corrected Voltage for analog channel ( )
VKC	Von Kármán Constant; set equal to 0.4
VP	Vapor Pressure
VPT	Virtual Potential Temperature in °C
VT	Virtual Temperature in °C
VV □ □ C	Vertical Velocity and □ □ Covariance
WD	Wind Direction
WM □ □ □	composite error Weighted Mean of the profile and bulk derived □ □ □ values.
WS	Wind Speed
WTB	Water Temperature (Bulk)
Z	height above escarpment surface which is considered to be equivalent to height above water

ZOL	Z Over L (Z/L or ζ) stability parameter
□ □ □ 1	upper height value for □ □ □
□ □ □ 2	lower height value for □ □ □
□ □ □ B	Bulk aerodynamic derived value or ten meter height value for □ □ □
□ □ □ D	vertical profile Differential value for □ □ □
□ □ □ EC	Escarpment Coefficent correction for □ □ □
□ □ □ FCAL	Field CALibration correction for □ □ □
□ □ K	value of □ □ in °K
□ □ □ M	geometric Mean height value for □ □ □
□ □ □SLOP or □ □ □ SL	profile SLOPe for □ □ □
□ □ □ T	Ten meter height value for □ □ □
□ □ □ W	Water level (or mean sea level) height value for □ □ □
□ □ □ WTB	□ □ □ at ten meter height minus the Water Temperature (Bulk)

Notation Description Listing

Listed below in alphabetical order are the definitions of the English shorthand notation symbols (with units) employed in the computer subroutions.

Symbol:	Units:	Description:
A	–	Variable in quadratic solution for profile derived Z/L (or ζ) stability parameter when Richardson's number > 0.
A1	–	Intermediate step in Goff-Gratch formulation of vapor pressure at the Z1 height.
A2	–	Intermediate step in Goff-Gratch formulation of vapor pressure at the Z2 height.
AB	–	Intermediate step in Goff-Gratch formulation of vapor pressure at the 10 meter height.
AIRD	kg/m^3	Air density of moist air at the geometric mean height (GMH).
AIRDB	kg/m^3	Air density of moist air at the 10 meter height.
AH1	kg/m^3	Absolute humidity (or water vapor density) at the Z1 height.
AH2	kg/m^3	Absolute humidity (or water vapor density) at the Z2 height.
AHB	kg/m^3	Absolute humidity (or water vapor density) at the 10 meter height.
AHW	kg/m^3	Absolute humidity (or water vapor density) estimated at water level by assuming the dew point temperature is equal to the water temperature.
arctan( )	radians	Arctangent of ( ).
AT1	°C	Air temperature in °C at the Z1 height.
AT2	°C	Air temperature in °C at the Z2 height.
ATB	°C	Air temperature in °C at the 10 meter height.
ATK1	°K	Air temperature in °K at the Z1 height.

ATK2	°K	Air temperature in °K at the Z2 height.
ATKB	°K	Air temperature in °K at the 10 meter height.
ATKM	°K	Air temperature in °K at the geometric mean height (GMH).
ATM	°C	Air temperature in °C at the geometric mean height (GMH).
ATWTB	°K	Air temperature at the 10 meter height minus the bulk water temperature.
AW	–	Intermediate step in Goff-Gratch formulation of vapor pressure at water level.
B	–	Variable in quadratic solution for profile derived Z/L (or ζ) stability parameter when Richardson's number > 0.
B1	–	Intermediate step in Goff-Gratch formulation of vapor pressure at the Z1 meter height.
B2	–	Intermediate step in Goff-Gratch formulation of vapor pressure at the Z2 height.
BB	–	Intermediate step in Goff-Gratch formulation of vapor pressure at the 10 meter height.
BP1	mb	Barometric pressure estimated for the Z1 height
BP2	mb	Barometric pressure *measured* at the Z2 height.
BPB	mb	Barometric pressure estimated for the ten meter height (ZB).
BPM	mb	Barometric pressure estimated for the geometric mean height (GMH).
BPW	mb	Barometric pressure estimated for mean sea level height.
BR	–	Profile derived Bowen Ratio.
BRB	–	Bulk aerodynamic derived Bowen Ratio.
BW	–	Intermediate step in Goff-Gratch formulation of vapor pressure at water level.
C	–	Variable in quadratic solution for profile derived Z/L (or ζ) stability parameter when Richardson's number > 0.
C1	–	Intermediate step in Goff-Gratch formulation of vapor pressure at the Z1 height.
C2	–	Intermediate step in Goff-Gratch formulation of vapor pressure at the Z2 height.
CB	–	Intermediate step in Goff-Gratch formulation of vapor pressure at the 10 meter height.

CW	–	Intermediate step in Goff-Gratch formulation of vapor pressure at the water level.
D1	–	Intermediate step in Goff-Gratch formulation of vapor pressure at the Z1 height.
D2	–	Intermediate step in Goff-Gratch formulation of vapor pressure at the Z2 height.
DB	–	Intermediate step in Goff-Gratch formulation of vapor pressure at the 10 meter height.
DFBR	%	Difference between the profile and bulk derived bowen ratio values as computed by the standard deviation from the composite error weighted mean (or measurement uncertainity value, whichever absolute value is larger).
DFDRAG	%	Difference between the profile and bulk derived drag coefficient values as computed by the standard deviation from the composite error weighted mean (or measurement uncertainty value, whichever absolute value is larger).
DFFRIC	%	Difference between the profile and bulk derived friction velocity values as computed by the standard deviation from the composite error weighted mean (or measurement uncertainty , whichever absolute value value is larger).
DFHEFX	%	Difference between the profile and bulk derived sensisible heat flux values as computed by the standard deviation from the composite error weighted mean (or measurement uncertainty value, whichever absolute value is larger).
DFLHFX	%	Difference between the profile and bulk derived latent heat flux values as computed by the standard deviation from the composite error weighted mean (or measurement uncertainty value, whichever absolute value is larger).
DFMOFX	%	Difference between the profile and bulk derived momentum flux values as computed by the standard deviation from the composite error weighted mean (or measurement uncertainty value, whichever absolute value is larger).
DFRI	%	Difference between the profile and bulk derived gradient Richardson number stability values as computed by the standard deviation from the composite error weighted mean (or measurement uncertainty value, whichever absolute value is larger).
DFRUFL	%	Difference between the profile and bulk derived roughness length values as computed by the standard deviation from the composite error weighted mean (or measurement uncertainty value, whichever absolute value is larger).
DFSLPT	%	Difference between the profile and bulk derived scaling potential temperature values as computed by the standard deviation from the composite weighted mean (or measurement uncertainty value, whichever absolute value is larger).

DFSLSH	%	Difference between the profile and bulk derived scaling specific humidity values as computed by the standard deviation from the composite error weighted mean (or measurement uncertainty value, whichever absolute value is larger).
DFSR	%	Difference between the profile and bulk derived sky and solar radiation heat flux values as computed by the standard deviation from the composite error weighted mean (or measurement uncertainty value, whichever absolute value is larger).
DFTHFX	%	Difference between the profile and bulk derived total heat budget flux values as computed by the standard deviation from the composite error weighted mean (or measurement uncertainty value, whichever absolute value is larger).
DFZOLT	%	Difference between the profile and bulk derived Z/L (or ζ) stability parameter at 10 meters values as computed by the standard deviation from the composite error weighted mean (or measurement uncertainty value, whichever absolute value is larger).
DH	watt/m^2	Sum of the absolute values of the profile derived solar radiation, latent, and sensible heat fluxes.
DHB	watt/m^2	Sum of the absolute values of the bulk derived solar radiaton, latent, and sensible heat fluxes.
DHEFLX	watt/m^2	Incremental change in profile derived heat flux equivalent to the calculated error × 100.
DHEFXB	watt/m^2	Incremental change in bulk aerodynamic derived heat flux equivalent to the calculated error × 100.
DLHFLX	watt/m^2	Incremental change in profile derived latent heat flux equivalent to the calculated error × 100.
DLHFXB	watt/m^2	Incremental change in bulk aerodynamic derived latent heat flux equivalent to the calculated error × 100.
DP1	°C	Dew point in °C at the Z1 height.
DP1FCAL	volt	Dew point field calibration correction at the Z1 height.
DP2	°C	Dew point in °C at the Z2 height.
DP2FCAL	volt	Dew point field calibration correction at the Z2 height.
DPB	°C	Dew point in °C at 10 meter height.
DPK1	°K	Dew point in °K at the Z1 height.
DPK2	°K	Dew point in °K at the Z2 height.
DPKB	°K	Dew point in °K at the 10 meter height.

DPTDZ	°K/m	Profile derived partial derivative of potential temperature with respect to height.
DRAG	—	Profile derived neutral atmospheric drag coefficient computed for the 10 meter height.
DRAGB	—	Bulk aerodynamic derived neutral atmospheric drag coefficient computed for the 10 meter height.
DSHDZ	kg/kg ·m	Profile derived partial derivative of specific humidity with respect to height.
DSR	watt/m^2	Incremental change in the sky and solar radiation heat flux equivalent to the measurement error × 100.
DSRB	watt/m^2	Same as DSR.
DW	—	Intermediate step in Goff-Gratch formulation of vapor pressure at water level.
DWSDZ	m/sec · m	Profile derived partial derivative of wind speed with respect to height.
EAHWB	%	Mean error referenced to the measurement accuracy for the computed absolute humidity difference between the 10 meter height and water level.
EBR	%	Mean error referenced to the measurement accuracy for the profile derived Bowen Ratio.
EBRB	%	Mean error referenced to the measurement accuracy for the bulk aerodynamic derived Bowen Ratio.
EDRAG	%	Mean error referenced to the measurement accuracy for the profile derived drag coefficient at the 10 meter height.
EDRAGB	%	Mean error referenced to the measurement accuracy for the bulk aerodynamic derived dray coefficient at the 10 meter height.
EFRICB	%	Mean error referenced to the measurement accuracy for the bulk aerodynamic derived friction (or scaling) velocity.
EFRICV	%	Mean error referenced to the measurement accuracy for the profile derived friction (or scaling) velocity.
EHEFLX	%	Mean error referenced to the measurement accuracy for the profile derived sensible heat flux.
EHEFXB	%	Mean error referenced to the measurement accuracy for the bulk aerodynamic derived sensible heat flux.
EHUFLX	%	Mean error referenced to the measurement accuracy for the profile derived humidity flux.

EHUFXB	%	Mean error referenced to the measurement accuracy for the bulk aerodynamic derived humidity flux.
ELHFLX	%	Mean error referenced to the measurement accuracy for the profile derive latent heat flux.
ELHFXB	%	Mean error referenced to the measurement accuracy for the bulk aerodynamic derived latent heat flux.
EMOFLX	%	Mean error referenced to the measurement accuracy for the profile derived momentum flux.
EMOFXB	%	Mean error referenced to the measurement accuracy for the bulk aerodynamic derived momentum flux.
EMOLB	%	Mean error referenced to the measurement accuracy for the bulk aerodynamic derived Monin-Obukhov (or Obukhov) length.
EMTC	%	Mean error estimated for the bulk aerodynamic moisture transfer coefficient.
EPSID	%	Combined mean error associated with the parameter profile slopes due to the [*Ln*(Z1)−PSI1Z1]−[*Ln*(Z2)−PSI1Z2] or [*Ln*(Z1)−PSI2Z1]−[*Ln*(Z2)−PSI2Z2] terms.
EPTD	%	Mean error referenced to the measurement accuracy for the profile potential temperature differential.
EPTPD	%	Mean error reference to the measurement accuracy for the partial derivative of potential temperature with respect to height.
EPTSLP	%	Mean error referenced to the measurement accuracy for the profile slope of the potential temperature.
EPTWTB	%	Mean error referenced to the measurement accuracy for the difference between the potential temperature at 10 meters and the bulk water temperature.
ERI	%	Mean error referenced to the measurement accuracy for the profile derived gradient Richardson number stability.
ERIB	%	Mean error referenced to the measurement accuracy for the bulk aerodynamic derived gradient Richardson number stability.
ERUFL	%	Mean error referenced to the measurement accuracy for the profile derived roughness length.
ERUFLB	%	Mean error referenced to the measurement accuracy for the bulk aerodynamic derived roughness length.
ESCLPT	%	Mean error referenced to the measurement accuracy for the profile derived scaling potential temperature.

ESCLSH	%	Mean error referenced to the measurement accuracy for the profile derived scaling specific humidity.
ESHD	%	Mean error referenced to the measurement accuracy for the profile specific humidty differential.
ESHPD	%	Mean error referenced to the measurement accuracy for the partial derivative of specific humidity with respect to height.
ESHSLP	%	Mean error referenced to the measurement accuracy for the profile slope of the specific humidity.
ESHTC	%	Mean error estimated for the bulk aerodynamic sensible heat transfer coefficient.
ESLPTB	%	Mean error referenced to the measurement accuracy for the bulk aerodynamic derived scaling potential temperature.
ESLSHB	%	Mean error referenced to the measurement accuracy for the bulk aerodynamic derived scaling specific humidity.
ESR	%	Mean error referenced to the measurement accuracy for sky and solar radiation heat flux.
ESRB	%	Same as ESR.
ESTRES	%	Mean error referenced to the measurement accuracy for the bulk aerodynamic derived shearing (or surface) stress.
ETHFLX	%	Mean error referenced to the measurement accuracy for the [illegible] derived total heat budget (or net heat) flux.
ETHFXB	%	Mean error referenced to the measurement accuracy for the bulk aerodynamic derived total heat budget (or net heat) flux.
EVVHC	%	Mean error referenced to the measurement accuracy for the bulk aerodynamic derived vertical velocity and absolute humidity covariance.
EVVLC	%	Mean error referenced to the measurement accuracy for the bulk aerodynamic derived vertical velocity and longitudinal velocity covariance.
EVVPTC	%	Mean error reference to the measurement accuracy for the bulk aerodynamic derived vertical velocity and potential temperature covariance.
EWSB	%	Mean error referenced to the measurement accuracy for the wind speed at the 10 meter height.
EWSD	%	Mean error referenced to the measurement accuracy for the profile wind speed differential.
EWSPD	%	Mean error referenced to the measurement accuracy for the partial derivative of the wind speed with respect to height.

EWSSLP	%	Mean error referenced to the measurement accuracy for the profile slope of the wind speed.
exp( )	–	Exponent to base of natural logarithm e of ( ), e = 2.71828....
EZB	%	Mean error refernced to the measurement accuracy of height at ten meters.
EZOL	%	Mean error referenced to the measurement accuracy of the profile derived Z/L (or ζ) stability parameter as computed at the geometric mean height (GMH).
EZOLB	%	Mean error referenced to the measurement accuracy of the bulk aerodynamic derived Z/L (or ζ) stability parameter as computed at the geometric mean height (GMH).
EZOLT	%	Mean error referenced to the measurement accuracy for the profile derived Z/L (or ζ) stability parameter as computed for the ten meter height.
EZOLTB	%	Mean error referenced to the measurement accuracy of the bulk aerodynamic derived Z/L (or ζ) stability parameter as computed for the ten meter height.
F	–	Variable in Newton-Raphson method solution for profile derived Z/L (or ζ) stability parameter when Richardson's number $\leqslant 0$.
F'	–	Variable in Newton-Raphson method solution for profile derived Z/L (or ζ) stability parameter when Richardson's number $\leqslant 0$.
F1	–	Intermediate step in Goff-Gratch formulation of vapor pressure at the Z1 height.
F2	–	Intermediate step in Goff-Gratch formulation of vapor pressure at the Z2 height.
FB	–	Intermediate step in Goff-Gratch formulation of vapor pressure at the 10 meter height.
FRICV	m/sec	Profile derived friction (or scaling) velocity.
FRICVB	m/sec	Bulk aerodynamic derived friction (or scaling) velocity.
FW	–	Intermediate step in Goff-Gratch formulation of vapor pressure at water level.
G1	–	Intermediate step in Goff-Gratch formulation of saturated vapor pressure at the Z1 height.
G2	–	Intermediate step in Goff-Gratch formulation of saturated vapor pressure at the Z2 height.
GA	m/sec^2	Gravitational acceleration constant; set equal to 9.7959 for the San Nicolas Island latitude.

GB	–	Intermediate step in Goff-Gratch formulation of saturated vapor pressure at the 10 meter height.
GGC10	–	Goff-Gratch formulation constant: −3.49149.
GGC11	–	Goff-Gratch formulation constant: 11.344.
GGC12	–	Goff-Gratch formulation constant: 5.02808.
GGC13	–	Goff-Gratch formulation constant: −7.90298.
GGC14	–	Goff-Gratch formulation constant: 8.1328×10^{-3}.
GGC15	–	Goff-Gratch formulation constant: -1.3816×10^{-7}.
GMH	meter	Geometric mean of heights Z1 and Z2. This is the equivalent to the mean measurement height as plotted on a *Ln* (height) vs. linear graph.
HEFLX	watt/m^2	Profile derived sensible heat flux.
HEFLXB	watt/m^2	Bulk aerodynamic derived sensible heat flux.
HUFLX	kg/sec · m^2	Profile derived specific humidity flux.
HUFLXB	kg/sec · m^2	Bulk aerodynamic derived specific humidity flux.
IPRZ	–	Interpolated logarithmic profile ratio of heights Z1 and Z2 employed for computing parameter values at the height of ten meters (ZB).
IPRTUR	–	Interpolated logarthmic profile ratio of heights ZTUR1 and ZTUR2 employed for computing the turbulence parameters values of the height at ten meters (ZB)
J	–	Variable in Newton-Raphson method solution for profile derived Z/L (or ζ) stability parameter when Richardson's number $\leqslant 0$.
J1	–	Intermediate step in Goff-Gratch formulation of saturated vapor pressure at the Z1 height.
J2	–	Intermediate step in Goff-Gratch formulation of saturated vapor pressure at the Z2 height.
JB	–	Intermediate step in Goff-Gratch formulation of saturated vapor at the 10 meter height.
K1	–	Intermediate step in Goff-Gratch formulation of saturated vapor pressure at the Z1 height.
K2	–	Intermediate step in Goff-Gratch formulation of saturated vapor pressure at the Z2 height.

KB	–	Intermediate step in Goff-Gratch formulation of saturated vapor pressure at the 10 meter height.
LAMBDA	meter	Wavelength employed for computing optical refractive index; set equal to 5.4×10^{-6}.
LHFLX	watt/m^2	Profile derived latent heat flux.
LHFLXB	watt/m^2	Bulk aerodynamic derived latent heat flux.
LHV	ITcal/kg	Profile derived latent heat of water vaporation.
LHVB	ITcal/kg	Bulk aerodynamic derived latent heat of water vaporation.
Ln ( )	–	Natural logarithm of ( ) with base e = 2.71828 ....
LOGFV	–	Logarithm to the base 10 of the profile derived friction velocity.
LOGFVB	–	Logarithm to the base 10 of the bulk derived friction velocity.
M1	–	Intermediate step in Goff-Gratch formulation of saturated vapor pressure at the Z1 height.
M2	–	Intermediate step in Goff-Gratch formulation of saturated vapor pressure at the Z2 height.
MB	–	Intermediate step in Goff-Gratch formulation of saturated vapor pressure at the 10 meter height.
MOFLX	Nt/m^2	Profile derived momentum flux.
MOFLXB	Nt/m^2	Bulk aerodynamic derived momentum flux.
MOL	meter	Profile derived Monin-Obukhov (or Obukhov) length.
MOLB	meter	Bulk aerodynamic derived Monin-Obukhov (or Obukhov) length.
MTC	–	Bulk aerodynamic moisture transfer coefficient; set equal to 1.32×10^{-3}.
N ( )$_n$	–	Digital channel number ( ) consisting of 10 parallel digital characters, n = 1, 2, . . . 10.
OPTIR1	°K/m$^{-2/3}$	Optical refractive index parameter (C_n^2) at the ZTUR1 height.
OPTIR2	°K/m$^{-2/3}$	Optical refractive index parameter (C_n^2) at the ZTUR2 height.
OPTIRT	°K/m$^{-2/3}$	Optical refractive index parameter (C_n^2) at the 10 meter height.
PSI1Z1	–	Businger wind speed profile stability correction (Ψ_1) for the *Ln* (Z1) height.

PSI1Z2	–	Businger wind speed profile stability correction (Ψ_1) for the *Ln* (Z2) height.
PSI2Z1	–	Businger temperature and humidity stability correction (Ψ_2) for the *Ln* (Z1) height.
PSI2Z2	–	Businger temperature and humidity stability correction (Ψ_2) for the *Ln* (Z2) height.
PT1	°C	Potential temperature in °C at the Z1 height.
PT2	°C	Potential temperature in °C at the Z2 height.
PTB	°C	Potential temperature in °C at the 10 meter height.
PTK1	°K	Potential temperature in °K at the Z1 height.
PTK2	°K	Potential temperature in °K at the Z2 height.
PTKB	°K	Potential temperature in °K at the 10 meter height.
PTKD	°K	Potential temperature vertical profile differential in °K.
PTKSLOP	–	Profile derived physical slope of *Ln* (height) with Businger stability corrections vs. potential temperature.
PTWTB	°K	Potential temperature at the 10 meter height minus the bulk water temperature.
Q1	–	Intermediate step in Goff-Gratch formulation of saturated vapor pressure at the Z1 height.
Q2	–	Intermediate step in Goff-Gratch formulation of saturated vapor pressure at the Z2 height.
QB	–	Intermediate step in Goff-Gratch formulation of saturated vapor pressure at the 10 meter height.
REHL	–	Ratio of the upwind escarpment height to length as computed from the horizontally integrated (±10°) near-field topography (within 25 meters of sensors) and the mean wind direction.
RH1	%	Relative humidity at the Z1 height.
RH2	%	Relative humidity at the Z2 height.
RHB	%	Relative humidity at the 10 meter height.
RI	–	Profile derived gradient Richardson number stability.
RIB	–	Bulk aerodynamic flux derived gradient Richardson number stability.
RLC10	–	Roughness length equation constant: −2.501

RLC11	–	Roughness length equation constant: +1.465
RLC12	–	Roughness length equation constant: −6.743
RLC13	–	Roughness length equation constant: −10.700
RLC14	–	Roughness length equation constant: −6.875
RUFL	meter	Profile derived roughness length.
RUFLB	meter	Bulk aerodynamic derived roughness length.
SCLPT	°K	Profile derived scaling potential temperature.
SCLPTB	°K	Bulk aerodynamic derived scaling potential temperature.
SCLSH	kg/kg	Profile derived scaling specific humidity.
SCLSHB	kg/kg	Bulk aerodynamic derived scaling specific humidity.
SDBR	–	Standard deviation of the profile and bulk derived bowen ratio values from the composite error weighted mean.
SDDRAG	–	Standard deviation of the profile and bulk derived drag coefficient values from the composite error weighted mean.
SDFRIC	m/sec	Standard deviation of the profile and bulk derived friction velocity values from the composite error weighted mean.
SDHEFX	watt/m^2	Standard deviation of the profile and bulk derived sensible heat flux values from the composite error weighted mean.
SDLHFX	watt/m^2	Standard deviation of the profile and bulk derived latent heat flux values from the composite error weighted mean.
*SDMOFX	Nt/m^2	Standard deviation of the profile and bulk derived momentum flux values from the composite error weighted mean.
SDRI	–	Standard deviation of the profile and bulk derived gradient Richardson number stability values from the composite error weighted mean.
SDRUFL	meter	Standard deviation of the profile and bulk derived roughness length values from the composite error weighted mean.
SDSLPT	°K	Standard deviation of the profile and bulk derived scaling potential temperature values from the composite error weighted mean.
SDSLSH	kg/kg	Standard deviation of the profile and bulk derived scaling specific humidity values from the composite error weighted mean.
SDSR	watt/m^2	Standard deviation of the profile and bulk derived sky and solar radiation heat flux values from the composite error weighted mean.

SDTHFX	watt/m^2	Standard deviation of the profile and bulk derived total heat budget flux values from the composite error weighted mean.
SDZOLT	–	Standard deviation of the profile and bulk derived Z/L (or ζ) stability parameter at 10 meters values from the composite error weighted mean.
SH1	kg/kg	Specific humidity at the Z1 height.
SH2	kg/kg	Specific humidity at the Z2 height.
SHB	kg/kg	Specific humidity at the 10 meter height.
SHD	kg/kg	Specific humidity vertical profile differential.
SHSLOP	–	Profile derived physical slope of Ln (height) with Businger stability corrections vs. specific humidity.
SHTC	–	Bulk aerodynamic sensible heat transfer coefficient; set equal to 0.92×10^{-3}.
SPHEAT	ITcal/kg °K	Profile derived specific heat of moist at constant pressure.
SPHEATB	ITcal/kg °K	Bulk aerodynamic derived specific heat of moist air at constant pressure.
SR	watt/m^2	Sky and solar short wave radiation heat flux.
SSTRES	kg/m · sec^2	Bulk aerodynamic derived shearing (or surface) stress.
SVP1	mb	Saturated water vapor pressure at the Z1 height.
SVP2	mb	Saturated water vapor pressure at the Z2 height.
SVPB	mb	Saturated water vapor pressure at the 10 meter height.
THFLX	watt/m^2	Profile derived total heat budget (sky & solar short wave radiation + sensible heat + latent heat) flux.
THFLXB	watt/m^2	Bulk aerodynamic derived total heat budget (sky & solar short wave radiation + sensible heat + latent heat) flux.
TRT	–	Intermediate step in computing the microthermal turbulence temperature structure parameter (C_t^2) at the 10 meter height from profile C_t^2 measurements.
TTABLE	meter	Tide table referenced to mean sea level.
TUR1	°K/m$^{-2/3}$	Microthermal turbulence temperature structure parameter (C_t^2) at the ZTUR1 height.
TUR2	°K/m$^{-2/3}$	Microthermal turbulence temperature structure parameter (C_t^2) at the ZTUR2 height.
TURD	°K/m$^{-2/3}$	Microthermal turbulence temperature structure vertical profile differential.

TURSLOP	—	Profile derived slope of *Ln* (height) vs. *Ln* (microthermal turbulence temperature structure parameter (C_t^2)).
TURT	°K/m$^{-2/3}$	Microthermal turbulence temperature structure parameter (C_t^2) at the 10 meters height.
UWPL	meter	Upwind path length from the water's edge to the sensors as approximated from mean wind direction and tide table data.
V( )	volt	Average raw data voltage for analog channel number ( ).
V' ( )	volt	Field calibration corrected average data voltage for analog channel number ( ).
VKC	—	Von Kármán constant; set equal to 0.4.
VP1	mb	Water vapor pressure at the Z1 height.
VP2	mb	Water vapor pressure at the Z2 height.
VPB	mb	Vapor pressure at the 10 meter height.
VPT1	°C	Virtual potential temperature in °C at the Z1 height.
VPT2	°C	Virtual potential temperature in °C at the Z2 height.
VPTB	°C	Virtual potential temperature in °C at the 10 meter height.
VPTK1	°K	Virtual potential temperature in °K at the Z1 height.
VPTK2	°K	Virtual potential temperature in °K at the Z2 height.
VPTKB	°K	Virtual potential temperature in °K at the 10 meter height.
VPTKM	°K	Virtual potential temperature at the geometric mean height (GMH).
VPTWTB	°K	Virtual potential temperature at the 10 meters height minus the bulk water temperature.
VPW	mb	Water vapor pressure estimated at water level by assuming the dew point temperature is equal to the water temperature.
VT1	°C	Virtual temperature in °C at the Z1 height.
VT2	°C	Virtual temperature in °C at the Z2 height.
VTB	°C	Virtual temperature in °C at the 10 meter height.
VTK1	°K	Virtual temperature in °K at the Z1 height.
VTK2	°K	Virtual temperature in °K at the Z2 height.
VTKB	°K	Virtual temperature in °K at the 10 meter height.

VTKM	°K	Virtual temperature at the geometric mean height (GMH).
VTWTB	°K	Virtual temperature at the 10 meter height minus the bulk water temperature.
VVHC	$m \cdot kg/sec \cdot m^3$	Bulk aerodynamic derived vertical velocity and absolute humidity covariance.
VVLC	m^2/sec^2	Bulk aerodynamic derived vertical velocity and longitudinal velocity covariance.
VVPTC	m °K/sec	Bulk aerodynamic derived vertical velocity and potential temperature covariance.
WD	degree	Wind direction referenced to true North.
WMBR	—	Composite weighted mean for the profile and bulk derived bowen ratio values inversely weighted as a function of the respective measurement error.
WMDRAG	—	Composite weighted mean for the profile and bulk derived drag coefficient values inversely weighted as a function of the respective measurement error.
WMFRIC	m/sec	Composite weighted mean for the profile and bulk derived friction velocity values inversely weighted as a function of the respective measurement error.
WMHEFX	$watt/m^2$	Composite weighted mean for the profile and bulk derived sensible heat flux values inversely weighted as a function of the respective measurement error.
WMHUFX	$kg/sec \cdot m^2$	Composite weighted mean for the profile and bulk derived humidity flux values inversely weighted as a function of the respective measurement error.
WMLHFX	$watt/m^2$	Composite weighted mean for the profile and bulk derived latent heat flux values inversely weighted as a function of the respective measurement error.
WMMOFX	Nt/m^2	Composite weighted mean for the profile and bulk derived momentum flux values inversely weighted as a function of the respective measurement error.
WMMOL	meter	Composite weighted mean for the profile and bulk derived monin-obukhov length values inversely weighted as a function of the respective measurement error.
WMRI	—	Composite weighted mean for the profile and bulk derived gradient Richardson number stability values inversely weighted as a function of the respective measurement error.

WMRUFL	meter	Composite weighted mean for the profile and bulk derived roughness length values inversely weighted as a function of the respective measurement error.
WMSLPT	°K	Composite weighted mean for the profile and bulk derived scaling potential temperature values inversely weighted as a function of the respective measurement error.
WMSLSH	kg/kg	Composite weighted mean for the profile and bulk derived scaling specific humidity values inversely weighted as a function of the respective measurement error.
WMSR	watt/m^2	Composite weighted mean for the profile and bulk derived sky and solar radiation heat flux inversely weighted as a function of the respective measurement error.
WMTHFX	watt/m^2	Composite weighted mean for the profile and bulk derived total heat budget flux values inversely weighted as a function of the respective measurement error.
WMZOL	—	Composite weighted mean for the profile and bulk derived Z/L (or ζ) stability parameter at the geometric mean height values inversely weighted as a function of the respective measurement error.
WMZOLT	—	Composite weighted mean for the profile and bulk derived Z/L (or ζ) stability parameter at 10 meters values inversely weighted as a function of the respective measurement error.
WS1	m/sec	Wind speed at the Z1 height.
WS1EC	—	Wind speed escarpment correction coefficient for the Z1 height.
WS2	m/sec	Wind speed at the Z2 height.
WS2EC	—	Wind speed escarpment correction coefficient for the Z2 height.
WSB	m/sec	Wind speed at the 10 meter height.
WSD	m/sec	Wind speed vertical profile differential.
WSM	m/sec	Mean wind speed of the measurements at the Z1 and Z2 heights.
WSSLOP	—	Profile derived physical slope of Ln (height) with Businger stability corrections vs. wind speed.
WTB	°C	Bulk water temperature in °C.
WTBFCAL	volt	Bulk water temperature field calibration correction.
WTKB	°K	Bulk water temperature in °K.
WVGC	Nt · m/kg °K	Water vapor gas constant; set equal to 4.6150×10^2.

W1	–	Intermediate step in computation of the Businger stability correction for wind speed profile when Richardson number $\leqslant 0$ at the Z1 height.
W2	–	Intermediate step in computation of the Businger stability correction for wind speed profile when Richardson number $\leqslant 0$ at the Z2 height.
Y1	–	Intermediate step in computation of Businger stability correction for temperature and humidity profiles when Richardson number $\leqslant 0$ at the Z1 height.
Y2	–	Intermediate step in computation of Businger stability correction for temperature and humidity profiles when Richardson number $\leqslant 0$ at the Z2 height.
Z1	meter	Upper level average measurement height of profile instruments (except C_t^2) referenced to ground surface.
Z2	meter	Lower level average measurement height of profile instruments (except C_t^2) referenced to ground surface.
ZB	meter	This is the standard height for the bulk aerodynamic calculations; set equal to 10 meters as referenced to ground surface.
Z1OL	–	Profile derived Z/L (or ζ) stability parameter computed for the Z1 height.
Z2OL	–	Profile derived Z/L (or ζ) stability parameter computed for the Z2 height.
ZOL	–	Profile derived Z/L (or ζ) stability parameter computed for the geometric mean height which is the relevant height for the conversion of Richardson number to Z/L.
ZOLB	–	Bulk aerodynamic flux derived Z/L (or ζ) stability parameters computed for the geometric mean height.
ZOLT	–	Profile derived Z/L (or ζ) stability parameter computed for the 10 meter height.
ZOLTB	–	Bulk aerodynamic flux derived Z/L (or ζ) stability parameter computed for the 10 meter height.
ZTUR1	meter	Upper level measurement height of microthermal turbulence temperature structure (C_t^2) sensors referenced to the ground surface.
ZTUR2	meter	Lower level measurement height of microthermal turbulence temperature structure (C_t^2) sensors referenced to the ground surface.

Computer Calculations: [May 1979 Data]

Presented below are the calculations performed to obtain the micrometeorological parameters. They are listed in a simple algebraic form and utilize a shorthand English notation developed for computer programming purposes. The calculations include the curve-fit equations for converting the raw average voltages into engineering units, the field calibration and wind speed escarpment corrections, the equations for computing the various profile and bulk aerodynamic derived stability and flux parameters, and the computations for the error analysis of various parameters. The MKS International System of units is employed throughout this work, with the exception of millibars (mb) for barometric and vapor pressures instead of newton/meter^2 or pascal, and International Steam Table calories (ITcal.) instead of joules. Both °K and °C are employed.

1 millibar = 10^2 newton/meter^2 = 10^2 Pascal
1 ITcal. = 4.18684 joules

The symbol * to the left of an equation indicates a modification or addition made since the previous experiment. Equations and symbols deleted since the previous experiment are listed at the end of this section.

$AT1 = N(1)_5 N(1)_6 \,.\, N(1)_7 N(1)_8 N(1)_9 N(1)_{10}$

and

$N(1)_1$ Mode: 1 = Primary Sensor, 2 = Backup Sensor

$N(1)_2$ Resolution: $3 = N(1)_7 \,.\, N(1)_8$, $4 = N(1)_6 \,.\, N(1)_7$

$N(1)_3$ Interface Number: 1 = 1, 2 = 2, 3 = 3, 4 = 4

$N(1)_4$ Polarity: 1 = +, 2 = −

$AT2 = N(2)_5 N(2)_6 \,.\, N(2)_7 N(2)_8 N(2)_9 N(2)_{10}$

and

$N(2)_1$ Mode: 1 = Primary Sensor, 2 = Backup Sensor.

$N(2)_2$ Resolution: $3 = N(2)_7 \,.\, N(2)_8$, $4 = N(2)_6 \,.\, N(2)_7$

$N(2)_3$ Interface Number: 1 = 1, 2 = 2, 3 = 3, 4 = 4

$N(2)_4$ Polarity: 1 = +, 2 = −

If $V(09) < 6.324$ volt, then:
$WD = 145 + 34 \times V(09)$

If $V(09) \geq 6.324$ volt, then:
$WD = -215 + 34 \times V(09)$

*If $-1 < WD < 10$, then: $WS1EC = .992$ and $WS2EC = .951$

REHL = .186 and UWPL = 17 + 24.2 (1.18 − TTABLE)

*If $10 \leq WD < 20$, then: $WS1EC = .993$ and $WS2EC = .956$

REHL = .168 and UWPL = 19 + 20.8 (1.18 − TTABLE)

* If $20 \leqslant WD < 30$, then: $WS1EC = .994$ and $WS2EC = .960$
REHL = .152 and UWPL = 20 + 21.2 (1.18 − TTABLE)

* If $30 \leqslant WD < 40$, then: $WS1EC = .994$ and $WS2EC = .965$
REHL = .136 and UWPL = 20 + 25.0 (1.18 − TTABLE)

* If $40 \leqslant WD < 230$, then: $WS1EC = 1.000$ and $WS2EC = 1.000$
REHL = "NOT COMPUTED" and UWPL = "NOT COMPUTED"

* If $230 \leqslant WD < 240$, then: $WS1EC = .998$ and $WS2EC = .985$
REHL = .087 and UWPL = 30 + 16.1 (1.18 − TTABLE)

* If $240 \leqslant WD < 250$, then: $WS1EC = .998$ and $WS2EC = .984$
REHL = .089 and UWPL = 30 + 14.8 (1.18 − TTABLE)

* If $250 \leqslant WD < 260$, then: $WS1EC = .998$ and $WS2EC = .983$
REHL = .090 and UWPL = 32 + 13.6 (1.18 − TTABLE)

* If $260 \leqslant WD < 270$, then: $WS1EC = .998$ and $WS2EC = .983$
REHL = .090 and UWPL = 36 + 10.6 (1.18 − TTABLE)

* If $270 \leqslant WD < 280$, then: $WS1EC = .997$ and $WS2EC = .982$
REHL = .092 and UWPL = 39 + 8.9 (1.18 − TTABLE)

* If $280 \leqslant WD < 290$, then: $WS1EC = .997$ and $WS2EC = .977$
REHL = .103 and UWPL = 38 + 14.4 (1.18 − TTABLE)

* If $290 \leqslant WD < 300$, then: $WS1EC = .995$ and $WS2EC = .969$
REHL = .125 and UWPL = 41 + 29.7 (1.18 − TTABLE)

* If $300 \leqslant WD < 310$, then: $WS1EC = .993$ and $WS2EC = .959$
REHL = .157 and UWPL = 34 + 65.3 (1.18 − TTABLE)

* If $310 \leqslant WD < 320$, then: $WS1EC = .992$ and $WS2EC = .952$
REHL = .183 and UWPL = 27 + 69.9 (1.18 − TTABLE)

* If $320 \leqslant WD < 330$, then: $WS1EC = .992$ and $WS2EC = .949$
REHL = .199 and UWPL = 21 + 48.7 (1.18 − TTABLE)

* If $330 \leqslant WD < 340$, then: $WS1EC = .991$ and $WS2EC = .947$
REHL = .206 and UWPL 19 + 36.9 (1.18 − TTABLE)

* If $340 \leqslant WD < 350$, then: $WS1EC = .991$ and $WS2EC = .947$

  REHL = .207 and UWPL = 16 + 29.7 (1.18 − TTABLE)

* If $350 \leqslant WD < 361$, then: $WS1EC = .992$ and $WS2EC = .948$

  REHL = .201 and UWPL = 16 + 24.2 (1.18 − TTABLE)

* If $V(05) \leqslant 2.570$ volt, then:

$$WS1 = [-6.32834 \times 10^{-2} + 2.42269 \times V(05) - 0.399002 \times V(05)^2 + 8.72726 \times 10^{-2} \times V(05)^3] \times WS1EC$$

* If $V(05) > 2.570$ volt, then:

$$WS1 = [3.08914 \times 10^{-2} + 1.93793 \times V(05) - 6.72817 \times 10^{-4} \times V(05)^2] \times WS1EC$$

* If $V(06) \leqslant 2.558$ volt, then:

$$WS2 = [-7.13544 \times 10^{-2} + 2.52039 \times V(06) - 0.404911 \times V(06)^2 + 8.22668 \times 10^{-2} \times V(06)^3] \times WS2EC$$

* If $V(06) > 2.558$ volt, then:

$$WS2 = [0.181091 + 1.92438 \times V(06) + 1.55926 \times 10^{-4} \times V(06)^2] \times WS2EC$$

* $DP1FCAL$ = (*as indicated on data printout*)

* $DP2FCAL$ = (*as indicated on data printout*)

$$V'(03) = V(03) + DP1FCAL$$

$$DP1 = -20.825 + 6.25047 \times V'(03) - 4.04968 \times 10^{-2} \times V'(03)^2 + 1.43719 \times 10^{-3} \times V'(03)^3$$

$$V'(04) = V(04) + DP2FCAL$$

$$DP2 = -20.5158 + 6.06103 \times V'(04) - 2.15130 \times 10^{-2} \times V'(04)^2 + 1.890459 \times 10^{-3} \times V'(04)^3$$

If $|V(01)| > 1.0$ volt, then:

$$TUR1 = \left[1.07722 \times 10^{\left|1 - \frac{|V'(01)|}{2}\right|}\right]^2$$

If $|V(01)| \leqslant 1.0$ volt, then:

$TUR1$ = " NO DATA"

If $|V(02)| > 1.0$volt, then:

$$TUR2 = \left[1.07722 \times 10^{\left|1 - \frac{|V'(02)|}{2}\right|}\right]^2$$

If $|V(02)| \leqslant 1.0$ volt, then:

$TUR2$ = " NO DATA"

* $BP2 = 941.51 + 14.123\ V(07) + 0.22644 \times V(07)^2 - 1.41907 \times 10^{-2} \times V(07)^3$

* $SR = -139.46 \times V(08)$

* $WTBFCAL$ = (*as indicated on data printout*)

* $V'(10) = V(10) + WTBFCAL$

* $WTB = 9.75329 + 0.969791 \times V'(10) + 6.10709 \times 10^{-4} \times V'(10)^2$

* $Z1 = 18.35$

$*Z2 = 9.20$

$ZB = 10.000$

$ZTUR1 = Z1 + 0.60$

$ZTUR2 = Z2 + 0.60$

$GMH = \sqrt{Z1 \times Z2}$

$*BP1 = BP2 - [(Z1-Z2) \times 0.12]$

$*BPB = BP1 + [(Z1-ZB) \times 0.12]$

$*BPM = BP1 + [(Z1-GMH) \times 0.12]$

$*BPW = BP1 + [(Z1) \times 0.12]$

$ATK1 = AT1 + 273.160$

$ATK2 = AT2 + 273.160$

$DPK1 = DP1 + 273.160$

$DPK2 = DP2 + 273.160$

$A1 = 373.160/DPK1$

$A2 = 373.160/DPK2$

$B1 = A1 - 1.000$

$B2 = A2 - 1.000$

$$C1 = 1.000 - \left(\frac{1}{A1}\right)$$

$$C2 = 1.000 - \left(\frac{1}{A2}\right)$$

$GGC10 = -3.49149$

$GGC11 = 11.344$

$GGC12 = 5.02808$

$GGC13 = -7.90298$

$GGC14 = 8.1328 \times 10^{-3}$

$GGC15 = -1.3816 \times 10^{-7}$

$D1 = [10^{(GGC10) \times (B1)}] - 1.000$

$D2 = [10^{(GGC10) \times (B2)}] - 1.000$

$*F1 = [10^{(GGC11) \times (C1)}] - 1.000$

$*F2 = [10^{(GGC11) \times (C2)}] - 1.000$

$VP1 = BP1 \times (A1)^{GGC12} \times 10^{[GGC13 \times B1] + [GGC14 \times D1] + [GGC15 \times F1]}$

$VP2 = BP2 \times (A2)^{GGC12} \times 10^{[GGC13 \times B2] + [GGC14 \times D2] + [GGC15 \times F2]}$

$G1 = 373.160/ATK1$

$G2 = 373.160/ATK2$

$Q1 = G1 - 1.000$

$$Q2 = G2 - 1.000$$

$$J1 = 1.000 - \left[\frac{1}{G1}\right]$$

$$J2 = 1.000 - \left[\frac{1}{G2}\right]$$

$$K1 = [10^{(GGC10)\times(Q1)}] - 1.000$$

$$K2 = [10^{(GGC10)\times(Q2)}] - 1.000$$

$$M1 = [10^{(GGC11)\times(J1)}] - 1.000$$

$$M2 = [10^{(GGC11)\times(J2)}] - 1.000$$

$$* SVP1 = BP1 \times (G1)^{GGC12} \times 10^{[GGC13\times Q1]+[GGC14\times K1]+[GGC15\times M1]}$$

$$* SVP2 = BP2 \times (G2)^{GGC12} \times 10^{[GGC13\times Q2]+[GGC14\times K2]+[GGC15\times M2]}$$

$$WVGC = 4.6150 \times 10^2$$

$$AH1 = (VP1) \times \left[\frac{100}{(WVGC)(ATK1)}\right]$$

$$AH2 = (VP2) \times \left[\frac{100}{(WVGC)(ATK2)}\right]$$

$$RH1 = \left[\frac{VP1}{SVP1}\right] \times 100$$

$$RH2 = \left[\frac{VP2}{SVP2}\right] \times 100$$

$$* SH1 = \frac{0.622 \times VP1}{BP1 - (0.378 \times VP1)}$$

$$* SH2 = \frac{0.622 \times VP2}{BP2 - (0.378 \times VP2)}$$

$$VTK1 = (ATK1) \times [1.000 + (SH1 \times 0.608)]$$

$$VTK2 = (ATK2) \times [1.000 + (SH2 \times 0.608)]$$

$$VT1 = VTK1 - 273.160$$

$$VT2 = VTK2 - 273.160$$

$$PTK1 = (ATK1) + (0.0098 \times Z1)$$

$$PTK2 = (ATK2) + (0.0098 \times Z2)$$

$$PT1 = PTK1 - 273.160$$

$$PT2 = PTK2 - 273.160$$

$$VPTK1 = (VTK1) + (0.0098 \times Z1)$$

$$VPTK2 = (VTK2) + (0.0098 \times Z2)$$

$$VPT1 = VPTK1 - 273.160$$

$VPT2 = VPTK2 - 273.160$

$WSM = \dfrac{WS1 + WS2}{2}$

$* WSD = (WS1 - WS2)$

If $|WSD| < (WSM \times .028)$, then set:

$WSD = +(WSM \times .028)$

$SHD = (SH1 - SH2)$

*If $|SHD| < .08 \times 10^{-3}$ and $DP2 > WTB$, then set:

$SHD = + .08 \times 10^{-3}$

*If $|SHD| < .08 \times 10^{-3}$ and $DP2 \leqslant WTB$, then set:

$SHD = -.08 \times 10^{-3}$

$*PTKD = (PTK1 - PTK2)$

*If $|PTKD| < .008$ and $PT2 \geqslant WTB$, then set:

$PTKD = +.008$

*If $|PTKD| < .008$ and $PT2 < WTB$, then set:

$PTKD = -.008$

$* DWSDZ = \dfrac{WSD}{GMH \times Ln(Z1/Z2)}$

$* DSHDZ = \dfrac{SHD}{GMH \times Ln(Z1/Z2)}$

$* DPTDZ = \dfrac{PTKD}{GMH \times Ln(Z1/Z2)}$

$ATKM = \dfrac{ATK1 + ATK2}{2}$

$VPTKM = \dfrac{VPTK1 + VPTK2}{2}$

$GA = 9.7959$

$RI = \dfrac{(GA) \times (DPTDZ)}{(VPTKM) \times [DWSDZ]^2}$

If $RI < -2.0$, then ZOL = "NOT COMPUTED"

If $-2.0 \leqslant RI \leqslant 0$, then compute ZOL as a function of RI solving the below equation in reverse via the Newton-Raphson Method for:

$$RI = [0.74(ZOL)] \times \frac{[1 - 15(ZOL)]^{1/2}}{[1 - 9(ZOL)]^{1/2}}$$

Let $J = RI$ as an arbitrary starting point and

$$ZOL^{J+1} = ZOL^J - \frac{F(ZOL^J)}{F'(ZOL^J)}$$

Where:

ZOL^J is the current guess.

ZOL^{J+1} is the next iteration.

and

$$F(ZOL) = \frac{.74(ZOL)[1 - 15(ZOL)]^{1/2}}{[1 - 9(ZOL)]^{1/2}} - RI$$

$$F'(ZOL) = \left[(.74)[1 - 15(ZOL)]^{1/2}\right] - \left[\frac{11.1(ZOL)}{[2-30(ZOL)]^{1/2}}\right] + \left[\frac{9(RI)}{[2-18(ZOL)]^{1/2}}\right]$$

Execute the iterations until:

$$\frac{|ZOL^{J+1} - ZOL^J|}{|ZOL^{J+1}|} < .0005$$

At which point an exceptable value for ZOL has been computed.

Then:

$$MOL = \frac{GMH}{ZOL}$$

$$Z1OL = \frac{Z1}{MOL}$$

$$Z2OL = \frac{Z2}{MOL}$$

$$W1 = [1 - 15(Z1OL)]^{1/4}$$

$$W2 = [1 - 15(Z2OL)]^{1/4}$$

$$Y1 = [1 - 9(Z1OL)]^{1/2}$$

$$Y2 = [1 - 9(Z2OL)]^{1/2}$$

With *arctan* expressed in radians:

$$PSI1Z1 = 2 \times Ln\left(\frac{1 + W1}{2}\right) + Ln\left(\frac{1 + (W1)^2}{2}\right) - [2\ arctan(W1)] + \frac{\pi}{2}$$

$$PSI1Z2 = 2 \times Ln\left(\frac{1 + W2}{2}\right) + Ln\left(\frac{1 + (W2)^2}{2}\right) - [2\ arctan(W2)] + \frac{\pi}{2}$$

$$PSI2Z1 = Ln\left(\frac{1 + Y1}{2}\right)$$

$$PSI2Z2 = Ln\left(\frac{1 + Y2}{2}\right)$$

If $RI > +0.2$, then ZOL = "NOT COMPUTED"

If $+0.2 \geqslant RI > 0$, then compute ZOL as a function of RI solving the below equation in reverse via the Quadratic Solution for:

$$RI = \frac{0.74(ZOL) + 4.7(ZOL)^2}{[1 + 4.7(ZOL)]^2}$$

Let:

$$ZOL = \frac{-B - \sqrt{B^2 - 4(A \times C)}}{2(A)}$$

Where:

$$A = (22.09 \times RI) - 4.7$$

$$B = (9.4 \times RI) - 0.74$$

$$C = RI$$

Then:

$$MOL = \frac{GMH}{ZOL}$$

$$Z1OL = \frac{Z1}{MOL}$$

$$Z2OL = \frac{Z2}{MOL}$$

$$PSI1Z1 = -4.7(Z1OL)$$

$$PSI1Z2 = -4.7(Z2OL)$$

$$PSI2Z1 = \frac{-4.7(Z1OL)}{0.74}$$

$$PSI2Z2 = \frac{-4.7(Z2OL)}{0.74}$$

$$ZOLT = \frac{ZB}{MOL}$$

$$*VKC = 0.4$$

$$*WSSLOP = \left| \frac{[Ln(Z1) - PSI1Z1] - [Ln(Z2) - PSI1Z2]}{WSD} \right|$$

$$*SHSLOP = \frac{[Ln(Z1) - PSI2Z1] - [Ln(Z2) - PSI2Z2]}{SHD}$$

$$*PTKSLOP = \frac{[Ln(Z1) - PSI2Z1] - [Ln(Z2) - PSI2Z2]}{PTKD}$$

$$*TURD = (TUR1 - TUR2)$$

*If $|TURD| < .05$, then set $[Ln(TUR1) - Ln(TUR2)] = -3.0$

$$*TURSLOP = \frac{[Ln(ZTUR1) - Ln(ZTUR2)]}{[Ln(TUR1) - Ln(TUR2)]}$$

$$FRICV = \frac{VKC}{WSSLOP}$$

$$*RLC10 = -2.501$$

$$*RLC11 = +1.465$$

$$*RLC12 = -6.743$$

$$*RLC13 = -10.700$$

$$*RLC14 = -6.875$$

$$*LOGFV = Log_{10}(FRICV)$$

$$*RUFL = 10^{RLC10 + RLC11(LOGFV) + RLC12(LOGFV)^2 + RLC13(LOGFV)^3 + RLC14(LOGFV)^4}$$

$$SCLSH = \frac{VKC}{0.74(SHSLOP)}$$

$$SCLPT = \frac{VKC}{0.74(PTKSLOP)}$$

$$VTKM = \frac{VTK1 + VTK2}{2}$$

$$*AIRD = \frac{.34838(BPM)}{VTKM}$$

$$SPHEAT = 0.240\left[1 + 0.90\left[\frac{SH1 + SH2}{2}\right]\right] \times 10^3$$

$$MOFLX = -(AIRD) \times (FRICV)^2$$

$$HUFLX = -(AIRD) \times (FRICV) \times (SCLSH)$$

$$HEFLX = -(AIRD) \times (FRICV) \times (SCLPT) \times [(SPHEAT) \times 4.18684]$$

$$ATM = ATKM - 273.160$$

$$LHV = [597.31 - [.56525(ATM)]] \times 10^3$$

$$*LHFLX = (HUFLX) \times [(LHV) \times (4.18684)]$$

$$*THFLX = HEFLX + LHFLX + SR$$

$$*BR = \frac{HEFLX}{LHFLX}$$

$$LAMBDA = 5.4 \times 10^{-6}$$

$$*OPTIR1 = \left[\frac{77.6(BP1)}{(ATK1)^2}\right]^2 \times \left[1 + \frac{7.53 \times 10^9}{(LAMBDA)^2}\right]^2 \times (TUR1) \times 10^{-12}$$

$$*OPTIR2 = \left[\frac{77.6(BP2)}{(ATK2)^2}\right]^2 \times \left[1 + \frac{7.53 \times 10^9}{(LAMBDA)^2}\right]^2 \times (TUR2) \times 10^{-12}$$

$$*IPRZ = \frac{Ln(Z1) - Ln(ZB)}{Ln(Z1) - Ln(Z2)}$$

$$*IPRTUR = \frac{Ln(Z1) - Ln(ZB)}{Ln(ZTUR1) - LN(ZTUR2)}$$

$$*WSB = WS1 - [IPRZ\ (WS1 - WS2)]$$

$$*DPKB = DPK1 - [IPRZ(DPK1 - DPK2)]$$

$$*ATKB = ATK1 - [IPRZ\ (ATK1 - ATK2)]$$

$$*TRT = Ln\ (TUR1) - \left[IPRTUR \times Ln\left(\frac{TUR1}{TUR2}\right)\right]$$

$$TURT = exp(TRT)$$

$$*DRAG = \left(\frac{FRICV}{WSB}\right)^2$$

$$DPB = DPKB - 273.160$$

$$ATB = ATKB - 273.160$$

$$AB = 373.160/DPKB$$

$$BB = AB - 1.000$$

$$CB = 1.000 - \left(\frac{1}{AB}\right)$$

$$DB = [10^{(GGC10)\times(BB)}] - 1.000$$

$$FB = [10^{(GGC11)\times(CB)}] - 1.000$$

$$*VPB = BPB \times (AB)^{GGC12} \times 10^{[GGC13\times BB]+[GGC14\times DB]+[GGC15\times FB]}$$

$$GB = 373.160/ATKB$$

$$QB = GB - 1.000$$

$$JB = 1.000 - \left(\frac{1}{GB}\right)$$

$$KB = [10^{(GGC10)\times(QB)}] - 1.000$$

$$MB = [10^{(GGC11)\times(JB)}] - 1.000$$

$$*SVPB = BPB \times (GB)^{GGC12} \times 10^{[GGC13\times QB]+[GGC14\times KB]+[GGC15\times MB]}$$

$$AHB = (VPB) \times \left[\frac{100}{(WVGC) \times (ATKB)}\right]$$

$$RHB = \left[\frac{VPB}{SVPB}\right] \times 100$$

$$*SHB = \frac{0.622 \times VPB}{BPB - (0.378 \times VPB)}$$

$$VTKB = (ATKB) \times [1.000 + (SHB \times 0.608)]$$

$$VTB = VTKB - 273.160$$

$$PTKB = (ATKB) + [0.0098 \times ZB]$$

$$PTB = PTKB - 273.160$$

$$VPTKB = (VTKB) + [0.0098 \times ZB]$$

$$VPTB = VPTKB - 273.160$$

$$WTKB = WTB + 273.160$$

$$ATWTB = ATKB - WTKB$$

$$PTWTB = PTKB - WTKB$$

$$VTWTB = VTKB - WTKB$$

$$VPTWTB = VPTKB - WTKB$$

$$SHTC = 0.92 \times 10^{-3}$$

$$SPHEATB = 0.240[1 + 0.90\ (SHB)] \times 10^{3}$$

$$*AIRDB = \frac{.34838(BPB)}{VTKB}$$

$$VVPTC = 0.002 - [(SHTC) \times (WSB) \times (PTWTB)]$$

$$HEFLXB = (AIRDB) \times (VVPTC) \times [(SPHEATB) \times 4.18684]$$

$$AW = 373.160/WTKB$$

$$BW = AW - 1.000$$

$$CW = 1.000 - \left[\frac{1}{AW}\right]$$

$$DW = [10^{(GGC10)\times(BW)}] - 1.000$$

$$FW = [10^{(GGC11)\times(CW)}] - 1.000$$

$$*VPW = BPW \times (AW)^{GGC12} \times 10^{[GGC13\times BW]+[GGC14\times DW]+[GGC15\times FW]}$$

$$AHW = (VPW) \times \left[\frac{100}{(WVGC) \times (WTKB)}\right]$$

$$MTC = 1.32 \times 10^{-3}$$

$$VVHC = (MTC) \times (WSB) \times [AHW - AHB]$$

$$HUFLXB = VVHC$$

$$LHVB = \{597.31 - [.56525(ATB)]\} \times 10^{3}$$

$$*LHFLXB = (HUFLXB) \times [(LHVB) \times (4.18684)]$$

$$*THFLXB = HEFLXB + LHFLXB + SR$$

$$*BRB = \frac{HEFLXB}{LHFLXB}$$

$$DRAGB = \{0.63 + [0.066(WSB)]\} \times 10^{-3}$$

$$*SSTRES = (DRAGB) \times (WSB)^{2} \times (AIRDB)$$

$$*VVLC = -SSTRES/AIRDB$$

$$*MOFLXB = -(SSTRES)$$

$$*FRICVB = \left[\frac{(SSTRES)}{(AIRDB)}\right]^{1/2}$$

$$*LOGFVB = Log_{10}(FRICVB)$$

$$*RUFLB = 10^{RLC10 + RLC11(LOGVB) + RLC12(LOGVB)^{2} + RLC13(LOGVB)^{3} + RLC14(LOGVB)^{4}}$$

$$SCLSHB = \frac{-HUFLXB}{(AIRDB) \times (FRICVB)}$$

$$SCLPTB = \frac{-HEFLXB}{(AIRDB) \times (FRICVB) \times [4.18684(SPHEATB)]}$$

$$MOLB = \frac{-(ATKB) \times [FRICVB]^3}{(GA) \times (VVPTC) \times (VKC)}$$

$$ZOLB = \frac{GMH}{MOLB}$$

If $ZOLB \leqslant 0$, then:

$$RIB = [0.74(ZOLB)] \times \frac{[1 - 15(ZOLB)]^{1/2}}{[1 - 9(ZOLB)]^{1/2}}$$

If $ZOLB > 0$, then:

$$RIB = \frac{(ZOLB) \times [0.74 + 4.7(ZOLB)]}{[1 + 4.7(ZOLB)]^2}$$

$$ZOLTB = \frac{ZB}{MOLB}$$

$$*OPTIRT = \left[\frac{(77.6) \times (BPB)}{(ATKB)^2}\right]^2 \times \left[1 + \frac{7.53 \times 10^9}{(LAMBDA)^2}\right]^2 \times (TURT) \times 10^{-12}$$

$$*EWSD = \frac{.028(WSM)}{|WSD|} \times 100$$

$$*ESHD = \frac{.08 \times 10^{-3}}{|SHD|} \times 100$$

$$*EPTD = \frac{.008}{|PTKD|} \times 100$$

$$*EWSPD = EWSD$$

$$*ESHPD = ESHD$$

$$*EPTPD = EPTD$$

$$*ERI = EPTPD + 2(EWSPD)$$

*If $RI \leqslant 0$, then set :

$$EZOL = ERI$$

*If $RI > 0$, then set:

$$EZOL = [1 + (10|RI|)] \times ERI$$

$$*EPSID = \left[\frac{|ZOL| + .2}{4}\right] \times EZOL$$

$$*EZOLT = EZOL$$

$$*EWSSLP = EPSID + EWSD$$

$$*ESHSLP = EPSID + ESHD$$

$$*EPTSLP = EPSID + EPTD$$

$$*EFRICV = EWSSLP$$

$$*EDRAG = 2(EFRICV)$$

$$*ERUFL = EFRICV + 20$$

$$*ESCLSH = ESHSLP$$

$$*ESCLPT = EPTSLP$$

$$*EMOFLX = 2(EFRICV)$$

$$*EHUFLX = EFRICV + ESCLSH$$

$$*EHEFLX = EFRICV + ESCLPT$$

$$*ELHFLX = EHUFLX$$

$$*EBR = EHEFLX + ELHFLX$$

$$*ESR = \frac{(|SR| + 14) \times .05}{|SR|} \times 100$$

$$*DHEFLX = |(HEFLX)| \times (EHEFLX)$$

$$*DLHFLX = |(LHFLX)| \times (ELHFLX)$$

$$*DSR = |(SR)| \times (ESR)$$

$$*DH = |HEFLX| + |LHFLX| + |SR|$$

$$*ETHFLX = \left[\left(\frac{DHEFLX}{DH}\right)^2 + \left(\frac{DLHFLX}{DH}\right)^2 + \left(\frac{DSR}{DH}\right)\right]^{1/2}$$

$$*EZB = 3$$

$$*EWSB = 3$$

$$*ESHTC = 55$$

$$*EMTC = 25$$

$$*EDRAGB = 40$$

$$*EPTWTB = \frac{0.5}{|PTWTB|} \times 100$$

$$*EAHWB = \frac{0.4 \times 10^{-3}}{|AHW - AHB|} \times 100$$

$$*EVVPTC = ESHTC + EWSB + EPTWTB$$

$$*EHEFXB = EVVPTC$$

$$*EVVHC = EMTC + EWSB + EAHWB$$

$$*EHUFXB = EVVHC$$

$$*ELHFXB = EHUFXB$$

$$*EBRB = EHEFXB + ELHFXB$$

$$*ESRB = ESR$$

$$*DHEFXB = |(HEFLXB)| \times (EHEFXB)$$

$$*DLHFXB = |(LHFLXB)| \times (ELHFXB)$$

$$*DSRB = DSR$$

$$*DHB = |HEFLXB| + |LHFLXB| + |SR|$$

$$*ETHFXB = \left[\left(\frac{DHEFXB}{DHB}\right)^2 + \left(\frac{DLHFXB}{DHB}\right)^2 + \left(\frac{DSRB}{DHB}\right)^2\right]^{1/2}$$

$*ESTRES = EDRAGB + 2(EWSB)$

$*EVVHC = ESTRES$

$*EMOFXB = ESTRES$

$*EFRICB = 0.5(ESTRES)$

$*ERUFLB = EFRICB + 20$

$*ESLSHB = EHUFXB + EFRICB$

$*ESLPTB = EHEFXB + EFRICB$

$*EMOLB = 3(EFRICB) + EVVPTC$

$*EZOLB = EMOLB + EZB$

$*EZOLTB = EZOLB$

* If $ZOLB \leqslant 0$, then set:

$$ERIB = EZOLB$$

* If $ZOLB > 0$, then set:

$$ERIB = \frac{EZOLB}{1+(10|RIB|)}$$

$$*WMRI = \left(\frac{RI}{ERI} + \frac{RIB}{ERIB}\right) / \left(\frac{1}{ERI} + \frac{1}{ERIB}\right)$$

$$*WMZOLT = \left(\frac{ZOLT}{EZOLT} + \frac{ZOLTB}{EZOLTB}\right) / \left(\frac{1}{EZOLT} + \frac{1}{EZOLTB}\right)$$

$$*WMMOFX = \left(\frac{MOFLX}{EMOFLX} + \frac{MOFLXB}{EMOFXB}\right) / \left(\frac{1}{EMOFLX} + \frac{1}{EMOFXB}\right)$$

$$*WMHUFX = \left(\frac{HUFLX}{ELMFLX} + \frac{HUFLXB}{ELHFXB}\right) / \left(\frac{1}{ELHFLX} + \frac{1}{ELMFXB}\right)$$

$$*WMLHFX = \left(\frac{LHFLX}{ELHFLX} + \frac{LHFLXB}{ELMFXB}\right) / \left(\frac{1}{ELHFLX} + \frac{1}{ELHFXB}\right)$$

$$*WMHEFX = \left(\frac{HEFLX}{EHEFLX} + \frac{HEFLXB}{EHEFXB}\right) / \left(\frac{1}{EHEFLX} + \frac{1}{EHEFXB}\right)$$

$*WMSR = SR$

$$*WMTHFX = \left(\frac{THFLX}{ETHFLX} + \frac{THFLXB}{ETHFXB}\right) / \left(\frac{1}{ETHFLX} + \frac{1}{ETHFXB}\right)$$

$$*WMBR = \left(\frac{BR}{EBR} + \frac{BRB}{EBRB}\right) / \left(\frac{1}{EBR} + \frac{1}{EBRB}\right)$$

$$*WMFRIC = \left(\frac{FRICV}{EFRICV} + \frac{FRICVB}{EFRICB}\right) / \left(\frac{1}{EFRICV} + \frac{1}{EFRICB}\right)$$

$$*WMSLSH = \left(\frac{SCLSH}{ESCLSH} + \frac{SCLSMB}{ESLSMB}\right) / \left(\frac{1}{ESCLSH} + \frac{1}{ESLSHB}\right)$$

$$* WMSLPT = \left[\frac{SCLPT}{ESCLPT} + \frac{SCLPTB}{ESLPTB}\right] / \left[\frac{1}{ESCLPT} + \frac{1}{ESLPTB}\right]$$

$$* WMRUFL = \left[\frac{RUFL}{ERUFL} + \frac{RUFLB}{ERUFLB}\right] / \left[\frac{1}{ERUFL} + \frac{1}{ERUFLB}\right]$$

$$* WMDRAG = \left[\frac{DRAG}{EDRAG} + \frac{DRAGB}{EDRAGB}\right] / \left[\frac{1}{EDRAG} + \frac{1}{EDRAGB}\right]$$

$$* SDRI = \left[\frac{(RI - WMRI)^2 + (RIB - WMRI)^2}{2}\right]^{1/2}$$

$$* SDZOLT = \left[\frac{(ZOLT - WMZOLT)^2 + (ZOLTB - WMZOLT)^2}{2}\right]^{1/2}$$

$$* SDMOFX = \left[\frac{(MOFLX - WMMOFX)^2 + (MOFLXB - WMMOFX)^2}{2}\right]^{1/2}$$

$$* SDLHFX = \left[\frac{(LHFLX - WMLHFX)^2 + (LHFLXB - WMLMFX)^2}{2}\right]^{1/2}$$

$$* SDHEFX = \left[\frac{(HEFLX - WMHEFX)^2 + (HEFLXB - WMHEFX)^2}{2}\right]^{1/2}$$

$$* SDSR = 0$$

$$* SDTHFX = \left[\frac{(THFLX - WMTHFX)^2 + (THFLXB - WMTMFX)^2}{2}\right]^{1/2}$$

$$* SDBR = \left[\frac{(BR - WMBR)^2 + (BRB - WMBR)^2}{2}\right]^{1/2}$$

$$* SDFRIC = \left[\frac{(FRICV - WMFRIC)^2 + (FRICVB - WMFRIC)^2}{2}\right]^{1/2}$$

$$* SDSLSH = \left[\frac{(SCLSH - WMSLSH)^2 + (SCLSHB - WMSLSH)^2}{2}\right]^{1/2}$$

$$* SDSLPT = \left[\frac{(SCLPT - WMSLPT)^2 + (SCLPTB - WMSLPT)^2}{2}\right]^{1/2}$$

$$* SDRUFL = \left[\frac{(RUFL - WMRUFL)^2 + (RUFLB - WMRUFL)^2}{2}\right]^{1/2}$$

$$* SDDRAG = \left[\frac{(DRAG - WMDRAG)^2 + (DRAGB - WMDRAG)^2}{2}\right]^{1/2}$$

$$* \text{If } |WMRI| > .02, \text{ then: } DFRI = \frac{SDRI}{|WMRI|} \times 100$$

$$* \text{If } |WMRI| \leqslant .02, \text{ then: } DFRI = \frac{SDRI}{.02} \times 100$$

$$* \text{If } |WMZOLT| > .02, \text{ then: } DFZOLT = \frac{SDZOLT}{|WMZOLT|} \times 100$$

$$* \text{If } |WMZOLT| \leqslant .02, \text{ then: } DFZOLT = \frac{SDZOLT}{.02} \times 100$$

$*\text{If } |WMMOFX| > .06, \text{ then: } DFMOFX = \frac{SDMOFX}{|WMMOFX|} \times 100$

$*\text{If } |WMMOFX| \leqslant .06, \text{ then: } DFMOFX = \frac{SDMOFX}{.06} \times 100$

$*\text{If } |WMLHFX| > 20, \text{ then: } DFLMFX = \frac{SDLMFX}{|WMLHFX|} \times 100$

$*\text{If } |WMLHFX| \leqslant 20, \text{ then: } DFLHFX = \frac{SDLHFX}{20} \times 100$

$*\text{If } |WMHEFX| > 3, \text{ then: } DFHEFX = \frac{SDHEFX}{|WMHEFX|} \times 100$

$*\text{If } |WMHEFX| \leqslant 3, \text{ then: } DFHEFX = \frac{SDHEFX}{3} \times 100$

$*DFSR = 0$

$*\text{If } |WMTHFX| > 30, \text{ then } DFTMFX = \frac{SDTMFX}{|WMTMFX|} \times 100$

$*\text{If } |WMTHFX| \leqslant 30, \text{ then } DFTMFX = \frac{SDTHFX}{30} \times 100$

$*\text{If } |WMBR| > .08, \text{ then } DFBR = \frac{SDBR}{|WMBR|} \times 100$

$*\text{If } |WMBR| \leqslant .08, \text{ then } DFBR = \frac{SDBR}{.08} \times 100$

$*\text{If } |WMFRIC| > 6 \times 10^{-2}, \text{ then } DFFRIC = \frac{SDFRIC}{|WMFRIC|} \times 100$

$*\text{If } |WMFRIC| \leqslant 6 \times 10^{-2}, \text{ then } DFFRIC = \frac{SDFRIC}{6} \times 10^{-2} \times 100$

$*\text{If } |WMSLSH| > 3 \times 10^{-5}, \text{ then } DFSLSH = \frac{SDSLSH}{|WMSLSH|} \times 100$

$*\text{If } |WMSLSM| \leqslant 3 \times 10^{-5}, \text{ then } DFSLSH = \frac{SDSLSH}{3 \times 10^{-5}} \times 100$

$*\text{If } |WMSLPT| > 2 \times 10^{-2}, \text{ then } DFSLPT = \frac{SDSLPT}{|WMSLPT|} \times 100$

$*\text{If } |WMSLPT| \leqslant 2 \times 10^{-2}, \text{ then } DFSLPT = \frac{SDSLPT}{2 \times 10^{-2}} \times 100$

$*\text{If } |WMRUFL| > 6 \times 10^{-5}, \text{ then } DFRUFL = \frac{SDRUFL}{|WMRUFL|} \times 100$

$*\text{If } |WMRUFL| \leqslant 6 \times 10^{-5}, \text{ then } DFRUFL = \frac{SDRUFL}{|WMDRAG|} \times 100$

$*\text{If } |WMDRAG| > 4 \times 10^{-4}, \text{ then } DFDRAG = \frac{SDDRAG}{|WMDRAG|} \times 100$

$*\text{If } |WMDRAG| \leqslant 4 \times 10^{-4}, \text{ then } DFDRAG = \frac{SDDRAG}{4 \times 10^{-4}} \times 100$

$* WMMOL = \frac{ZB}{WMZOLT}$

$* WMZOL = \frac{GMH}{WMMOL}$

Equations and symbols deleted since the previous experiment:

BP

DVPTDZ

VPTKSLOP

SCLVPT

SCLVPTB

BOYFLX

BOYFLXB

RSTRES